Heat and water transfer in bare topsoil and the lower atmosphere
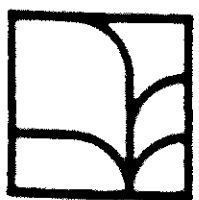
H.F.M. ten Berge

Heat and water transfer
in bare topsoil and
the lower atmosphere

H.F.M. ten Berge

Contents

Acknowledgements

1 Introduction

1.1 The occurrence and significance of bare soils

Bare soil surfaces occur for part of the year in all agro-climatological zones. Often, the lack of plant cover is the result of the adverse physical conditions of certain seasons. In the humid temperate and cold regions, large tracts of arable land remain bare in winter because of low temperatures. Under Mediterranean conditions, both winter cold and summer drought may limit crop growth, and in the semi-arid and subhumid tropics, where arable land is often cultivated during a short growing season, drought and sometimes also high temperatures inhibit plant establishment and growth during the dry season. In semi-arid zones, rangeland may also be very sparsely vegetated for much of the year. Aside from this seasonal absence of vegetation, certain crops are cultivated in a manner that keeps most of the soil surface bare continuously, and in some dry farming systems one may find rotation schemes that include a year fallow, in order to store soil moisture for the next growing season.

After the oceans, the land surface is the major distributor of solar energy on the earth's surface. Accordingly, surface conditions have a strong influence on our everyday environment. Heat and moisture, momentum and kinetic energy are carried to and from the earth's surface by a variety of transport processes in soil and atmosphere, thus providing a buffering mechanism that keeps the planet habitable. The transitions from liquid water to vapour flow, from molecular diffusion to bulk mass transport, and from conductive to radiative heat transfer all occur at or very near the soil-atmosphere interface. In addition, the interaction between surface and atmosphere is essential for the production of turbulence, and it also creates a 'sink' for momentum through frictional drag at the earth's surface. Clearly, surface conditions affect the developments in the lower atmosphere through various processes, as much as they affect the behaviour of the soil itself.

On bare surfaces, the physical properties of soil determine the hydraulic and thermal response of the topsoil to variations in meteorological conditions. Examples of seasonal variations that are of agronomic interest include the spring warming of seedbed and rootzone in cold and temperate climates, the formation of soil structure and the process of slaking and crusting, macrofauna migration, and the storage and conservation of soil water. The physical response of the topsoil to daily variations in the weather plays a role in a wide variety of processes: the germination of weed and crop seeds, the occurrence of ground-frost, the movement of solutes (e.g. herbicides and nutrients), the formation of dew and the development of fungi and pests in the vegetation canopy, early

crop establishment, the moisture regime of 'dry' agricultural products near the surface, etc.

Soil management practices often intend to influence these physical processes in the topsoil. Various tillage and crop residue treatment systems have been developed ever since Neolithic times. New and old concepts continue to be evaluated, mostly empirically. A better understanding of surface processes is crucial to further developments in research on the management of the earth's surface, varying from the extrapolation of results from crop establishment trials, to water conservation, crop-weed competition and many other processes at field scale.

Now that land use is rapidly changing on a global scale, the importance of peculiarities of the different types of land surfaces in terms of physical behaviour is increasing beyond the field scale. There is general concern that changes in the vegetation cover of the earth's surface will have an impact on climate, at least on a regional scale. Bare soil represents one extreme in terms of vegetative cover, and therefore it is important to know more about the soil-atmosphere interaction over bare land surfaces on a regional scale.

1.2 Bare soils and remote sensing

In the last two decades, remote sensing techniques have become an increasingly attractive means of obtaining information about the conditions and processes occurring at the earth's surface at various scales. Radar, passive microwave and thermal infrared (TIR) systems – either airborne or operating from satellites – have been used to study bare soils. These systems provide information about a thin surface 'skin' of the soil, i.e. a layer of a few tens of micrometres (TIR) up to a few centimetres (microwaves). Although in these cases the absolute value of the measured variable is often of little interest, the relative ease with which data can be collected by remote sensing – at the desired time intervals and from large areas – is a promising aspect in itself. Being able to interpret surface signals quantitatively in terms of physical processes would greatly benefit the inventory of relevant time-dependent phenomena. Such 'monitoring' would not only yield a continuous record of conditions that determine the potential plant environment, it would also be helpful in the evaluation of soil treatments and might permit the survey of more permanent material properties associated with surface processes.

Consequently, along with the development of remote sensing capabilities, the need has evolved to relate 'superficial' signals, as registered by remote sensors, to processes and conditions that have a practical significance. Two main approaches to this problem can be distinguished in the literature on soils and remote sensing: correlation, and analysis based upon physical abstractions of reality.

In the first approach, the signal is directly correlated with the variable of practical interest. Examples of such analyses are given by Bouten & Janse

(1979) (topsoil moisture, roughness and radar backscatter), Stolp & Janse (1985) (surface slaking and radar backscatter), Lynn (1984) (soil texture, organic matter and multispectral reflectance), Heilman & Moore (1980) and Idso et al. (1975a) (topsoil moisture and radiation temperature), Idso et al. (1975b) (topsoil moisture and albedo), Reginato et al. (1976) (evaporation and radiation temperature), ten Berge et al. (1983) (texture, moisture and radiation temperature), Lynn (1985) (soil taxonomy and radiation temperature), Lamers (1985) (surface slaking and radiation temperature) and many other authors.

The alternative methods to this approach employ physical relations between fluxes and state variables (e.g. moisture content, temperature) in combination with relations between measured variables or derived parameters and the actual conditions of interest. Examples of the latter type are models expressing thermal inertia in terms of soil moisture content and bulk density (e.g. Pratt & Ellyett, 1979), or microwave emittance in terms of moisture content and temperature (e.g. Tsang et al., 1975; Choudhury et al., 1982; Dobson et al., 1985). The procedures based on physical relations use the remotely measured course of a surface state variable as a starting point to calculate the desired surface flux or state variable and usually involve the balance concept (for mass or energy). If the goal is to obtain fluxes and soil state variables (profiles), straightforward physical models are often used, with the remotely sensed boundary conditions and known system parameters as input (as applied by e.g. Stroosnijder et al. (1984) and Prevot et al. (1984) in calculations of the soil water regime, and by Hares et al. (1985) in monitoring the thermal regime of soil). If, on the other hand, system parameters (e.g. thermal inertia) and surface fluxes are sought, one encounters the so-called 'inversion' problem: now the measured course of a state variable must be used to infer system parameters and fluxes. Then, analytical approximations to a balance equation can be used, for example, to estimate evaporation and thermal inertia (Price, 1980). To do this, semi-analytical approaches are also followed, as exemplified by Menenti (1984) in his extensive treatment of calculating evaporation from thermal imagery. An alternative method of coping with the inversion problem is to use 'lookup' tables constructed from numerical simulation models (Rosema, 1975; Schieldge et al., 1980).

1.3 Simulation of transport processes and the SALSA model

In many research fields where different processes interact in an intricate way (such as the physical environment), a powerful tool for analysis is obtained by integrating existing knowledge about the various subsystems into dynamic simulation models. Remote sensing and simulation have both been used to elucidate the behaviour of the 'near surface' system through integration in time, in space or both. At the same time, both techniques should be mutually supportive: remote sensing might characterize 'states' of the system to be used in modelling, and models may help interpret images. The complementary use of both

3

techniques will certainly aid in answering questions related to the problems mentioned in Section 1.1, both on a field scale and on larger scales.

This monograph focuses on soil surface temperature as the 'remotely sensible' variable of interest. Temperature plays a central role both in the mass and the energy balance of the bare surface, and it can be measured reasonably accurately. For these reasons, surface temperature would seem to be an attractive variable to be measured by remote sensing, thus enabling one to keep track of topsoil behaviour. The questions then arise as to which phenomena can actually be monitored by infrared technology and at what accuracy, or how much noise is produced by phenomena irrelevant to us.

The study reported here attempts to answer the above questions, using a simulation model that integrates soil and atmospheric processes, and their interactions. The model is called SALSA (Soil-Atmosphere Linking Simulation Algorithm). It is a compilation of current theories about exchange processes near the bare surface. As a one-dimensional model, it describes in detail the dependence of processes on local conditions (e.g. soil properties), but on the other hand it assumes a certain lateral homogeneity in atmospheric conditions. The former characteristic allows the use of SALSA in studying phenomena of agronomic interest on a field scale (see Section 1.1). The assumption of lateral homogeneity in atmospheric conditions enables the model to be used for climate studies on a regional scale, large enough to ignore advection, but at the same time small enough to justify the use of conditions that are imposed – by larger-scale systems – at the upper end of the atmospheric boundary layer. This particular aspect, however, is beyond the scope of the present report.

In Chapter 2, many data from the literature are presented, together with the theory relevant to the formulation of the model. The ranges found for the various parameter values are later employed in a sensitivity analysis (Chapter 6) which demonstrates how simulation models may be used to look for relations between surface temperature and surface processes. Chapter 4 describes field experiments and Chapter 5 the use of field data for model validation. An error analysis is included in these chapters, and spatial variability and the scaling concept are touched on. A short description of the actual algorithm, subdivided in modules, is given in Chapter 3. The final Chapter 7 is devoted to thermal remote sensing and its potential for bare soil monitoring. It is not intended to be an exhaustive overview, but merely an illustration of how modelling can be used in remote sensing.

1.4 Other models

One might question the need for yet another numerical simulation model on transport processes in the environment. In an earlier review (ten Berge, 1986) of existing models on surface energy balance and soil thermal behaviour, 25 models to solve the combined surface energy balance and soil heat conduction equations were found in the literature. They ranged from relatively simple ana-

lytical expressions, sometimes neglecting important processes, to complicated and comprehensive numerical simulation models. Several of these have indeed been used in thermal remote sensing research, others were devised chiefly for agronomic predictions. In addition to these physical models, that review also lists many statistically-based models of soil temperature in relation to soil and environmental variables.

Irrespective of the above, however, it was felt that an 'update' would be timely. None of the models reported appeared to include a fully two-way soil-atmosphere interaction. Describing such interaction is now thought to be essential for understanding and quantitatively predicting the various surface processes. Also, concepts that allow simpler formulations (thermodynamics, matric flux potential) or enable more thorough validation procedures (scaling, spatial variability analysis) have developed in soil physics in the meantime. Finally, as soil and atmosphere should be studied as one continuum, it is desirable to compile the relevant aspects of transport theory for both 'spheres' in a single volume.

2 Transport processes: theory and modelling

2.1 General overview

This chapter deals with the theory of transport processes in soil and atmosphere underlying the formulation of the SALSA (Soil-Atmosphere Linking Simulation Algorithm) simulation model in the next chapter. Before embarking on the detailed description of the various transport processes, a global overview of the system is presented briefly.

Figure 1 shows a relational diagram of the soil-atmosphere system as viewed here: a one-dimensional system, subdivided by the soil surface into two semi-infinite sections. Although in the present context the interest is basically in the surface energy balance, it is convenient to take four budgets into account: those of mass, heat, momentum, and turbulent kinetic energy. The equations for momentum transfer are treated separately for the two orthogonal horizontal components. Also, soil temperature and air temperature are considered as two separate state variables, as are the humidity of the soil and of the atmosphere. Consequently, although only four budgets are recognized, a total of seven main variables is employed to characterize the state of the soil-atmosphere system. These state variables are temperature and moisture content in the soil, potential temperature and specific humidity in the atmosphere, the two orthogonal components of horizontal wind speed, and the turbulent kinetic energy. All of these, of course, are a function of location on the vertical axis.

As an alternative to the formulation in Figure 1 (SALSA Option A), prescribed courses of temperature, humidity and wind speed may be used – for some applications – as boundary conditions at Stevenson screen height, thus almost eliminating the atmospheric component from the continuum to be modelled. The relational diagram corresponding to such an abridged version of the modelled system is shown in Figure 2. This abridged version is called 'Option B'.

In numerical simulation, the value of each of the main state variables is calculated for each compartment of the discretized system by integrating its rate of change over time. The remaining state variables are then assumed to be in equilibrium with these main variables, and are calculated subsequently. The values of state variables apply to the centres of so-called compartments; in contrast, the fluxes operate at compartment interfaces. In the atmosphere, NN layers are distinguished, increasing in thickness from the order of 1 m at the surface to a few hundreds of metres at the top of the boundary layer. In the soil, compartment size increases from the surface downward from a few millimetres to several centimetres, and a total of N layers is used. Certain fragments

7

Figure 1. Relational diagram of the modelled soil-atmosphere system (Option A): rectangles for main state variables, valves for rates and fluxes; circles and ellipses indicate auxiliary soil and atmospheric boundary layer variables. Solid lines represent flows of entities, broken lines flows of information. Within each column, feedback mechanisms between flux and state variables are underlined. Boundary conditions are underlined.

a : albedo
ε : emissivity
λ : thermal conductivity
C : heat capacity
D : vapor diffusivity
K : hydraulic conductivity
Z_o: roughness length

replaces

indicates a pool without feedback to the system

Figure 1. Relational diagram of the modelled soil-atmosphere system (Option A). Symbols are according to Forrester (1961): rectangles for main state variables, valves for rates and fluxes; circles and ellipses indicate auxiliary soil and atmospheric boundary layer variables. Solid lines represent flows of entities, broken lines flows of information. Boundary conditions are underlined. Within each column, feedback mechanisms between flux and state variable (gradient) — usually indicated by broken lines — have been omitted.

Erratum

Berge, H.F.M. ten, 1990. Heat and water transfer in bare top-soil and the lower atmosphere. Simulation Monographs 33. Pudoc, Wageningen.

Page 8

Figure 1 should be replaced with the complete version printed overleaf.

Figure 2. Relational diagram of the simplified system, with prescribed atmospheric boundary conditions near the surface (Option B). For the explanation of symbols, see Figure 1.

of the model are based on already existing models, such as those by van Keulen (1975), van Bavel & Lascano (1979) and Nieuwstadt & Driedonks (1979).

In the following, the energy balance will be discussed first (Section 2.2) as it provides the key equation for the system under consideration. Subsequently, the terms appearing in this energy balance equation and the related mechanisms will be discussed: radiative transfer (Section 2.3), bulk turbulent transport in the atmosphere (Section 2.4), and soil thermal and hydraulic processes (Sections 2.5 and 2.6, respectively).

9

2.2 The surface energy balance

The central equation that sets boundary conditions to both the soil and the atmosphere subsystems is the energy balance equation of the surface (Lettau, 1957; Geiger, 1961):

$$R_n + H + LE + G = 0 \qquad \text{Equation 1}$$

where R_n is net radiation, H and LE are the sensible and latent heat fluxes respectively, and G is the soil heat flux, all in $W\ m^{-2}$. The equation implies that the surface itself has no capacity, i.e. no energy can be stored in it. The same assumption is made for matter. Also, Equation 1 implies that fluxes towards the surface have a sign opposite to those directed away from it. Throughout the SALSA algorithm this convention is maintained: in the programmed model, all fluxes are designated positive if directed towards the surface, and negative if directed away from it. In this text, on the other hand, this rule is not always strictly applied.

There is a strong feedback between the fluxes in Equation 1 and surface properties and conditions. Net radiation, the sum of incoming and outgoing radiation terms, is affected by soil moisture content and temperature, because these variables influence soil albedo, emissivity and emittance, respectively. The atmospheric sensible and latent heat fluxes are governed by surface temperature and humidity, and by air temperature, air humidity and an exchange coefficient. This latter coefficient depends on the magnitude of the sensible heat flux itself (stability), on wind speed, and on surface roughness. The soil heat flux is determined by thermal conductivity and heat capacity of the soil, both of which are functions of soil moisture content.

A complication that should be mentioned explicitly in this context is the relation between G and LE in Equation 1. The soil heat flux is often expressed as $G = -\lambda(\partial T/\partial z)_s$, where the index s refers to the soil surface. In the case of a dry soil surface, however, a large fraction of the required latent heat of evaporation is supplied by downward conduction through the solid soil mass. Therefore, the use of G as calculated by this expression (or as measured by heat flux plates) in Equation 1 is erroneous. Instead, the soil heat flux for field application of Equation 1 could be calculated by a variety of calorimetric methods (e.g. Horton, 1982; Kimball & Jackson, 1975). This subject has been elaborated upon by Menenti (1984), who presented several evaporation formulas that incorporate the relation between G and LE. This complication has also been recognized and accounted for by several modellers (e.g. van Keulen, 1975), but is often not accorded due attention. See also Subsection 5.1.2.

The examples mentioned indicate the mutual interdependence of surface properties and the various fluxes composing the energy balance. Van Keulen (1975) presented an elegant solution for the energy balance equation in the form of an explicit expression for surface temperature. Nevertheless, for didact-

10

ic reasons it is preferred to use an implicit solution here to obtain surface temperature from the surface energy balance equation, because errors easily creep in when a program that includes such tangled explicit expressions is being amended. An implicit solution as applied here was also used by van Bavel & Lascano (1979). It comes down to formulating the fluxes in Equation 1 as a function of surface temperature, and subsequently solving the resulting set of equations in an implicit loop to obtain surface temperature such that the sum of surface energy fluxes is equal to zero. The various fluxes will now be discussed in more detail.

2.3 Radiation

2.3.1 Shortwave radiation terms

Global radiation
Global radiation, the major fraction of daytime incoming radiation, sets one of the main boundary conditions to the system. It is the shortwave radiant flux density (W m^{-2}) received at the surface; it results from the integration of radiance (W m^{-2}sr^{-1}) over a solid angle 2π sr. The term 'shortwave' is only roughly delineated by the spectral transparancy of the glass domes employed on solarimeters. Global radiation is then defined as

$$R_{glob} = \int_{\varphi=0}^{2\pi} \int_{\psi=0}^{\pi/2} \int_{\lambda\approx0.3}^{\pi\approx3\mu m} \sin\psi \cos\psi \, R(\lambda,\psi,\varphi)d\lambda d\psi d\varphi \qquad \text{Equation 2}$$

where φ is the azimuth angle (rad), ψ the elevation (rad), λ the wavelength, and R the spectral radiance. Global radiation in crop modelling is frequently calculated from latitude, date and time (e.g. Goudriaan, 1977) and such relations could of course be used as an alternative to a measured course of global radiation, as employed in the present model.

Albedo
For a given surface and wavelength, the sum of reflectivity ρ, absorptivity α and transmissivity τ equals unity. As the soil is considered to be an opaque body, it is assumed that $\alpha + \rho = 1$. Reflectivity depends on the wavelength of incoming radiation, and in general increases with wavelength up to $\lambda = 1.2$ μm (Gerbermann, 1979; Van der Heide & Koolen, 1980; Coulson & Reynolds, 1971). As surface reflectivity is also dependent on azimuth and elevation, it will be clear that the overall fraction of shortwave radiation reflected by the surface is not a constant in reality, but depends on atmospheric conditions and the position of the sun. Therefore, albedo, the overall fraction of global radiation that is reflected, is defined as

$$a \equiv \frac{\displaystyle\int_{\varphi=0}^{2\pi}\int_{\psi=0}^{\pi/2}\int_{\lambda\approx 0.3}^{3\mu m} \rho(\lambda,\psi,\varphi)\ \sin\psi\ \cos\psi\ R(\lambda,\psi,\varphi)d\lambda d\psi d\varphi}{\displaystyle\int_{\varphi=0}^{2\pi}\int_{\psi=0}^{\pi/2}\int_{\lambda\approx 0.3}^{3\mu m} \sin\psi\ \cos\psi\ R(\lambda,\psi,\varphi)d\lambda d\psi d\varphi} \qquad \text{Equation 3}$$

which roughly corresponds to the reflected fraction of shortwave radiation as measured with a double dome solarimeter.

Several authors have reported that the albedo of bare soil depends on solar elevation (Feddes, 1971; Aase & Idso, 1975; Idso et al., 1975c). It is generally found that albedo for bare soils reaches a maximum at incidence angles ranging from 70 to 80 degrees. At a solar elevation of less than 10 degrees, Coulson & Reynolds (1971) measured a decrease of reflectivity over a wide range of wavelengths, which was attributed to the high ratio of diffuse to direct radiation that naturally occurs at sunrise and sunset. Kalma & Badham (1972) also pointed at cloud cover as a factor affecting soil albedo. Menenti (1984) mentioned several expressions to account for the position of the sun and for the distribution of radiation over direct and diffuse components. The latter author also reported a strong dependence of albedo on local time (for rough-surface playa soils). Most other sources reporting on bare field soils gave only a moderate dependence, noticeable in early morning and late afternoon. This was also the case in the field experiments conducted for the present study. As this dependence is only evident at hours when total global radiation is low, no relations between albedo and solar elavation have been incorporated in the SALSA model. Also, albedo is assumed to be independent of cloud cover and fraction of diffuse radiation, because the experiments discussed here yielded only minor variations in albedo under strongly changing sky conditions.

Clearly, soil conditions affect albedo. The influence of surface roughness on albedo as reported by van der Heide & Koolen (1980) from slaking experiments, and by Bowers & Hanks (1965) may very well be related to differences in distribution of incidence angles for different surface geometries. Mineral composition and organic matter content are known to have strong effects on albedo. Bowers & Hanks increased the albedos of different soils by up to a factor of two, oxidizing the small amounts (< 1.5%) of organic matter and carbonates present in the samples. Gerbermann (1979) mentioned that dry soil albedo generally increased with quartz content in a soil-mixing experiment, a result comparable to that obtained by Karamanov (1970), who studied the effect of ferric coatings on quartz grains. Table 1 lists albedo values for a wide range of soils under both wet and dry conditions.

The effect of moisture on albedo is marked. Angström (1925) proposed that the relation between dry soil albedo and albedo at saturation be expressed as

Table 1. Albedo values for wet and dry soils.

Soil type	Wet	Dry	Source
Dune sand	0.24	0.37	Buttner & Sutter, 1935
Arenosa sand	0.22	0.38	Graser & Bavel, 1982
Yuma sand	0.18	0.42	Gold & ben Asher, 1976
Williams loam	0.14	0.26	Aase & Idso, 1975
Avondale loam	0.14	0.30	Idso et al., 1975
Tippera clay loam	0.14	0.23	Kalma & Badham, 1972
Swifterbant silt loam	0.13	0.31	ten Berge, 1985
Grey soil	0.11	0.27	Kondrat'ev, 1954
Red-brown clay loam	0.10	0.20	Piggin & Schwertfeger, 1973
Sandy loam	0.10	0.17	Feddes, 1971
Oudelande sandy loam	0.08	0.20	van der Heide & Koolen, 1980
Clay	0.08	0.14	Feddes, 1971
Black soil	0.08	0.14	Kondrat'ev, 1954

After Idso & Reginato, 1974.

$$a_{wet} = \frac{a_{dry}}{n^2(1 - a_{dry}) + a_{dry}}$$ Equation 4

where n is the index of refraction of the liquid. This expression was supported by Planet (1970) after experiments employing fluids with different refraction indices. However, the simple relation $a_{dry} = 2\, a_{wet}$, suggested by Idso & Reginato (1974), holds better in reality, as demonstrated in Figure 3. This relation might be employed safely in modelling when more accurate data are not available.

Few data are available for intermediate moisture contents. Under laboratory conditions, Graser & van Bavel (1982) measured an exponential decrease of albedo with increasing moisture content on core samples. From field experiments, Idso et al. (1975c) reported a linear dependence of albedo on volumetric water content for Avondale loam. The Flevoland measurements discussed in the present report (Chapter 4) also yielded a linear relationship. The linear relationship between albedo, a, and volumetric soil moisture content, θ, as found for different field situations has been adopted in SALSA:

$$a(\theta) = a_{wet} + \frac{\theta_{crit} - \theta}{\theta_{crit}}(a_{dry} - a_{wet})$$ Equation 5

where θ_{crit} is the moisture content below which albedo starts increasing during drying.

13
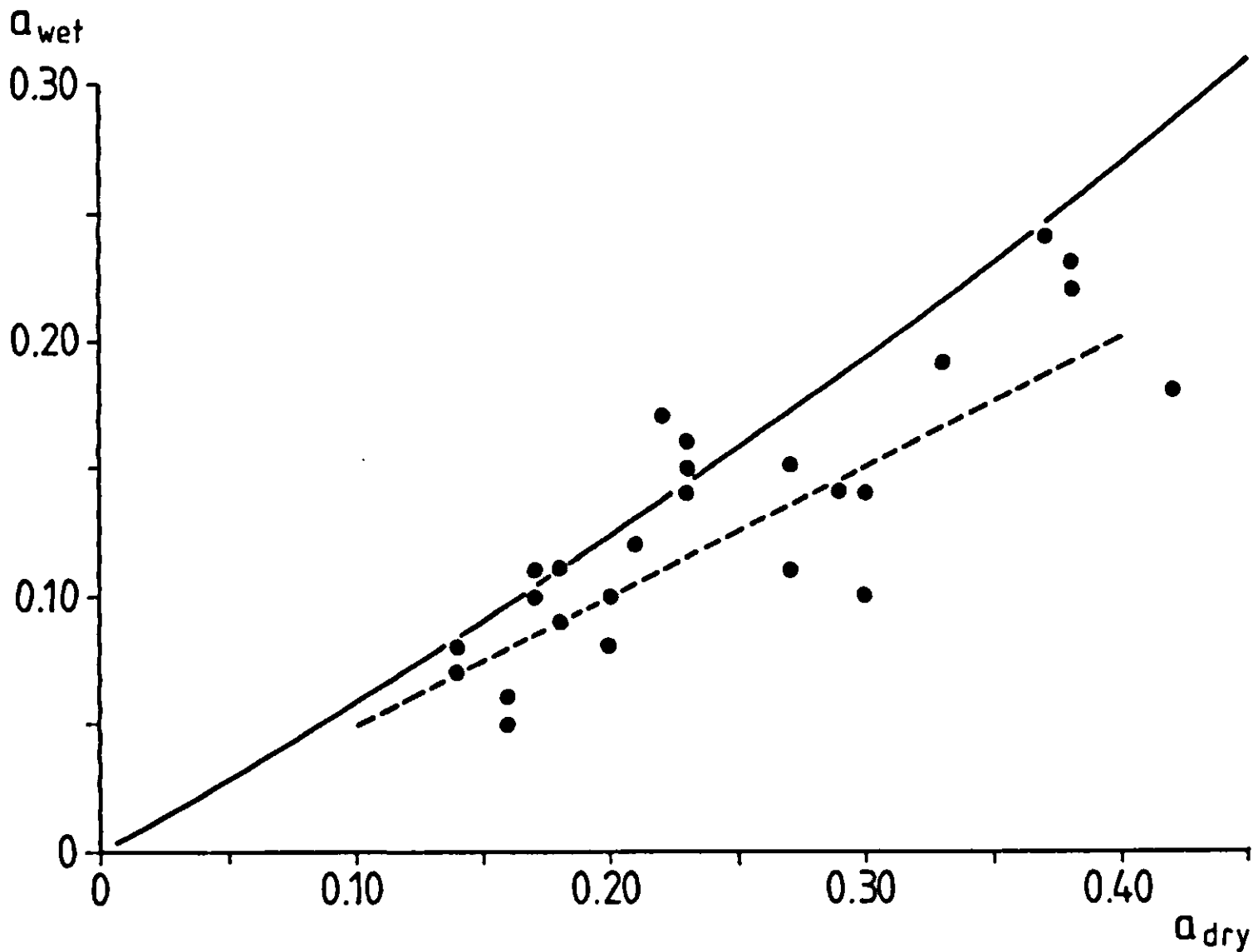
Figure 3. Wet soil albedo versus dry soil albedo for a number of soils (ten Berge, 1986). Solid line: Ånström's formula; broken line $a_{dry} = 2\,a_{wet}$.

2.3.2 Longwave radiation terms

Sky radiation

Thermal sky radiation or, more accurately, the incoming longwave radiant flux density or longwave irradiance (W m^{-2}), also constitutes an important term in the surface energy balance, its value ranging from 200 to 500 W m^{-2}. It is defined in analogy to global radiation as an integral over azimuth, elevation and wavelength (see Equation 2). In practice, the longwave radiation is often taken to be a function of air temperature at screen height (1.5 m):

$$R_{ld} = \varepsilon_{sky}\sigma T_a^4 \qquad\qquad \text{Equation 6}$$

which defines the apparent sky emissivity ε_{sky} as an empirical constant; σ is the Stefan-Bolzmann constant. It must be noted that the value of ε_{sky} is also the result of an integration over the sky hemisphere (Jacobs, 1982). The apparent clear sky emissivity has been related to water content in the atmosphere, i.e. vapour pressure or specific humidity, by empirical formulas employing power or exponential functions of these properties. Gupta (1983) has reviewed this type of expressions. In the present model, the relation proposed by Brunt (1939) is used:

Table 2. Constants for longwave sky radiation.

a	b (mbar$^{-0.5}$)	Source
0.51 –0.60	0.059–0.065	Unsworth & Monteith, 1975
0.60 –0.75	0.017–0.057	Wartena, 1973
0.605–0.75	0.048	Sellers, 1965
0.61	0.050	Budyko, 1958
0.62	0.035	Stroosnijder & van Heemst, 1982

$$\varepsilon_{sky} = a + b\sqrt{e} \qquad \text{Equation 7}$$

where e is the vapour pressure at screen height (hPa). Table 2 lists some measured values for the constants a and b. It must be realized that measuring techniques and circumstances (characteristics of the governing air mass) definitely affect the values found for these parameters (Wartena, 1973). For cloudy skies, Sellers (1965) formulated the apparent sky emissivity as

$$\varepsilon_{sky} = \varepsilon_{sky}(0)(1 + nc^2) \qquad \text{Equation 8}$$

where c is the fraction of cloud cover, and n is a parameter ranging from 0.04 for high (cirrus) cloud, to 0.2 for low cloud (Monteith, 1973). In the SALSA model, Equations 7 and 8 are used to calculate longwave radiant flux density from the sky hemisphere if measured data are not available.

Surface emittance

The longwave radiation leaving the surface (apparent emittance) consists of the terms emittance and reflection. As a reminder, the assumptions underlying the formulation of emittance will be set forth.

Planck's law for black body radiation expresses the spectral radiance in a direction normal to the surface, $R_{n\lambda}$, as a function of wavelength and absolute temperature. Applying Lambert's cosine law, the spectral emittance R_λ is found by integrating the radiance over a hemisphere. Finally, integrating R_λ over the whole wavelength interval yields the emittance. The well known Stefan-Bolzmann law expresses this radiant flux density as:

$$R_{le} = -\varepsilon\sigma T_s^4 \qquad \text{Equation 9}$$

where R_{le} is the emittance (W m^{-2}), σ the Stefan-Bolzmann constant (5.67 10^{-8}W m^{-2}K^{-4}) and T_s is the temperature of the emitting body (K); the emissivity ε is introduced as a reduction factor for non-black bodies, and is equal to the absorption factor for the corresponding wavelengths (Kirchhoff's law). For the present case, the soil is assumed to be a grey (ε independent of λ) body

15

Table 3. Soil emissivity values.

Soil type	ε dry	wet	λ (μm)	Source
Coarse silica sand	0.914	0.936	8–12	Buettner & Kern, 1965
White sand	0.890	0.925	10.4–11	Schurer, 1975
Plainfield sand	0.900	0.940	8–12	Fuchs & Tanner, 1968
Avondale loam	0.967	0.980	8–13	Idso & Jackson, 1969 and Conaway & van Bavel, 1967
Swifterbant silt loam	0.910	0.940	8–14	ten Berge, 1986

with a flat, homogeneous surface, obeying Lambert's law. Analogous to the case for the visible spectrum, opaqueness is assumed for thermal radiation as well.

Emissivity is a soil-specific property that ranges from 0.9 (dry quartz sand) to approximately 1.0, depending on organic matter content, mineral composition and moisture content. As can be seen from the data listed in Table 3, the difference in ε found between wet and dry soil, is usually 0.02-0.04. Relatively few data are available on the relation between emissivity and other soil properties. Some interesting results have been obtained in this respect by using quotients of measured emittances in small bands of different wavelength intervals within the thermal range, thus eliminating temperature. This yields quotients of spectral emissivities, sensitive to surface properties (Palluconi, 1983).

Although differences in soil emissivity are hardly significant in the energy balance of bare soils (having a negligible effect on actual surface temperature), they are of course important in the interpretation of thermal infrared imagery. Differences in ε have been reported to make cool, wet sand appear warmer on surface imagery than warm, dry sand (Buettner & Kern, 1963). The SALSA model expresses the dependence of ε on soil moisture by the empirical relationship

$$\varepsilon(\theta) = \varepsilon_{dry} + \frac{\theta}{\theta_s} (\varepsilon_{wet} - \varepsilon_{dry}) \qquad \text{Equation 10}$$

where θ_s is the moisture content at saturation (cf. Chapter 4).

The reflection compound of longwave radiation leaving the soil surface is calculated as a fraction $(1 - \alpha)$ of incoming thermal radiation, where α is the absorptivity, assumed to equal the emissivity for a given wavelength. Naturally, the same type of assumptions discussed for reflection in the visible spectrum apply to this integral quantity. Emissivity values are usually measured in the 'atmospheric window' (roughly 8-14 μm), for the obvious reason that this is the most attractive wavelength interval for remote sensing, because of low absorption by the atmopheric gases. At the same time, however, a large fraction

of the sky radiation – aside from cloud radiation – is of other wavelengths, which raises doubts about the wisdom of using $\varepsilon_{8-14 \ \mu m}$ in longwave reflectance calculations. The present author has been unable to find accurate data on reflectivity in the desired intervals, but an estimate of 0.05-0.15 could be derived from data collected by Jackson and his colleagues at USDA Water Conservation Laboratory, Phoenix, Arizona. From these data no significant dependence of longwave reflectivity on soil moisture content could be recognized.

The radiation terms discussed in Subsections 2.3.1 and 2.3.2 are finally merged into the net radiation term. In turn, this flux is included in the energy balance implicit loop, because of the temperature dependence of the emittance term:

$$R_n = (1 - a) \, R_{glob} + R_{le} + (1 - \varepsilon) \, R_{ld}$$
Equation 11

Alternatively, net radiation can be used as a driving variable imposed on the system if measured data are available, thus avoiding uncertainties in the radiative properties of soil and sky; this is useful when the model is applied to investigate fluxes and corresponding processes not directly related to radiation.

2.4 Transport in the atmospheric boundary layer

2.4.1 Exchange at the surface

As was set forth in Section 2.1, boundary conditions to the system can be chosen such that the model does or does not simulate the development of the atmospheric boundary layer (Options A and B, respectively). The equations for surface exchange are almost identical for the two cases, and will be discussed first.

Air temperature, humidity and wind speed at given height near the surface, e.g. at screen height, are either given as measured boundary conditions, or are calculated by the model as conditions resulting from surface fluxes (Subsection 2.4.2). Employing these conditions, the surface fluxes of momentum, heat and mass are expressed as functions of the vertical gradients of the relevant properties, under the assumption of no horizontal advection.

Although the flux of momentum itself is of no direct interest to the surface energy balance, it is important because the atmospheric 'resistance' to heat and mass transport is closely related to this flux. The objective now is to write the vertical turbulent fluxes of respectively momentum, heat and vapour as

$$\tau_x = \rho \, \frac{u(z_m) - u(z_o)}{r_{aM}}$$
Equation 12a

$$\tau_y = \rho \, \frac{v(z_m) - v(z_o)}{r_{aM}}$$
Equation 12b

17

$$H = \rho C_p \frac{T(z_m) - T(z_o)}{r_{aH}}$$

Equation 13

$$E = \rho \frac{q(z_m) - q(z_o)}{r_{aV}}$$

Equation 14

where the subscripts x and y refer to the two orthogonal horizontal axes. z_o is the roughness length (m), and z_m is the height (m) at which the state variables are measured or calculated; u,v are the horizontal wind velocity components (m s^{-1}), T the air temperature (°C) and q the specific humidity of the air (kg water per kg dry air). For the 'resistances' r_a, the subscripts M, H, and V refer to momentum, heat and vapour, respectively. In the calculation of these fluxes it is assumed that T and q at height z_o are equal to their values at the soil surface. The remainder of this subsection will focus on the formulation of r_a.

An important characteristic in that formulation is atmospheric stability, a function of the ratio between the fluxes of momentum and sensible heat. In an unstable situation, temperature decreases with height, which implies a decrease of atmospheric resistance because of the effect of buoyancy. Following Obukhov (1946), stability is expressed by the dimensionless parameter $\zeta \equiv z/L$, where z is the height (m) and L is the well-known Monin-Obukhov length (m), defined as

$$L \equiv \frac{\theta u_*^3}{k\, g(H/\rho C_p)} = \frac{\theta}{k} \frac{(\tau/\rho)^{3/2}}{g(H/\rho C_p)}$$

Equation 15

(k is the Von Kármán constant for wich a value of 0.41 is used here, and g the gravity acceleration constant). The friction velocity u_* is defined by the relation $\tau \equiv \rho u_*^2$ and the potential temperature θ by the equation $\theta = T(1000/p)^{0.288}$, where T and p are the actual temperature (K) and pressure (hPa) of the air, respectively. Potential temperature is the temperature an air parcel would attain if brought dry-adiabatically to a pressure of 1000 hPa. For the first metres of the surface layer the difference between θ and T is usually ignored. The stability parameter ζ has been related to the non-dimensional gradients of potential temperature and wind velocity by the semi-empirical so-called flux-profile relationships. Reviews on this topic have been given by Dyer (1974), Businger (1975), Viswanadham (1982) and others. These dimensionless gradients are defined as (Businger, 1975):

$$\varphi(z) \equiv \frac{kz}{u_*} \frac{\partial u(z)}{\partial z}$$
M

Equation 16

$$\varphi(z) \equiv \frac{kz}{\theta_*} \frac{\partial \theta(z)}{\partial z}$$
H

Equation 17

where $\theta_* \equiv (H/\rho C_p)/u_*$. The flux-profile relationships for the unstable situation are of the form

18

$$\varphi_{M,H} = (1 - a\,\zeta)^b \qquad\qquad \text{Equation 18}$$

where a and b are empirical constants, approximately 16 and -0.25 for momentum, and 16 and -0.50 for heat transfer respectively; for stable stratification, the relation $\varphi_M = \varphi_H = 1 + \beta\zeta$ is used, with $\beta = 4.7$ (Businger, 1975; Businger et al., 1971).

Equations 16 and 17 employ the local derivatives at height z. In numerical simulation, where distance is discretized into steps or compartments, the transcription of these equations into the finite difference form may be hazardous when the gradient changes rapidly with height, i.e. close to the surface. Therefore, the integral form of Equations 16 and 17, derived by Paulson (1970), is used for the expression of surface fluxes in the SALSA model. Paulson's integration, employing Equation 18, results in the wind and temperature profile equations respectively:

$$u = \frac{u_*}{k}\left(\ln\!\left(\frac{z}{z_{o,M}}\right) - \Psi_M\right) \qquad\qquad \text{Equation 19}$$

$$\theta = \theta_o + \frac{\theta_*}{k}\left(\ln\!\left(\frac{z}{z_{o,H}}\right) - \Psi_H\right) \qquad\qquad \text{Equation 20}$$

The roughness lengths $z_{o,M}$ and $z_{o,H}$ are assumed to be equal. It is directly verified that for neutral stratification ($\Psi_M = 0$) Equation 19 reduces to the well-known logarithmic wind profile equation (e.g. Monteith 1963, 1973). Now, the combination of Equations 12 and 19 (with $\tau = \rho u_*^2$) yields for the resistance to momentum transfer:

$$r_{aM} = \frac{1}{k^2 u}\left(\ln\!\left(\frac{z}{z_o}\right) - \Psi_M\right)^2 \qquad\qquad \text{Equation 21}$$

Similarly (with $\theta \approx T$), Equations 13 and 20 combine to

$$r_{aH} = \frac{1}{k^2 u}\left(\ln\!\left(\frac{z}{z_o}\right) - \Psi_M\right)\left(\ln\!\left(\frac{z}{z_o}\right) - \Psi_H\right) \qquad\qquad \text{Equation 22}$$

The stability correction functions Ψ_M and Ψ_H in Equations 19-22 are defined (Paulson, 1970) for unstable stratification as

$$\Psi_M = 2\ln((1 + \varphi_M^{-1})/2) + \ln((1 + \varphi_M^{-2})/2) - 2\arctan(\varphi_M^{-1}) + \pi/2 \quad \text{Equation 23}$$

$$\Psi_H = 2\ln((1 + \varphi_H^{-1})/2) \qquad\qquad \text{Equation 24}$$

and for stable conditions as

On the basis of similarity theory it is assumed that the aerodynamic resistance of the atmospheric boundary layer is identical for all transported constituents expressed as conservative properties, this resistance being related only to the eddy structure of the flow. Because the specific humidity q is such a property, r_{aV} in Equation 14 is taken to be equal to r_{aH}.

The sets of Equations 12-14 and 21-25, in combination with the energy balance equation, enable one to calculate stability and aerodynamic resistance with a single-level air temperature only. This is so because the Paulson integration allows the use of soil surface temperature – calculated from the surface energy balance – in conjunction with air temperature at some height above the surface. This 'integrated' procedure was also applied by Hammel et al. (1981) and Mahrer (1982). In the SALSA model the variables Ψ_M and Ψ_H are tabulated as functions of the stability parameter ζ. Note that Equations 12-14 and 21-25 are only used for the calculation of surface fluxes, i.e. the fluxes between the soil surface and the centre of the lowermost compartment of the boundary layer. For the remainder of the atmospheric boundary layer, the expressions expounded in the next subsection, including the 'differential' formulation of stability, are used (SALSA Option A).

2.4.2 Boundary layer development

The atmospheric boundary layer is the lower part of the atmosphere, which by turbulent mixing responds to the diurnal course of fluxes at the earth's surface. During daytime, its height usually ranges between a few hundred metres and a few kilometres, occasionally up to the tropopause for very unstable situations. The daytime boundary layer develops rapidly as a result of intensive mixing triggered by surface heating. At night, turbulence diminishes as one of its major sources, buoyancy, reverses its effect; a stable stratification is then built up by radiative cooling of the surface. Typically, the nocturnal boundary layer may extend to heights in the order of a few hundred metres.

The diurnal development of the boundary layer is the subject of discussion in this subsection. It involves the equations of motion, of enthalpy and mass conservation, the gradient expressions of the fluxes, and the kinetic energy budget equation. The theory set forth here is used only in the 'complete' SALSA model (Option A, Figure 1) and may be of minor importance to those interested in soil behaviour under given near-surface boundary conditions. The work by Nieuwstadt & Driedonks (1979) on the nocturnal boundary layer was used as a guideline in formulating this section of the model.

The equations of motion
Following the Reynolds theory, the three orthogonal components of velocity along the axes x, y and z respectively are usually written as

$$u = \bar{u} + u'$$
$$v = \bar{v} + v'$$

Equation 26

$$w = \bar{w} + w' \qquad \text{with } \bar{u'} = \bar{v'} = \bar{w'} = 0$$

where the bars indicate time averages, and u', v', w' are the turbulent fluctuations about the mean; w is taken along the vertical axis. The fluidum is considered incompressible, except where the buoyancy term is concerned and density depends on temperature (a Boussinesque approximation; for a summary of Boussinesque assumptions see Busch (1973) and Nieuwstadt & van Dop (1981)). The equations of motion for the mean horizontal flow then express the total or barycentric differentials respectively as

$$\frac{d\bar{u}}{dt} = \underbrace{\frac{\partial \bar{u}}{\partial t}}_{\text{I}} + \underbrace{\bar{u}\,\frac{\partial \bar{u}}{\partial x} + \bar{v}\,\frac{\partial \bar{u}}{\partial y} + \bar{w}\,\frac{\partial \bar{u}}{\partial z}}_{\text{II}}$$

$$= \underbrace{-\frac{1}{\rho}\frac{\partial \bar{p}}{\partial x}}_{\text{III}} + \underbrace{v\left[\frac{\partial^2 \bar{u}}{\partial x^2} + \frac{\partial^2 \bar{u}}{\partial y^2} + \frac{\partial^2 \bar{u}}{\partial z^2}\right]}_{\text{IV}} \underbrace{- \frac{\partial \overline{u'v'}}{\partial y} - \frac{\partial \overline{u'w'}}{\partial z}}_{\text{V}} \underbrace{+ 2\Omega\eta_3\bar{v}}_{\text{VI}} \qquad \text{Equation 27a}$$

$$\frac{d\bar{v}}{dt} = \frac{\partial \bar{v}}{\partial t} + \bar{u}\,\frac{\partial \bar{v}}{\partial x} + \bar{v}\,\frac{\partial \bar{v}}{\partial y} + \bar{w}\,\frac{\partial \bar{v}}{\partial z}$$

$$= -\frac{1}{\rho}\frac{\partial \bar{p}}{\partial y} + v\left[\frac{\partial^2 v}{\partial x^2} + \frac{\partial^2 v}{\partial y^2} + \frac{\partial^2 v}{\partial z^2}\right] - \frac{\partial \overline{u'v'}}{\partial x} - \frac{\partial \overline{v'w'}}{\partial z} - 2\Omega\eta_3\bar{u} \qquad \text{Equation 27b}$$

where v is the kinematic viscosity and Ω is the angular frequency of rotation of the earth; η is the unit vector, parallel to the axis of rotation, and η_3, its component along the z axis, equals sin φ at latitude φ. The equation for the mean flow in the vertical (analogous to Equations 27, but including a buoyancy term) is omitted because it is assumed that the mean flow $\bar{w}$ is negligible by comparison with its fluctuations w'.

In the Eulerian expressions 27, Term I is the rate of change of the local mean flow velocity at a point with fixed coordinates in space. Term II represents acceleration due to advection of momentum; III denotes acceleration down the pressure gradient; IV and V are the viscous stress terms and Reynolds terms respectively (when multiplied by ρ, these are the divergencies of the fluxes of momentum by viscous forces and turbulence, respectively). Finally, the last term, VI, in Equations 27 results from the rotation of the earth.

As molecular interaction plays a very minor role in atmospheric momentum transfer as compared with turbulence, Term IV can virtually be ignored. Further simplification is achieved if the advection terms (II) are omitted. This is a more serious limitation, because advection may play a significant role, e.g. in the nocturnal boundary layer when vertical mixing is low (Nieuwstadt & Driedonks, 1979). Nevertheless, advection is ignored for practical reasons at the moment. Moreover, horizontal divergences of the turbulent fluxes $\partial(\overline{u'v'})/\partial x$

and $\partial(\overline{u'v'})/\partial y$ are considered small in comparison with $\partial(\overline{u'w'})/\partial z$ and $\partial(\overline{v'w'})/\partial z$, and are ignored. If the vertical fluxes of momentum are then written as:

$$\tau_x = \rho\overline{u'w'} \quad \text{and} \quad \tau_y = \rho\overline{v'w'} \qquad \text{Equation 28}$$

the equations of motion reduce to

$$\frac{\partial \bar{u}}{\partial t} = -\frac{1}{\rho}\frac{\partial \bar{p}}{\partial x} - \frac{\partial}{\partial z}\frac{\tau_x}{\rho} + f\eta\bar{v} \qquad \text{Equation 29a}$$

$$\frac{\partial \bar{v}}{\partial t} = -\frac{1}{\rho}\frac{\partial \bar{p}}{\partial y} - \frac{\partial}{\partial z}\frac{\tau_y}{\rho} - f\eta\bar{u} \qquad \text{Equation 29b}$$

where the Coriolis parameter f is defined by $f\eta = 2\Omega\eta_3$ (s^{-1}); for simplicity of notation, the bars to indicate mean values will be left out in the following. Geostrophic wind is substituted for the pressure gradient term in Equations 29. For a given height z, the relations between pressure gradient and geostrophic wind are given by $u_g = (-1/f\rho)(\partial p/\partial y)$ and $v_g = (1/f\rho)(\partial p/\partial x)$ (e.g. Busch, 1973).

The difference between geostrophic winds at different levels, called thermal wind, is a function of the horizontal temperature gradient. Ignoring thermal wind by replacing the pressure gradient term by geostrophic wind at a pre-scribed level may introduce a significant error in the case of strong horizontal temperature gradients. Since the required input conditions will seldom be available, however, thermal wind is ignored, following Nieuwstadt & Driedonks (1979). Then, finally, the equations of motion for the two orthogonal horizontal components as used in the SALSA model become

$$\frac{\partial u}{\partial t} = f(v - v_g) - \frac{\partial}{\partial z}\frac{\tau_x}{\rho} \qquad \text{Equation 30a}$$

$$\frac{\partial v}{\partial t} = -f(u - u_g) - \frac{\partial}{\partial z}\frac{\tau_y}{\rho} \qquad \text{Equation 30b}$$

Conservation of mass and enthalpy

Omitting the advection terms and horizontal turbulent flux divergence as indicated above, the conservation equation for enthalpy in the vertical is written as (e.g. Businger, 1981):

$$\frac{\partial \theta}{\partial t} = -\frac{\partial}{\partial z}(\overline{w}\theta + \overline{w'\theta'}) + \Sigma S_i \qquad \text{Equation 31}$$

where again θ is the potential temperature and the S_i terms represent sources and sinks of enthalpy. These include changes in local enthalpy caused by ther-

mal conduction, divergence of net radiation, dissipation of kinetic energy, and changes in mass content, composition or state of a given parcel of air. All these terms will be ignored here. For most terms this means no severe violation of reality, because they are usually small. Only the change of state of available water may constitute an important term. If cloud formation occurs, divergence of net radiation also becomes important. Therefore, the omission of these terms in Equation 31 limits the validity of the model to cases where no condensation occurs in the atmosphere. The equation now reduces to

$$\frac{\partial \theta}{\partial t} = - \frac{\partial}{\partial z}\left(\frac{H}{\rho C_p}\right)$$
Equation 32

Similarly, the equation of mass conservation is expressed for water vapour as

$$\frac{\partial q}{\partial t} = - \frac{\partial}{\partial z}\,(\overline{wq} + \overline{w'q'}) = - \frac{\partial}{\partial z}\left(\frac{E}{\rho}\right)$$
Equation 33

Fluxes in terms of gradients

The fluxes in the boundary layer are expressed somewhat differently from the surface fluxes described in Subsection 2.4.1. For momentum, sensible heat and moisture, the equations read

$$\frac{\tau_x}{\rho} = - K_M\,\frac{\partial u}{\partial z}; \quad \frac{\tau_y}{\rho} = - K_M\,\frac{\partial v}{\partial z}$$
Equation 34

$$\frac{H}{\rho C_p} = - K_H\,\frac{\partial \theta}{\partial z}$$
Equation 35

$$\frac{E}{\rho} = - K_V\,\frac{\partial q}{\partial z}$$
Equation 36

Clearly, combination with Equations 30, 31 and 32, respectively, yields the well-known second order equations of flow. Although this gradient formulation is a coarse approximation, based on similarity with molecular transfer processes, it is still the most widely used approach, because of its simplicity and relatively low computing cost (Businger, 1981). The transport coefficients K are expressed as functions of e, the available local turbulent kinetic energy:

$$K_{M,H,V} = l_{M,H,V}(c\,e)^{1/2}$$
Equation 37

where the kinetic energy is in J kg^{-1}. The length scales $l_{M,H,V}$ are functions of the dimensionless gradients φ (Subsection 2.4.1) and are given by

$$l_{M,H,V}^{-1} = \frac{\varphi_{M,H,V}(\zeta)}{k\,z} + \frac{f}{\alpha\,u_g}$$
Equation 38

23

where $\varphi_M^2 = \varphi_H = \varphi_V$ (Businger, 1975); for the empirical constants α and c, the values 4.10^{-4} and 0.2, respectively, are used (Nieuwstadt & Driedonks, 1979).

The kinetic energy budget
The system is closed by the turbulent kinetic energy (TKE) equation (Tennekes & Lumley, 1972; Driedonks, 1981):

$$\underbrace{\frac{\partial e}{\partial t}}_{I} = \underbrace{\frac{\tau_x}{\rho}\frac{\partial u}{\partial z} + \frac{\tau_y}{\rho}\frac{\partial v}{\partial z}}_{II} + \underbrace{\frac{g}{T}\frac{H}{\rho C_p}}_{III} + \underbrace{\frac{\partial}{\partial z}K_M\frac{\partial e}{\partial z}}_{IV} - \underbrace{\frac{(c\,e)^{3/2}}{l_M}}_{V}$$

Equation 39

The Term I is the local rate of change of TKE per unit of mass; II are the mechanical production terms of TKE resulting from vertical wind shear; III is the TKE production by buoyancy, IV represents the divergence of the vertical TKE flux, and the last term is the loss of TKE by dissipation, where the constant c is identical to that in Equation 37. Driedonks (1981) extensively discussed the relative importance of each term at different locations in the developing boundary layer.

Boundary conditions
The lower boundary conditions to the atmosphere, dictated by the surface energy balance, have been treated in Subsection 2.4.1, except for the TKE flux. This term is taken to be zero at the surface. In the present study, the conditions at the upper boundary of the system were defined as given below, but of course other conditions can be chosen:

$u = u_g$

Equation 40a

$v = v_g \equiv 0$

Equation 40b

$\tau_x = \tau_y = 0$

Equation 40c

$H = 0$

Equation 40d

$E = 0$

Equation 40e

$\dfrac{\partial e}{\partial z} = 0$

Equation 40f

It will be clear that the choice of these boundary conditions prescribes that the height of the upper boundary in a model be chosen safely above the actual top of the developing boundary layer.

24

2.5 Transport of heat in the soil

The one-dimensional flow equation for heat in the soil can be written as

$$\frac{\partial(CT)}{\partial t} = \frac{\partial}{\partial z}\left(\lambda \frac{\partial T}{\partial z}\right) + \Sigma_i P_i \qquad \text{Equation 41}$$

where λ is the thermal conductivity (W m^{-1} K^{-1}), C the volumetric heat capacity (J m^{-3} K^{-1}) and the P_i terms represent the rates of change in local heat content by mechanisms other than conduction. These other mechanisms are associated with liquid or gas movement, and some of them are still poorly understood. In the case of actual measurements, the P_i terms are often 'incorporated' in the first term on the RHS and all heat transport is ascribed to conduction. Thermal conductivity in the above equation is then replaced by λ^*, the apparent thermal conductivity, and the P_i terms are consequently omitted. The use of λ^* in modelling coupled mass-heat flow in soil is not attractive for reasons explained in Subsection 2.5.2. Hence, the two main heat transfer terms are maintained separately in the model.

Heat transport by conduction will be discussed first (Subsection 2.5.1). Subsequently, the heat associated with a change of state of the soil water will be treated (Subsection 2.5.2).

2.5.1 Conduction

Naturally, soil thermal conductivity and heat capacity have a strong influence on soil thermal behaviour. Both can be formulated on the basis of soil composition.

Heat capacity
The soil heat capacity in SALSA is defined on the basis of the capacities of the different soil components (de Vries, 1963):

$$C_s = f_q C_q + f_c C_c + f_o C_o + \theta C_w + f_a C_a \qquad \text{Equation 42}$$

where f is the volume fraction and C the volumetric heat capacity of the components clay, quartz, organic matter, water and air, respectively; θ is the volume fraction of soil water. Water content determines heat capacity to a large extent, since water has a much higher specific heat capacity than the other soil constituents, as shown in Table 4.

Thermal conductivity
Thermal conductivity is less obviously related to soil composition than heat capacity. Aside from the conductivities of the individual soil particles, the arrangement and shape factors of the particles also affect bulk thermal conductiv-

25

Table 4. Thermal properties of soil components (after de Vries, 1963).

Component	Density	Specific heat	Thermal conductivity	Thermal diffusivity
	$Mg\,m^{-3}$	$J\,g^{-1}\,K^{-1}$	$W\,m^{-1}\,K^{-1}$	$10^{-6}\,m^2s^{-1}$
Quartz	2.66	0.80	8.80	4.18
Clay minerals	2.65	0.90	2.92	1.22
Organic matter	1.30	1.92	0.25	0.10
Water	1.00	4.18	0.57	0.14
Air (20°C)	$1.20\,10^{-3}$	1.01	0.025	20.50

ity. Extremes in soil conductivity may differ by a factor of 100 (Hillel, 1980), although for arable soils variability is somewhat less and a factor of 10 seems more appropriate to characterize the range of λ values occurring in the field. Several empirical expressions for $\lambda(\theta)$ have been proposed, e.g. by Woodside & Messmer (1961) and Nerpin & Chudnovski (1970). Table 5 lists measured thermal conductivities of soil at different water contents as found in the literature; most data refer to apparent thermal conductivity λ^*, thus covering not only conduction but also mass-associated heat transfer. For field soils, $\lambda(\theta)$ is fairly well described by a linear relationship; Table 5 can be used for interpolation purposes. See also Section 4.5.

In the SALSA model, either tabulated (measured) functions of λ vs θ are used, or λ is calculated on the basis of the electrical conductivity analogon by de Vries (1963, 1975). De Vries's model considers soil as a continuous medium (gas or liquid), in which soil particles and water or air, respectively, are dispersed. Conductivity is then calculated as a weighted average of the conductivities of the individual components. For $\theta > 0.05$, the liquid is used as the continuous phase, and the expression becomes

$$\lambda = \frac{k_{qw}f_q\lambda_q + k_{cw}f_c\lambda_c + k_{ow}f_o\lambda_o + k_{ww}\theta\lambda_w + k_{aw}f_a\lambda_a}{k_{qw}f_q + k_{cw}f_c + k_{ow}f_o + k_{ww}\theta + k_{aw}f_a}$$

Equation 43

The weighting factors k_{qw}, k_{cw}, k_{ow}, and k_{aw} depend on the ratio of specific thermal conductivity of respectively quartz, clay, organic matter, and air to that of water ($k_{ww} \equiv 1$). At very low water contents ($\theta < 0.02$), air is viewed as the continuous phase, and an equivalent expression is used, including an empirical correction factor:

$$\lambda = 1.25 \cdot \frac{k_{qa}f_q\lambda_q + k_{ca}f_c\lambda_c + k_{oa}f_o\lambda_o + k_{wa}\theta\lambda_w + k_{aa}f_a\lambda_a}{k_{qa}f_q + k_{ca}f_c + k_{oa}f_o + k_{wa}\theta + k_{aa}f_a}$$

Equation 44

26

Table 5. Thermal conductivity of soil materials; values refer to different dry bulk densities ρ.

	λ dry		λ wet		ρ	Source
	θ	$W\,m^{-1}K^{-1}$	θ	$W\,m^{-1}K^{-1}$	$Mg\,m^{-3}$	
Fairbanks sand	.00	0.33	.21	2.30	1.70	de Vries, 1963
Sand	.00	0.30	.40	1.68	1.46	van Duin, 1956
Sand	.00	0.15	.38	2.30	1.60	Riha et al., 1980
Pumice (Ac)	.00	0.16	.70	0.71	0.76	Cochran et al., 1967
Loamy sand	.00	0.20	.21	1.80	1.50	Hartmann et al., 1972
Loamy sand	.01	0.30	.35	1.50	1.69	Sepaskhah & Boersma, 1979
Yolo silt loam	.16	0.75	.40	1.18	1.35	Wierenga et al., 1969
Muir silty clay loam	.04	0.30	.31	0.90	1.25	Asrar & Kanemasu, 1983
Healy clay	.03	0.16	.36	1.55	0.36–0.61*	de Vries, 1963
Fairbanks peat	.02	0.05	.80	0.45	0.84–0.79*	de Vries, 1963
Forest litter	.02	0.10	.55	0.30	0.21	Riha et al., 1980

* porosity

with $k_{aa} \equiv 1$.

For component x in medium y, k_{xy} is defined for a temperature gradient in the direction i as

$$k_{xy_i} = 1/(1 + (\lambda_x/\lambda_y - 1) \cdot g_{x_i})$$

Equation 45

where g_{x_i} is the shape factor for direction i, determined by the ratio of the main axes of the particle. The particles are assumed to be spheroid. If the particle axes have random directions in the bulk soil, the weight factors are expressed by

$$k_{xy} = \tfrac{1}{3}(k_{xy_{i=1}} + k_{xy_{i=2}} + k_{xy_{i=3}})$$

Equation 46

which for spheroids results in

$$k_{xy} = \tfrac{2}{3}\, 1/(1 + (\lambda_x/\lambda_y - 1)\, g_{x_i}) + \tfrac{1}{3}\, 1/(1 + (\lambda_x/\lambda_y - 1)(1 - 2g_{x_i}))$$

Equation 47

with $i = 1$.

De Vries (1975) mentioned an inaccuracy of 5% in the λ predictions for soil by the above equations, increasing to 10% for the range where neither water nor air are considered as the continuous medium ($0.02 < \theta < 0.05$). An example of λ calculated according to the above model is given for Swifterbant silt loam in Chapter 4.

Several authors compared predictions by the 'analogue model' with measured data of thermal conductivity, obtained from both laboratory and field experiments. Although some of them reported disagreement (Nagpal & Boersma, 1973; Hadas, 1977b), others found good agreement between measured and calculated values (de Vries, 1963; Cochran et al., 1967; Wieringa et al., 1969; Sepaskhah & Boersma, 1979; Horton, 1982). The air shape factor g_a in the De Vries model is sometimes used to match calculations with data. Kimball et al. (1976) extensively discussed this air shape factor, indicating its dependence on temperature and moisture content. Horton (1982) found best agreement when using the values of the air shape factor given by Kimball et al. When the de Vries λ model is used to simulate soil temperatures, an error interval should be used to account for uncertainties in g_a, instead of optimizing the fit between predicted and observed courses by modifying g_a.

The continuing discussions on thermal conductivity in the literature on soils indicate the difficulties involved in the measurement of λ and in the determination of the parameters required for the de Vries model. The actual relevance of λ with respect to soil surface temperature behaviour will be studied in Chapter 6.

Soil water may be present in various states or phases, each of which is characterized by a corresponding entropy. The condition of local thermodynamic equilibrium signifies that at any point in the macroscopic sense, the local chemical potentials μ_i and the temperatures T_i are the same for all phases i. Then, when water passes from one state into another, the change in partial specific entropy is accompanied by the release or absorption of a certain amount of heat ΔH, equal to $T(S_2 - S_1)$ where S_1 and S_2 are the partial specific entropies (J kg^{-1} K^{-1}) corresponding to the initial and final states, respectively. This follows from the equilibrium condition $\mu_1 = \mu_2$ and the relation

$$\mu = H - TS \hspace{4cm} \text{Equation 48}$$

where H is the partial specific enthalpy (J kg^{-1}). Although, in reality, at the scale of a pore the state of soil water changes gradually in space, i.e. with respect to its position relative to the solid phase, it is considered satifactory to distinguish only three water phases. Each phase has its characteristic transport coefficient, pressure (p), partial specific entropy (S) and specific volume (V). These three phases are the 'free' or 'extramatric' liquid phase, the adsorbed or 'matric' phase, and the vapour phase (Kay & Groenevelt, 1974). (See also Subsection 2.6.1).

Heat of wetting

When liquid water is added to dry soil, the temperature changes because the integral heat of wetting, $\Delta \overline{H}_a$, is liberated when water molecules are adsorbed by the soil particles and their state changes from 'free' liquid to 'matric' liquid. The heat of wetting has also been called 'heat of transport' (Nielsen et al., 1972). This is confusing, because $\Delta \overline{H}_a$ is not directly related to the transport itself but to a local change of state; the term should therefore be avoided; it does not specifically adress the phenomenon involved. Table 6 lists the $\Delta \overline{H}_a$ values for a number of soil materials, as measured directly in adsorption or immersion experiments. It can be seen that $\Delta \overline{H}_a$ differs over a wide range of values, depending on the type of clay mineral and the adsorbed cation species. It is generally acknowledged that upon wetting up to a relative humidity of 20%, the heat of wetting has evolved almost completely. This state is identified by the presence of a monolayer of water molecules adsorbed on the active surfaces. The actual concern being the relevance of the reported data to the soil energy balance, it may be stated that the heat of evaporation of adsorbed water, down to a relative humidity of 20%, is equal to that of free water, i.e. 2.4-2.5 10^6 J kg^{-1} (depending on temperature). Only for the last molecular layer, is this value increased by 5-25% as a result of $\Delta \overline{H}_a$, as can be seen from Table 6. In the context of the surface energy balance, this amount can be ignored because it applies to a very small fraction of the soil water. In addition, in nature this ulti-

Table 6. Integral heat of adsorption $\Delta \overline{H}_a$ (free liquid → adsorbed liquid) for different soil materials.

	kJ kg$_{dry\ soil}^{-1}$ (complete wetting)	kJ kg$_{water}^{-1}$ (from dry to $h = 0.2$)	Source
Millville silt loam	.	80	Cary et al., 1964
Millville silt loam	.	510	Kijne et al., 1964
Red–brown loam	.	380	Orchiston, 1953
Illite	8.2	350	Orchiston, 1954
Kaolinite	0.9	500	Orchiston, 1954
Na-kaolinite	6.8*	.	East, 1950
Ca-montmorillonite	95.0	791	Kijne, 1969
Na-montmorillonite	28.0	700	Kijne, 1969

* Calculated from original data assuming specific surface area of 25 m^{2}g^{-1} for kaolinite.

mate amount of adsorbed water will only be removed under very extreme conditions. Hence, the heat of adsorption is not accounted for by the SALSA model. (Note that to derive $\Delta \overline{H}_a$ from vapour adsorption experiments, the latent heat of vaporization ΔH_v should of course be subtracted from the total value of ΔH).

Heat of vaporization

In analogy to the above, the well-known latent heat of vaporization ΔH_v accompanies the increase in entropy when water evaporates. In contrast to $\Delta \overline{H}_a$, this particular change in partial specific enthalpy has been observed to contribute considerably to soil heat transport (e.g. Hadas (1977b) and Westcot & Wierenga (1974) for field and laboratory experiments, respectively). Condensation at the soil surface, in addition to conductive transport of heat, may play an important role in the surface energy balance at night, compensating for radiative cooling and thus maintaining net radiation at a steady minimum level. A brief exercise on this topic will be presented in Chapter 6 to illustrate the significance of heat-vapour coupling in the context of the surface energy balance.

As mentioned before, the latent heat carried by the vapour can be taken into account by using an 'apparent thermal conductivity', λ^*. As an example, Figure 4 shows its contribution as calculated by the de Vries model (Equations 43 and 44), in which λ_a can either signify the true conductivity of air (to yield λ), or the apparent conductivity of air, i.e. including vapour diffusion (to yield λ^*). Since both vapour diffusivity and saturated vapour density are temperature-dependent, this temperature dependence also holds for λ^*, which is, therefore, not an attractive soil characteristic. It must be realized, in addition, that the curves in Figure 4 represent the case of saturated soil air only. In other
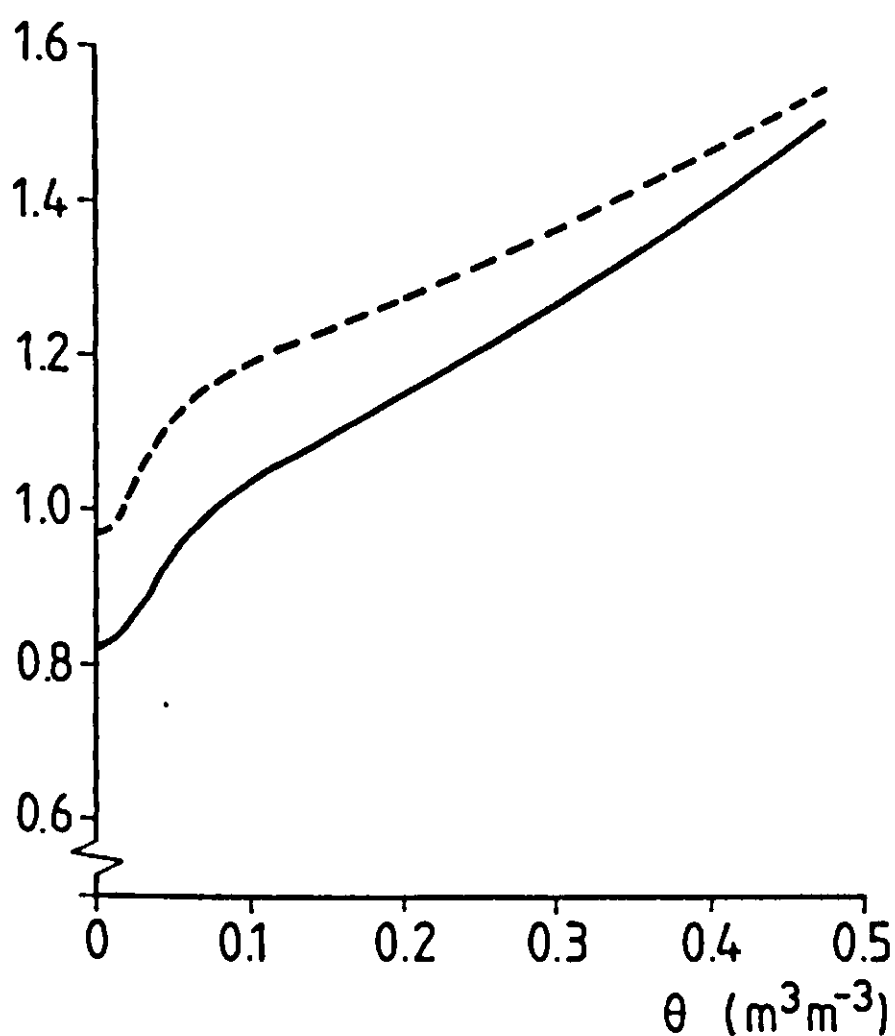
Figure 4. Thermal conductivity and apparent thermal conductivity as calculated by the de Vries model (saturated soil air).

cases, the effect of vapour movement on heat transfer may even be in the reverse direction. Such happens when vapour diffuses upwards along the gradient of relative humidity towards the warm soil surface; this occurs at very shallow depths during daytime in soils with a dry surface. Then, vapour flow can decrease apparent thermal conductivity, provided condensation takes place. (If not, the vapour transport has no direct effect on heat transport). For these two reasons λ^* has not been used in the SALSA model.

Heat flux associated with water transport

The basis of heat transport associated with mass transport has been mentioned in the previous paragraphs: the latent heat of phase changes is responsible for coupling between mass and heat flow. Now, the flux density equations resulting from this mechanism must be formulated.

The heat flux through soil with simultaneous water transport is easily misinterpreted. Different definitions are possible (de Groot & Mazur, 1962) and this has given rise to much confusion in soils literature (Nielsen et al., 1972; Chu et al., 1983; Sposito, 1986). Careful analysis of the thermodynamics involved in these phenomena of mass-heat coupling shows, however, that there should be no doubt – at least not on a theoretical level – about the interpretation of the various heat fluxes. For a more detailed treatment of the theory on the basis of the entropy production equation the reader is referred to ten Berge & Bolt

(1988) who also discuss the Onsager relations for mass-heat transfer.

For the description of the SALSA model, a brief discussion on the heat flux as employed in the model is considered sufficient. The total heat flux is written as (de Groot & Mazur, 1962; Katchalsky & Curran, 1965):

$$J_q = TJ_s + \sum_i \mu_{w_i} J_{w_i} \qquad\qquad \text{Equation 49}$$

where J_s is the total entropy flux (resulting from both conduction and mass transport) and J_{w_i} are the different mass fluxes of water in state i, with chemical potential μ_{w_i}. In Appendix 1 it is shown that it is the convergence of this flux J_q that is equal to the local rate of change of volumetric heat content $\partial(CT)/\partial t$, introduced in Equation 41. The flux J_q thus comprises both a true conduction term and some terms related to mass flow, which were lumped into the terms $\sum_i P_i$ in Equation 41. This equation may now be written as (see Appendix 1)

$$\frac{\partial(CT)}{\partial t} = \frac{-\partial}{\partial z}\left(-\lambda\frac{\partial T}{\partial z} + H_w J_w - J_v \Delta H_v - J'_w \Delta \overline{H}_a\right) \qquad\qquad \text{Equation 50}$$

where J_w is the total water flux (summation all phases), J_v is the vapour flux, and J'_w is the flux of matric liquid; H_w is the enthalpy of the water in the reference state ('extramatric'). Note that the sign of ΔH_v and $\Delta \overline{H}_a$ is determined by the direction of the phase transition: from extramatric liquid to vapour (negative) and from extramatric to adsorbed liquid (positive), respectively. The last RHS term, which results from adsorption, is ignored in SALSA: it is assumed to be much smaller than the remaining three terms, because of the low values of both $\Delta \overline{H}_a$ and the transport coefficient for matric water.

Furthermore, the fraction $T\partial C/\partial t$ of the LHS differential is cancelled against $-(H_w\partial J_w/\partial z + J_w\partial H_w/\partial z)$. This implies ignoring $J_w\partial H_w/\partial z$, because it is easily verified that $T(\partial C/\partial t)$ is identical with $-H_w\partial J_w/\partial z$. It can be demonstrated that in the context of the diurnal surface energy balance this simplification is not severe: even under a temperature gradient of 100 K m^{-1}, a water flux of 1 mm h^{-1} would give rise to a temperature change in the order of only 0.1 K h^{-1}. With these simplifications, the expression as used in SALSA may finally be written as

$$C\frac{\partial T}{\partial t} = -\frac{\partial}{\partial z}\left(-\lambda\frac{\partial T}{\partial z} - J_v \Delta H_v\right) \qquad\qquad \text{Equation 51}$$

which implies that in the numerical scheme the heat capacity at time t is indeed used to evaluate the temperature at time $t + \Delta t$.

2.6 Transport of water in the soil

The general flow equation for one-dimensional transport of liquid water in the soil is written as

$$\rho_1 \frac{\partial \theta}{\partial t} = \frac{\partial}{\partial z}\left(K(\theta,T)\frac{\partial p(\theta,T)}{\partial z}\right) - \rho_1 g \frac{\partial}{\partial z} K(\theta,T) \qquad \text{Equation 52}$$

where p is the pressure potential (Pa), K is the hydraulic conductivity (in kg(m Pa s)$^{-1}$), ρ_1 is the density of the liquid, g the acceleration by gravity, and θ the volumetric water content. The moisture characteristic $p(\theta)$ and the hydraulic conductivity function $K(\theta)$ will be treated in subsection 2.6.2, along with the so-called 'matric flux potential' concept. The latter is a combination of the $p(\theta)$ and $K(\theta)$ functions, which may be used as a substitute for these in the first RHS term of Equation 52.

Since moisture transport near the soil surface is rarely isothermal, attention must be paid to the phenomenon of coupling between heat and moisture fluxes in analogy to what was written about the soil heat flux (Subsection 2.5.2). Various models that include coupling phenomena have been published, and some aspects have been evaluated quantitatively in simulation studies (e.g. Milly, 1984; Hopmans & Dane, 1985). Nevertheless, a reconciliation of the classical approaches – mechanistic and thermodynamic – would be useful for modelling and is therefore elaborated here. Subsection 2.6.1 summarizes some of the theory and conclusions regarding the driving forces for liquid flow under a temperature gradient. For its counterpart, the transport of heat associated with water transport, see Subsection 2.5.2.

The equivalent of Equation 52 for vapour transfer is expressed as

$$\rho_1 \frac{\partial \theta}{\partial t} = \frac{\partial}{\partial z}\left(D_e(\theta,T)\frac{\partial \rho_v(\theta,T)}{\partial z}\right) \qquad \text{Equation 53}$$

where ρ_v is the vapour density (kg m^{-3}) and D_e the effective vapour diffusivity (m^{2}s^{-1}). In analogy to the treatment of liquid transfer, some comments will be given on the theory of coupling and on the relation $\rho_v(\theta)$ in Subsection 2.6.3; the effective diffusivity D_e, including the various enhancement mechanisms that have been reported in literature (Subsection 2.6.4), will also be touched upon.

2.6.1 Coupling: non-isothermal transport in the liquid phase; the formulation of $p(\theta,T)$

In soils literature, two distinct approaches have traditionally been followed to analyse coupling between mass and heat transport: on the one hand the 'mechanistic' approach of Krischer & Rohnalter (1940), Philip & de Vries (1957) and later many others, and on the other hand the 'thermodynamic' approach

(Taylor & Cary, 1964; Cary, 1965; Weeks et al., 1968, Bolt & Groenevelt, 1972). Comparison of the two formulations shows that the effect of temperature on the driving force for liquid flow is smaller than previously thought. In the SALSA model it is therefore ignored. The justification for doing this is given below.

The mechanistic analysis employs the concepts of fluid mechanics and heat conduction. Using the gradient of the hydrostatic pressure (here, tensiometer pressure p) as the only driving force for liquid flow, Philip & de Vries indicated that at constant value of the volumetric water content θ, a temperature gradient should induce liquid flow in the direction of the cold side. This is because of the effect of temperature on the surface tension γ and hence on the Laplace pressure jump over the curved meniscus in pores.

Several authors have published experimental evidence of the temperature dependence of the isothermal moisture characteristic $p(\theta)$. An extensive treatment can be found in Nimmo & Miller (1986). In general, a hyperbolic relationship of the form $(\partial p/\partial T) = a(\theta - b)^{-1} + c$ can be fitted to the data (Ritsema, 1985). The empirical constants a, b and c, as calculated from the original data taken from literature, are listed in Table 7 to give an impression of the magnitude of the temperature effect on extramatric liquid pressure. It will be clear that this relation only summarizes the data and has no direct physical significance, as appears for θ approaching the b value.

The thermodynamic approach distinguishes many different water phases on the basis of the local entropy of soil water, e.g. ice, bulk liquid and vapour. For the present purpose, only the liquid phase is considered in more detail. At the scale of a pore then, a gradual change in local entropy can be found within the liquid phase: it decreases as the solid-liquid interface is approached as a result of the force field extending from the solid surface. Thus, an infinity of subphases can be defined. For each subphase i, the macroscopic gradient in chemical potential μ_w is expressed as a linear combination of pressure and temperature gradients by the Gibbs-Duhem equation:

Table 7. Constants in empirical $(\partial p/\partial T)_\theta - \theta$ relationship, Equation 89.

	a (Pa K^{-1})	b	c (Pa K^{-1})	Source
Sand	6.90	.069	− 32	Constantz, 1982
Fine sand	0.40	.035	+ 17	Wilkinson & Klute, 1962
Silt	8.40	.085	+ 240	Wilkinson & Klute, 1962
Fine silt	37.50	.000	− 97	Chahal, 1965
Sandy loam	13.60	.150	− 46	Constantz, 1982
Silt loam	277.20	.000	− 1249	Taylor & Stewart, 1960
Silt loam	44.40	.210	− 167	Haridasan & Jensen, 1972
Silt loam	104.20	.180	− 512	ten Berge, 1986

$$\frac{d\mu_{w_i}}{dz} = -S_i \frac{dT}{dz} + V_i \frac{dp_i}{dz}$$
Equation 54

where S_i, V_i, and p_i are the partial specific entropy, volume and pressure, respectively. This implies that, when a temperature gradient exists, the pressure gradients are different for the subphases distinguished. Kay & Groenevelt (1974) simplified this picture by recognizing only two phases of the liquid water: the 'extramatric' water, i.e. water outside the force field emanating from the solid phase, and water under direct influence of these surface forces. For brevity, the latter will be called 'matric' water, although it is stressed that both phases may be present concomitantly within the soil matrix. 'Extramatric' water is the water as present in a measuring device, such as a psychrometer or a tensiometer. The measured tensiometer pressure gradient is a gradient in the pressure p of the 'extramatric' liquid, in equilibrium with the soil water, i.e. also at the same local temperature.

The condition of local thermodynamic equilibrium implies that the chemical potentials μ_{w_i} are the same for all subphases, at any (macroscopic) point. If then the water present in the soil system is satisfactorily typified by some average value of the 'matric' phase pressure $p'(\neq p)$ and specific volume $V \approx \overline{V}$, combination of this equilibrium condition with Equation 54 yields the well-known Clapeyron equation:

$$\overline{V} \, dp - V'dp' = (S - S') \, dT \equiv \Delta \overline{H}_a \frac{dT}{T}$$
Equation 55

where S' is the partial specific entropy of liquid in the 'matric' phase, and S represents the same variable for the 'extramatric' phase. The positive value of the heat of wetting $\Delta \overline{H}_a \equiv T(S - S')$ found for most soils (hydrophilic materials) signifies that $dp' < dp$ for $dT > 0$. Thus, thermo-osmosis ($dp \equiv 0$) is directed towards the warm side. Some measured values of $\Delta \overline{H}_a$ were listed in Table 6.

Unification of approaches; implications for modelling.
To sum up, the mechanistic formulation predicts (in the absence of $\nabla\theta$) a liquid flux in the direction of the lower temperature because of a macroscopic surface tension gradient, whereas thermodynamic theory prescribes a liquid flux in the direction of the higher temperature according to the Clapeyron equation (in the absence of ∇p!). The actual overall ∇T-driven flux at constant θ is found by summing both effects. Making use of the extensive analysis by Kay & Groenevelt (1974) and Groenevelt & Kay (1974) and of interface thermodynamics for the solid-liquid-gas interfacial region, it may be shown that in addition to having opposite directions, the magnitude of the two ∇T-driven fluxes is likely to be of the same order. Such analysis (ten Berge & Bolt, 1988) involves the relation between the interfacial tensions of the gas-liquid and liquid-solid interfaces, and their respective temperature dependences. As a result, the con-

nection between the two approaches sketched above finally appears as:

$$(dp)_\theta = \left(\frac{\partial p}{\partial T}\right)_\theta dT = \frac{\Delta \overline{H}_a}{\overline{V}T} dT \qquad \text{Equation 56}$$

Combining Equations 55 and 56 shows that the assumed average driving force for flow of 'matric' water, $\nabla p'$, must be zero. This conclusion is based upon the assumption that all soil water is in the matric state, and that $\nabla p'$ is therefore the overall driving force. It can be shown, however, that for any schematic division of soil water into two subphases, the driving forces on the respective subphases caused by a temperature gradient cancel each other. The widely accepted Philip and de Vries formulation of thermally induced liquid flow apparently does not take into account true coupling in the thermodynamic sense. Such coupling arises, as explained, from the relation between pressure and entropy differences as defined by the Clapeyron equation. It must be added that in reality, not only the driving forces, but also the mobilities of water in the different phases determine the fluxes, and that as a result the flow towards the cold side will prevail in the situation with $\nabla \theta = 0$. In the SALSA model this difference is ignored, thus assuming that the above compensation mechanism gives enough justification for completely ignoring temperature-induced flow of liquid water.

The remaining driving forces for liquid water movement are now $(\partial p/\partial \theta)_T \nabla \theta$ and $(\partial p'/\partial \theta)_T \nabla \theta$ for the two-phase situation. According to the Clapeyron equation (Equation 55), the derivatives $(\partial p/\partial \theta)_T$ and $(\partial p'/\partial \theta)_T$ must be equal, and they simply represent the slope of the well-known moisture characteristic curve (Subsection 2.6.2). This slope is used in the SALSA model to calculate water flow in the liquid phase.

Having eliminated the gradient of temperature as a driving force for movement in the liquid phase, the dependence of $(\partial p/\partial \theta)_T$ on temperature still remains. This relation can hardly be analysed on a theoretical basis, the moisture characteristic itself being an empirical characteristic. Empirical results are therefore invoked here to justify ignoring this particular temperature effect as well. Data from different authors, applying to a wide range of soils, θ values and temperatures were processed and the results are combined in Figure 5. This figure shows for various temperatures the ratio of $(\partial p/\partial \theta)_T$ to its value at a reference temperature (20 °C). Viewing these results, one may be tempted to qualify this temperature effect as being relevant. Since ∇p is multiplied by the conductivity K in calculating the flux, however, the $K(T)$ relation must also be inspected in this context. The conductivity at given moisture content is inversely proportional to the temperature-dependent viscosity of the liquid (e.g. Hopmans & Dane, 1985). The ratio of viscosity $\eta(T)$ to its value at reference temperature T_o is therefore plotted in Figure 5 as well. Both effects now appear to counteract each other:
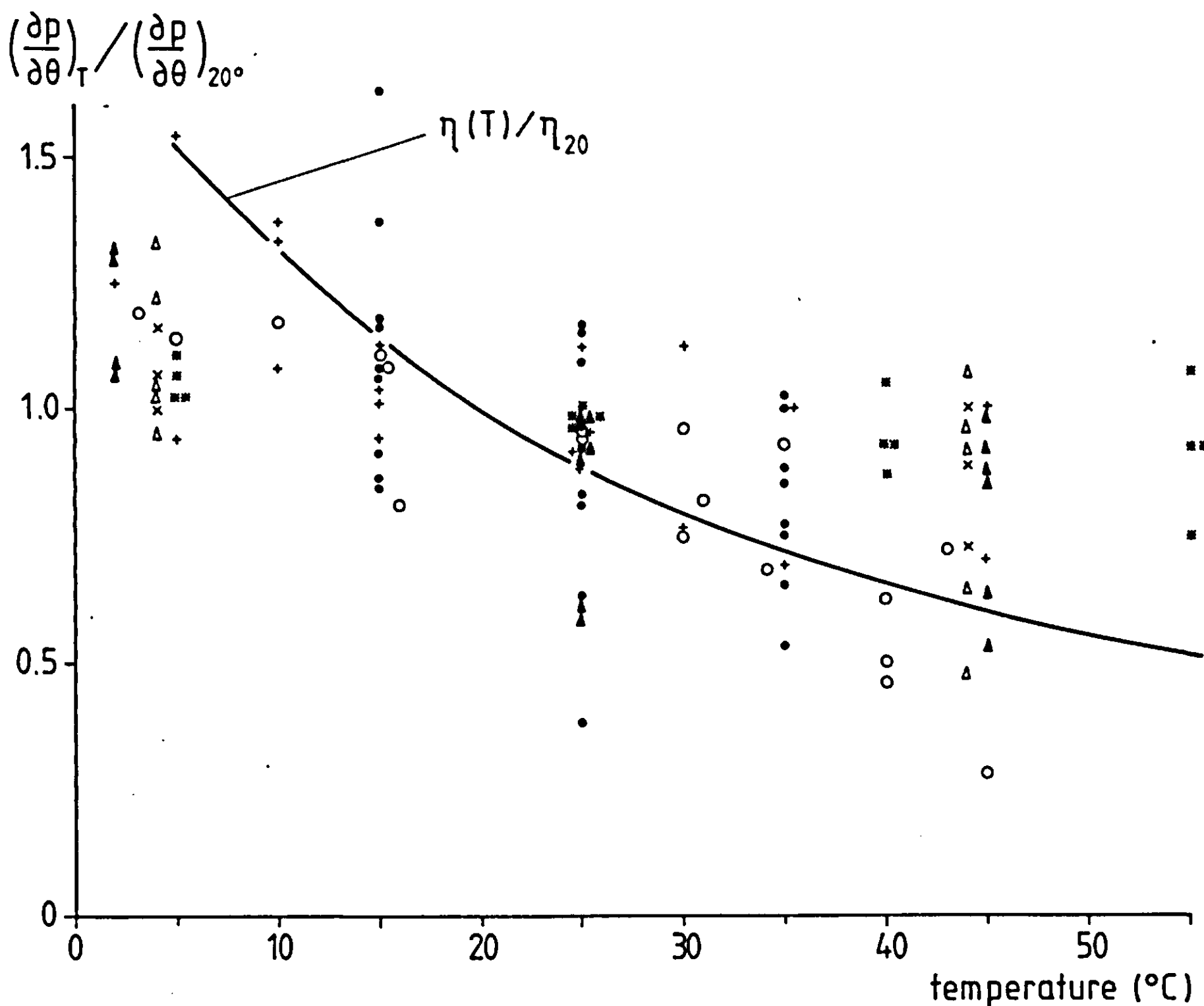
Figure 5. The ratio $(\frac{\partial p}{\partial \theta})_T/(\frac{\partial p}{\partial \theta})_{20°C}$ versus temperature, as calculated from literature data, applying to a variety of soil water contents. • silt loam, Haridasan & Jensen (1972); o silt loam, Taylor & Stewart (1960); x fine sand, Wilkinson & Klute (1962); Δ silt, Wilkinson & Klute (1962); ▲ sandy loam, Constantz (1982); + silt loam, this report; * fine silt, Chahal (1965).

$$\frac{\eta(T)}{\eta(T_o)} \approx \frac{\left(\frac{\partial p}{\partial \theta}\right)_T}{\left(\frac{\partial p}{\partial \theta}\right)_{T_o}}$$

Equation 57

Therefore, the temperature dependence of the moisture characteristic slope is also omitted from the SALSA model.

37

2.6.2 The moisture characteristic, hydraulic conductivity and matric flux potential

The moisture characteristic

The relation between moisture content and pressure potential is determined by soil texture and structure. Empirical and semi-empirical models have been proposed to express the moisture characteristic on the basis of these properties (e.g. Arya & Paris, 1981; Gupta & Larson, 1979) but a main problem remains the distribution of total pore space over the fractions related to particle size classes and those related to structure. In the present model it is therefore preferred to use measured relationships, which may be specified in the form of an analytical expression. The function proposed by van Genuchten (1980) is employed in SALSA, because it applies to a wide range of soils:

$$p = -\frac{1}{\alpha}(\varXi^{-1/m} - 1)^{1/n}$$ Equation 58

where $\varXi$ is the relative saturation according to

$$\varXi \equiv \frac{\theta - \theta_r}{\theta_s - \theta_r}$$ Equation 59

with θ_r and θ_s as the residual moisture content and the moisture content at saturation, respectively. The parameters α, n, and θ_r can be determined for a given set of $p(\theta)$ measurements by an optimization procedure. The parameter α appears to be related to soil structure, and n and θ_r to texture; m is defined by $m \equiv 1 - 1/n$. For the present purpose, data from a number of soils covering a wide range of textures have been analysed. The resulting sets of parameter values are listed in Table 8. A distinct advantage of van Genuchten's function is that it allows the use of the theoretically based $K(\theta)$ model given by Mualem (1976), as proposed by van Genuchten (1980).

At very low water contents, the above concept presents some difficulties, because it is based on transport in the liquid phase only. Equations 58 and 59 define the residual water content θ_r as the moisture content at which an infinitely high pressure must be exerted to liberate more water from the matrix. At infinitely low pressure potential, however, no vapour transport could occur either, because the vapour concentration approaches zero. Consequently, the soil could never dry beyond θ_r. Of course, this paradox arises because liquid continuity and mobility cease at very low θ values. Therefore, θ_r has no physical meaning in terms of pressure and should not be used as such.

In SALSA, the above set of equations is used down to a pressure potential of -1.5 MPa, where the relative humidity h is still approximately 100%. For moisture contents lower than the corresponding $\theta_{1.5}$, liquid pressure is calculated from relative humidity, using the Kelvin equation (Equation 70) and adsorption isotherms for water to soil particles. The liquid pressure is then only

Table 8. Hydraulic properties of various soils. The original $p(\theta)$ and $K(\theta)$ data for most soils were taken from references listed by Mualem & Dagan (1976).

Soil	α 10^{-4} Pa^{-1}	n	θ_r	θ_s**	K_s 10^{-8} kg(m s Pa)$^{-1}$	A 10^{-6} kg(m s)$^{-1}$	B	Source
Beit Netofa clay	0.1390	1.1693	0.000	0.446	0.81	.	.	Rawitz, 1965
Rideau clay	8.2510	1.1740	0.000	0.478	34.20	639.0	0.0899	Staple, 1969
Yolo light clay	2.9200	1.2725	0.006	0.495	1.00	36.9	0.1250	Moore, 1939
Buffalo silty clay	7.1028	1.1275	0.000	0.416	7.90	51.9	0.0088	this monograph
Glendale clay loam	22.4680	1.5856	0.232	0.525	109.00	510.2	0.0965	Sisson et al., 1980
Avondale loam	2.2670	1.1929	0.000	0.400	27.80	642.0	0.0402	Jackson, 1973
Guelph loam	1.3470	1.7036	0.176	0.520	30.49	1816.5	0.0595	Elrick, 1964
Gilat loam	1.8000	3.2259	0.133	0.440	21.62	759.0	0.0208	Bresler et al., 1971
Swifterbant loam	46.7063	1.0927	0.033	0.430	5.20*	.	.	this monograph
Swifterbant silt loam	4.0397	1.1610	0.000	0.420	5.20*	.	.	this monograph
Grenville silt loam	0.6700	1.4346	0.149	0.475	6.40	496.4	0.0242	Staple, 1965
Columbia silt loam	1.4990	1.6260	0.095	0.400	5.85	315.9	0.0736	Davidson et al., 1963
Ida silt loam	0.8470	1.3895	0.049	0.550	9.22	355.2	0.0248	Green et al., 1964
Mont Cenis silt loam	1.8070	1.2814	0.000	0.442	1.41	150.4	0.1670	Vachaud, 1966
Yolo fine sandy loam	0.9440	3.1091	0.171	0.375	1.48	200.2	0.0726	Moore, 1939
Vernal sandy loam	5.6060	1.2562	0.000	0.475	22.10	485.9	0.1100	Nimah & Hanks, 1973
Bet Dagan 1 loamy sand	2.7610	3.0224	0.044	0.375	638.32	16313.0	0.0404	Russo & Bresler, 1980
Panoche soil	1.6560	1.8033	0.249	0.450	44.28	13119.0	0.0230	Nielsen et al., 1973
Gravelly sand G.E.-9	1.4960	2.8043	0.080	0.326	27.40	1365.0	0.0450	Reisenauer, 1963
Hygiene sandstone	0.8010	7.3563	0.150	0.250	124.96	12380.0	0.0090	Brooks & Corey, 1964
River sand	3.6260	5.2091	0.000	0.350	222.84	3841.0	0.0135	Jensen et al., 1967
Sable S2	10.0220	1.3741	0.000	0.410	409.58	470.9	0.0046	Stroosnijder, 1982
Lakefield fine sand 3	2.7140	3.5955	0.077	0.360	529.10	14463.0	0.0328	Elseftawy & Mansell, 1975
Lakefield fine sand 1	2.4070	3.6334	0.103	0.365	463.73	12149.0	0.0254	Elseftawy & Mansell, 1975
Uplands sand	7.0870	1.8103	0.049	0.304	182.92	2164.0	0.0605	Staple, 1969
Nahal Sinai sand	2.4700	5.7633	0.036	0.270	344.79	11038.0	0.0182	Bresler et al., 1971

* at -1 kPa; ** or highest θ reported.

39

of interest for $\theta_r < \theta < \theta_{1.5}$; at lower θ, hydraulic conductivity is set to zero and liquid pressure is not a relevant variable.

The vapour adsorption isotherms will be discussed in Subsection 2.6.3.

Hysteresis

Although SALSA does not include a formulation for hysteresis, some remarks must be made regarding this phenomenon. A theoretical concept of hysteresis to be used in the study of diurnal topsoil behaviour should take into account the hysteresis in both the $p(\theta)_T$ and the $p(T)_\theta$ relations. The former represents the classic hysteretic behaviour, for which some theoretical models have been formulated (Poulovassilis, 1962; Mualem, 1973; Mualem & Morel-Seytoux, 1978). Evidence of the latter case, called 'thermal' hysteresis for short, was reported by Moore (1940), Gardner (1955), Taylor & Stewart (1960), and Richter (1972), and was also found for Swifterbant silt loam in the study discussed in this report. However, observations are inconsistent. In addition to the well-known 'pore neck' explanation, both classic and 'thermal' hysteresis are possibly related to wetting angle hysteresis and changes in soil structure. Rose (1971) reported on hysteresis down to very low moisture contents, in the range of physical adsorption ($p \approx -1$ GPa) where significant liquid movement is unlikely; from his observations it can be expected that mechanisms other than 'pore-neck' are involved.

Although it is recognized (Chapter 5) that hysteresis may play a significant role in diurnal soil water evaporation cycles (see also Hillel (1976) for a simulation exercise), the phenomenon is not included in the SALSA model. Hysteresis is viewed as a refinement at a stage where 'coarser' effects of soil properties on the surface energy balance still have to be generalized.

Hydraulic conductivity

For the description of moisture flow in simulation models, the $K(\theta)$ relation can be introduced in different ways. One possibility is to use a tabulated function, obtained by direct measurement. Care should be taken that the $K(\theta)$ curve used is realistic at its drier end, because in the present context evaporation rather than infiltration cases are studied.

In the SALSA model, the $K(\theta)$ function can either be specified as a table of measured data, or be calculated on the basis of the model by Mualem (1976), using Equations 58 and 59 to express the moisture characteristic. The resulting equation for the hydraulic conductivity reads:

$$K = K_s \, \varXi^{1/2}(1 - (1 - \varXi^{1/m})^m)^2 \qquad \text{Equation 60}$$

where K_s is the conductivity at saturation and $\varXi$ and m are defined as for Equations 58 and 59. This implies that K is zero for $\theta \leqslant \theta_r$. The K values at the interfaces of two neighbouring compartments in the model are averaged by using the square root from the product of the two K values (Vauclin et al., 1979).

40

Temperature also affects the hydraulic conductivity, because the viscosity η (Pa s) is temperature dependent (see Figure 5). The $K(T)_\theta$ function is usually expressed satisfactorily by the relation

$$K_\theta(T) = K_\theta(T_o) \frac{\eta(T_o)}{\eta(T)} \qquad \text{Equation 61}$$

where T_o is a reference temperature (Philip & de Vries, 1957; Haridasan & Jensen, 1972; Rahi & Jensen, 1975; Saha & Tripathy, 1979; Hopmans & Dane, 1986). Constanz (1982) reported a stronger temperature influence than predicted by this relation. As shown in Figure 5 and explained in Subsection 2.6.1, the $\eta(T)$ relation appears to counteract the effect of temperature on the slope $(\partial p/\partial\theta)_T$. Although this compensation is only a rough approximation, and considerable scatter and inconsistency occur in the reported data of both $K(T)$ and $f(T) \equiv (\partial p/\partial\theta)_T$, it seemed warranted to exclude both functions from the simulation model.

Matric flux potential
According to Darcy's law, the flux density equation for flow in the vertical contains the sum of a 'matric' component and a gravity component:

$$J_w = -K \frac{\partial p}{\partial z} + \rho_l g K \qquad \text{Equation 62}$$

The flux by the matric term can be written as the gradient of a flux potential Φ, called 'matric flux potential' (Raats, 1970). This matric flux potential is defined as

$$\Phi \equiv - \int_p^o K(p)\, dp = - \int_\theta^{\theta_s} D(\theta)\, d\theta \qquad \text{Equation 63}$$

Because the transport coefficient K is incorporated into Φ, the latter is not a common potential in the sense that its gradient should represent a force per unit mass or per unit volume. The associated gradient vector field is the flux field that results from matric forces. The transformation involved is also called the Kirchhoff transform. Klute (1952) introduced the concept into soil physics. It has since been used in mainly analytical solutions of the flow equation for multidimensional systems, in combination with an exponential $K(p)$ relation (e.g. Philip, 1971; Warrick, 1974; Raats, 1977). As the integral in the above equation converges for realistic $K(p)$ functions (Raats & Gardner, 1971), the $\Phi(p)$ and also $\Phi(\theta)$ curves all show the same characteristic shape (see Chapter 4).

In numerical simulation, the use of the matric flux potential has some advantages over the $K - p$ formulation (Shaykewich & Stroosnijder, 1977). The major

gain is that averaging of transport coefficients, a problem encountered in numerical solutions of the flow equation (e.g. see Vauclin et al., 1979), is avoided. This is especially advantageous to the simulation of the evaporation process and of infiltration into dry soil, where very large potential gradients occur. In such cases it is difficult to choose a representative average K value; this may result in significant errors in the calculated flux. Moreover, the $\Phi(\theta)$ curve is more easily interpreted in terms of fluxes than a combination of $K(\theta)$ and $p(\theta)$. An additional advantage is that $\Phi(\theta)$ can be measured directly over a wide range of θ by a relatively easy procedure, as proposed by ten Berge et al. (1987).

A drawback is that the matric flux potential concept applies best to homogeneous soils, although its use for inhomogeneous soils is possible (Penning de Vries et al., 1989). It also loses its physical significance if hysteresis in the $p(\theta)$ function occurs, and if the driving force for liquid movement is affected by temperature or by the temperature gradient; this, however, is assumed not to be the case (see Subsection 2.6.1).

In SALSA, either the $\Phi(\theta)$ or the $K(\theta)$-$p(\theta)$ option can be chosen. In the former case, $\Phi(\theta)$ can be given in tabulated form, or can be specified by an analytical function, involving two empirical constants:

$$\Phi(\theta) = \frac{-Ax}{x + B} \qquad\qquad \text{Equation 64}$$

where x is defined as $x \equiv 1 - \theta/\theta_s$. The scale parameter A determines the maximum stationary flux $A/(1 + B)$ that can be attained through a soil slab of thickness unity, and the 'saturation constant' B is related to the shape of the curve. Table 8 lists these coefficients for a number of soils. Equation 64 approximates very well the Φ curve for almost every soil given in the table.

Scale length

A scale parameter has been introduced in SALSA, to allow for easy changes in hydraulic scale, simultaneously affecting moisture characteristic, conductivity and matric flux potential. The subject of scaling will be treated in Chapter 4.

2.6.3 Coupling: non-isothermal transport in the vapour phase; the formulation of $\rho_v(\theta, T)$

Vapour transport in the soil plays an important role in the surface energy balance when evaporation takes place below the surface, but generally also at night, when condensation may occur in the topsoil.

This subsection expounds how the driving force for vapour transfer in Equation 53 – i.e. the gradient of vapour density $\rho_v(\theta, T)$ – is formulated. Again, local thermodynamic equilibrium is assumed between water phases in the soil. This is probably realistic, except for extremely high infiltration rates into coarse soils (Milly, 1982). Furthermore, the total gas pressure of soil air is assumed to be

atmospheric, although some caution must be taken on this point (Subsection 2.6.4).

The density gradient of water vapour can be written as (Philip & de Vries, 1957):

$$\frac{\partial \rho_v}{\partial z} = \left(\frac{\partial \rho_v}{\partial T}\right)_\theta \frac{\partial T}{\partial z} + \left(\frac{\partial \rho_v}{\partial \theta}\right)_T \frac{\partial \theta}{\partial z} \qquad \text{Equation 65}$$

with respectively the so-called 'thermal' and 'isothermal' terms on the RHS; these terms will be discussed below in that order.

Vapour density versus temperature
In analogy to Equation 55 the Clapeyron equation for the liquid vapour system (Kay & Groenevelt, 1974) states

$$\overline{V}dp - \tilde{V}d\tilde{p} = (S - \tilde{S})\, dT \equiv \Delta H_v \frac{dT}{T} \qquad \text{Equation 66}$$

where $\tilde{p}$ and p are the pressure in the vapour and in the 'extramatric' liquid phases, respectively, and $\overline{V}$, $\tilde{V}$ and S, $\tilde{S}$ are the specific volume ($m^3\, kg^{-1}$) and partial specific entropy ($J\, kg^{-1}\, K^{-1}$) for both phases respectively; ΔH_v is the latent heat of vaporization ($J\, kg^{-1}$).

For thermo-osmosis (in this context the transport of vapour resulting from a temperature gradient under the condition $dp = 0$), combining the universal gas law with Equation 66 yields

$$d\tilde{p} = \frac{-\Delta H_v \tilde{p} M}{R T^2}\, dT \qquad \text{Equation 67}$$

Since it is preferred, however, to use the moisture content θ as the independent variable instead of p, a formulation is sought for the situation where $\nabla\theta = 0$ and $\nabla T \neq 0$. The driving force $\nabla\tilde{p}$ is then not obtained exactly by Equation 67, because the gradient of the extramatric pressure, ∇p, is not necessarily zero for this case (see Subsection 2.6.1). The term $\overline{V}(\partial p/\partial T)$ as encountered when defining $\nabla\tilde{p}$ from Equation 67, however, is two orders of magnitude smaller than $\tilde{V}(\partial\tilde{p}/\partial T)$. The former can therefore be virtually ignored, and Equation 67 remains a valid approximation, for $d\theta = 0$ also. Thus, in contrast to the liquid case, where ∇p and $\nabla p'$ had the same order of magnitude but opposite directions, it is found here that the two gradients ∇p and $\nabla\tilde{p}$ are of the same direction but of different order of magnitude, at constant θ.

Furthermore, differentiation of the gas law with respect to temperature results in the relation

$$\frac{\partial \rho_v}{\partial T} = \frac{M}{RT} \frac{\partial \tilde{p}}{\partial T} - \frac{\tilde{p} M}{R T^2} \qquad \text{Equation 68}$$

where ρ_v is the vapour density (kg m^{-3}), R is the gas constant (J mol^{-1} K^{-1}) and M the specific molar mass of water (kg mol^{-1}). So, the transformation of $\partial \tilde{p}/\partial T$ into $\partial \rho_v/\partial T$ involves a second term on the RHS of Equation 68, which is negligible under natural field conditions; it represents only approximately 5% of the first term. This may explain the absence of the latter term in the analysis by Jury & Letey (1979). Now, combining Equations 67 and 68 (with the simplifications mentioned), gives the expression used by Jury & Letey (1979):

$$\frac{\partial \rho_v}{\partial T} \approx \frac{-\Delta H_v \tilde{p} M^2}{R^2 T^3} = \frac{-\Delta H_v^* \tilde{p} M}{R^2 T^3} \qquad \text{Equation 69}$$

(where ΔH_v is expressed in J kg^{-1} and ΔH_v^* in J mol^{-1}!).
The 'mechanistic' formulation (Philip & de Vries, 1957) uses the first term in Equation 69 to formulate the driving force as $(\partial \rho_v/\partial T)\nabla T$. Alternatively, the last term in this equation is employed in combination with ∇T (e.g. Cary, 1963).

Usually, (in SALSA, too) the derivative $(\partial \rho_v/\partial T)_\theta$ is calculated as $h(\partial \rho_{vs}/\partial T)$, where h is the relative humidity and ρ_{vs} is the saturated vapour density. This
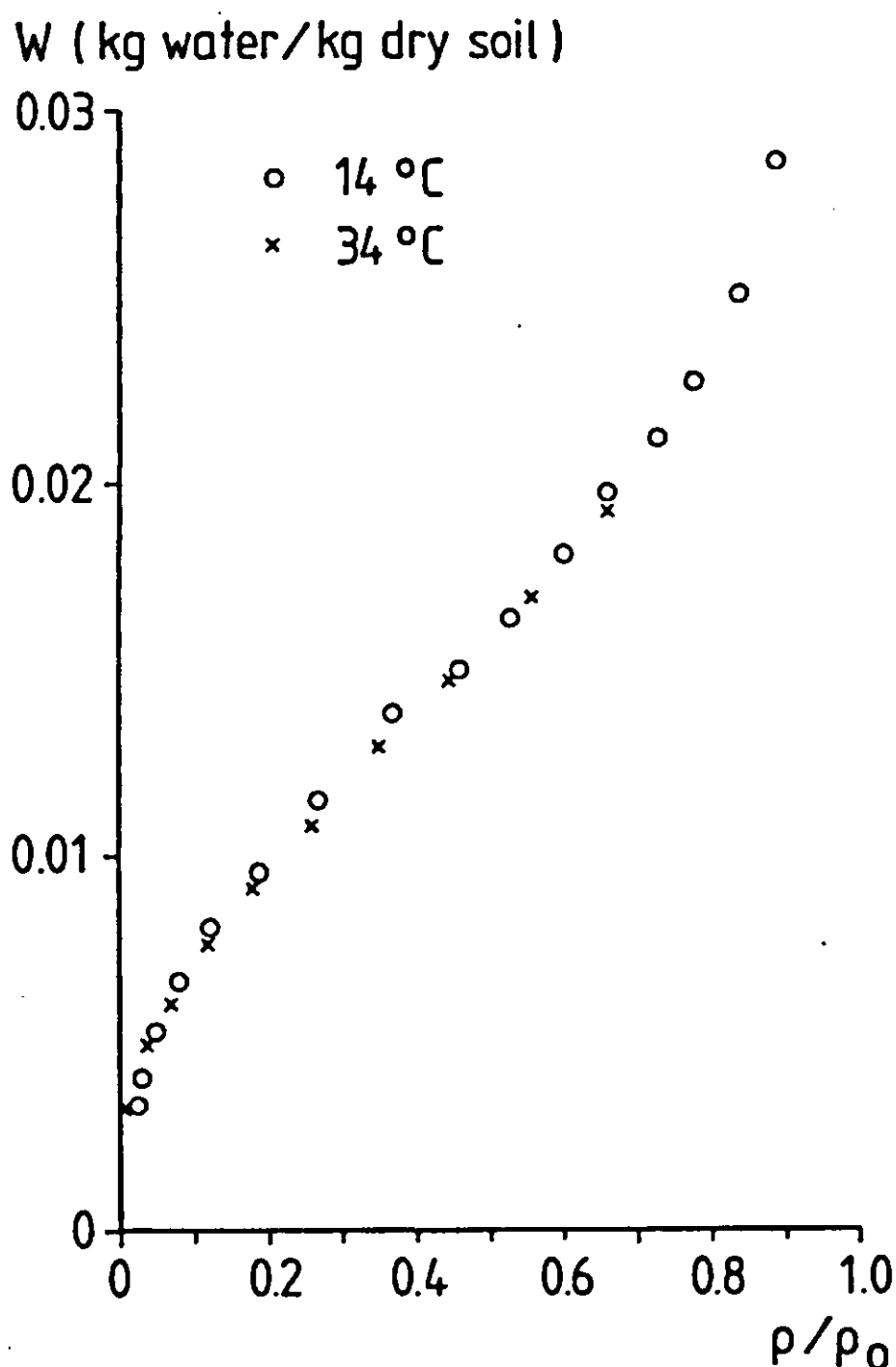

Figure 6. Adsorption isotherms for water on Millville silt loam at two temperatures. After Cary et al. (1964).

44

implies assuming that the term $\rho_{vs}(\partial h/\partial T)$ is negligible, as Philip and de Vries did. This is in accordance with results found by Cary et al. (1964) and Kijne & Taylor (1964), who showed that at constant gravimetric water content the relative humidity h changed by only 1-5% of its average value, for temperatures ranging from 15 to 35°C (Figure 6). However, few experimental data are available to verify the general validity of this behaviour for soil materials. In SALSA, $\rho_{vs}(T)$ is read from tabulated data.

Vapour density versus water content

At soil water pressures below -1.5 MPa, common at the soil surface, the decrease of relative humidity has a marked effect on vapour density in the soil atmosphere. Vapour fluxes may then be governed by the gradient in relative humidity, and the second term in Equation 65 becomes important. Without this term, soils with a dry surface would not lose water during daytime, at least not by diffusion; the temperature gradient would then dictate downward vapour diffusion.

The derivative $\partial\rho_v/\partial\theta$ can be replaced by $\rho_{vs}(\partial h/\partial\theta)$. In modelling, the relative humidity $h(\theta)$ is usually calculated by combining the Kelvin equation

$$h = \exp\left(\frac{\psi M}{RT}\right)$$

Equation 70

with a given moisture characteristic (ψ is the moisture potential in J kg^{-1}). Here it is preferred not to do so, because the $p(\theta)$ or $\psi(\theta)$ curve is often based exclusively on measurements at higher values for θ and hence must be extrapolated to the range of interest, where the curves are extremely steep. Instead, it is more appropriate to employ adsorption isotherms of water to clay minerals, combined with an estimate of the clay content of the soil. Some of these adsorption isotherms are depicted in Figure 7, showing the characteristic sigmoidal shape found for soil materials (Thomas, 1928; Orchiston, 1954; Rose, 1971; Scotter, 1976).

The clay content of soil materials largely determines the gravimetric water content at given relative humidity, as is well known from moisture characteristics. At low relative humidity ($h < 0.8$), the thickness of the water layer on the surface of clay platelets does not differ much from one clay mineral to another, although the species of adsorbed cations present may have a considerable influence (Table 9). In general, a monolayer of water molecules is thought to be adsorbed at $h = 0.2$, and twice the amount of water at $h = 0.6$ (Quirk, 1955; Orchiston, 1954; Vershinin et al., 1966). The large differences in specific surface area of the various clay minerals, however, are reflected in the different isotherms. As is well known, the specific surface area of the different clays varies over about two orders of magnitude, in the following order: 5-50 m^{2}g^{-1} for kaolinite, 50-200 m^{2}g^{-1} for illite, and 200-800 m^{2}g^{-1} for montmorillonite.

For application in the SALSA model, the exact shape of the isotherm is not

W (kg water/kg dry clay)

1. montmorillonite
2. illite
3. kaolinite

p/p_0
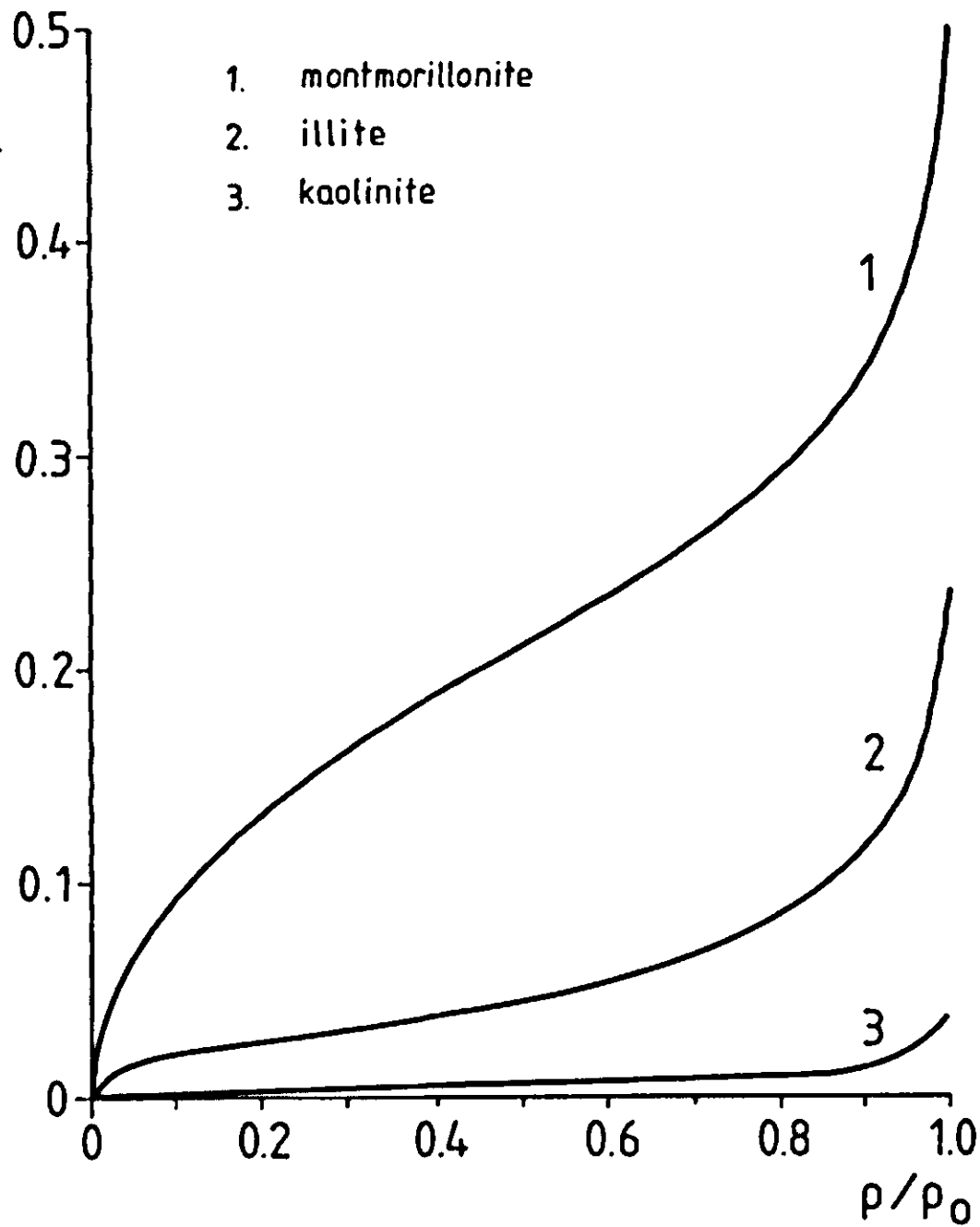
Figure 7. Adsorption isotherms for water on different clay minerals. After Orchiston (1954).

relevant, and the curves are simplified to a set of linear segments, characterized by a single parameter, A. This parameter represents the gravimetric moisture content (mass of liquid per mass of clay) at $h = 0.8$. The corresponding volumetric water content is then calculated on the basis of the mass of clay per unit volume of bulk soil, and is here indicated by θ_{30} ($-$ 30 MPa being the pressure equivalent of a relative humidity $h = 0.8$). The values of A for different soil materials are listed in Table 9, along with the moisture content at $h = 0.2$.

As liquid pressure drops below -1.5 MPa ('wilting point', $h \approx 0.99$) relative humidity starts departing from unity and hence this point, indicated by $\theta_{1.5}$, is another mark to characterize the adsorption isotherm. So, finally, SALSA calculates $h(\theta)$ by the equations

$$h = \frac{\theta \rho_1}{f_c \rho_c} \frac{0.8}{A} \qquad \text{for } 0 < \theta < \theta_{30} \qquad \text{Equation 71}$$

$$h = 0.8 + 0.2 \left(\frac{\theta - \theta_{30}}{\theta_{1.5} - \theta_{30}} \right) \qquad \text{for } \theta_{30} \leq \theta < \theta_{1.5} \qquad \text{Equation 72}$$

Table 9. Characteristics of adsorption isotherms: gravimetric water content at relative humidities h of 0.2 and 0.8.

	$h = 0.2$ (kg$_{water}$ kg$^{-1}_{dry\ soil}$)	$h = 0.8$ (kg$_{water}$ kg$^{-1}_{dry\ soil}$)	Source
Loamy sand	0.010	0.025	Scotter, 1976
Millville silt loam	0.010	0.024	Cary et al., 1964
Ca^{++} sat. chernozem	0.049	0.092	Vershinin et al., 1966
Illite	0.050	0.080	Orchiston, 1954
Li-kaolinite	0.003	0.008	Jurinak, 1963
Montmorillonite	0.130	0.300	Orchiston, 1954.
Ca-montmorillonite	0.120		Kijne, 1969
Na-montmorillonite	0.040		Kijne, 1969

$$h = 1.0 \qquad \text{for } \theta_{1.5} \leq \theta \qquad \text{Equation 73}$$

where ρ_1 is the specific density of the liquid and $f_c\, \rho_c$ the mass of clay per unit of bulk soil volume.

By definition, isotherms are valid for a specified temperature. The wisdom of using a given isotherm over a range of temperatures to calculate $h(\theta)$ may therefore be questioned. Nevertheless, as mentioned before, experimental evidence suggests that $(\partial h/\partial T)_\theta$ is negligible and that it is justifiable to use one single isotherm.

2.6.4 The transport coefficient of water vapour in soil; enhancement effects

Diffusion enhancement

The transport of water vapour in soil is still subject to extensive discussion and the mechanisms involved are not yet fully understood. Originally, water vapour was viewed as an inert gas, the diffusion of which is determined by the concentration gradient and D_a, the diffusivity of vapour in free air (Krischer & Rohnalter, 1940):

$$J_v = -D_a v_\cdot \alpha f_a \frac{\partial \rho_v}{\partial z} \qquad \text{Equation 74}$$

where α, f_a, and v are correction factors for tortuosity, airfilled pore space and mass flow, respectively. Many experiments, however, have shown that the actual water vapour flux considerably exceeds the estimates made on the basis of molecular diffusion and the density gradient, determined by the bulk temperature gradient. This discrepancy is referred to as 'enhancement' of vapour

transfer. Several explanations have been proposed. After distinguishing between a 'thermal' and an 'isothermal' component of the density gradient (Equation 65), Philip & de Vries (1957) suggested that enhancement is caused in the thermal term by two effects. One is the interaction between vapour and liquid: transport is increased by condensation on the 'warm' end of so-called 'liquid islands', accompanied by evaporation at the 'cool' end. The other effect would be caused by the difference between the local temperature gradient in the gas phase and the bulk soil temperature gradient. These authors formulated the thermal vapour flux by

$$J_v = -\left\{ (f_a + f(a)\theta)\, v\, \xi\, D_a \frac{\partial \rho_v}{\partial T} \right\} \frac{\partial T}{\partial z} \qquad \text{Equation 75}$$

The term in major brackets was designated as the 'thermal vapour diffusivity'. In the above equation, $f(a)$ is a function to account for liquid continuity, and ξ is a correction function for the local temperature gradient. Both $f(a)$ and ξ do have a precise definition, but it is not relevant to cite the equations here.

Cary (1963), on the other hand, used a phenomenological coefficient β to account for all local interactions, without an attempt to explain the enhancement phenomenon in further detail. He wrote the vapour flux as

$$J_v = \beta D_a \frac{M\, \tilde{p}\, \Delta H_v^*}{R^2 T^3} \frac{\partial T}{\partial z} \qquad \text{Equation 76}$$

(for the derivation and the use of symbols see Subsection 2.6.3).
So β is simply the ratio of the measured vapour flux to the flux calculated for molecular diffusion through free, saturated air under the same (macroscopic) temperature gradient. It not only accounts for the enhancement effects mentioned, but it also includes the corrections for pore space and path length.

The combination of Equations 69, 75 and 76 shows that Cary's β corresponds to the term $(f_a + f(a)\theta)v\xi$ in Equation 75; so β can be combined directly with $D_a(\partial \rho_v/\partial T)\nabla T$ to express the vapour flux density.

On the basis of this conclusion, Jury & Letey (1979) analysed experimental data from a number of sources. They showed that the Philip and de Vries formulation usually underestimates enhancement in the vapour phase. The coefficient β nearly always appears to be greater than unity, whereas the corresponding term in the mechanistic formulation is reduced to values below one. The values measured for β seem to be fairly independent of moisture content, as appears from Table 10. Several models for the $\beta(\theta)$ relationship have been developed (Jury & Letey, 1979; Cary, 1979; Cass et al., 1984) but there is little agreement between them. In SALSA, β is taken to be a constant, independent of θ.

The above discussion applies to 'thermal' vapour transfer only. On the basis of experiments, Rose (1963a), however, suggested that the 'liquid island' enhancement mechanism is valid for isothermal diffusion as well. In view of this,

Table 10. Reported values for the vapour diffusion enhancement factor β.

Soil	θ (-)	T (°C)	β (-)	Source
Valentine sand	0.02–0.33	26–41	1.06–1.53	Hanks et al., 1967
Rago silt loam	0.07–0.36	3–41	0.75–1.08	Hanks et al., 1967
Portneuf silt loam.	.	.	0.90–3.80	Nielsen et al., 1972
Columbia loam	> 0.192	6–35	0.72–2.37	Cary, 1965
Millville loam	0.16–0.17	15–35	2.34–3.39	Cary & Taylor, 1962a,b
Pachappa loam	0.13–0.18	21–24	1.79–2.05	Weeks et al., 1968
Portneuf silt loam	0.00–0.35	32.5	0.40–2.10	Cass et al., 1984
Sand	0.01–0.19	3.5	0.40–3.50	Cass et al., 1984

(Most data in this table were collected and transformed by Jury & Letey (1979) and Nielsen et al. (1972))

it seems warranted to combine Cary's β with the full density gradient in formulating the vapour flux by diffusion, as is done in the SALSA model:

$$J_v = - \beta D_a(T) \frac{\partial \rho_v(\theta, T)}{\partial z}$$

Equation 77

Vapour flux enhancement by mass transfer

Thus far, the theory discussed has been restricted to diffusion. However, two other enhancement mechanisms may also act in field situations. Hadas (1977a, b) used the term 'mass transfer enhancement' to indicate their combined effect. The supposed mechanisms are forced convection of soil air by pressure fluctuations at the surface, and free or thermal convection under reversed temperature gradients during night-time.

Forced convective transfer was studied by Fukuda (1955), Scotter & Raats (1969), Kimball & Lemon (1971), and Farrell et al. (1966). The latter expressed the increase of effective vapour diffusivity as a function of soil air velocity and frequency of pressure fluctuations. The reported enhancement factors range from 1 for soil materials with particles smaller than 1 mm, to 2-4 for 5 mm aggregates, and up to a factor 100 for coarse mulches (10 mm aggregates). These numbers could well be relevant to tilled soil.

Various authors have discussed free convective transport (e.g. Hadas, 1977a; Menenti, 1984). The former ascribed enhancement factors of about 2.5, derived by comparing day- and night-time values of λ^* (see Section 2.5), to this process. For laboratory experiments, Hadas (1969) reported factors up to 5 for the combined effect of pressure and temperature fluctuations. Menenti extensively elaborated upon stability of soil air, making use of the critical Rayleigh number Ra_{cr} for different idealized cases. As Menenti showed, free convection is supposed to start start at different values of the Rayleigh number, depending on

the model chosen. A difficulty encountered in the usual formulation of stability is the choice of a fixed gradient and corresponding characteristic length. Given the nature of nocturnal soil cooling, it would seem advisable to use, instead, the expressions for local stability in semi-infinite media, subject to surface cooling (Rudraiah et al., 1980 and 1982). This was not done in the present study.

No detailed verifications of enhancement effects for field soils are available, because of the complexity of the required measurements, but the subject certainly merits more attention. Effective vapour diffusivity is one of the major factors affecting evaporation and surface temperature. At the same time, it is one of the parameters that may be strongly influenced by soil management. The extensive and controversial discussion in literature regarding the effect of tillage and mulches on the surface energy balance, and particularly on soil evaporation, is partly caused by the poor understanding of the processes mentioned above.

In the present model, mass enhancement is not formulated separately and must be effectuated by modifying the factor β, which then becomes a 'mixed' coefficient accounting for both diffusion enhancement and convective mass transfer.

3 The SALSA algorithm

3.1 General structure

As described in this monograph, SALSA has a modular structure. This makes it easy for the user to amend the program according to his personal interests, and provides the reader with a clear picture of the different steps involved in solving the transport equations governing the soil-atmosphere system. The main module is written in CSMP (IBM, 1975). All subroutines are written in standard FORTRAN. The flow diagrams given in Appendix 2 illustrate the structure of the algorithm.

The main module, called SALSA, provides the frame for the calling of subroutines and for run control. It also integrates the rates of change of the main state variables. An explicit numerical scheme is used to solve the seven main differential equations (Equations 29a, 29b, 32, 33, 39, 41, and 52). The subroutines reduce these second order partial differential equations, for each time step, to ordinary first order equations. This results in seven main rate equations, which are solved by the 'variable time step Runge-Kutta' fourth order scheme, or by the Milne fifth order predictor-corrector method; the latter method also employs a variable time step.

The subroutines can be divided into three main groups: those describing atmosphere processes, those for soil water transport, and a third group for the thermal regime of the soil. A separate subroutine solves the surface energy balance equation. Furthermore, there are routines for opening and closing of files, reading input data, and preparing output.

System parameters, functions and option switches are read from the input file RUNCON.DAT, physical constants are defined in DATA statements, and wheather data are entered from the input file WEATHER.DAT. Examples of these input files are listed in Appendix 5.

Initialization

After the reading of input values and option switches, the state variables are initialized by an 'INITIAL' call from the main program to the corresponding rate calculating routines. These calls are characterized by a switch that is entered as an input argument to the rate calculating routines. Set to a value of 1, the switch indicates initialization. For 'DYNAMIC' calls, the value of 2 is employed. Auxiliary variables that do not change during one run are calculated by 'initial' calls. The initial phase also sets up a grid to discretize space, in soil and atmosphere.

Dynamic calculations

The DYNAMIC section starts with reading the dynamic boundary conditions from the input file WEATHER.DAT. These boundary conditions are global radiation or net radiation in the case of Option A; in addition to these, Option B requires wind speed, air temperature and humidity data at specified screen height. (The two options were defined in Section 2.1.) For the cases simulated in this monograph, inputs were available at half hour intervals, but other intervals are, of course, possible. The lower boundary conditions to the soil profile are implied in the flux subroutines: zero heat flux and free drainage at the bottom of the soil profile. The flux routine for the atmospheric boundary layer assigns zero values to all the fluxes at the upper boundary of the system.

The rate calculations are subsequently performed by the calling of the rate calculating routines; the rates returned are then integrated by the main program.

3.2 Nomenclature

To make it easier to read the program listings included in this monograph (Appendix 3), some of the general rules followed when designating names to subroutines and variables will be given below. A brief description of all subroutines in alphabetic order, with references to the expressions given in Chapter 2, can be found in Section 3.4.

Soil subroutines

The names of subroutines that refer exclusively to the soil begin with S. The next two characters indicate whether the module describes soil water (WA) or soil heat (HE) processes.

The soil water modules (SWA) are further subdivided according to the aspect of transport that is described: the fourth character indicates whether liquid (L) or vapour (V) is involved. For the routines dealing with liquid (SWAL), a further distinction is made: SWALK for routines that are used in options where a 'hydraulic conductivity formulation' is chosen, SWALM for calculations involving matric flux potential. The sixth letter shows whether a table is used (T) or an expression that calculates (C) the relevant transport coefficient (or flux potential). An F for the fifth character indicates flux calculations. The last character then refers to the 'transport coefficient': either matric flux potential (M) or hydraulic conductivity (K).

The soil heat modules (SHE) are named in a similar way. A distinction is made between conduction (SHEC) and latent (i.e. associated with vapour) heat movement (SHEV). A further C refers to thermal conductivity: CC for calculation based upon an expression, CT for reading from an input table. HC for the last two characters implies heat capacity calculations. Again, the flux routines can be recognized by having an F for the fifth character in their name.

Atmosphere subroutines

The names of all modules that deal with atmospheric processes begin with A. The second character is A for routines that are used in simulations with the full SALSA model (option A), and B for simulations where the development of the atmospheric boundary layer is not taken into account (option B). Contrary to the soil routines, in naming the atmosphere routines no distinction is made between heat, water, momentum and kinetic energy transports. This is reflected in the characters ALL for positions 3-5 in subroutine names. The last letter then indicates whether fluxes (F) or transport coefficients (K) are calculated.

Variables

Appendix 4 lists all the variables included in the SALSA algorithm. Many of the variable names are either derived from the standard name (e.g. BOLZ for the Stefan-Bolzmann constant) or from the name of the symbol that is generally used to indicate that particular variable (e.g. RHOCP for the heat capacity of air under constant pressure).

The main state variables are W and T for soil water content and temperature, U and V for wind speed, TP and Q for potential temperature and specific humidity in the atmosphere, and TKE for turbulent kinetic energy. Most other variable names are composed of one of these main state variable names and some additional characters. These can be FLX or FL for fluxes, I for initial conditions, VAP or LIQ for vapour or liquid, etc.

Space and time derivatives of state variables are written as D..DZZ and · D..DT, respectively. Names of variables denoting a divergence of flux start with DIV. Option switches can be recognized by their two initial characters SW. From the list of variables in Appendix 4 the reader will be able to identify more groups of names with common components.

3.3 Structure of the 'DYNAMIC' section

The calculations in the DYNAMIC section start with solving the surface energy balance equation by ENBAL. This provides the soil and atmosphere with surface temperature as the governing condition at the interface between the two subsystems. Then, atmospheric processes are treated by the subroutine AAALL, using separate routines for the calculation of transport coefficients, fluxes, the production rates of turbulence, and for the indentification of the rates of change of the five main state variables in the atmosphere. As an alternative to AAALL, the routine ABALL is used in the abridged version of SALSA, i.e. option B.

The module SWA coordinates the soil water regime calculations. It is called up by SALSA after AAALL. SWA calls up a number of subroutines, depending on how certain option switches are set. In all options, routines are invoked to calculate the vapour state profile and vapour flux in the soil, respectively. The

matric component of liquid flow is subsequently determined by two routines for the conductivity-pressure option or, if the matric flux potential formulation is chosen, by one different routine. The gravity term is then calculated optionally by the SWALGR subroutine. Total soil liquid fluxes are assessed by a flux routine according to the chosen option, and the rates of change of volumetric soil water content are finally found by SWADDT after summing the liquid and vapour fluxes.

Calculations on the soil thermal regime are ordered by the SHE routine. In analogy to the soil water regime, two transport mechanisms are treated separately, in this case heat transport resulting from conduction, and latent heat transport. Auxiliary state variables such as heat capacity and thermal conductivity are treated individually by separate routines. The two heat fluxes are then calculated, and finally the rate of change of soil temperature is established by SHEDDT as the divergence of the total heat flux .

Output is prepared by OUTPUT. This routine performs some additional calculations associated with output preparation, such as integration over time of output variables (e.g. surface fluxes of heat, moisture and radiation) that, in an experimental set-up, are measured as time-integrated variables.

3.4 Option switches

All options within SALSA are chosen by setting the appropriate parameter to the value 0 or 1. The names of these switch parameters all start with SW. A main switch is SWBLD, which allows a choice to be made between running the full model option A (SWBLD = 1) or the model without boundary layer development (option B). If this abridged version is chosen, all processes described in Subsection 2.4.2 are excluded. This means that all subroutines named AA.... are not used in the simulation.

SWNET is a switch related to the surface energy balance. It is to be given a value of 1 if net radiation is used as an input to the model. In that case, all processes described in Section 2.3 of this report are excluded. This option will be mostly of interest in cases where one prefers to focus on soil transport processes, thus avoiding uncertainties arising from the radiative behaviour of the sky and surface. It must be borne in mind that net radiation is a site-specific variable, which is much dependent on soil processes. This limits the application of SALSA with option SWNET = 1 to simulations of experiments that have actually been conducted, and where net radiation has been measured accurately along with the soil variables of interest.

The remaining switches are related to soil processes. SWMFLP indicates whether or not soil water transport is described in terms of the matric flux potential concept. If so (SWMFLP = 1), then one can choose between using an input table for matric flux potential as a function of moisture content (SWMTB = 1) or using an expression for this relation (see Equation 64). For SWMFLP = 0, a K-p option is effectuated, using hydraulic conductivity and

soil water pressure instead of the flux potential. In the latter case, it must be specified whether the hydraulic conductivity-moisture content relation is presented as an input table (SWKTB = 1) or as the van Genuchten-Mualem expression (Equation 60). For both options SWMFLP = 0 and SWMFLP = 1, the effect of gravity can be included or excluded by setting the SWGRAV switch to 1 or 0, respectively.

Soil thermal conductivity must be specified as an input table if SWCHTB is set to 1, and is calculated according to the de Vries formulation (Equations 43-47) if SWCHTB = 0.

3.5 SALSA subroutines

Below, all subroutines are described briefly in alphabetical order. For the rules of nomenclature, see Section 3.2. For all subroutines that make direct use of expressions presented in the previous chapter, reference is made to the relevant equation numbers. The subroutines are listed in Appendix 3.

Atmosphere routines

AAALL calculates the regimes of heat, moisture, momentum and turbulent kinetic energy in the atmosphere. All processes are treated by calling up four subroutines: AAALK, AAALF, AATKEP, and AADDT. AAALL is only a structure for calling up these routines, and contains no mathematical expressions. It is activated only if SWBLD = 1.

AAALLF calculates fluxes in the atmosphere. It expresses Equations 12-14, for the exchange between surface and atmosphere, and Equations 34-36 for the transfer of momentum, heat, and moisture within the boundary layer. In addition, the kinetic energy flux is calculated in accordance with term IV in Equation 39. In the same way as in the equations quoted here, the fluxes are written as 'fluxes of state variables', rather than fluxes of energy and mass. This is achieved through dividing by the associated capacity, i.e. density or heat capacity. The 'temperature flux' being a generally accepted concept, 'velocity' and 'humidity' fluxes are defined in analogy. It will be clear that the reason for this choice is the non-uniform density profile of the atmosphere.

AAALLK expresses the transport coefficients in the atmosphere. This routine is only required for SALSA option A. Transport coefficients are calculated at compartment interfaces. Stability is expressed according to Equation 15, and the dimensionless gradients according to Equation 18. With the help of these, AAALLK expresses Equation 38 to find the length scales, which are introduced into Equation 37 to finally obtain the transport coefficients for heat, moisture and momentum. Exchange coefficients at the surface are identified on the basis of Equations 21 and 22. The Paulson stability corrections are read from tables established according to Equations 23-25.

AADDT first determines the flux divergences to assess subsequently the rates of change of the five main state variables in the atmosphere: wind speed in two

directions, specific humidity, potential temperature and kinetic energy. The simplified equations of motion (Equations 30a, 30b) are effectuated, and Equations 32 and 33 are used for heat and moisture. The rate of change of kinetic energy is based on the production rates as supplied by the routine AATKEP, and on the divergence of the energy flux, according to Equation 39.

AATKEP first calculates wind shear. Subsequently, it expresses – at the compartment centres – the production rates of turbulent kinetic energy arising from friction, buoyancy and dissipation according to Equation 39.

ABALL is only invoked in SALSA option B. For option A, statements corresponding to those in ABALL are included in the AAALLK module. In ABALL the surface exchange coefficients given by Equations 21 and 22 are determined. For this, the stability near the surface must be identified. This is done by using Equations 12, 13 and 15. Subsequently, the Paulson stability corrections as given in Equations 23-24 are used, with the help of the PSIMTB and PSIHTB tables.

ADISCR discretizes the atmosphere with the help of given compartment sizes (TCMM) to yield heights at the centres of compartments, and distances between these centres. AINI calculates an auxiliary static variable, to be used in atmosphere calculations: the second term on the RHS of Equation 38. This is the only non-dynamic variable used in the description of the atmosphere that is not entered as a system parameter.

Input/output routines

The subroutine CLOSES closes the output files. The subroutine OPENS opens the input and output files. OUTPUT prepares the output variables and writes output to specified data files. Additional calculations are the integration of dynamic variables over time intervals, corresponding to intervals over which experimental observations were recorded. This only applies to variables that are also integrated over time during measurement in an experimental set-up. After writing, the integrals are reset to zero. Bowen ratio and wind speed are also calculated by OUTPUT.

Soil routines

SDISCR calculates the distances between soil compartment centres from the input table TCM, which contains the compartment sizes.

SHE treats the soil thermal regime. The SHE routine contains no expressions other than the formulation of total soil heat flux from the components conduction and latent heat flux. It serves as a frame for calling up of the modules SHECHC, SHECCC, SHECCT, SHECCA, SHECF, SHEVF, and SHEDDT.

SHECCA calculates average thermal conductivities at the soil compartment interfaces from the individual conductivities at the adjoining compartment centres.

In SHECCC, soil thermal conductivity is calculated as a function of soil composition, according to the de Vries formulation expressed in Equations 43

and 44. This routine is only used when the switch SWCHTB is set to zero. A number of variables in the de Vries formulation are non-dynamic (and are calculated by the routine SHEINI), but all variables that depend on soil moisture content are updated at each time step. SHECCC distinguishes between the domains where air or water, respectively, are viewed as the continuous phase, and interpolates linearly in the intermediate domain; fixed boundaries of 0.02 and 0.05 volume % are assigned to the latter domain.

SHECCT reads data on the thermal conductivity of the soil from a table (CHTB) at actual values of soil moisture content. SHECCT is only activated if the SWCHTB switch is set to 1.

SHECF determines the soil heat conduction fluxes according to the flux density equation implied in Equation 41, omitting the second RHS term. This second term is included by SHEVF.

Subroutine SHECHC expresses the de Vries soil heat capacity in Equation 42 on the basis of soil composition.

SHEDDT determines the divergence of the total soil heat flux (conduction plus latent heat transfer) and the rate of change of soil temperature according to an approximation to Equation 41. The second term on the RHS of this equation is taken into account implicitly: it is the divergence of the latent heat flux. The soil heat capacity as resulting from the previous timestep and given by SHECHC is used. Accordingly, the LHS of Equation 41 is approximated by ignoring the rate of change in soil heat capacity during the actual time step. For the ensuing inaccuracy, see also the end of Subsection 2.5.2.

SHEINI determines non-dynamic auxiliary variables that play a role in the heat budget calculations. This routine is only invoked if the option SWCHTB = 0 is chosen, i.e. the de Vries expression of thermal conductivity. For soils with a homogeneous composition of the solid phase with depth, the course of bulk density can be used to assess fractions of all solid constituents at different depths. SHEINI calculates the weight factors k according to Equation 47 and thermal conductivity at 2% and 5% moisture content for interpolation, on the basis of Equations 43 and 44.

SHEVF expresses the latent heat flux in the soil in accordance with the second RHS term of Equation 51, using the soil vapour flux as given by SWAVF. Since the heat of evaporation at the surface has not been involved explicitly in the energy balance equation, the vapour flux crossing the soil surface must be treated as a loss (or gain) of heat, stored in the uppermost compartment of the soil.

The SWA routine provides the frame for calculations regarding the soil water regime. It offers a choice from several options: formulation of the flow equation in terms of matric flux potential or, alternatively, in terms of water pressure and conductivity, and the inclusion or omission of gravity. Also, choices can be made between calculation or use of input tables for conductivity and matrix flux potential relations, as a function of water content. First, potentials and transport coefficients are calculated; subsequently, fluxes of vapour and liquid

are determined through various subroutine calls. SWA contains no expressions other than the formulation of the total water fluxes at compartment interfaces.

SWADDT determines the rate of change of soil water content for each soil compartment. Total water fluxes at all compartment interfaces are inputs, and are used to assess the flux divergences as implied in Equations 52 and 53.

SWAINI performs non-dynamic actions to initialize soil water variables: it assigns values of the system parameters to all soil compartments and assesses a few auxiliary variables. The moisture content at -1.5 MPa is calculated according to Equations 58 and 59.

SWALFK calculates the matric component of the liquid soil water flux with the help of the conductivity-pressure formulation, as given in the first term on the RHS of Equation 62. Subsequently, it adds the gravity component to determine the total liquid flux. SWALFK is only invoked if SWMFLP equals zero. SWALFM determines the same term, but this time on the basis of matric flux potential, thus replacing the differential $K \, dp$ in Equation 62 by the finite difference in matric flux potential between two adjacent compartments. Like SWALFK, it adds optionally the gravity component of the flux.

SWALGR determines the gravity component of the liquid flux if SWGRAV = 1. This serves as input to either of the flux routines. For SWGRAV = 0, it assigns the value of zero to the gravity component.

In SWALKA the K values at compartment interfaces are averaged by taking the geometric mean of the individual K values that prevail in the contiguous compartments. The use of matric flux potential (i.e. SWMFLP = 1) restricts the averaging procedure to only the gravity component of the flow.

For all soil compartments, SWALKC determines the hydraulic conductivity as a function of moisture content, using Equation 60. No temperature correction is applied, as explained in Subsection 2.6.2. For water contents below the residual water content, liquid continuity is assumed to be absent, which reduces hydraulic conductivity to zero. SWALKC is only activated if SWMFLP = 0, or SWGRAV = 1 combined with SWKTB = 0.

As an alternative to SWALKC, conductivity may be read from an input table by SWALKT if the SWKTB switch is set to 1.

When the option SWMFLP = 1 is chosen in combination with SWMTB = = 0, then the matric flux potential is calculated by SWALMC at the actual moisture contents with the help of Equation 64. Alternatively, a tabulated function is used in SWALMT when SWMTB = 1.

SWALPR calculates soil water pressure from relative moisture content for the higher values of moisture content (greater than the value corresponding to -1.5 MPa), and from relative humidity of the soil air for the lower moisture contents. The latter is done on the basis of Equation 70, whereas at higher moisture contents the Equations 58-59 are employed. Soil water pressure at moisture contents below -1.5 MPa may be relevant if residual moisture content is lower than $\theta_{1.5}$, and liquid transport may therefore occur beyond $\theta_{1.5}$.

SWAVD determines the effective vapour diffusivity in the soil as a function

of temperature and the enhancement coefficient BCARY. Diffusivity is assumed to be independent of soil water content. The theoretical justification for this controversial assumption is given in Subsection 2.6.4.

SWAVF calculates the flux of soil water vapour according to Equation 77. The routine SWAVS formulates the vapour state profile (density). It first reads saturated vapour density at the governing temperature from an input table, and subsequently uses Equations 71-73 to assess relative humidity and absolute vapour density, taking into account the parameter A derived from adsorption isotherms (see Subsection 2.6.3).

4 Field experiments

4.1 Introduction

Few detailed field experiments have been carried out to study the diurnal and spatial course of moisture content and temperature in bare topsoils. The most extensive set of data available is that obtained by Jackson and his colleagues at the USDA Water Conservation Laboratory in Phoenix, Arizona. This group collected data on soil moisture and temperature at small intervals of time and depth, along with meteorological data, for several weeks in spring 1971 (Jackson, 1973).

For the present study, two similar field experiments were conducted under different climatological and soil conditions, in order to obtain different independent data sets to be used for model validation trials. In 1982 an experiment was conducted in Oostelijk Flevoland, The Netherlands; a second experiment took place one year later in the USA with the group of van Bavel at Texas A&M University. The 1982 experiment yielded two data sets, because the weather varied markedly during the measurement period, allowing the results to be divided into two distinct series. Including the data obtained by Jackson, four different data sets from detailed bare soil energy balance experiments were therefore available for model validation. In this monograph, only the Dutch sets Flevo-1 and Flevo-2 will be discussed in detail. For a more elaborate description of field data collection, including the Texas and Arizona sets, see ten Berge (1986).

This chapter discusses the experimental set-up, the type of measurements, the calculation procedures and the results of the Flevoland field experiments. Some of the results will, however, be given in Chapter 5. As the measurements will be used in the next chapter to compare model predictions with actual system behaviour, the experiments are described here in terms of initial conditions, system parameters and functions, boundary conditions, and 'output variables'. The latter are the soil state variables, and the surface fluxes of heat and moisture. They are called 'output variables' because they are to be predicted by simulation. Their measured values are therefore not discussed here but will be presented in Chapter 5, along with simulation results. However, the measurement and calculation procedures and the errors involved are treated in this chapter, for all variables.

The initial conditions are the profiles of the soil state variables. At the upper boundary of the system, incoming or net radiation and rainfall or irrigation determine the flux boundary conditions. Air temperature, humidity and wind speed at a given height above the soil surface are the state boundary conditions.

The lower boundary conditions to the system are set by the fluxes of heat and moisture at a given depth below the soil surface. System parameters and functions express the radiative, thermal and hydraulic properties of the soil, and a soil-atmosphere exchange coefficient. Detailed specifications of equipment, measuring depths and heights, frequencies etc. can be found in ten Berge (1986).

In the experiments, soil behaviour was the principal phenomenon studied. The atmospheric variables at screen height or lower were measured as boundary conditions. The data are not suitable for checking models that include mixed layer development in the lower atmosphere – such as SALSA option A – because of the limited size of the experimental field, and the lack of measurements at elevations high above the surface.

4.2 Variability and errors

As model predictions are to be compared with observations, the uncertainties, both in measurements and in predictions, must be known. Comparisons between model performance and reality that do not specify errors, have a somewhat limited significance at best. Before discussing the results of the measurements, some attention will therefore be paid to error analysis. The term 'uncertainty' as used here refers to the possible deviation of a measured value at some point in the field from the actual value at a particular location for which a prediction is made. Clearly then, spatial variability may play an important role and must be studied when model predictions are to be compared with field observations.

In this monograph, variance resulting from measurement errors is used as a measure of uncertainty. Chapter 5 shows how both the variance in predicted 'output variables', resulting from errors in model input, and in measured 'output variables', can be used to validate the model. Therefore, Chapter 4 includes a brief discussion on errors in measured input and output, i.e. errors in system parameters, boundary conditions and driving variables, and errors in fluxes and soil state variables, respectively.

Errors in measurement are caused by calibration errors, by violation of certain assumptions underlying the experimental method, and by inertia of apparatus. Instantaneous values of boundary layer variables are especially sensitive to problems of inertia. In the present experiments, all meteorological variables were integrated over half-hour or one-hour intervals, and it was assumed that the time-averaged values were representative for these intervals. Calibration errors were either known or estimated. Uncertainties arising from erroneous model assumptions are often more difficult to deal with. An example is the measurement of thermal conductivity by means of the 'probe method' in the field. In that case, the contact resistance at the probe surface and inhomogeneity of the surrounding soil conflict with the assumptions underlying the method. The measurements of hydraulic conductivity and matric flux potential

curves are also susceptible to this type of error. In such cases, variance resulting from measurement errors was estimated from a comparison between results obtained by different methods, or it was assumed that measurement errors were small in relation to measured field variability.

Spatial variability gives rise to a particular type of variance. Since soil and atmosphere are laterally inhomogeneous, uncertainty is not only the result of measurement errors, but also of the spatial dependence of the variable under consideration. For the boundary layer variables and radiation terms, this dependence was not measured and the simplifying assumption of lateral homogeneity was made. In soil physics and related fields, on the other hand, this problem of spatial variability has rapidly gained more attention during the last decade, and several techniques are now available to account for field variability of soil properties. For reviews see Nielsen et al. (1983), Nielsen & Bouma, (1985) and Philip (1980). Two of these techniques, applied in this report, will be discussed briefly below. They are 'semivariance analysis' and the 'scaling' approach.

Semivariance analysis

Spatial variability analysis prior to detailed study of dynamic (i.e. time-dependent) soil behaviour can be useful for selecting sampling plots and for assessing variability within these plots. Semivariance data were used to do this in the Flevoland field experiments. Let $Z(x)$ be a regionalized variable, i.e. a variable which describes a property in space (here, along a transect). The semivariance for this variable is then defined as

$$\gamma(h) \equiv \tfrac{1}{2} \, \text{var} \, (Z(x) - Z(x + k\Delta x)) \qquad \text{Equation 78}$$

where $Z(x)$ denotes the variable in location x along the transect, and $Z(x + k\Delta x)$ denotes the variable in location $x + k\Delta x$, at k steps Δx from x along the transect (Journel & Huijbregts, 1978). The semivariance at level k is half the population variance of differences $(Z(x) - Z(x + k\Delta x))$. It is an indicator of the spatial structure of the variable $Z(x)$. It can be shown that $\gamma(k)$ is equal to the variance of $Z(x)$ in the case of second order stationarity, i.e. when both the expectation and the variance exist and do not depend on the location x. In that case one may write

$$\tfrac{1}{2} \, \text{var} \, (Z(x) - Z(x + k\Delta x)) = \tfrac{1}{2}(\text{var} \, Z(x) + \text{var} \, Z(x + k\Delta x)$$
$$- 2 \, \text{cov} \, (Z(x),Z(x + k\Delta x))) \qquad \text{Equation 79}$$

or

$$\gamma(k) = C(0) - C(k) \qquad \text{Equation 80}$$

63

where $C(0) \equiv \text{var}(Z(x))$ and $C(k) \equiv \text{cov}(Z(x),Z(x + k\Delta x))$, the so-called co-variance function.

The semivariance is estimated as

$$\hat{\gamma}(k) = \frac{1}{2(N - k)} \sum_{i=1}^{N-k} (z(x_i) - z(x_i + k\Delta x))^2 \qquad \text{Equation 81}$$

where N is the total number of observations along the transect and $z(x_i)$ is an observation on the variable $Z(x)$ at location x_i. One would expect that $\gamma(0)$ be equal to zero. In practice, however, we have to deal with the nugget effect: as a result of sampling and measurement errors, spatial variability within the minimum sampling distance Δx, $\lim_{k \to 0} \gamma(k)$ is often greater than zero. The semivariogram then shows a jump around zero.

The inputs collected on a small test plot of size $(\Delta x)^2$ to feed a dynamic model such as SALSA are therefore also afflicted with this nugget effect (see Chapter 5). Semivariance analysis quantifies the variance at this level. So, a preliminary semivariance study not only provides information that is useful for identifying suitable study locations within a field (e.g. extremes, or 'representative' sites), but also allows estimating the error in variables measured on these study plots. Both these aspects were employed in designing the field experiments.

Scaling of hydraulic soil properties
The concept of scaling was developed in microhydrology to relate transport phenomena in media that have identical pore geometries, except for a multiplication factor called 'scale length'. Assuming this similitude of media is valid, the pressure potential of water in a particular medium at given water content is derived from that of a reference medium at the same water content, and the scale length involved. For some well defined problems, solutions of the water flow equation can then be scaled by dimension analysis. A detailed discussion was given by Miller (1980).

Scaling on the basis of the similitude hypothesis has also been applied to express the field heterogeneity of soil hydraulic properties and of soil water profiles during infiltration. Philip (1967) introduced the term 'scale heterogeneity' to confine field heterogeneity to that specific class of variability that can be eliminated by scaling. A clear picture of the scaling technique applied to the field heterogeneity problem was given by Warrick & Nielsen (1980). In general, scaling is effectuated by assigning a factor α_r to a particular point r such that the local hydraulic properties may be translated into a scaled value by multiplying by α_r. So one finds that $p_{sc} = \alpha_r \, p_r$, where p_r is the observed pressure for a given water content, and p_{sc} is a field averaged pressure at that particular water content. It can be shown that for similar media the scaled hydraulic conductivity must be expressed as $K_{sc} = \alpha_r^{-2} \, K_r$ (e.g. Warrick & Amoozegar-Fard, 1979). It then follows directly that the Kirchhoff transformation – which will be used later in this report – defined as

$$\Phi \equiv - \int_{p}^{0} K(p)dp$$

Equation 82

in a scaled form should be written as $\Phi_{sc} = \alpha_r^{-1} \, \Phi_r$. (See also Subsection 2.6.2) In describing lateral field heterogeneity, it is assumed that α_r is a site-specific constant, valid for all values of water content and for all depths.

Rao et al. (1983) discussed the validity of the assumptions underlying the scaling technique in an extensive evaluation of the approach to field variability. They concluded that in their data sets three basic requirements were not met: (1) saturated water contents were not the same for all sites, (2) the values of the scaling factor, derived from different measured hydraulic properties, were not the same, and (3) the values of the scaling factor were not depth-independent. On the other hand, Warrick et al. (1977) and Simmons et al. (1979) stated that they did not find this disagreement.

In this study, the scaling factors for hydraulic conductivity and for moisture retention curves are assumed to be equal. In addition, a type of 'geometry scaling' has been introduced by using θ/θ_s (the moisture content relative to saturation) in the scaling procedure, instead of θ itself.

Scaled solutions would be attractive because they enable the result of a single simulation run to be translated directly into solutions for similar media. It is noted, however, that even if soil materials at different locations differed only by a scale length parameter, in the present case probably no advantage could be taken from fully scaled solutions of the transport equations. This should be so for two reasons. First, the naturally imposed boundary conditions are variable in time. This is caused by the diurnal courses of atmospheric evaporative demand and of the diurnal soil heat wave, and by the irregularity of rainfall. Because time is also scaled in the process, the frequency at which boundary conditions change in a given location would be prescribed by the local scale length. In reality, however, the whole field shares one common set of boundary conditions.

The second reason is that scaling of the complete flow equation for water is rendered impossible by the presence of thermodynamic coupling (relevant to evaporation).

Nevertheless, scaling remains an effective tool for data compression. The frequency distribution of the scaling factor as derived from measured moisture retention curves is used here both to represent field data, and to calculate the variances in model output associated with scale variance. This is simply done by incorporating the scale factor in the water flow equation, which is then solved numerically.
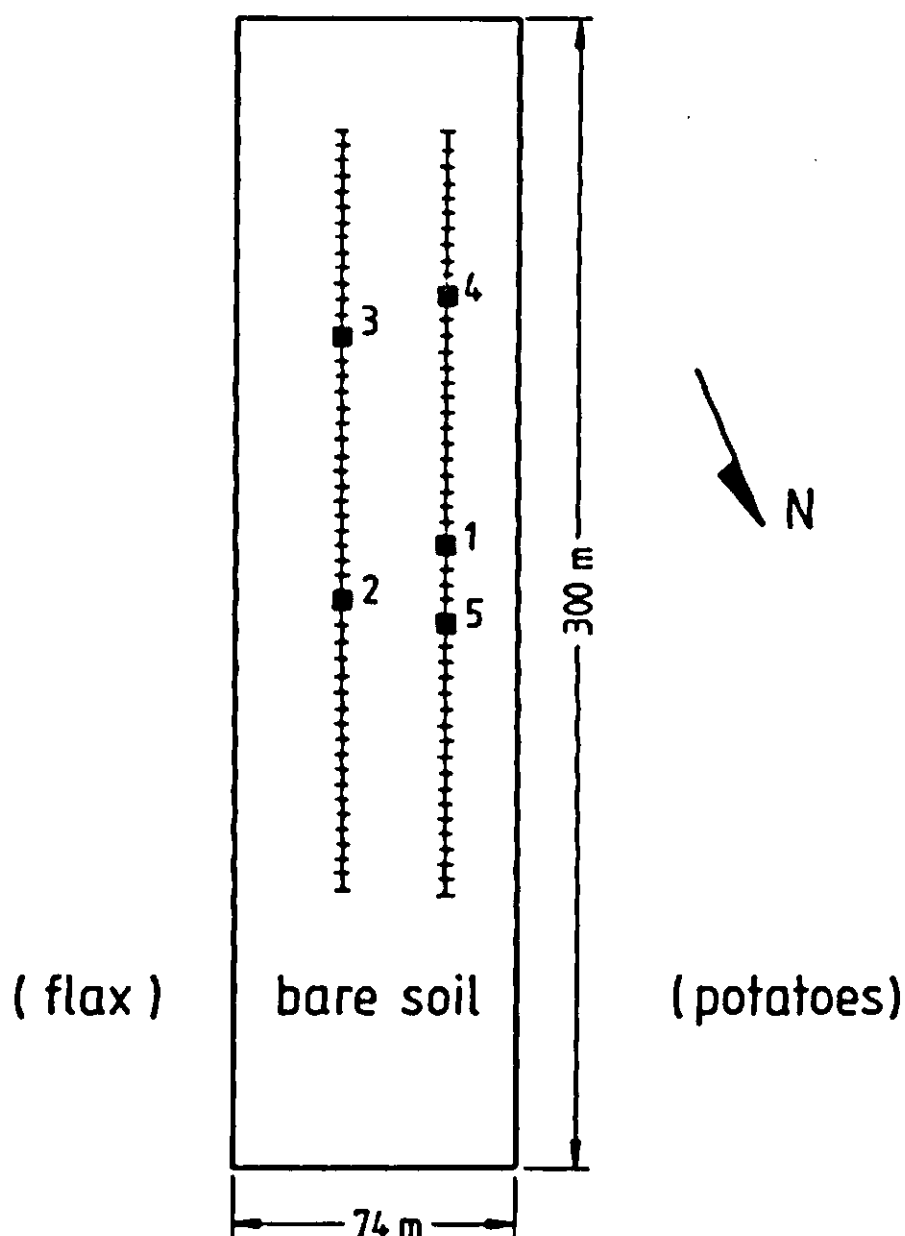
Figure 8. Design of the experimental field at the Ir. A.P. Minderhoudhoeve farm, Swifterbant, Oostelijk Flevoland. The two transects with 50 sampling sites each are indicated. Numbers refer to plots for detailed (time-series) observations.

4.3 Location and general conditions

The site of the measurements was located in the Oostelijk Flevoland polder at the Ir. A.P. Minderhoudhoeve experimental farm of Wageningen Agricultural University. Figure 8 shows the layout of the experimental field. Slight changes in soil texture were observed within the field, so that it could be subdivided into areas of different hydraulic and thermal behaviour. The soils were designated Swifterbant silt loam and Swifterbant loam respectively, although their textural differences barely met the formal requirements for this distinction. The courses of two texture fractions along one of the transects over the field are shown in Figure 9. Figure 10 gives the corresponding semivariograms. The soil surface was levelled by rolling the moist soil in spring, directly after superficial tillage.

Soil state variables were measured at various sites. Sites 3 and 4 (Figure 8) were situated on loam soil, and 1 and 2 on silt loam; each site was actually a plot measuring 4 m × 4 m. These sites were located on the basis of a spatial variability study of moisture retention and texture data along the transects shown in Figure 8 (ten Berge et al., 1983). As the minimum sampling distance along these transects was also 4 m, the semivariograms can be used to deter-
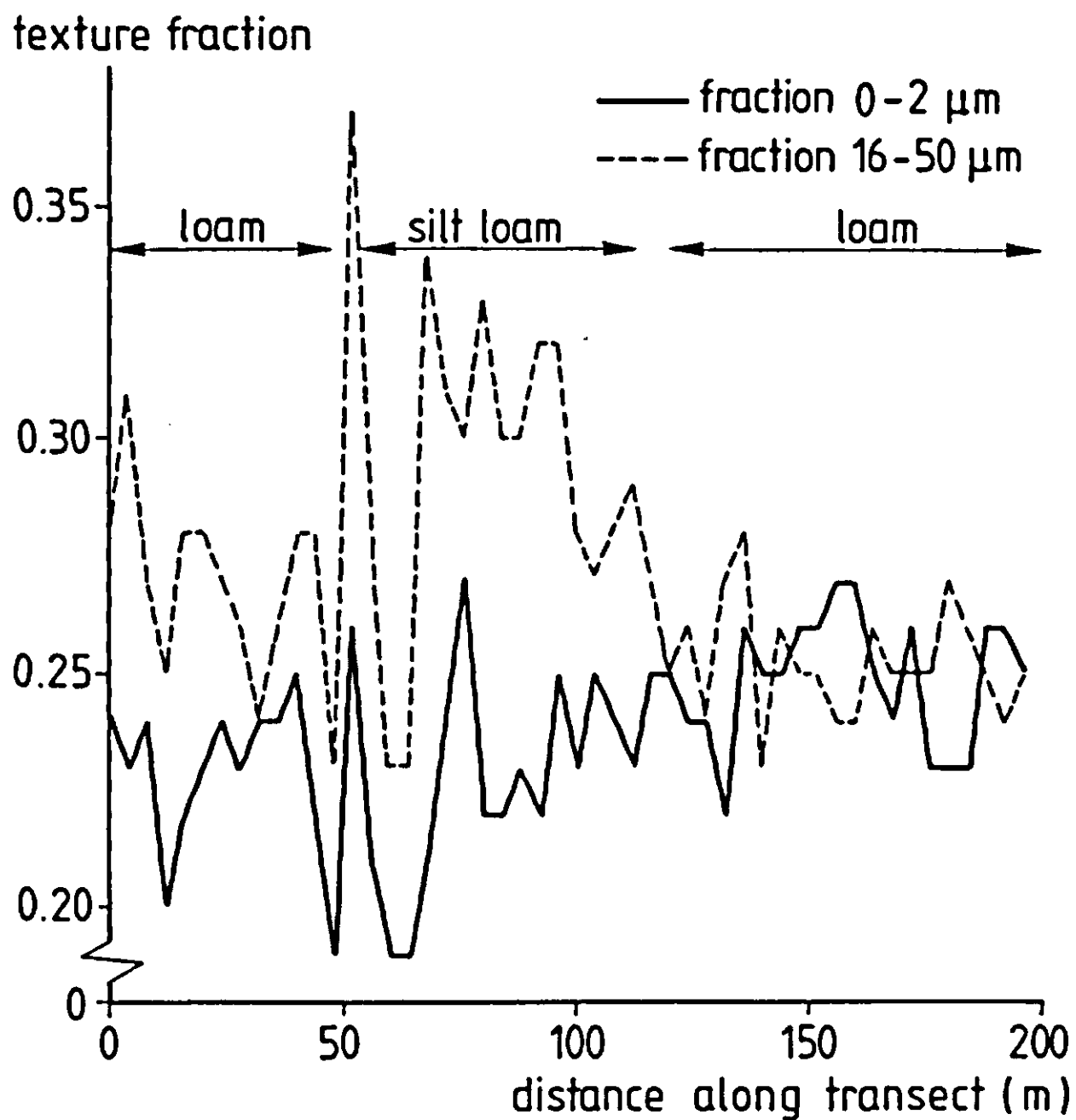
66

Figure 9. Two texture fractions along one of the transects indicated in Figure 8.
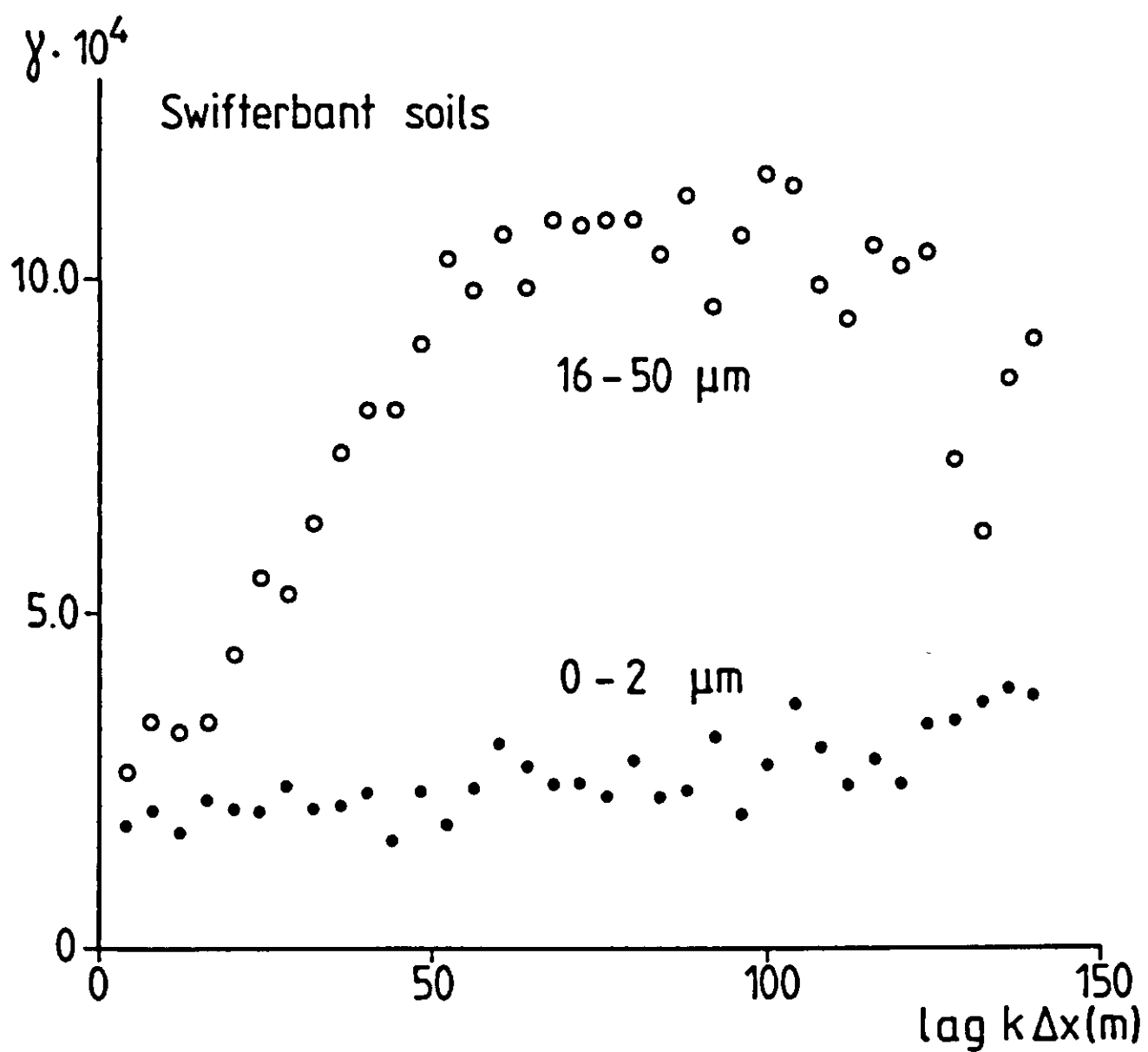

Figure 10. Semivariograms for two texture fractions at the Flevo experimental site.

mine the residual variance $C(0)$-$C(k)$ of the observations within the four plots (with $k = 1$), resulting from measurement errors and within-plot spatial dependence (see previous section). Although, strictly speaking, this is only correct in the idealized case of isotropy and second order stationarity, it does yield a useful estimate of the variance. Time series of soil variables are discussed for plots 1 (silt loam) and 4 (loam) only, because these plots represent the extremes occurring in the experimental field.

The campaign covered the period from 28 May to 28 June, 1982. The first two weeks of this period were characterized by high evaporation, following a period of rain. During the second half of the experiment, low radiation, high humidity and scattered rain predominated. For this reason, the two different sequences Flevo-1 and Flevo-2 have been distinguished as separate data sets.

4.4 Boundary conditions

Radiation
One can choose which radiation flux is used as the driving variable in SALSA. If global and sky radiation are used to determine the energy flux boundary condition, net radiation is viewed as an 'output' variable. This was done in the present case (see also Chapter 5). If, on the other hand, net radiation is used, it must be realized that this term is influenced by the system one wishes to model. The radiation terms measured are treated briefly below.

Global radiation, reflected shortwave radiation and net radiation were measured as integrated values over half-hour periods. Daily totals of global radiation ranged between 21.5 and 23.5 MJ m^{-2} d^{-1} for data set Flevo-1, and between 14.5 and 16.5 MJ m^{-2}d^{-1} for the second period, Flevo-2.

Net longwave sky radiation $(1 - \rho_l)R_{ld}$ can be estimated by using the relation

$$R_n = (1 - a)R_{glob} + (1 - \rho_l)R_{ld} + R_e \qquad \text{Equation 83}$$

where ρ_l is the surface reflectivity for longwave radiation and the subscripts n, glob, ld and e refer to net, global, longwave downward and emitted radiation terms, respectively. The latter term is calculated as $R_e = -\varepsilon\sigma T_s^4$, where the surface temperature T_s is in Kelvin, σ is the Stefan-Bolzmann constant, and ε the surface emissivity. In the present case, however, longwave radiation was calculated from Equation 6, and reflectivity was estimated (Section 4.5).

Both for measured net radiation and global radiation the variance resulting from measurement errors was estimated by a coefficient of variation of 5% in the recorded signals. Figures 11 and 12 depict the measured courses of global radiation for the two experiments. Measured net radiation will be presented in Chapter 5 as an output variable, along with predictions, and is therefore not given here.

68

global radiation (W m^{-2})

Flevo set 1

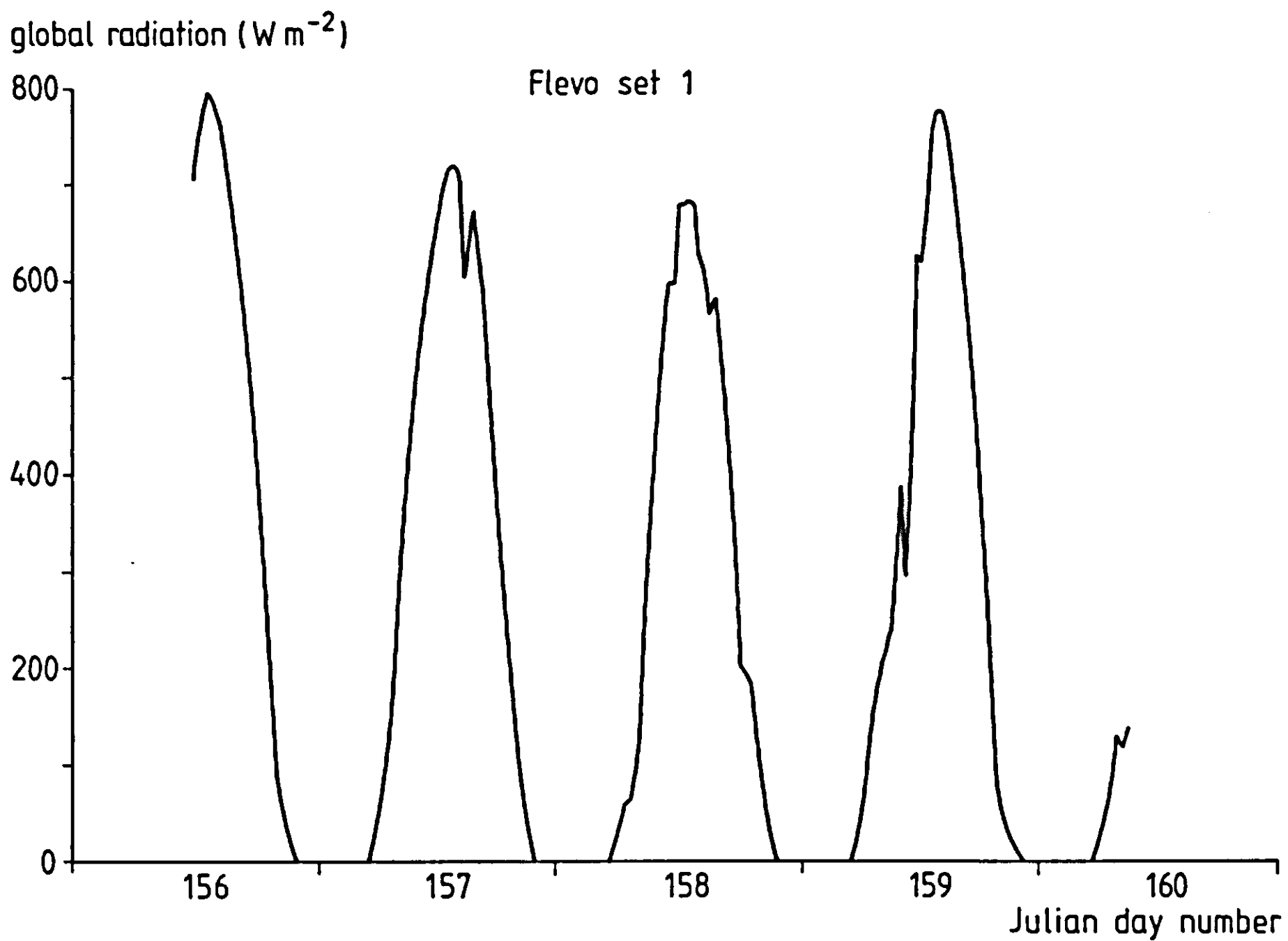
Figure 11. Measured global radiation, Flevo-1.

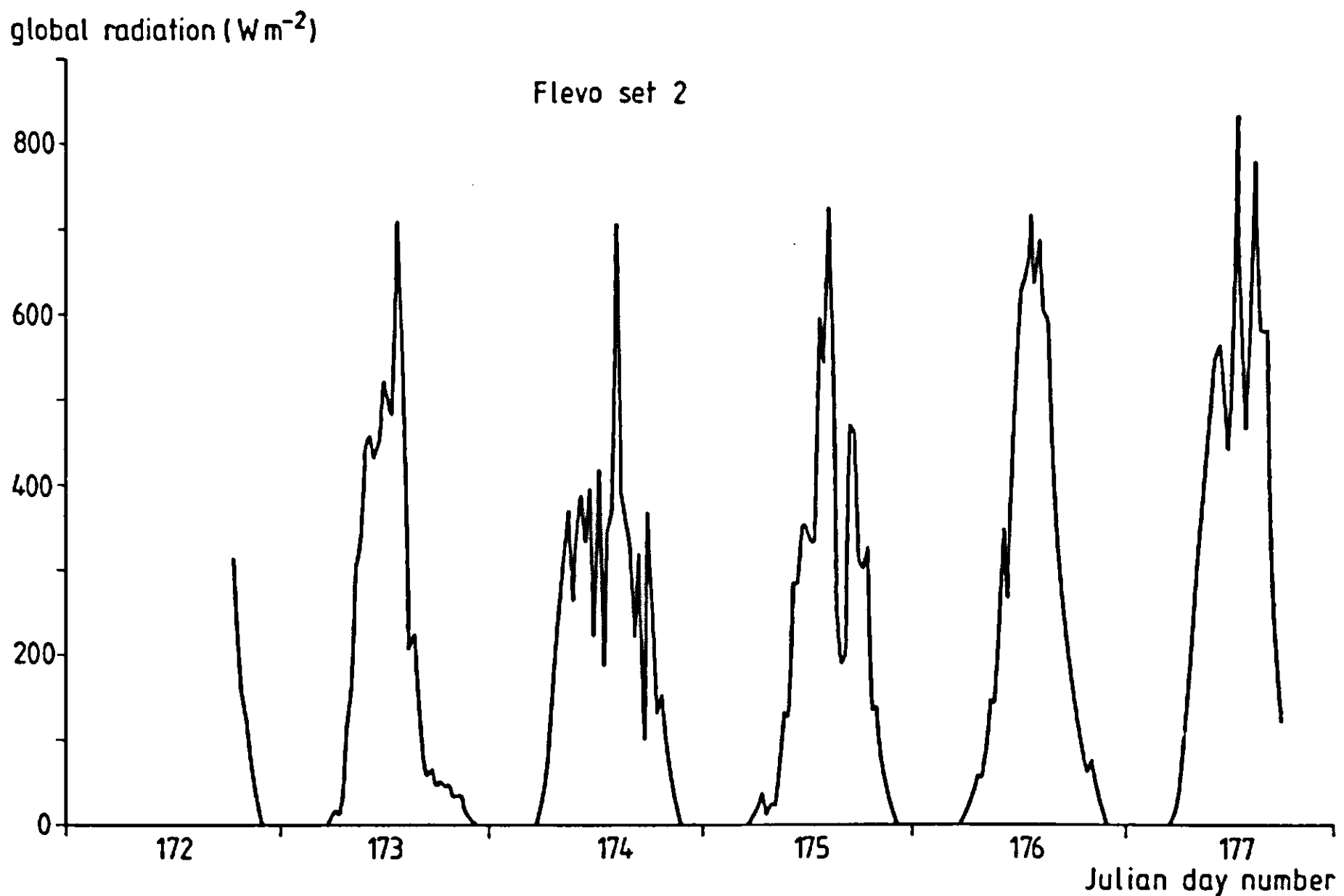global radiation (W m^{-2})

Flevo set 2

Figure 12. Measured global radiation, Flevo-2.
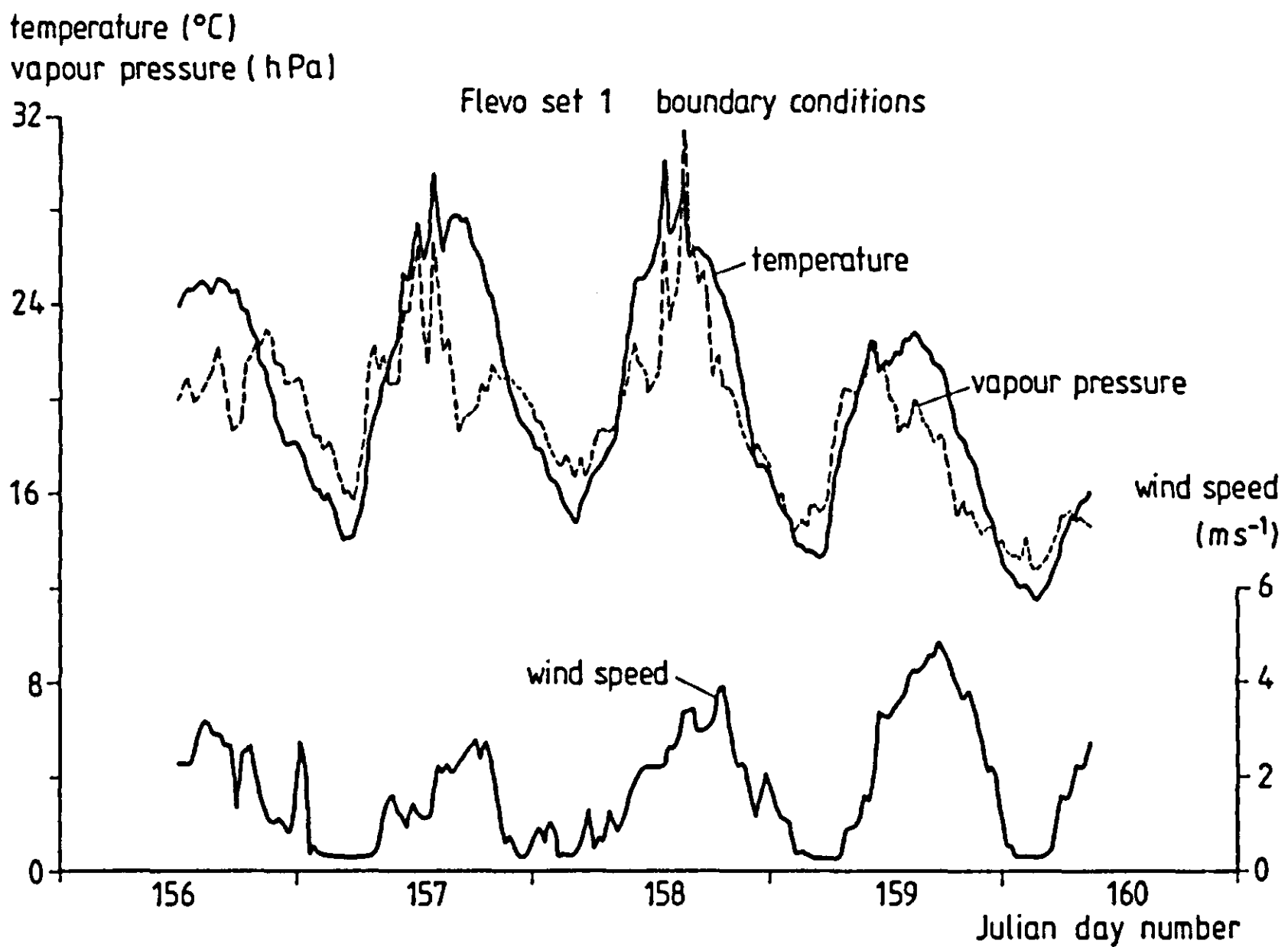
69

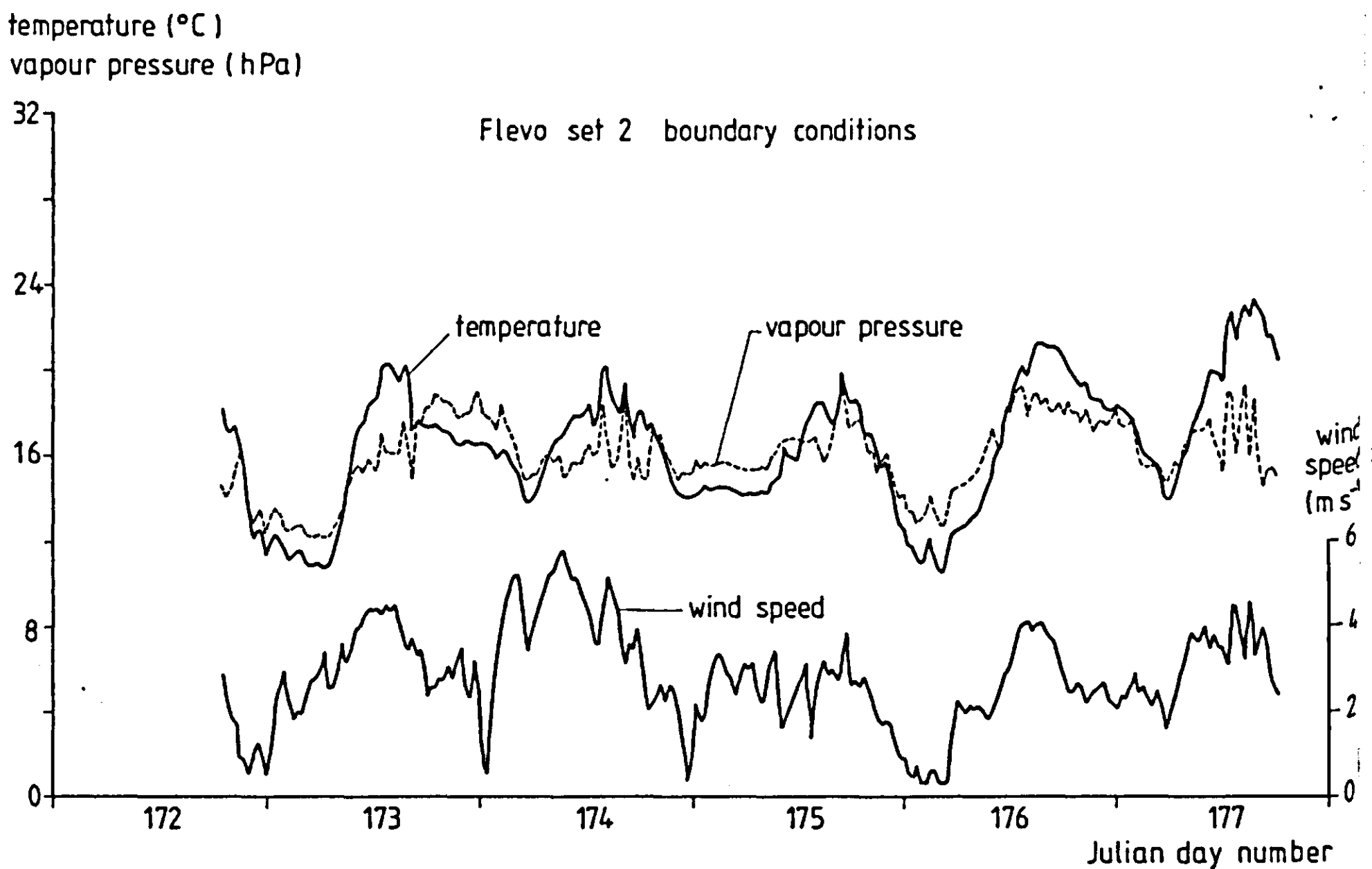Figure 13. Atmospheric boundary conditions, measured at 0.5 m height, Flevo-1.

Figure 14. Atmospheric boundary conditions, measured at 0.5 m height, Flevo-2.

Water
During the experiments, rain fell in the second period (Flevo-2) only; a total of 33.4 mm was measured.

Atmospheric state variables
Air temperature, vapour pressure and wind speed at 0.5 m height were measured as boundary conditions (Figures 13 and 14). The masts for profile measurements were moved in accordance with the prevailing wind direction to obtain a maximum fetch (ranging from 74 to 300 m length) over the bare soil surface. It was assumed that these measurements represented the field as a whole, in spite of soil heterogeneity. The standard deviations in the measurement errors of dry and wet bulb temperatures were 0.1 K. This corresponds to an absolute error of 15 Pa for the vapour pressure. The coefficient of variation in the wind speed data amounted to 4%.

At the lower end of the soil profile (0.5 m depth), soil temperature and water potential were monitored and appeared nearly constant. Temperature showed a slight trend of 1 K week^{-1} for both sets Flevo-1 and Flevo-2, as a result of seasonal warming.

4.5 System parameters and functions

The measured system parameters mostly express soil properties as functions of volumetric water content. These properties are the surface characteristics albedo and emissivity, the transport coefficients hydraulic and thermal conductivity, and the capacities for water (moisture characteristic) and heat. The only parameter not directly related to soil physical properties is the roughness length, a boundary layer property.

Roughness length
Roughness length z_0 over the smoothly rolled field was derived directly from wind profile measurements. Although wind and temperature profiles were measured continuously during a one-month period, only few times were suitable for the determination of z_0. Requirements for reliable determinations are a near-neutral stability, a wind speed high enough for accurate anemometer performance, and no rain in the preceding days, because moisture affects anemometer calibration. Moreover, wind direction should allow for long enough 'fetch'. Only observations corresponding to an absolute value of less than 0.02 for the Richardson number Ri were used to derive z_0; Ri is defined as $(g/T)(\partial T/\partial z)/(\partial u/\partial z)^2$. Combination of the log-linear wind profile equation with the assumption $\varphi_H = \varphi_M$ for the dimensionless gradients of temperature and wind speed (Equations 16 and 17) gives the expression (Thom, 1975):

$$u(z) = \frac{u_*}{k} \ln\left(\frac{z-d}{z_o}\right) + 5(z - d - z_o)\frac{g}{T}\frac{dT}{du}$$

Equation 84

where d is the displacement height, generally taken to be zero for unvegetated surfaces. Equation 84 is assumed to be valid for stable and moderately unstable situations ($|Ri| < 0.1$). The values of u_* and z_0 were determined from the wind profiles (three heights) by a non-linear optimization procedure. This yielded z_0 values ranging between 0.02 and 0.15 mm for most days, although values up to 0.9 mm were occasionally determined.

Albedo

Bare soil albedo was measured in situ as a function of moisture content. Double solarimeters were used, and topsoil moisture content was determined by gravimetrically sampling the top 5 mm layer. The data were converted to volumetric water contents by using bulk density values measured for this thin top layer.

To avoid the effects of high incidence angles, data pertaining to early morning and late evening hours (global radiation < 100 W m^{-2}) were omitted. Albedo appeared to be fairly well described by the relations

$$a(\theta) = a_{\text{wet}} \qquad \text{for} \quad \theta > \theta_{\text{crit}} \qquad \text{Equation 85}$$

$$a(\theta) = a_{\text{wet}} + \frac{\theta_{\text{crit}} - \theta}{\theta_{\text{crit}}} (a_{\text{dry}} - a_{\text{wet}}) \qquad \text{for} \quad \theta < \theta_{\text{crit}} \qquad \text{Equation 86}$$

Linear regression on Swifterbant silt loam data yielded values of 0.13 and 0.31 for a_{wet} and a_{dry}, respectively, and a value of 0.26 for θ_{crit} (Figure 15). The standard deviation in the residuals amounted to 0.020. Spatial dependence of $a(\theta)$ was not measured.
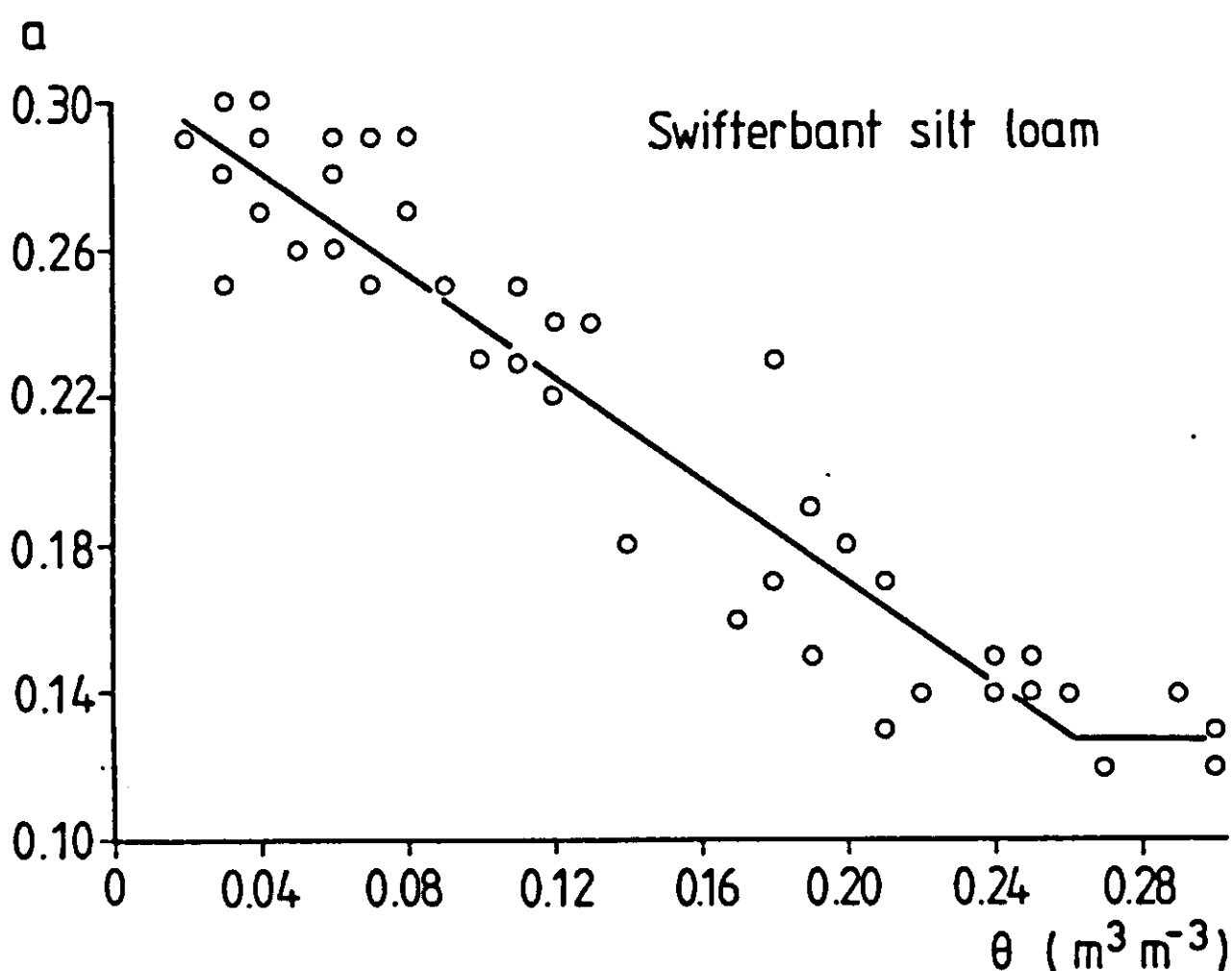
Figure 15. In situ measured albedo versus volumetric moisture content (0-5 mm) for Swifterbant silt loam.

Longwave reflectivity

Longwave reflectivity could not be derived from the data measured in Flevoland. Its value was assumed to range between 0.05 and 0.15, these values being identified from the Arizona data set mentioned earlier. In contrast to albedo, a relation with surface moisture content was not evident from those data. An average value of 0.10 was used for longwave reflectivity, with a standard deviation of 0.05 for the error.

Emissivity

Emissivity of Swifterbant silt loam, as a function of moisture content, is shown in Figure 16. Measurements were taken on core samples by the Fuchs & Tanner (1966) reflection method under stratus cloud cover. Measurements were conducted on the roof of the 'Dreijenborch' building in Wageningen, which provides a free horizon. Only under these conditions was the distribution of radiance in the 8-14 μm wavelength interval over the sky hemisphere fairly even and within the range of the measurement instrument. Although the data suggest a step increase of the emissivity as the moisture content increases (which could be explained physically on the basis of the soil water energy state), a simple linear $\varepsilon(\theta)$ relationship was adopted because of the large scatter observed:

Figure 16. Emissivity (18-14 μm) measured on core samples of Swifterbant silt loam by the Fuchs-Tanner method.

73

$$\varepsilon(\theta) = \varepsilon_{dry} + \frac{\theta}{\theta_s} (\varepsilon_{wet} - \varepsilon_{dry})$$

<div align="right">Equation 87</div>
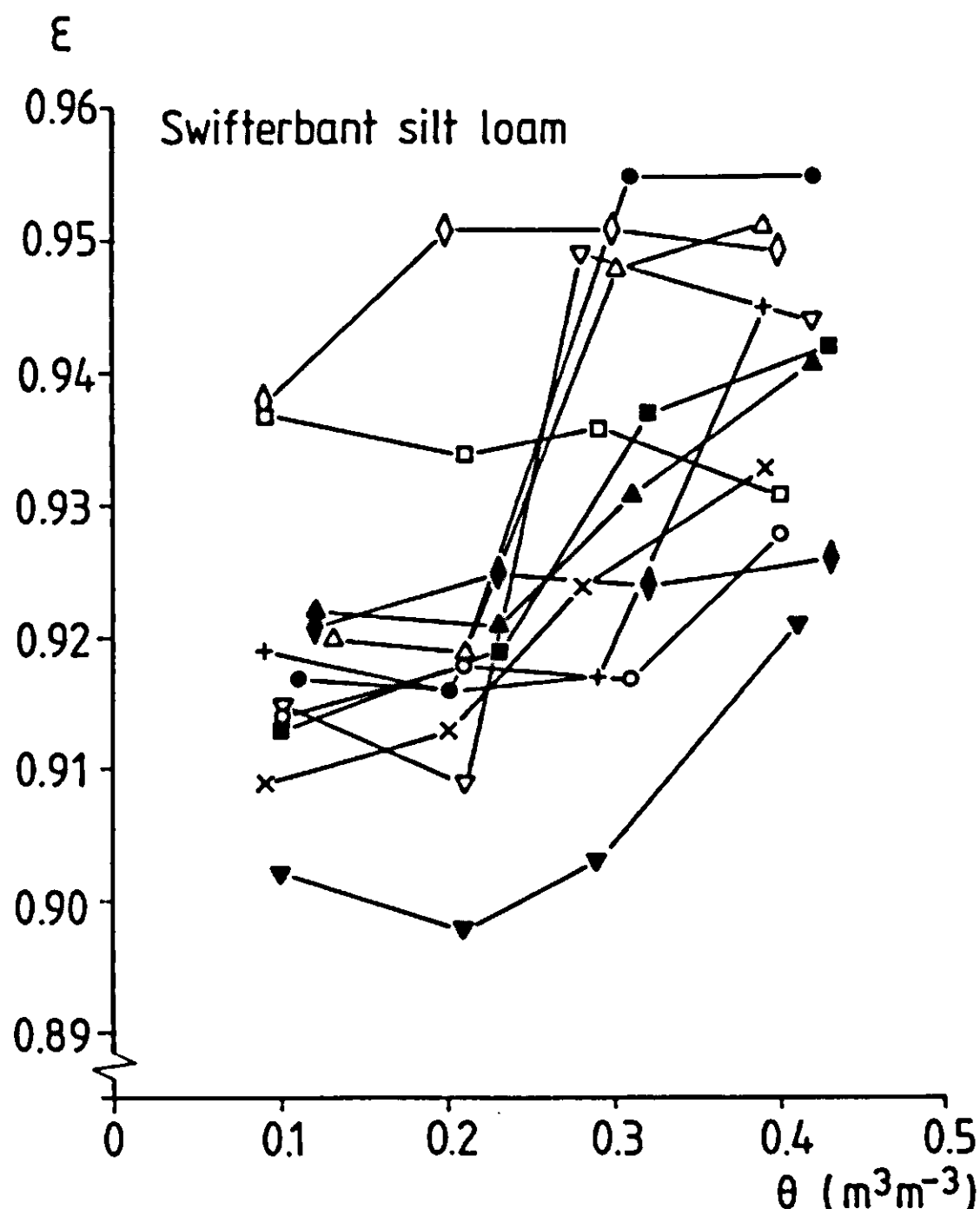
with $\varepsilon_{dry} = 0.90$ and $\varepsilon_{wet} = 0.94$. The scatter is partly caused by inaccuracies in the non-destructive determination of θ, which involved averaging weight changes over $0.1 \ 10^{-3} \ m^3$ core samples. The results obtained by an alternative method, using measured gravimetric moisture contents of the top 5 mm soil layer instead, were no better, however. The accuracy in emissivity at a given θ value was taken to be 0.01.

Thermal soil properties

The damping depth of the diurnal temperature wave in homogeneous soil profiles can be inferred from the attenuation of the temperature amplitude and from the phase shift, both with respect to depth (de Vries, 1963). For a review of these and related methods, see Horton (1982). Damping depth and phase shift are obtained for the different wave numbers by Fourier analysis; thermal conductivity can then be calculated, using an estimated value of the soil heat capacity. During the field experiments, however, soil moisture distribution was such that thermal properties were not constant with depth. Moreover, bulk density ρ increased with depth: using amplitude attenuation of the first harmonics of the temperature wave, a layer of increased thermal diffusivity was indeed found at 0.2-0.3 m depth.

Two other field methods were employed instead: direct measurement by heat probes, and the so-called 'null alignment' method. The results of both methods were compared with predictions, made by the de Vries thermal conductivity model. However, since significant changes in moisture content occurred in the top few centimetres only, field measurements only yielded the $\lambda(z)$ function, rather than the $\lambda(\theta,z)$ or $\lambda(\theta,\rho)$ relation needed for dynamic simulation. Additional laboratory measurements were therefore performed to obtain $\lambda(\theta)$ for topsoil core samples.

The measurement of λ by heat probes inserted in the soil has been extensively discussed by de Vries (1952), and later by several other authors; the theoretical aspects are not repeated here. The probes were installed at various depths to measure *in situ* thermal conductivity. Figure 17 shows the results for different depths. Some scatter is observed, possibly because of the problem of contact resistance, also discussed by Nagpal & Boersma (1973) and by van Haneghem (1981).

The results obtained by the 'null alignment' method proposed by Kimball & Jackson (1975) are also depicted in Figure 17. This calorimetric method employs $T(z)$ profiles at different times, and infers heat fluxes by numerical integration, making use of a point with a zero temperature gradient as reference level.

Figure 17 also shows thermal conductivity as predicted by the de Vries model on the basis of bulk density, texture and moisture content. Since both measurement procedures mentioned above yield apparent instead of true thermal con-
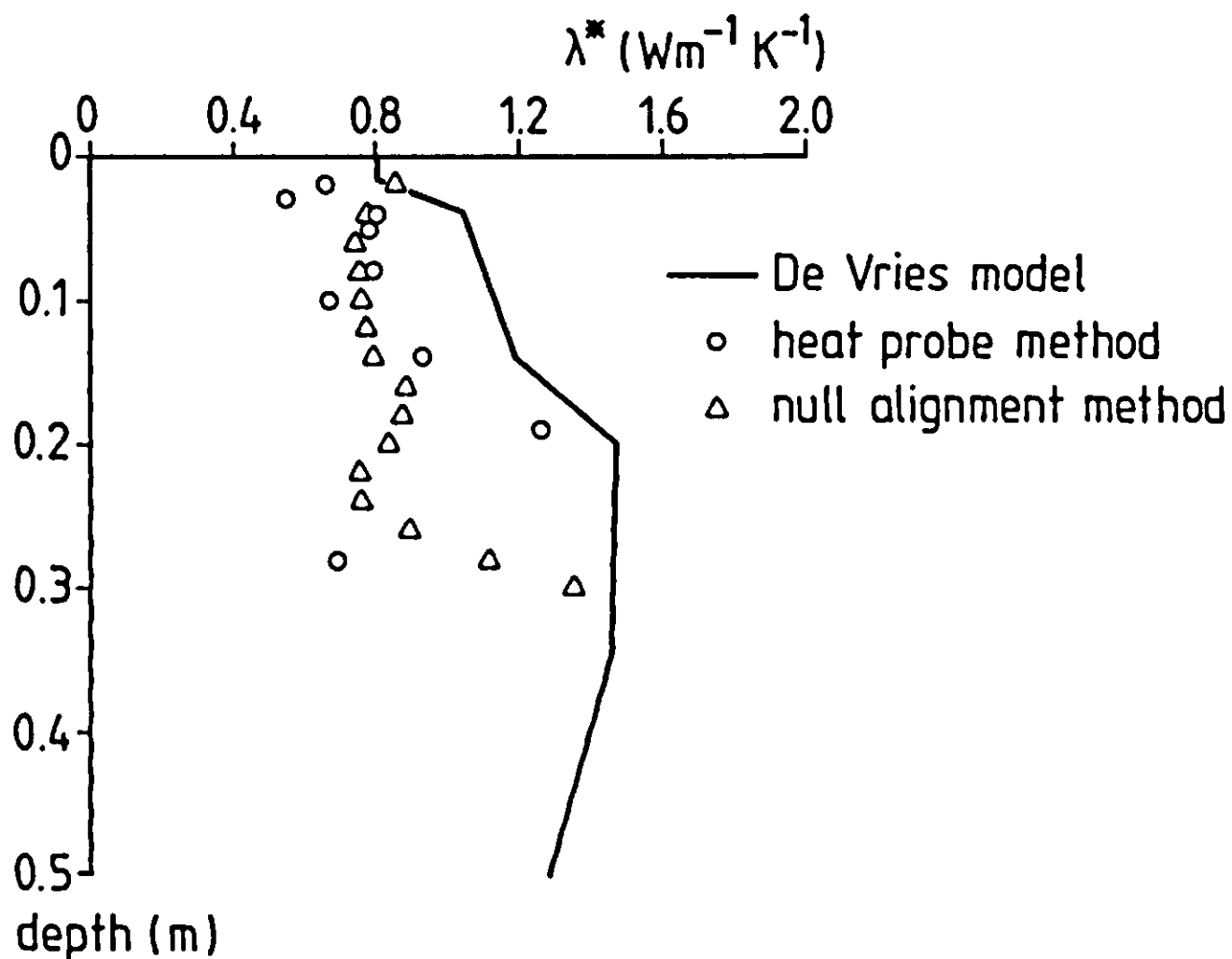
Figure 17. Profiles of apparent thermal conductivity λ^*, obtained by different methods, for Swifterbant silt loam.

ductivity, the vapour term was included in the de Vries model in order to obtain estimates that can be compared with the measured results (see also Section 2.5). This vapour contribution to thermal conductivity was calculated for a temperature of 20° C, approximately the average profile temperature. As indicated in the previous chapter, the choice of the air shape factor g_a (Equation 45) reduces the predictive value of this conductivity model. For the curve as given in Figure 17, an air shape factor of 0.05 was used; higher values of g_a gave even higher estimates of λ. Figure 18 compares measured and predicted $\lambda(\theta)$ curves for Swifterbant silt loam.

It can be concluded from Figure 17 that for Swifterbant silt loam the conductivity model does not well predict λ as measured by the probe method nor by the 'null alignment' method, whereas the results of these two methods agree fairly well.

The thermal conductivity of the top 5 cm soil layer was measured in the laboratory on a number of undisturbed core samples. The 'contact method' for the determination of λ in the surface region (Stigter, 1969) was used. The method is based on the existence of a constant interface temperature when contact is made between two semi-infinite, homogeneous bodies, each with a given initial temperature. Like the field methods discussed above, the method yields apparent thermal conductivity, provided that the heat capacity of the soil is known. The results are shown in Figure 18. Only for the higher water contents do these measured data agree with the de Vries predictions. The observed data can be approximated by a straight line. A linear behaviour is frequently encountered for aggregated field soils, in contrast to the typical curves for packed granular
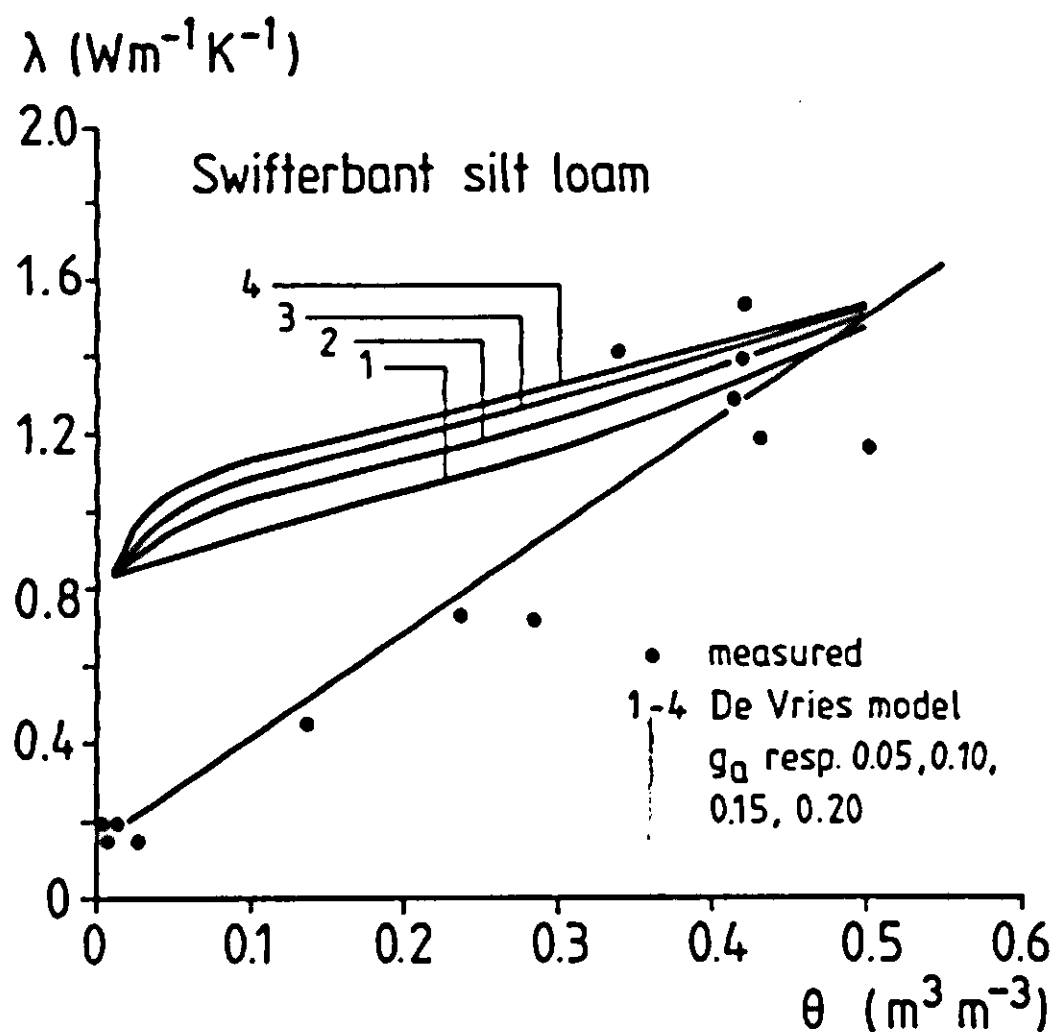
Figure 18. Apparent thermal conductivity of Swifterbant silt loam (0-5 cm) determined on core samples by the contact method.

materials (e.g. Figure 4). See also Kimball & Jackson (1975).

Two problems arise when the $\lambda(\theta)$ function, to be used in the context of a simulation model, must be defined from the measured data as available here: (1) whereas bulk density was variable, moisture content hardly varied at depths where field measurements of λ^* were made, and (2) true conductivity is used in simulation (for reasons explained in Subsection 2.5.2), while apparent thermal conductivity was actually measured. To overcome these, two simplifications present themselves: (1) $\lambda(\theta)$ curves for the different bulk densities (depths) are calculated from the laboratory-measured curve by multiplication by a factor ρ/ρ^* (where ρ^* is the reference bulk density), and (2) the vapour diffusion term (estimated at 0.05-0.10 W m^{-1}K^{-1}) is subtracted from the measured apparent thermal conductivity. The latter involves an increase in uncertainty, because of the choice of an average temperature and the unknown role of vapour transfer enhancement (Subsection 2.6.4). The function $\lambda(\theta,\rho)$ resulting from application of the above procedure to the Swifterbant data is given in Figure 19. This relation was used in validation runs with the simulation model. The coefficient of variation that quantifies the error in this λ function is estimated to amount to 20%, based on the scatter in field and laboratory measurements. In subsequent chapters, the extent to which such an inaccuracy in λ affects predicted soil behaviour with respect to the surface energy balance and to soil temperatures will be assessed.

Heat capacity profiles were calculated by Equation 42 from bulk density, moisture content and texture. The bulk density profile for the experimental field is given in Figure 20. The standard deviation of the error in bulk density
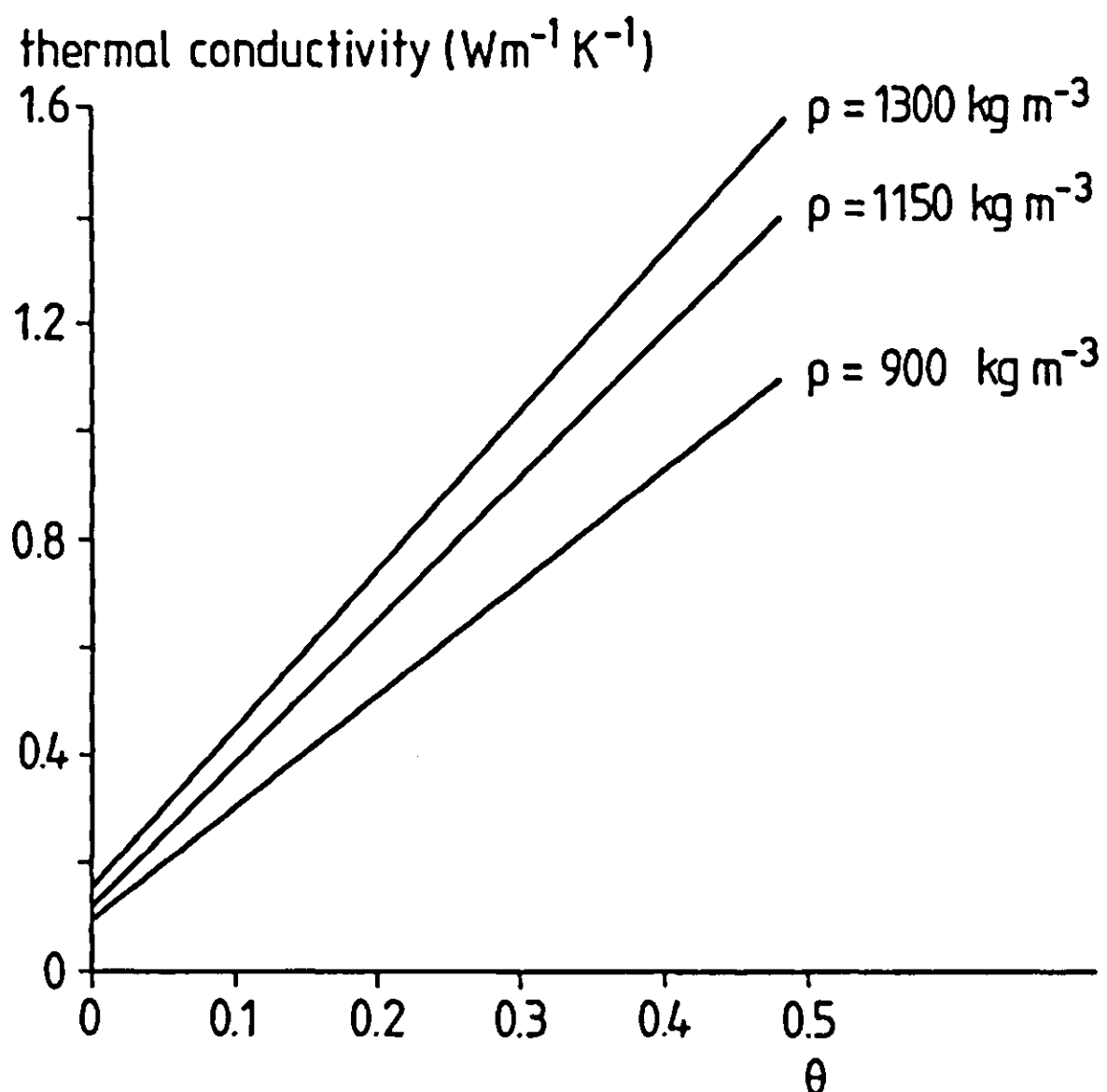
Figure 19. Thermal conductivity of Swifterbant silt loam as used in simulation (Chapter 5).
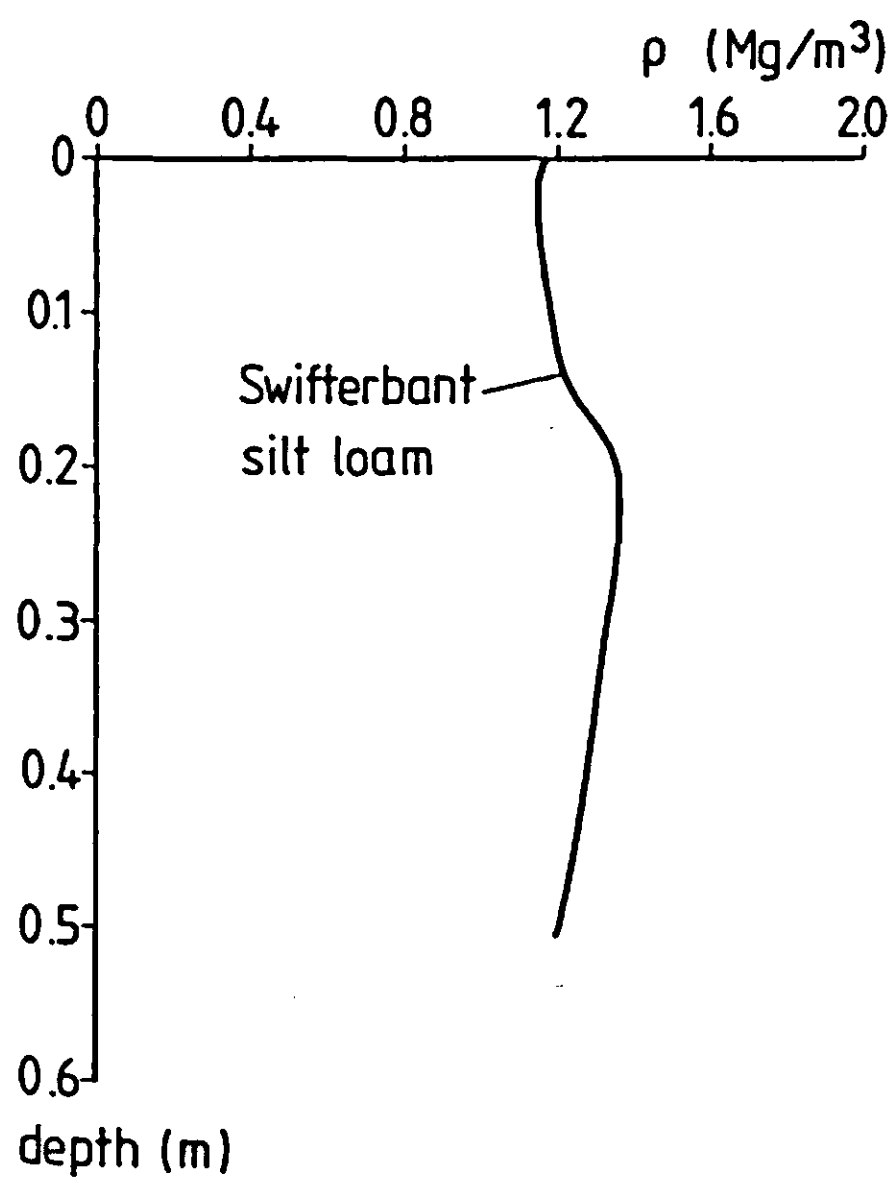
Figure 20. Dry bulk density profile for the Flevo experimental site.

was 60 kg m^{-3}, and was derived by semivariance analysis at the 4 m 'lag' level. Based on this error value, the error in the calculated heat capacity was at least 6%.

The moisture characteristic

Moisture characteristics of the Swifterbant soils were determined as part of the spatial variability study. At 100 locations, core samples were taken from two depth intervals: the 0-5 cm and 5-10 cm layers. The samples were grouped into a loam class and a silt loam class, and intermediate samples were left out. For each of the two groups, average curves were determined by first averaging – at given fixed pressure potentials – the corresponding measured moisture contents. Subsequently, van Genuchten's expression for the moisture characteristic (Equation 58) was fitted to these averaged data. Figure 21 shows the results for the two soils. The parameters α and n are 4.04 10^{-4} Pa^{-1} and 1.161 for the silt loam as obtained by curve fitting, and 4.67 10^{-3} Pa^{-1} and 1.093 for the loam, respectively. (Here, the parameter α is not dimensionless, unlike the scaling factor α). See also Figure 9.
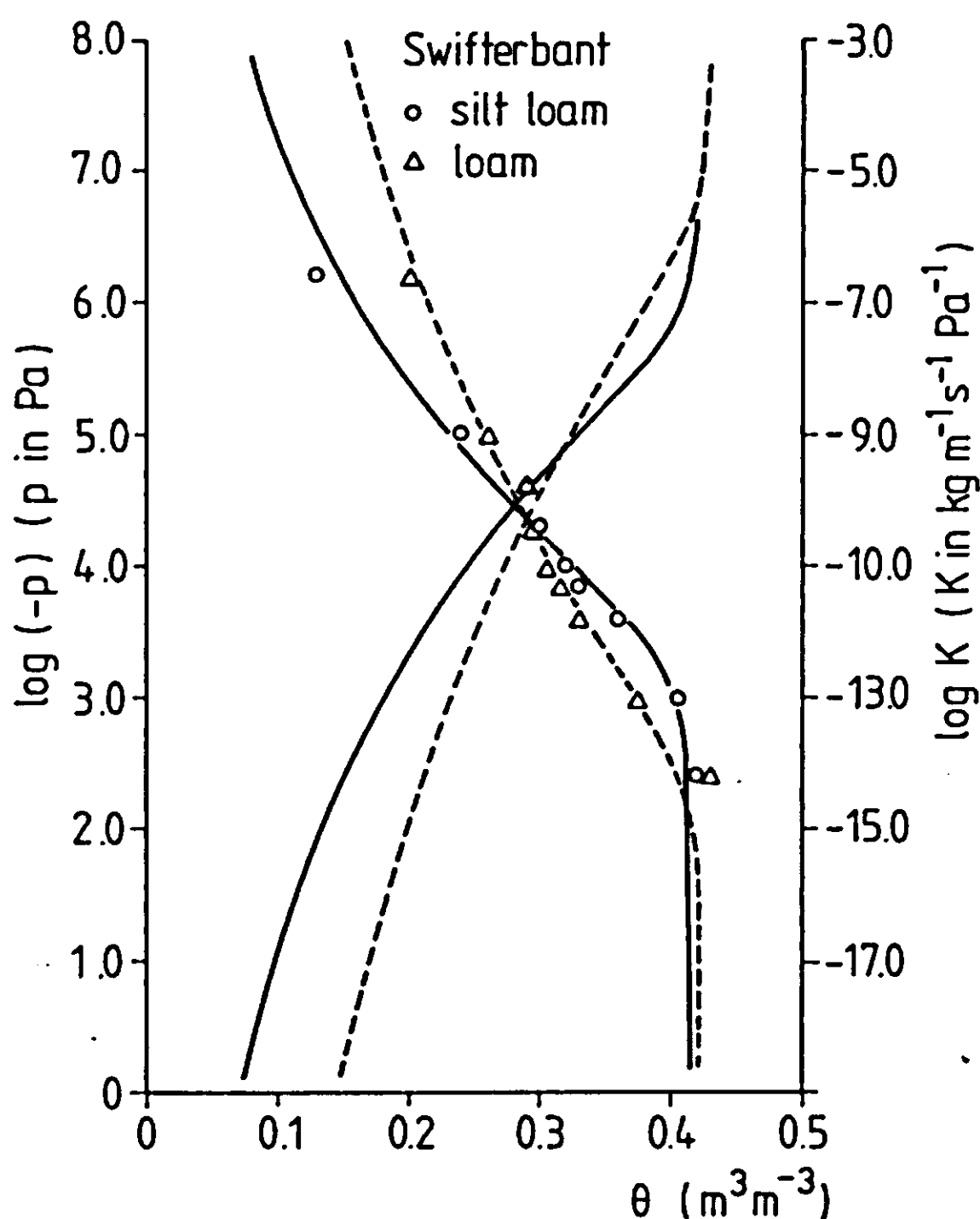
Figure 21. Moisture characteristics for Swifterbant silt loam and Swifterbant loam. Lines represent best fits by the van Genuchten (1980) model. Also indicated are the hydraulic conductivity curves according to the van Genuchten-Mualem model.

Variability of the moisture characteristic, as explained in Section 4.2, was taken into account by scaling. A prerequisite for scaling is that curves have similar shapes, that is, the $\log(p) - \theta$ curves should be parallel. Since this was clearly not the case for the two Swifterbant soils, field heterogeneity could not be classified as pure 'scale heterogeneity' (Philip, 1967). Distinguished first on the basis of texture, the loam and silt loam data were therefore scaled separately. The scaled pressure p_{sc} was taken to be a function of $s \equiv \theta/\theta_s$, and was determined by fitting the curve given by Equation 58, with Ξ replaced by s, to the whole set of data points pertaining to each texture class. Subsequently, one scaling factor α_r was determined for each sample, by minimizing the sum of squares

$$SSQ = \sum_{i=1}^{N} (\lg p_{sc}(s) - \lg \alpha_r p_r(s))^2 \qquad \text{Equation 88}$$

This optimization criterion is preferred to the alternative where pressures are used instead of their logarithms, because it reduces the weight of the points at low θ values; these points would determine the scaling factor almost entirely. Scaling by means of Equation 88 reduced the variance $(1/(N-1)) \sum (p_{sc}(s)-p_r(s))^2$ by two orders of magnitude for both soils. Unscaled and scaled water pressures as a function of relative saturation are depicted in Figures 22-25 for both soils. The scale factors show log-normal distributions (Figures 26-29). Log α_r variances amounted to 0.095 (silt loam) and 0.140 (loam) for the two Swifterbant soils. (Strictly speaking, these values represent the entire population variances for the two groups. Therefore they overestimate to some extent the variability at the 4 m level, in which, as explained before, one is interested for validation purposes. However, it was difficult to do a semivariance analysis on the α data in order to obtain the residual variance at the 4 m level, because the observations were grouped into the two texture classes 'silt loam' and 'loam' for scaling; as a consequence, the transects had to be divided into smaller sections representing patches of loam or silt loam).

A special feature of the moisture characteristic, its temperature dependence, deserves mention. Soil water pressures measured at various depths in the field exhibited a marked diurnal course. Pressure potential increased (becoming less negative) during daytime, and recovered during the night. To investigate whether this course could be explained fully by only taking the temperature fluctuations into account, the effect of temperature on $p(\theta)$ was examined in the laboratory. Measurements were done on confined samples at constant θ, using pencil-type tensiometers and pressure transducers. The results are shown in Figure 30 for various water contents. These data can be summarized by the expression

$$\left(\frac{\partial p}{\partial T}\right)_\theta = a(\theta - b)^{-1} + c \qquad \text{Equation 89}$$
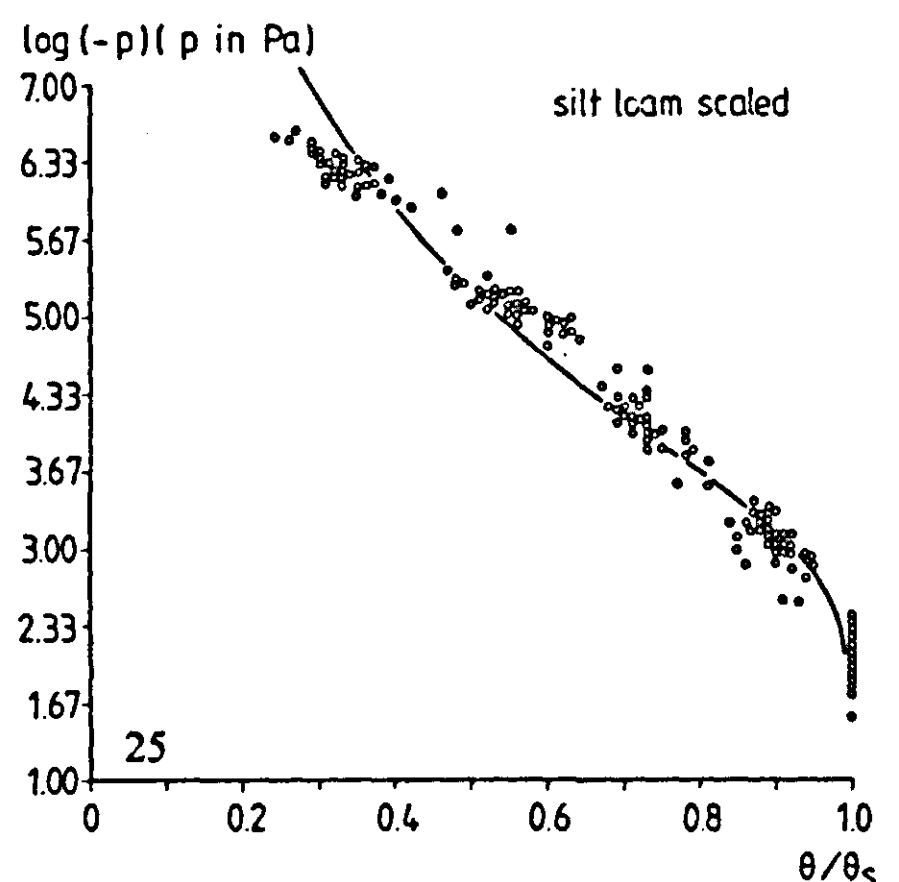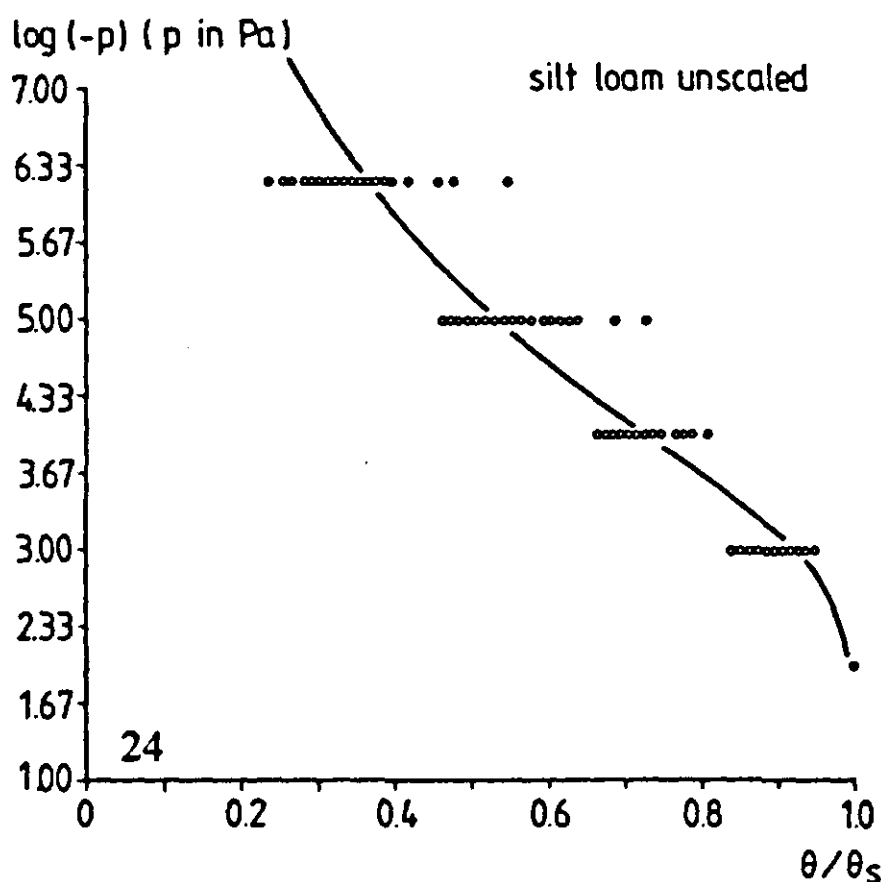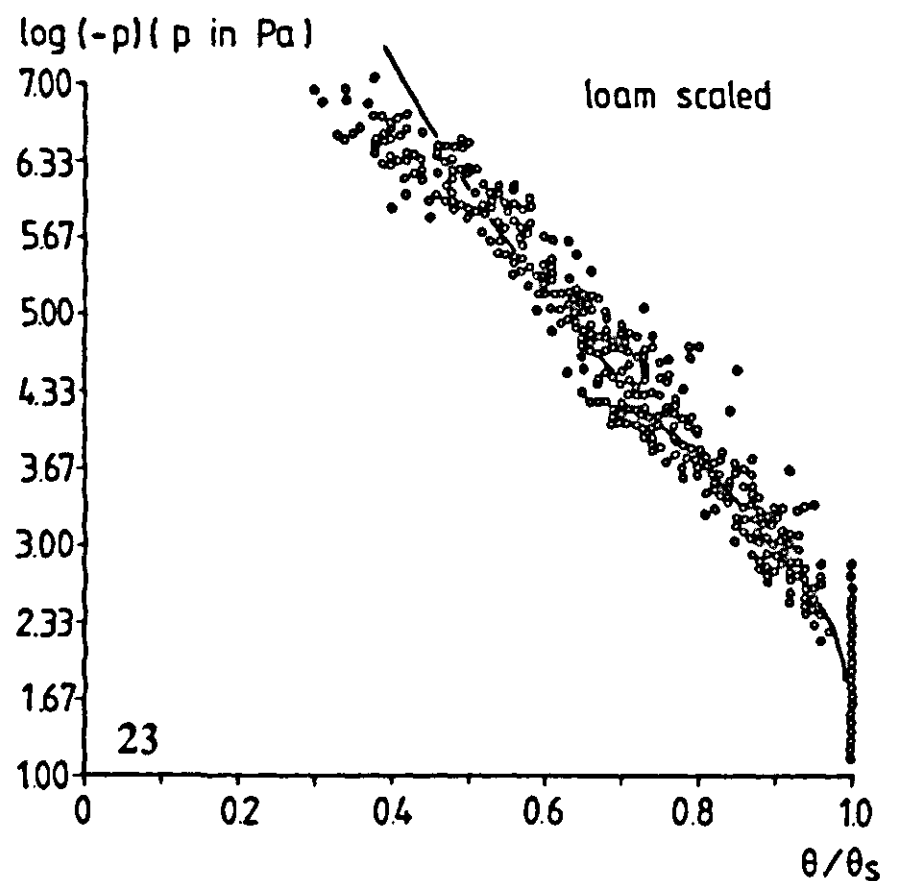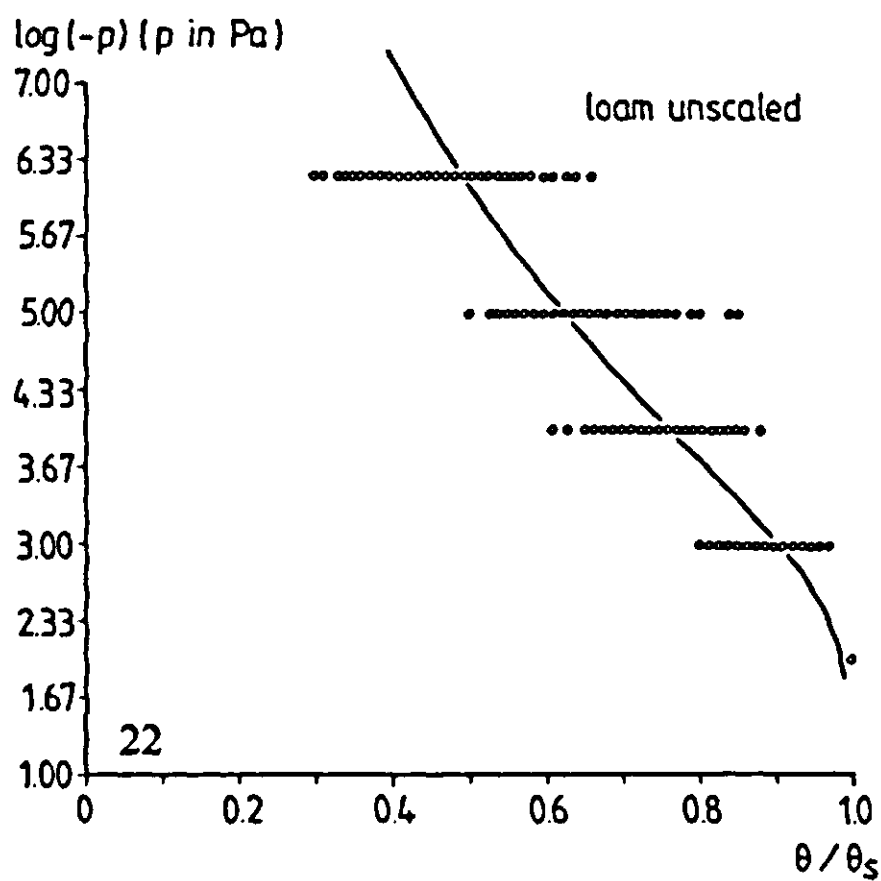
Figures 22-25. Actual and scaled moisture characteristics for Swifterbant silt loam and Swifterbant loam.

where the constants a, b and c have the values 104.2 Pa K^{-1}, 0.18 and 5.1 Pa K^{-1} (Ritsema, 1985). In Section 2.6 it is demonstrated that a temperature-induced pressure gradient should not be used as the driving force for flow, and so the above expression is not for use in flux calculations. Nevertheless, the relation can be used to verify whether the pressure fluctuations observed in the field may have been caused by temperature variations only. (See Figure 44, Chapter 5.)

Hydraulic conductivity and matric flux potential
$K(\theta)$ curves (Figure 21) were calculated for the two soils according to the van
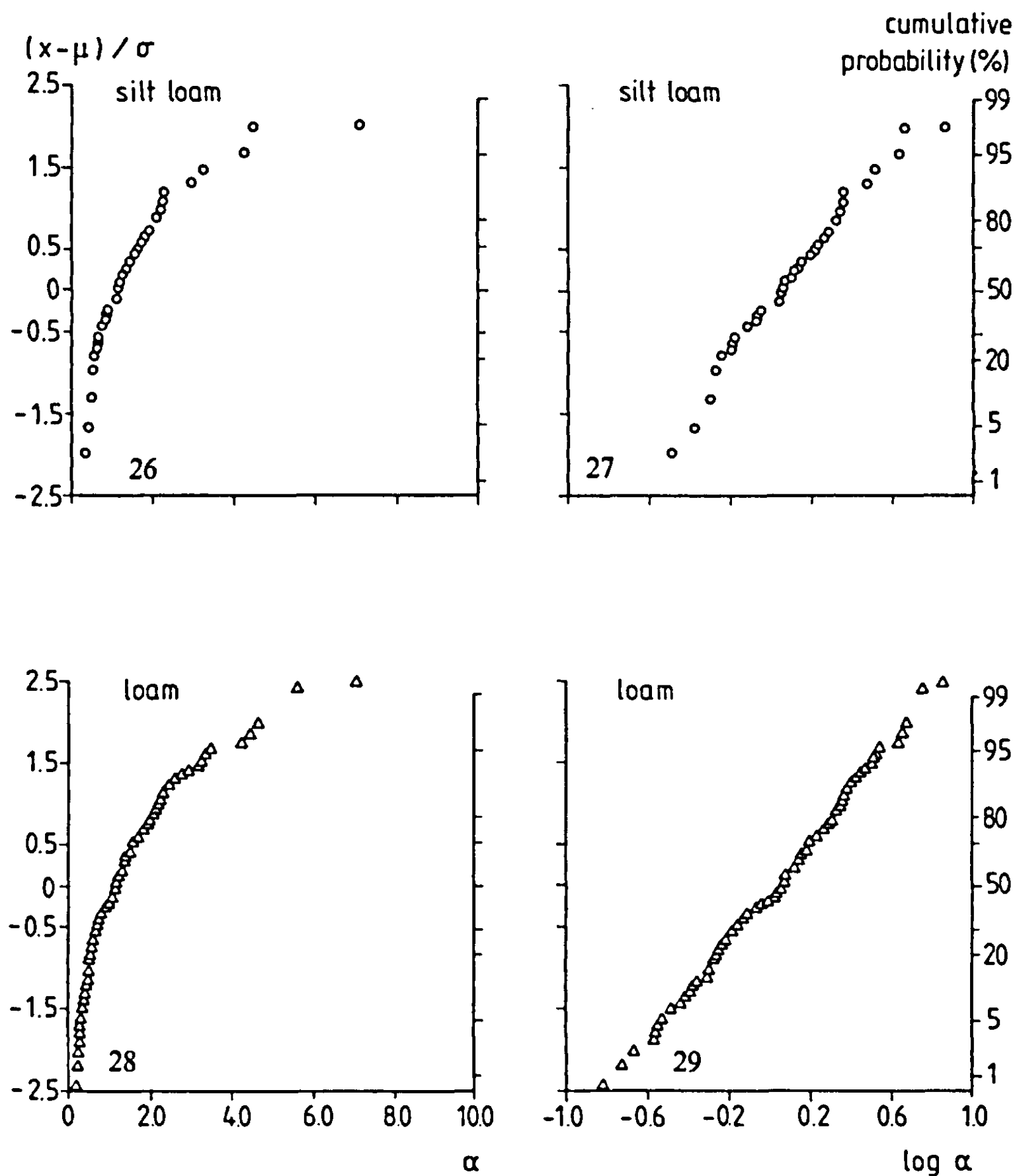
Figures 26-29. Probability distribution of the scale factor for both Swifterbant soils.

Genuchten-Mualem model (Equation 60). The parameter n, used in that model, was derived from the average moisture characteristics of silt loam or loam, obtained as described before. K-values measured at $p = -1.0$ kPa were used as a reference.

According to the scaling concept for similar media, hydraulic conductivity at a given location r is related to the average value K_{sc} by the equation $K_r = \alpha_r^2 K_{sc}$, where α_r may be derived from the scaling of moisture characteristics. This relation was used, and since the scaling factor shows a log-normal distribution, the estimated variability of K is based upon the variance of $\log \alpha_r$.

In addition, matric flux potential curves (Section 2.6.2) were measured to characterize the hydraulic properties of the Swifterbant soils. The matric flux potential $\Phi(\theta)$ is usually calculated from measured $p(\theta)$ and $K(\theta)$ curves by numerical integration (Equation 82). As an alternative, in this study a new steady
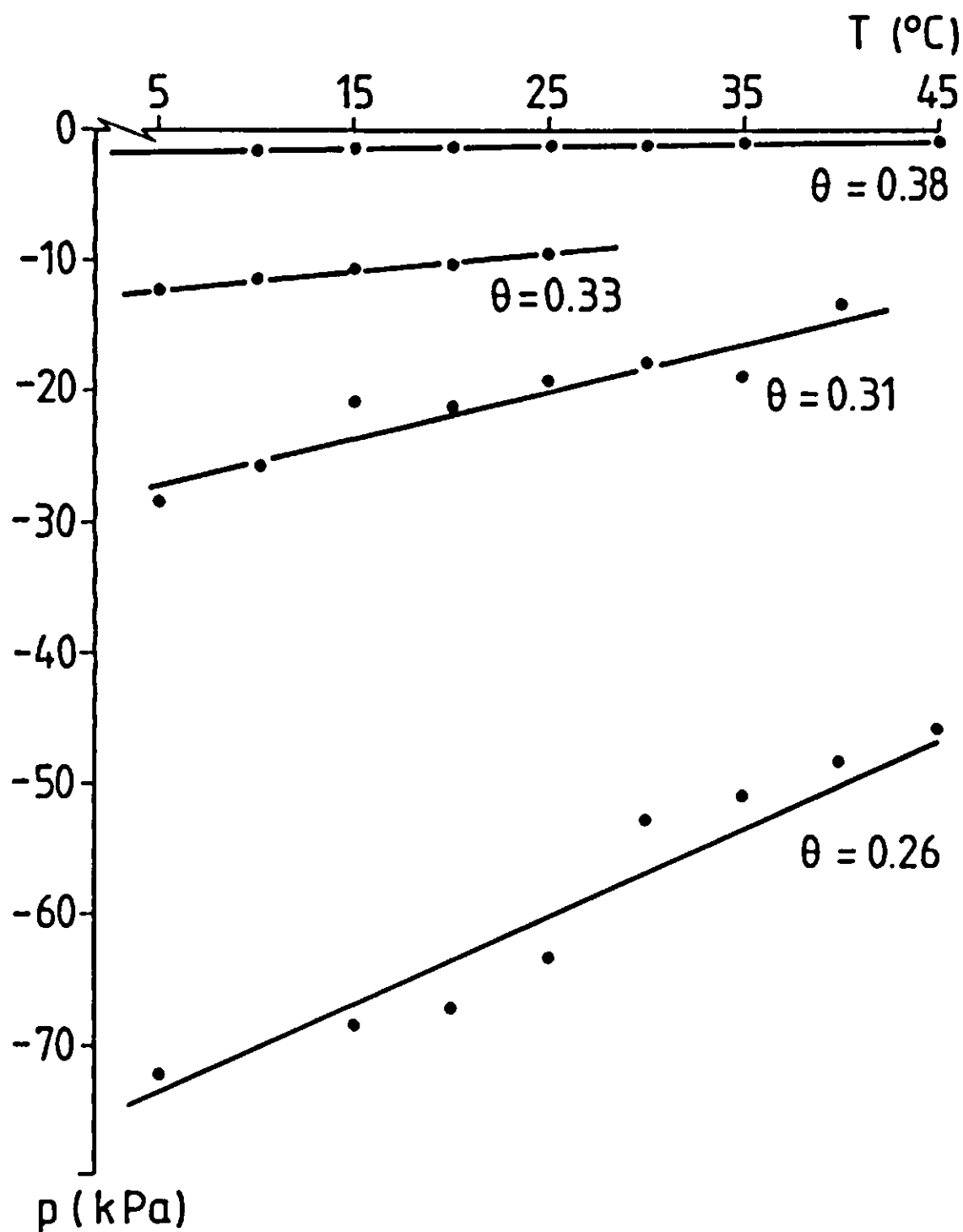
Figure 30. Temperature-dependence of soil liquid pressure at various moisture contents, obtained from laboratory measurements on undisturbed core samples of Swifterbant silt loam (see also Table 7).

state method was developed to allow direct measurement of the $\Phi(\theta)$ function (ten Berge, 1986; for an improved procedure see ten Berge et al., 1987). This function can then be used as a substitute for the separate $K(\theta)$ and $p(\theta)$ curves. The results of the measurements are shown in Figure 31. The numerically calculated curves are given in the same figure; they were obtained by integration (Equation 82) of the van Genuchten-Mualem $K(\theta)$ function, used in combination with measured $p(\theta)$ curves. Both these curves were shown in Figure 21.

The difference between the two Swifterbant soils expressed in Figure 31 is the main explanation of local differences in surface temperature behaviour, observed from thermal imagery each spring at the Ir. A.P. Minderhoudhoeve experimental farm. Variability in the $\Phi(\theta)$ function is expressed by the variability of the hydraulic scaling factor α_r discussed above; the scaling relation used for matric flux potential is $\Phi_r = \alpha_r \Phi_{sc}$.

82
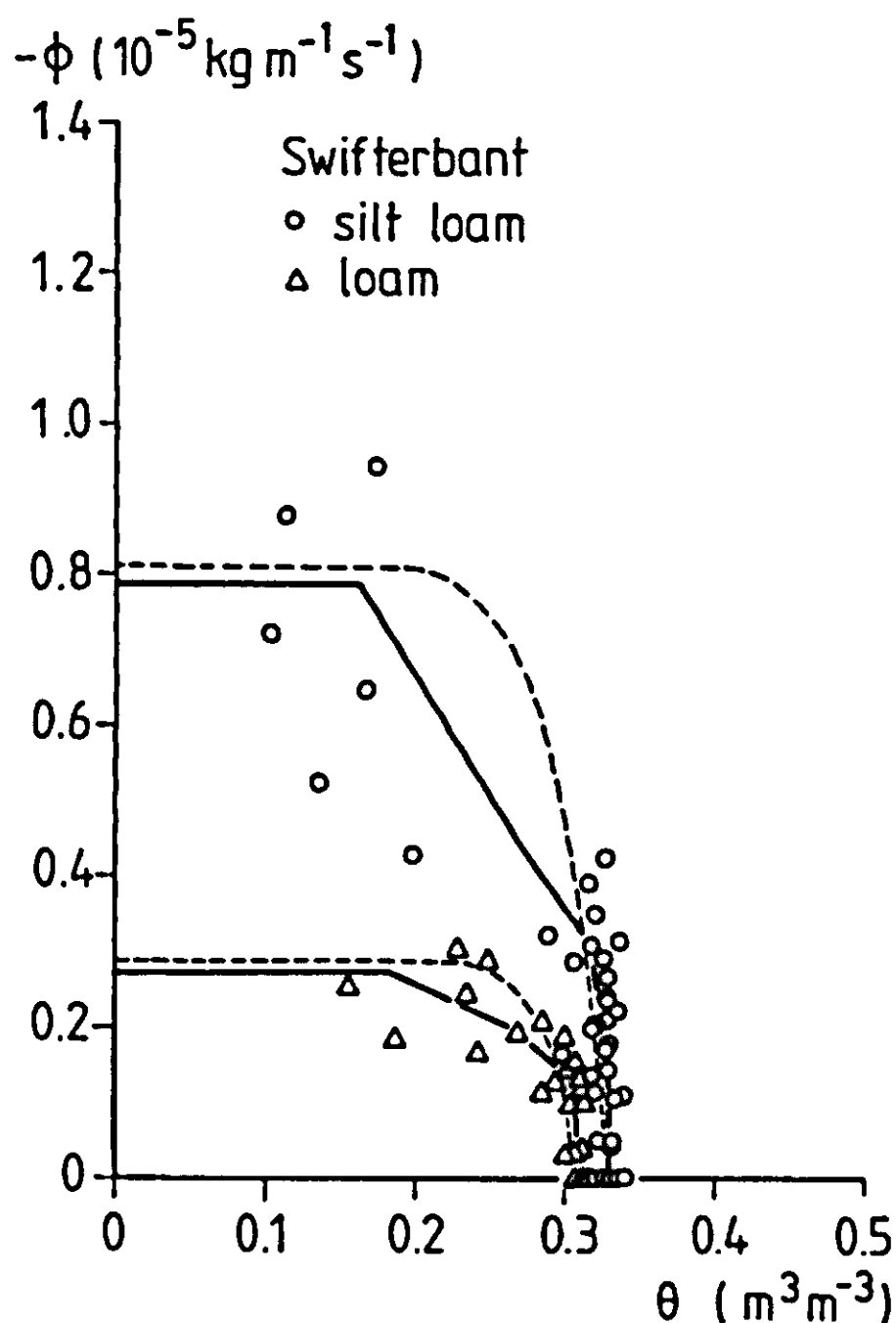
Figure 31. Measured matric flux potential curves for both Swifterbant soils. Solid lines were obtained by considering all core samples as a single soil volume. Broken lines are the result of numerical integration of $K(p)$ curves.

4.6 Validation variables: soil state variables and surface fluxes

The soil state variables measured were moisture content, temperature, and soil water tension. These 'output' variables are not only used for model validation, but also to initialize simulation runs.

The other variables that are to be predicted by simulation and were also measured in the field, are the fluxes of heat and moisture at the soil surface. Observed and simulated time series of all these 'output' variables will be presented in Chapter 5. Here, only a brief description of measurement conditions in the field is given.

Soil moisture

Soil state variables were monitored within small sampling plots at various locations in the field. Only the data from two plots (plots 1 and 4, Figure 8) are used in this report. The other plots gave similar results.

Soil moisture content was determined by gravimetric sampling of four depth intervals of increasing thickness, down to 55 mm. All samples were composites

of five subsamples. A razor blade device was used to section these top centimetres into thin layers. To convert gravimetric moisture contents to volumetric moisture contents θ, a dry bulk density of 1150 kg m^{-3} was used for the silt loam, and one of 1050 kg m^{-3} for the loam. These averages are based on a total of 100 transect samples. Throughout the experiment, significant changes in moisture content occurred only in the top 35 mm. Below this (35-55 mm), changes were less than 2% by volume, and θ averaged 0.33 for silt loam and 0.31 for loam, as determined by gravimetric sampling.

Errors in volumetric moisture content are caused by within-plot variability of gravimetric moisture content and of bulk density. The standard deviation of the error in gravimetric moisture content was 0.005-0.02 (mass fraction); the standard deviation of the error in bulk density was 50 kg m^{-3}. Both values were obtained from semivariograms at the 4 m lag level. Based on these data, an accuracy of 0.025 m^3 m^{-3} may be estimated for the measured volumetric water contents, as an average for all depths.

It is well known that spatial variability of moisture content is dependent on the average level of moisture content itself, but extensive sampling to study the spatial variability could only be done on a few occasions; hence the temporal behaviour of spatial variability is little known.

Soil water tension was measured at various depths. Tension readings showed a marked diurnal course. In the next chapter these fluctuations will be related to those of soil temperature.

Soil temperature

Soil temperature profiles were measured down to 0.5 m depth. Errors related to measurement equipment were 0.1 K, but again the total error was larger because of spatial variability. Similar to soil water content, the spatial variability of soil temperature depends on drying stage, depth and time of day. Semivariance analyses of noon soil temperatures at 10 mm depth under fair weather conditions yielded standard deviations of 0.2-0.4 K at the 4 m lag level. A value of 0.4 K will be used in model validation, for all depths and drying stages.

Surface radiation temperature

The measured surface radiation temperature T_{sr} as used in this report is defined by

$$\sigma T_{sr}^4 = \int_{\lambda = 8}^{14\,\mu m} \{\varepsilon(\lambda)\ W(\lambda,T_s) + R'(\lambda)\}\ d\lambda \qquad \text{Equation 90}$$

where $W(\lambda,T_s)$ is the blackbody emittance at temperature T_s, and $R'(\lambda)$ the reflectance by sky radiation. This radiation temperature was measured by ground-based IR thermometers. The accuracy of the detector was 0.25 K in the relevant temperature range. The error in radiation temperature caused by

84

within-plot spatial dependence was derived from semivariance analysis; its standard deviation ranged from 0.5 to 1.0 K, depending on the weather and field conditions. Combined with the instrument error, a standard deviation of 1.03 K resulted for the overall error.

True surface temperature may deviate from radiation temperature by several K because of ambient radiation in combination with soil emissivity values below unity. Sky radiation temperature can only be measured accurately if various precautions are taken (e.g. Jacobs, 1982); this variable was not measured regularly in the experiments discussed here. As the surface radiation temperature is to be predicted by the SALSA model for a comparison with measured data, a value of sky radiation temperature should be assumed in the simulation for converting the actual surface temperature – which is obtained from the energy balance equation – into radiation temperature; this is done in the model by adding reflected ambient radiation to calculated emittance. For this, sky radiation temperatures were assumed to vary over a 40 K range; this increases the variance in predicted surface radiation temperature, resulting from uncertainty in input, by 2.25 K^2 (Subsection 5.1.1).

All surface energy fluxes were derived from the measured data. The fluxes of interest are the net radiation, the sensible and latent heat fluxes above the surface, and the soil heat flux. Net radiation has already been discussed in Section 4.4, along with the other radiation terms. The remaining fluxes will be discussed below.

Soil heat flux

The surface soil heat flux was determined by a calorimetric method, i.e. by using the temporal development of soil temperature profiles in the layer between the surface and a chosen reference depth. An estimated value of the flux at reference depth is added to the rate at which the heat content of that layer (per unit soil surface) changes, to obtain the surface heat flux. The heat content is calculated by numerical integration of the product of temperature and volumetric heat capacity over depth. The reference depth should be chosen such that the heat flux at that depth is small in comparison to the rate of heat storage in the overlying layer.

The reference depth was chosen at 0.30 m below the surface. The heat flux at 0.30 m was calculated from the local temperature gradient and an estimated value of the apparent thermal conductivity (Section 4.5). Note that, other than by the use of flux plates, this calorimetric method does not take into account that particular fraction of the surface soil heat flux that is spent on evaporation within the topsoil (i.e. below the surface). This is convenient and correct, because the procedure used to assess the evaporation term (Bowen ratio method) already takes into account this subsurface evaporative heat loss.

The errors involved, both in estimating the heat flux at the reference depth and in calculating the rate of heat storage above this depth, were approximately 10%. As the two terms were summed to yield the surface soil heat flux, the error

in this flux was also estimated to be 10% of the nominal value.

Latent heat flux
The latent heat flux was determined by the Bowen ratio method, using the combined equations

$$H + LE = -R_n - G$$
Equation 91

and

$$\beta \equiv \frac{H}{LE} = \gamma \frac{dT}{de}$$
Equation 92

where β is the Bowen ratio and γ the psychrometer constant. Measurements of wet and dry bulb temperature gradients were performed with sensors that were independent of those used to assess the absolute levels of these variables. In this manner, relatively accurate figures for β could be obtained. Measurements were taken at 0.2 m and 0.5 m above ground level, and were integrated over half-hour periods. The temperature differences between these elevations were measured with an accuracy of 0.0025 K (both for wet and dry bulb temperature). For most daytime conditions ($dT/dz > 0.04$ K m^{-1}; $de/dz > 10$ Pa m^{-1}) this corresponded to a maximum error of 10% in the Bowen ratio. Combined with errors in net radiation and soil heat flux, this resulted in a relative error in the evaporation term that ranged between 10 and 20% during daytime.

In addition to the above method, total daily evaporation was determined on several days by using microlysimeters (Boast & Robertson, 1982). This was done in order to compare evaporative losses from the two different soils (loam and silt loam). The silt loam consistently showed a higher daily total evaporation than the loam, the difference ranging from 15 to 40%. For predicted differences in evaporation rate, see Chapter 5.

Sensible heat flux
The sensible heat flux was determined along with the latent heat flux by application of Equations 91 and 92. Like for latent heat, the error was calculated as a function of time, with the help of the above mentioned values. It appeared to be 10 to 20% during daytime. This figure increased at low net radiation, but in those cases the absolute error was usually below 5 W m^{-2}. The same was true for the latent heat flux.

5 Validation

In this chapter an attempt will be made to validate the SALSA model. The results of the experiments discussed in the previous chapter are the basis of the experimental validation presented in Section 5.1. In the comparison of the theory with these sets of experimental data only the abridged version of the model (option B, Figure 2) will be used, because the data available are intrinsically too limited to be used to predict boundary layer development. Hence, the upper boundary conditions to the system (at 0.5 m) are the measured values of air temperature, humidity and wind speed over the experimental field, and the measured course of global radiation.

A qualitative validation of the complete model, i.e. including boundary layer development, is discussed in Section 5.2, where a number of general boundary layer characteristics are inspected.

5.1 Experimental validation

The experimental results of the field studies will be compared to model predictions. Attention will be focused on the measured and simulated courses of surface fluxes (R_n, G, H, LE) and on the developments in surface radiation temperature, topsoil moisture content, and soil temperature (the latter two at various depths). These variables were designated 'output variables' to indicate that they are to be predicted by simulation; since the measured values of these 'output variables' are presented in this chapter for validation purposes, they were not discussed in the previous chapter along with the other experimental results.

In the validation of models by field observations, it is necessary to take errors into account. These result from inaccurate measurement and spatial variability. This applies both to the fluxes and state variables actually measured, and to their predicted values. Errors in the latter result from errors in the system parameters and boundary conditions used as inputs to the model.

5.1.1 Input and output variance resulting from measurement errors

For a model with m output variables and n input variables, the variance of an output variable $z_j = f(x_i, i = 1, n)$ can be expressed as a function of (1) the variance of the measurement error in the input variables x_i, and (2) the sensitivity of the prediction z_j to changes in input. Thus for the case of non-correlated input variables x_i, the variance in output z_j is written as (e.g. Hahn & Shapiro, 1967)

$$\text{var}(z_j) = \sum_{i=1}^{n} \left(\frac{\partial z_j}{\partial x_i}\right)^2 \text{var}(x_i) \qquad \text{Equation 93}$$

where the derivative $\partial z_j/\partial x_i$ is the sensitivity of z_j to changes in x_i. It is assumed here that the measurement errors in x_i are symmetrically distributed about the mean, so the third moment of x_i is zero. With differentials replaced by finite differences, the error variance is approximated by

$$\text{var}(z_j) \cong \sum_{i=1}^{n} \left(\frac{\Delta z_j}{\Delta x_i}\right)^2 \text{var}(x_i) \qquad \text{Equation 94}$$

The model outputs z_j are output variables such as soil surface temperature, latent heat flux, etc. The inputs are soil properties such as thermal conductivity at given moisture content; or boundary conditions, such as global radiation.

The sensitivity $(\Delta z_j/\Delta x_i)$ was assessed by running the simulation model for two values of x_i: the mean value of x_i, and the mean plus one standard deviation $\sigma(x_i)$. Using one standard deviation in determining the sensitivity of z_j to x_i may seem arbitrary, but it gives a sufficiently accurate estimate of sensitivity for the present purpose. It implies that $n + 1$ model runs be made in order to determine var(z_j). It is assumed that the sensitivity as defined here is constant over small Δx_i intervals, and that the error in x_i is distributed normally; furthermore, interactions between the effects $(\Delta z_j/\Delta x_i)$ of the various x_i are ignored. Various authors have applied the above procedure in a hydrological context (e.g. Coleman & DeCoursey (1976), who compared different evapotranspiration formulas). It can be expected that the variance as calculated by Equation 94 depends on the state of the system, which has a dynamic character. Hence, in validating a model the temporal behaviour of the variance must be accounted for.

Now, if for each output variable a measured course $z_j(t)$ and a predicted course $\hat{z}_j(t)$ are available, along with the associated variances for both time series, one may evaluate the predictions by using q, defined as

$$q(t) \equiv \frac{\hat{z}_j(t) - z_j(t)}{\sqrt{[\text{var}(\hat{z}_j(t)) + \text{var}(z_j(t))]}} \qquad \text{Equation 95}$$

In Subsections 5.1.2 and 5.1.3 the course of this quotient, which is similar to the Student t parameter, will be inspected as an indicator of model validity, for the two data sets. Predictions will be considered acceptable in this context if the value of q ranges between -2 and $+2$.

One data set covers a time span of five days, the other six days. For these intervals, the observed behaviour of the following variables will be compared with their predicted courses:

- net radiation
- soil heat flux ($z = 0$)
- latent heat flux
- sensible heat flux
- surface radiation temperature
- soil temperature (three depths)
- volumetric soil moisture content (four depth intervals).

Table 11 summarizes the standard deviations of the error, or the relative error, of the measured input variables as used in the simulation runs. It also includes the nominal values of the system parameters which, by definition, do not vary in time. For more details, see Chapter 4. The uncertainty in the predic-

Table 11. Inputs for validation runs: reference value, and standard deviation of error (σ) or coefficient of variation (CV).

Variable	Flevo 1 and 2	
	Reference value	σ or CV (%)
global radiation	*	5%
air temperature	*	0.1 K
vapour pressure	*	15 Pa
wind speed	*	4%
initial soil temperature	f(depth)	0.4 K
initial soil moisture content	f(depth)	0.025
cloud cover	f(time)	20%
a (Equation 7)	0.70	0.05
b (Equation 7)	$0.04\,hPa^{-0.5}$	$0.02\,hPa^{-0.5}$
n (Equation 8)	0.10	0.05
sky rad. temperature	273 K	20 K
roughness length	0.08 mm	0.06 mm
albedo	f(moisture content)*	0.02
soil emissivity	f(moisture content)*	0.01
longwave reflectivity	0.10	0.05
thermal conductivity	f(moisture content, bulk density)*	20%
heat capacity	f(moisture content, bulk density)*	6%
hydraulic scale α	1.0 **	$-0.51/+1.04$
	1.0 ***	$-0.58/+1.37$
β	2.0	1.0

* see Chapter 4; ** silt loam; *** loam

Table 12. Standard deviations of the error in measured and predicted output variables.

	Flevo-1		Flevo-2		Units
	measured	predicted	measured	predicted	
net radiation	0–20*	20–80	0–20	20–40	$W\,m^{-2}$
soil heat flux	0–20*	10–40	0–15	5–25	$W\,m^{-2}$
sensible heat flux	0–25*	5–80	0–15	5–15	$W\,m^{-2}$
latent heat flux	0–35*	10–100	0–35	5–35	$W\,m^{-2}$
surface rad. temperature	1.0	2–6	1.0	2.0–3.0	K
soil temperature (0.03 m)	0.4	1.5–2.5	0.4	1.0–2.0	K
soil temperature (0.11 m)	0.4	0.5–1.8	0.4	0.5–1.5	K
soil temperature (0.20 m)	0.4	0.5–1.5	0.4	0.5–1.5	K
volumetric moisture content at 0–5 mm	0.025	0.05–0.15	0.025	0.01–0.05	–
volumetric moisture content at 5–15 mm	0.025	0.05–0.15	0.025	0.01–0.04	–
volumetric moisture content at 15–35 mm	0.025	0.02–0.03	0.025	0.02	–
volumetric moisture content at 35–55 mm	0.025	0.02–0.03	0.025	0.02	–

* 5, 10, 20 and 20% of measured values of R_n, G, H, LE, respectively.

tions, caused by input errors, is expressed as the variance according to Equation 94. The corresponding standard deviations of the error, or the relative errors, are listed in Table 12. Where ranges are indicated instead of single values, the error depends on the state of the sytem, i.e. on time. Table 12 shows also the error in the measured series of 'output' variables. Employing these numbers and following the procedure described above, the course of $q(t)$ may now be calculated for each 'output' variable.

The resulting $q(t)$ series will be shown for each 'output' variable. To avoid division through very small numbers, – the night-time fluxes and their variances are very small – a q value of zero is assigned in cases where the difference $|\hat{z}_j(t) - z_j(t)|$ is below a critical level c. Where a non-zero value of c has been used, this critical value is indicated in the corresponding figure.

5.1.2 Flevo-1

The Flevo-1 set represents some days of fine late spring weather in the Netherlands (see Section 4.4). The initial condition of the soil was homogeneously wet after heavy showers, and the strong drying conditions brought about high initial evaporation rates. Subsequent drying of the topsoil dramatically affected the Bowen ratio, rendering this series of data an interesting case for model vali-

dation. Moreover, the occurrence of two soil types within a single trial field offers an extra opportunity to test model performance. The data used for the silt loam case were taken from plot 1; the loam data used here refer to plot 4 (Figure 8). The model option switches for the Flevo-1 analysis were set as follows:

SWBLD   = 0 (no boundary layer simulation)
SWMFLP = 1 (use of matric flux potential)
SWMTB   = 1 (matric flux potential specified in a table)
SWGRAV = 0 (gravity not taken into account in water flow equation)
SWCHTB = 1 (soil thermal conductivity specified in a table)
SWRNET = 0 (net radiation not used as boundary condition)

All results of one particular simulation run are depicted in the Figures 32-35 (surface energy fluxes) and 38-45 (state variables), along with the time series of actual observations. The inputs for this run were as listed in Table 11. The corresponding $q(t)$ series are shown in Figures 37 (fluxes) and 46 (state variables).

Some remarks must first be made regarding the two soil types distinguished in the experimental field. Soil inhomogeneity complicates model validation. In terms of system parameters, the two soils are assumed to differ only in hydraulic properties and – slightly – in topsoil bulk density (Chapter 4). Of the surface fluxes, net radiation and the soil heat flux were observed at the silt loam plot in particular. In the measurement of sensible and latent heat fluxes, however, the use of the Bowen ratio method introduces the complication that the fluxes
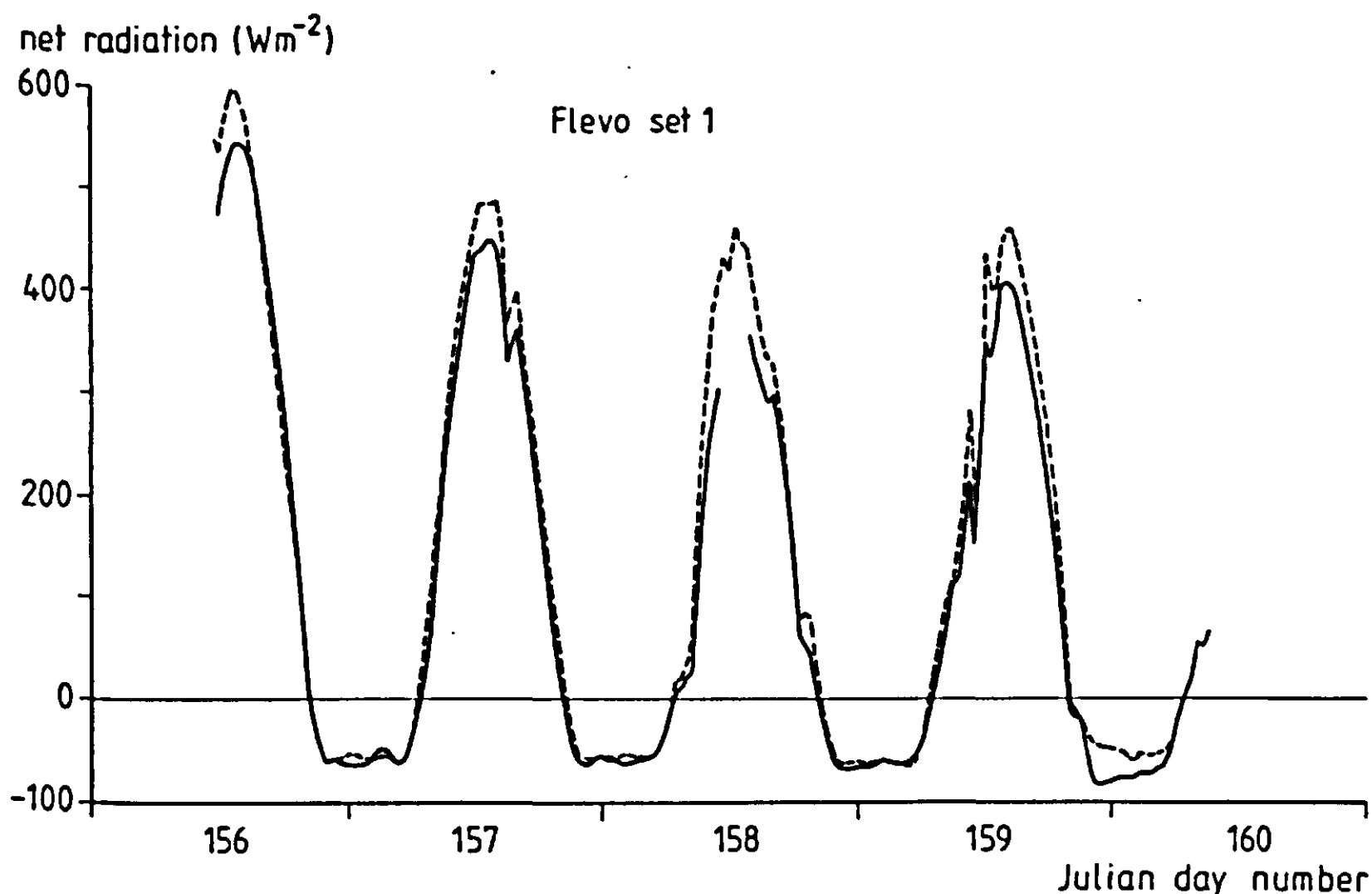
Figure 32. Measured (——) and simulated (---) net radiation, Flevo-1.

soil heat flux (Wm⁻²)

Flevo set 1
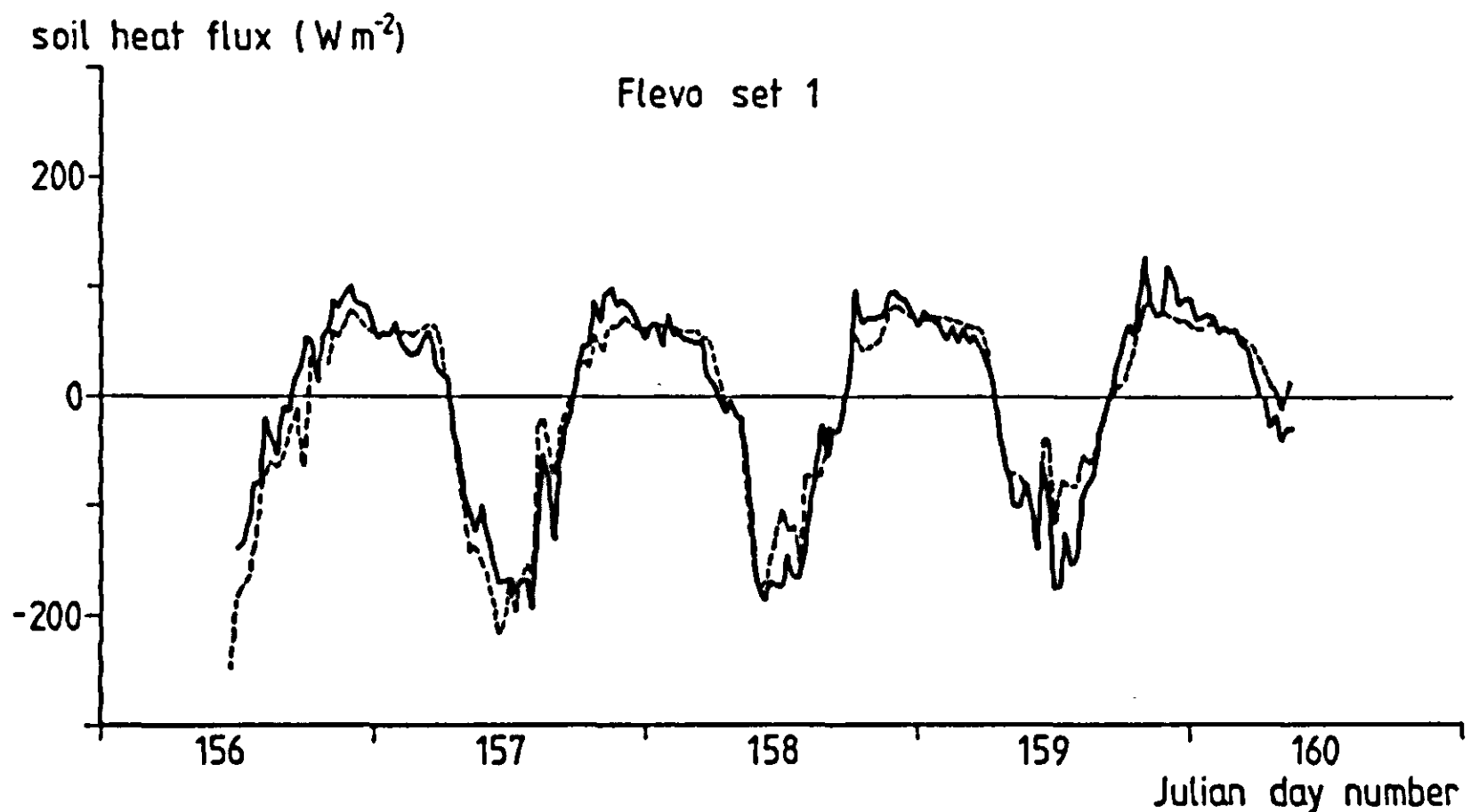
Figure 33. Measured (——) and simulated (---) soil heat flux, Flevo-1.

sensible heat flux (Wm⁻²)

Flevo set 1
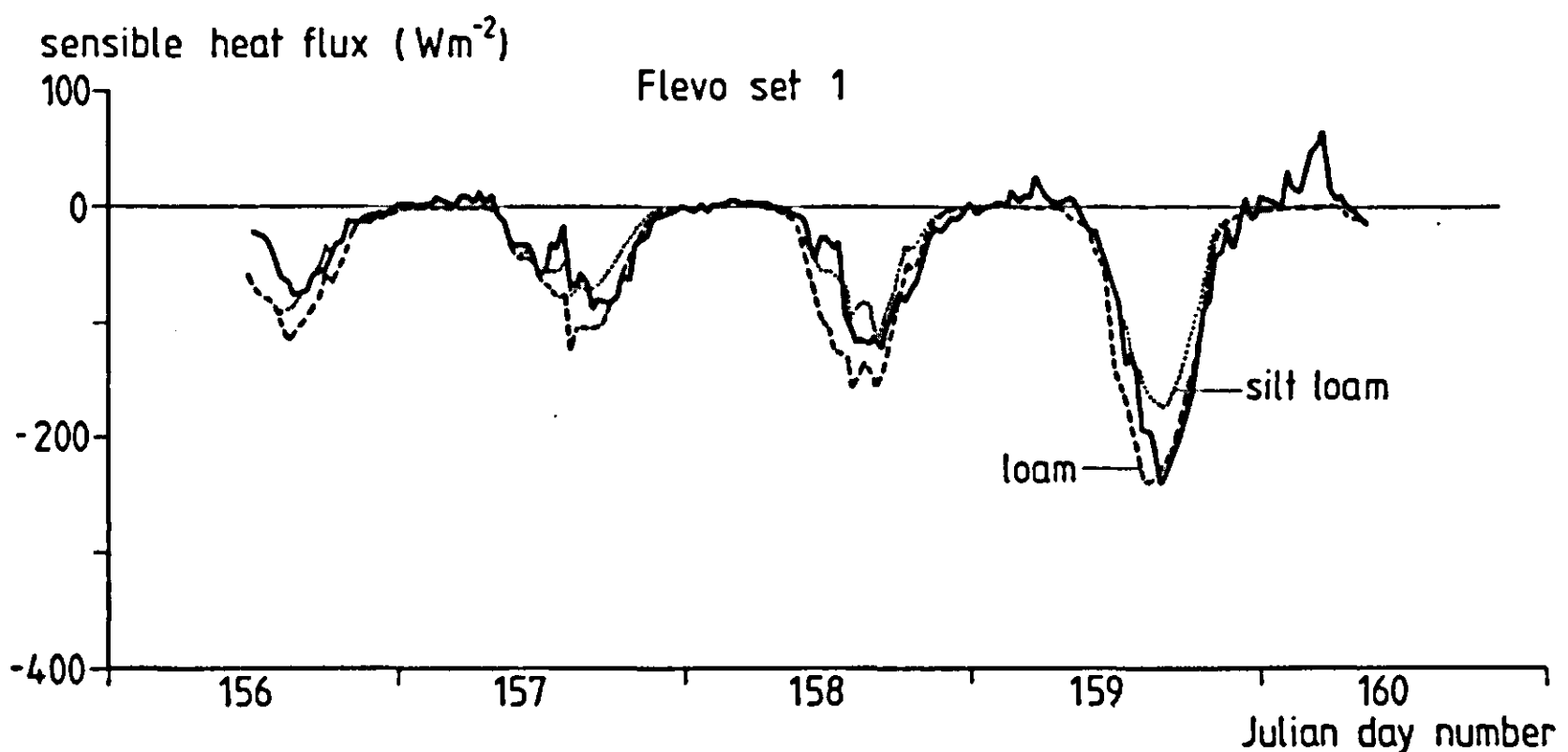
Figure 34. Measured (——) and simulated (--- and ···) sensible heat flux, Flevo-1.

obtained represent some 'field averaged' values; they cannot be ascribed to a particular soil type or location within the heterogeneous field, whereas model predictions are linked to an explicitly defined soil type. Therefore, in the simulation effort, the model was run for the two soil types present. Identical sets of boundary conditions (wind speed, global radiation, air temperature, and humidity) were used.

The sensible and latent heat fluxes thus simulated are depicted in Figures 34 and 35, along with the observations. From the above, it may be expected for each of these fluxes that the observed course should run somewhere between the two simulated curves, corresponding to the two distinguished soil types.

In contrast, the developments in topsoil moisture content, soil temperature, and radiation temperature are, of course, more site-specific. Moisture content

latent heat flux (Wm⁻²)

Flevo set 1

loam

silt loam

Julian day number
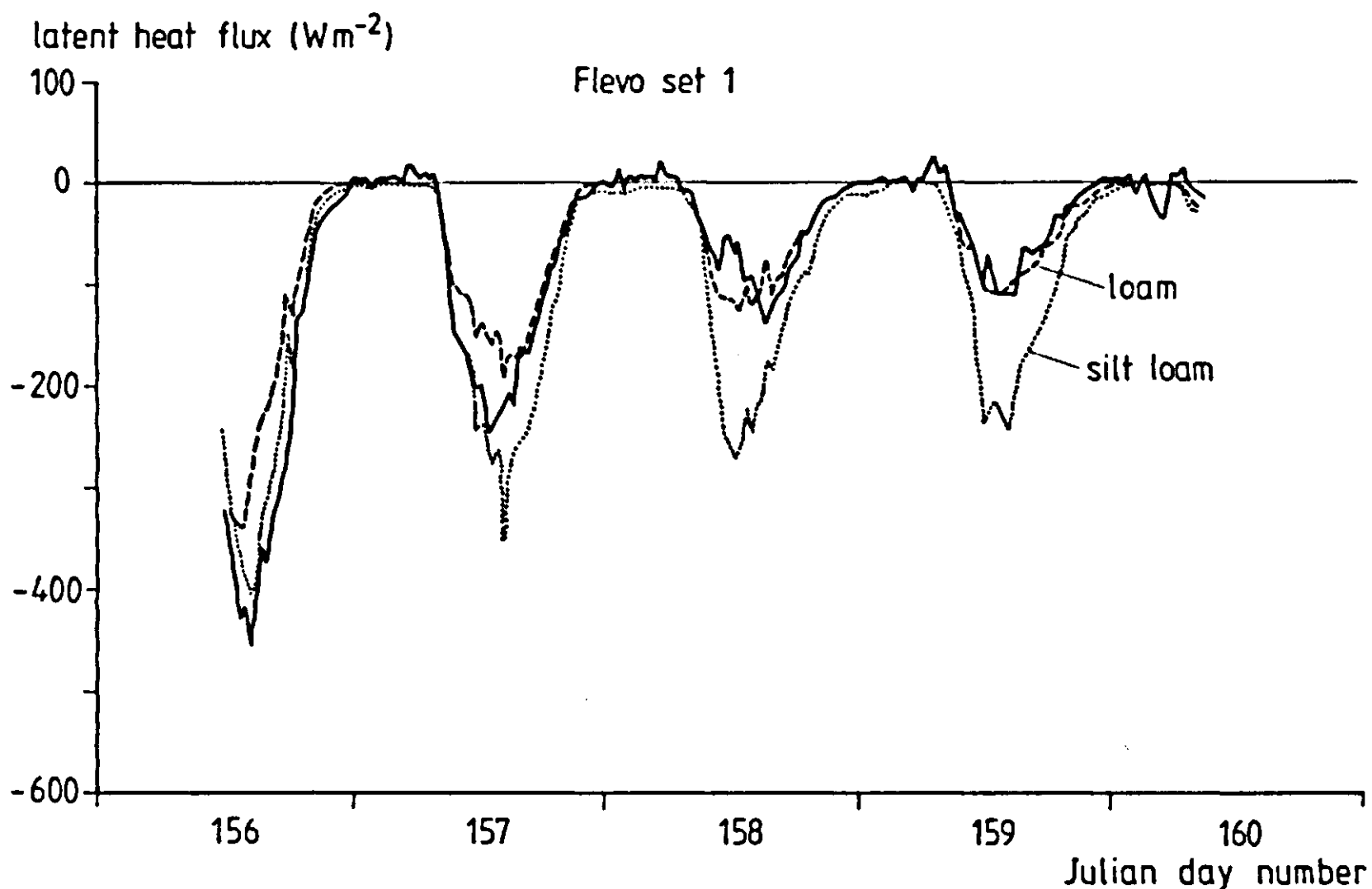
Figure 35. Measured (——) and simulated (--- and ···) latent heat flux, Flevo-1.

and radiation temperature were observed separately for the loam and silt loam plots. The results, therefore, are also presented separately (Figures 38-43).

Continuous records of soil temperature are only available for the silt loam plot (Figure 45). Occasional measurements revealed, however, negligible differences between temperatures in the two soils at depths below 30 mm.

Evaluation of flux predictions

To prevent confusion, it is recalled that fluxes are assigned a positive value if directed towards the surface, and are negative when directed away from the surface. Of the surface fluxes, net radiation (Figure 32) is described fairly well. For daytime conditions, this is not unexpected, because global radiation (a measured boundary condition to the model) constitutes a major fraction of net radiation. At night, however, when net radiation is determined solely by surface emittance and sky radiation, predictions are also good. For the sky emissivity parameters a and b (Equation 7) constant values were used, whereas in reality these values may vary over a considerable range (Table 11). For the Flevo-1 data set, this uncertainty accounted for up to 75% of the variance in the nighttime predictions of net radiation. A deviation in net radiation as observed for the night of Julian dates 159/160 may be explained by variations in a and b. The q values for net radiation (Figure 37) range between -1 and $+1$ throughout the experimental period; this is acceptable.

The soil heat flux at the surface is also described reasonably well, although the peaks in both curves (Figure 33) do not always match. This causes q to fluctuate more than in the case of other surface energy fluxes. The accuracy attained in the field registration of peaks and dips in the surface soil heat flux

93

(by integration of temperature profiles) was limited by the spacing of temperature sensors just below the surface. Also, in contrast with most other variables, soil temperatures were registered in terms of momentary half-hour values, i.e. without integration. These are the probable causes of the observed discrepancy between the measurements and the simulation results.

To illustrate that the validation is conceptually sound, it is recalled how the 'calorimetric' surface soil heat flux G, which is the flux plotted in Figure 33 for both the measured and simulated courses, is calculated by the model. First, the conduction flux at the surface is obtained by multiplication of the linearized temperature gradient (between the surface and the centre of the first soil compartment) with the local soil thermal conductivity. Then, that part of the surface heat flux which is associated with soil heating or cooling (hence the term 'calorimetric') is obtained by subtracting the calculated surface latent heat flux from this conduction flux at the surface. (So, in SALSA the conduction flux converges in the centre of those soil compartments where net evaporation occurs: the heat required for evaporation is 'carried' by true conduction from the surface downward into the soil, as happens also in reality; at night, the reverse should occur). The field-measured 'calorimetric' soil heat flux, on the other hand, is directly derived from measured temperature profiles and bulk soil heat capacity, by integration over depth, as explained in Section 4.6. The predicted 'calorimetric' flux is therefore fully independent of the measured flux, but represents the same variable.

The latent and sensible heat fluxes, as determined in the field by the Bowen ratio method, fit well between the simulated courses depicted in Figures 34 and 35 for the two respective soils. The model considerably underestimates the latent heat flux during the first day only. The decrease in daily maximum latent heat flux, observed during the four days after the 'wet' start, is steeper than the corresponding decrease in the predicted values, for both soils. (The inverse applies, though somewhat mitigated, to the sensible heat flux). This may be because vapour transfer within the topsoil was overestimated; or because hysteresis was ignored in the soil hydraulic properties: only using desorption curves implies that the night-time moisture redistribution (surface wetting; see also Figures 40 and 41) is overestimated. A value of 2.0 for the phenomenological coefficient β (Equation 77) was used in SALSA to calculate vapour transport, but other values have been reported, as mentioned in Subsection 2.6.4. In the field experiments, no measures were taken to enable a separate assessment of vapour and liquid transport in the topsoil; therefore β could not be determined independently.

The $q(t)$ series shown in Figure 37 for the latent and sensible heat fluxes refer to the 'silt loam' simulation. The predictions for the 'loam' case, when compared with field observations, gave better q figures on days 159-160, but poorer results on the first two days. With q ranging mostly between -1.5 and $+1.5$, the discrepancy between prediction and observation is considered acceptable.
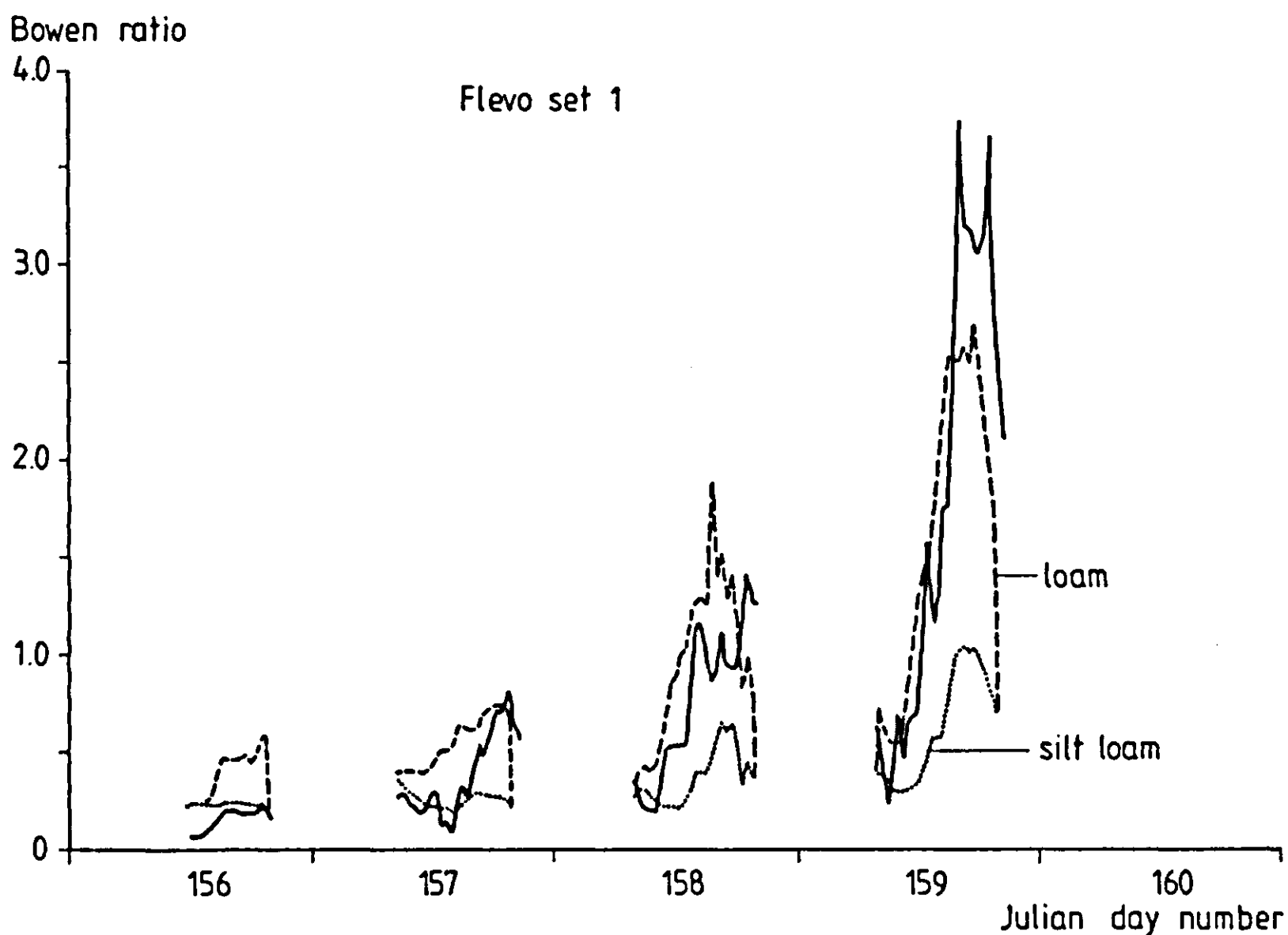
Figure 36. Measured (——) and simulated (--- and ⋯) development of the Bowen ratio, Flevo-1.
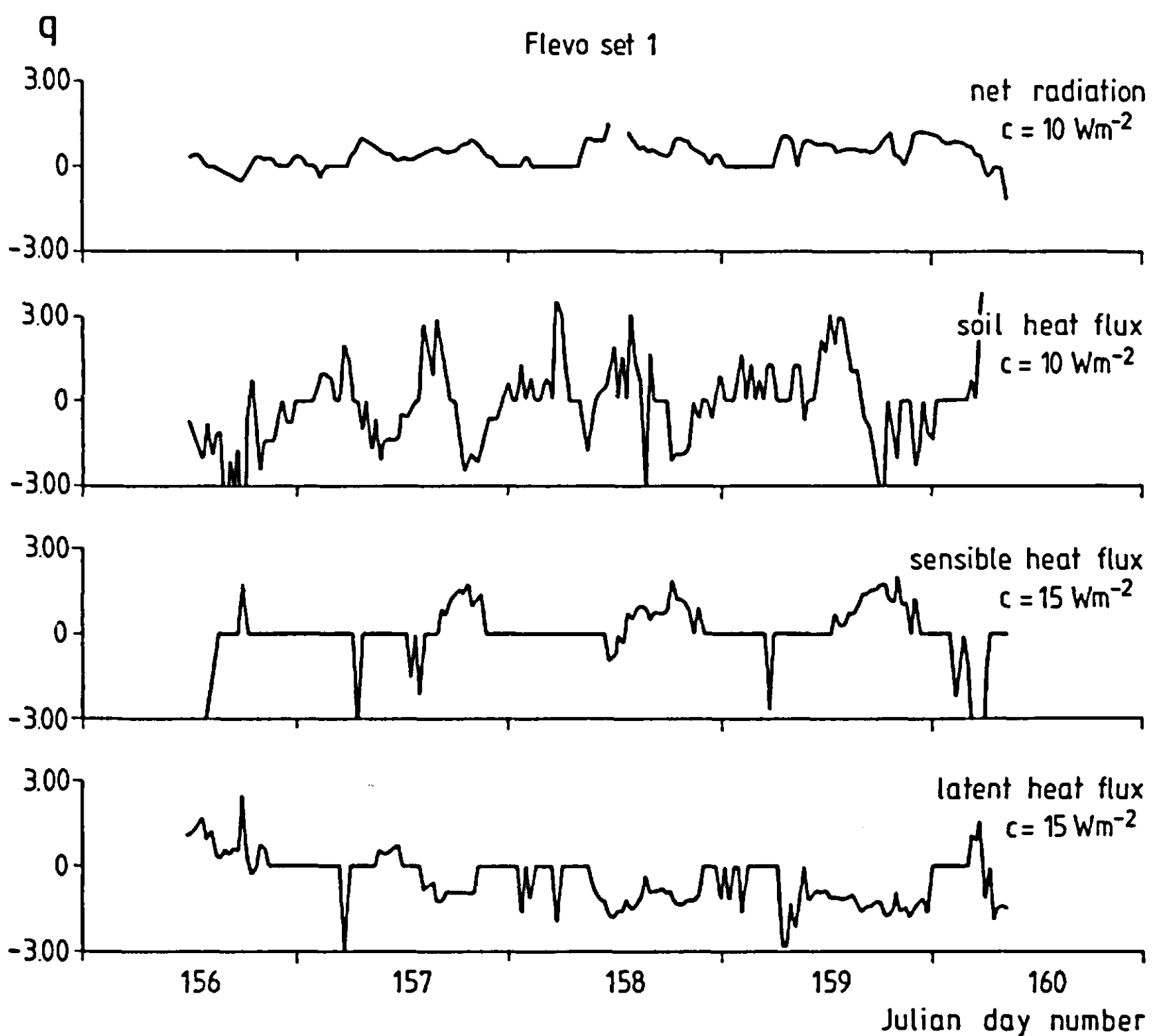
Figure 37. Values of q for the surface fluxes, Flevo-1. For explanation see text.

95

Evaluation of state variable predictions

For the silt loam, surface radiation temperature (Figure 38) is predicted reasonably well. The slight nocturnal overestimation may be associated with the excessive night-time surface wetting, discussed above. However, sky radiation temperature also has a marked effect on surface radiation temperature during the night; uncertainty in the former accounted for a contribution of up to 45% to the variance of the predicted value (calculated according to Equation 94). For the last night of the sequence, overestimation of net radiation is associated with an erroneous surface temperature prediction. In view of the expected errors (Table 12), the deviations as normalized in the parameter q (Figure 46) should not be interpreted as disturbing.

A comparison between loam and silt loam radiation temperatures (Figures 38 and 39) shows the impact of the different surface drying behaviour. As mentioned earlier (Section 4.5), this difference between the soils results from the difference in matric flux potential curves. The model, however, overestimates to some extent the radiation temperature for the loam plot, during daytime as well as during night-time.

surface radiation temperature (°C)
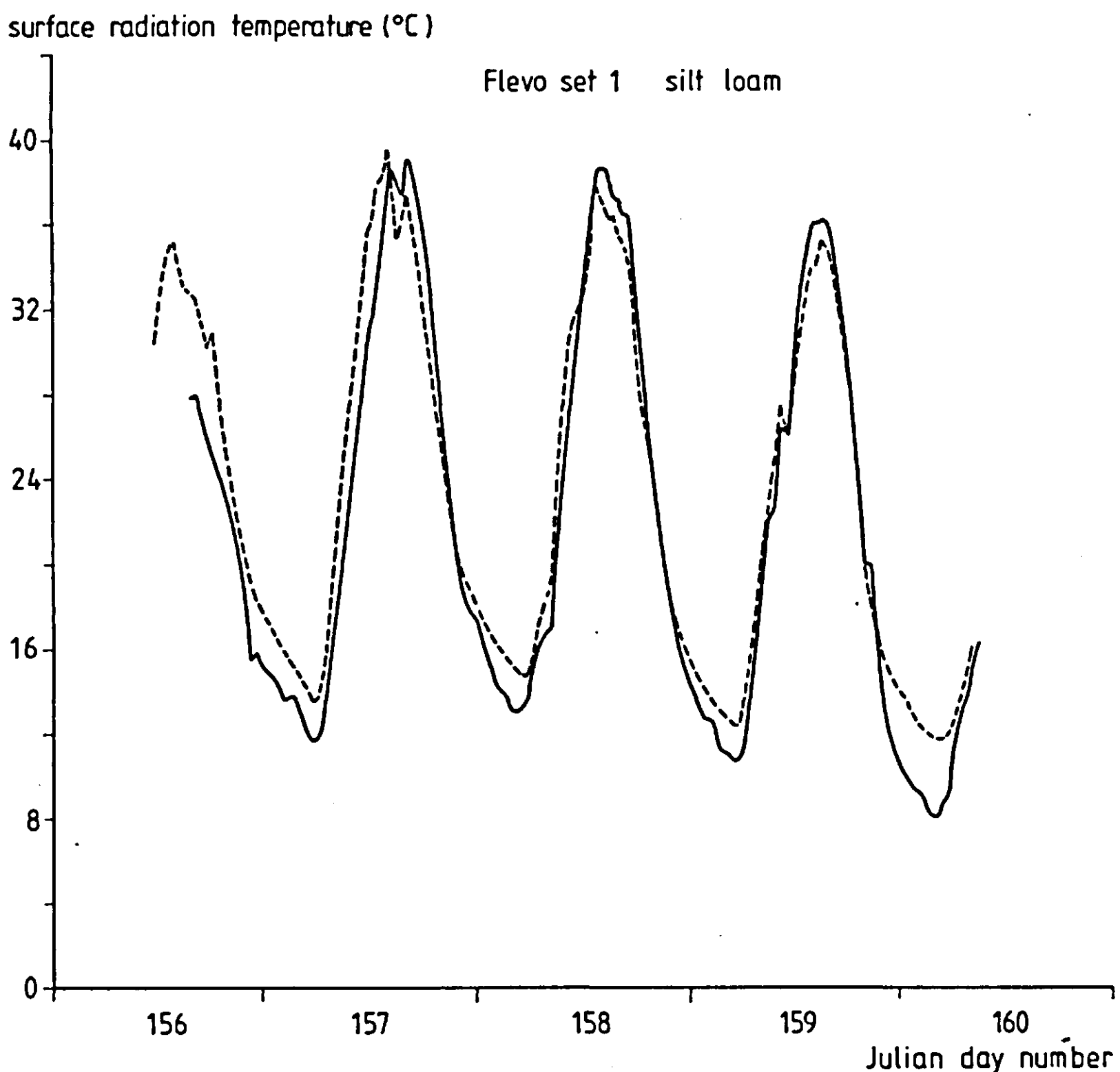
Figure 38. Measured (——) and simulated (---) surface radiation temperature for silt loam, Flevo-1.

surface radiation temperature (°C)

Flevo set 1   loam

Julian day number
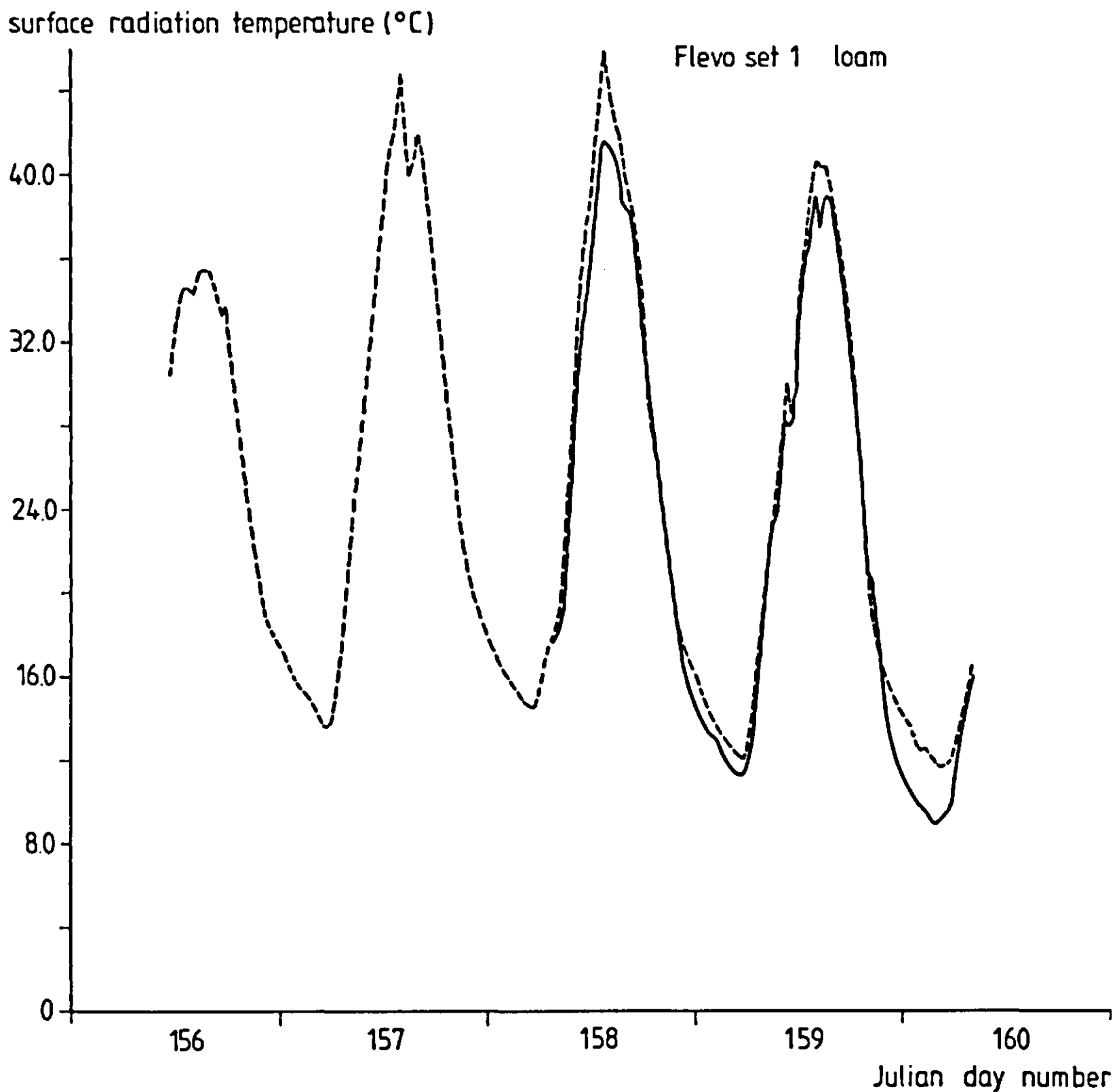
Figure 39. Measured (——) and simulated (---) surface radiation temperature for loam, Flevo-1.

Topsoil moisture contents (Figures 40-43) only changed slightly at depths of 15-35 mm and 35-55 mm, in both soils; the simulation results are in accordance with this observation. The gradual decrease in daytime moisture content over the four-day period is predicted correctly for the various layers in both soils (note the faster drying for the loam surface layers). The amplitude for the 0-5 mm layers, however, is grossly overestimated in the silt loam case. As stated before, the cause of this deviation might be ignoring hysteresis, or an erroneous value of the vapour transport coefficient. For the loam case, where the same value for the vapour transfer coefficient was used in simulation, no such discrepancy is observed. Moisture content in the 5-15 mm layer is consistently slightly overestimated for the silt loam. The diurnal amplitudes at this depth are predicted accurately for both soils. The values of q as depicted in Figure 46 mostly range from -1.5 to 1.5. The major sources of variance in predicted values of moisture content for the top two layers (Table 12) were the uncertainties in the sky emissivity parameters (accounting for up to 30% of the variance in predicted values), in the hydraulic scale parameter α (up to 40%), and in the

97
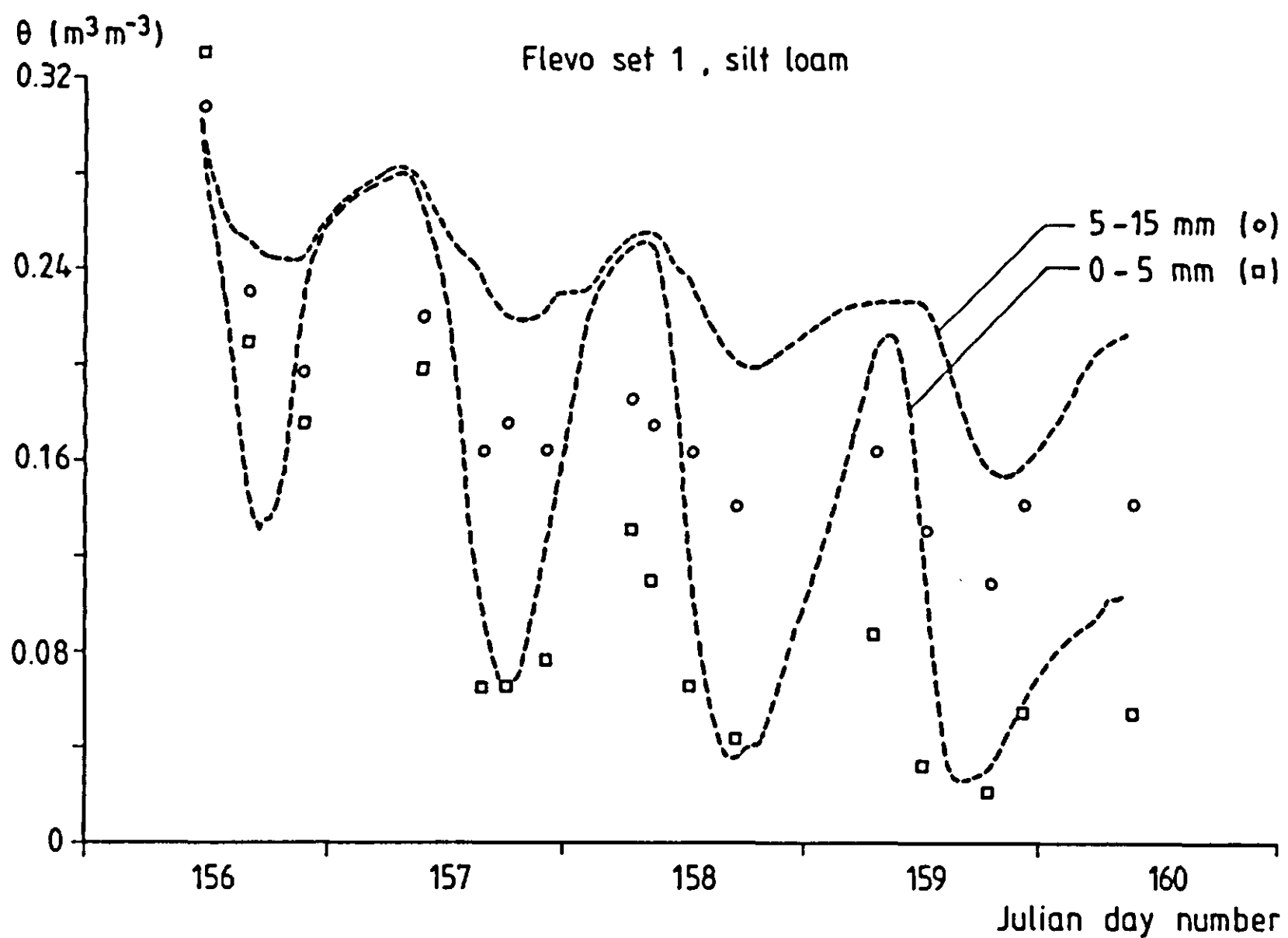
Figure 40. Soil moisture contents at two depths, silt loam. Symbols represent observations, broken lines simulation results, Flevo-1.
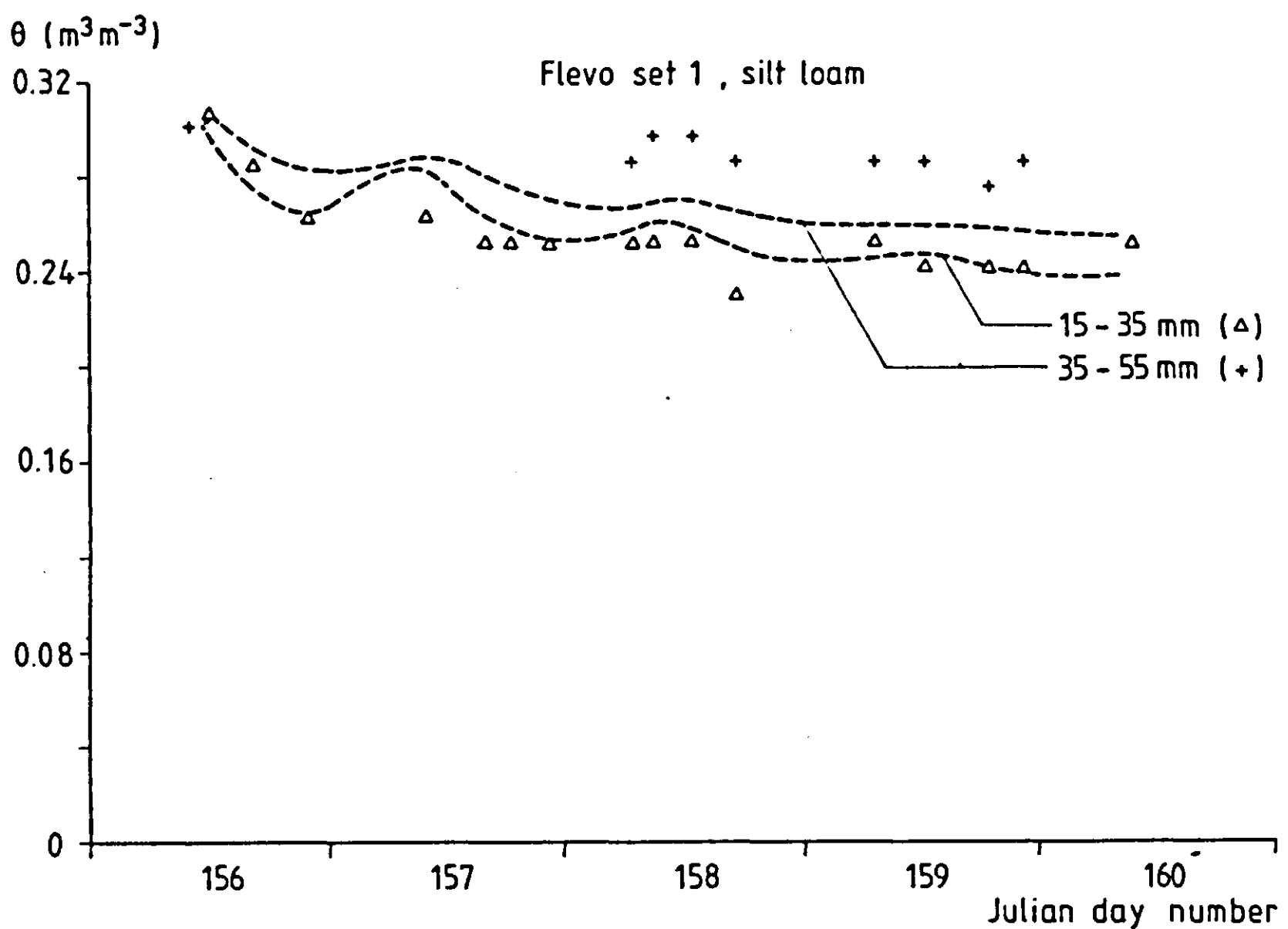
Figure 41. Soil moisture contents at two depths, silt loam, Flevo-1.
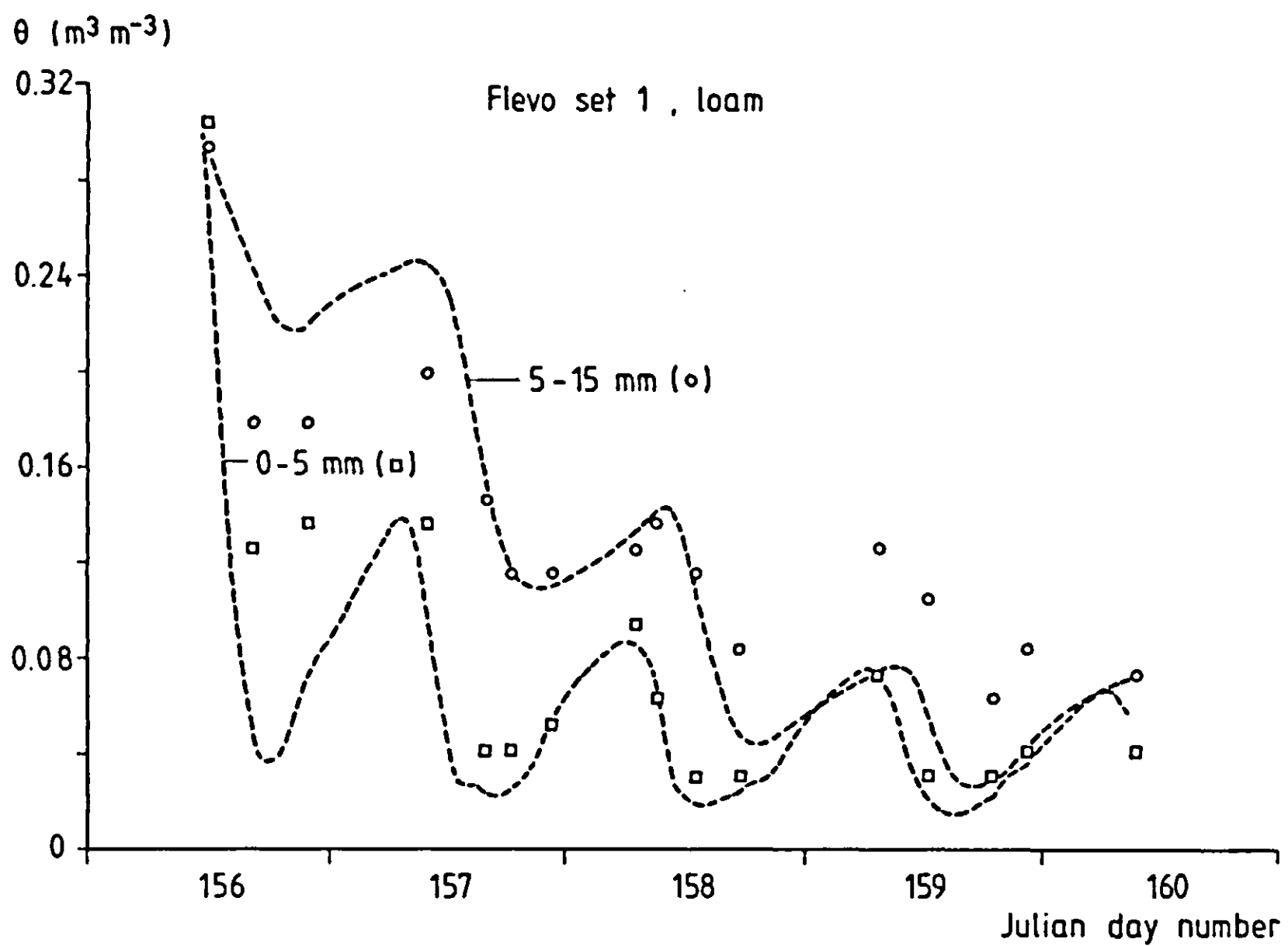
Figure 42. Soil moisture contents at two depths, loam, Flevo-1.
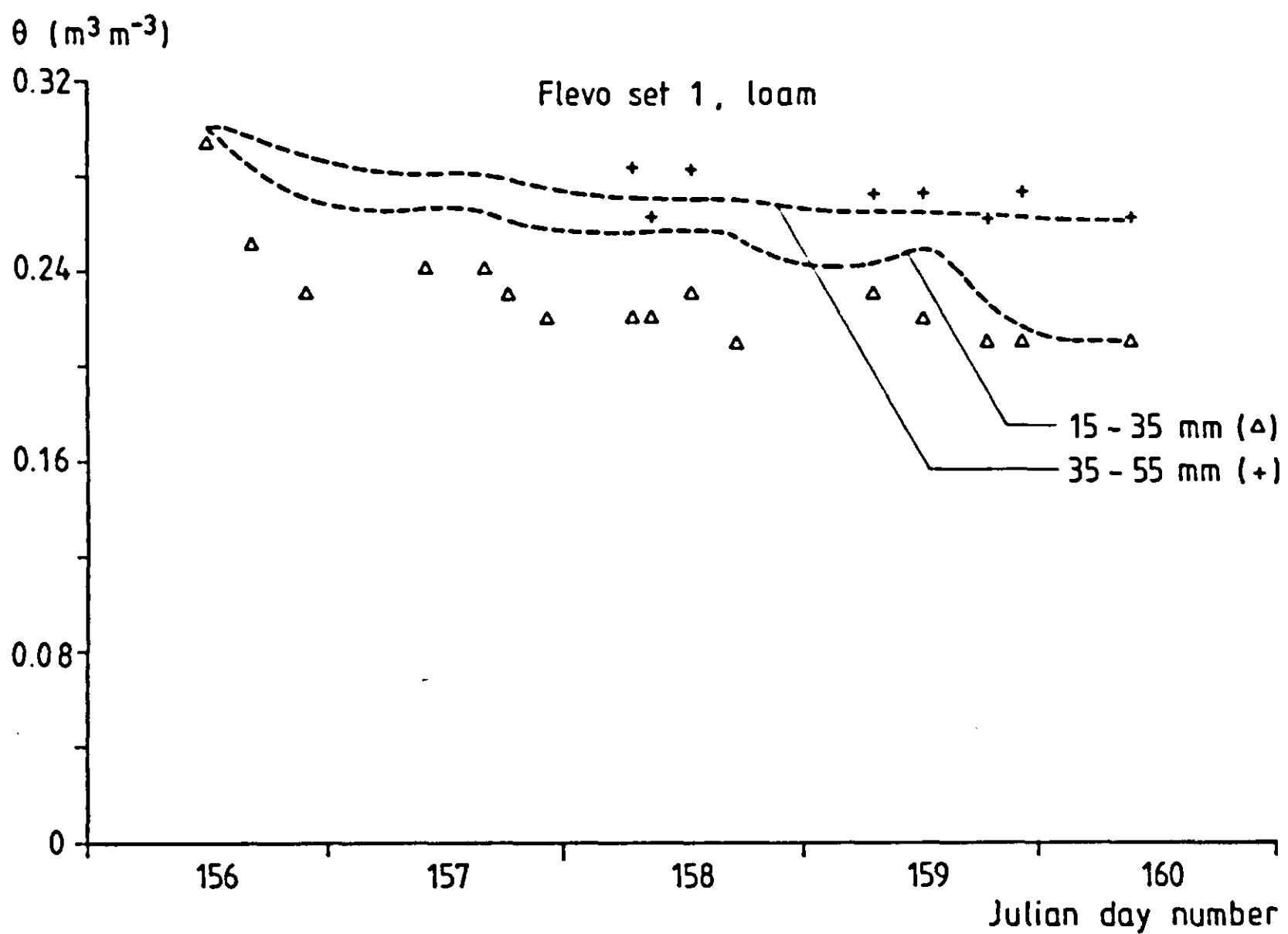
Figure 43. Soil moisture contents at two depths, loam, Flevo-1.

99

initial moisture content (up to 80%). For the layers 15-35 and 35-55 mm, the latter factor alone accounted for almost all the variance.

Soil water pressure, as measured in the field by a total of 28 tensiometers equipped with mercury manometers, clearly showed a diurnal periodicity, the suction decreasing during the day and rising at night. Since one would rather expect the suction to increase during daytime (because of evaporative drying), this behaviour called for a series of more detailed measurements under laboratory conditions, to ascertain the effect of temperature on the $p(\theta)$ relationship. The results of these measurements were shown in the previous chapter (Figure 30) and were condensed in Equation 89. Figure 44 is given here to merely illustrate the behaviour of topsoil water suction under field conditions, rather than to verify model predictions (SALSA ignores the effect of temperature on $p(\theta)$, as explained before). The broken line in Figure 44 represents the development of soil water suction, as calculated from Equation 89. In applying this equation, field-measured soil temperatures and water contents (both at the depth of the corresponding tensiometer cup, 0.04 m) were combined with laboratory-meas-
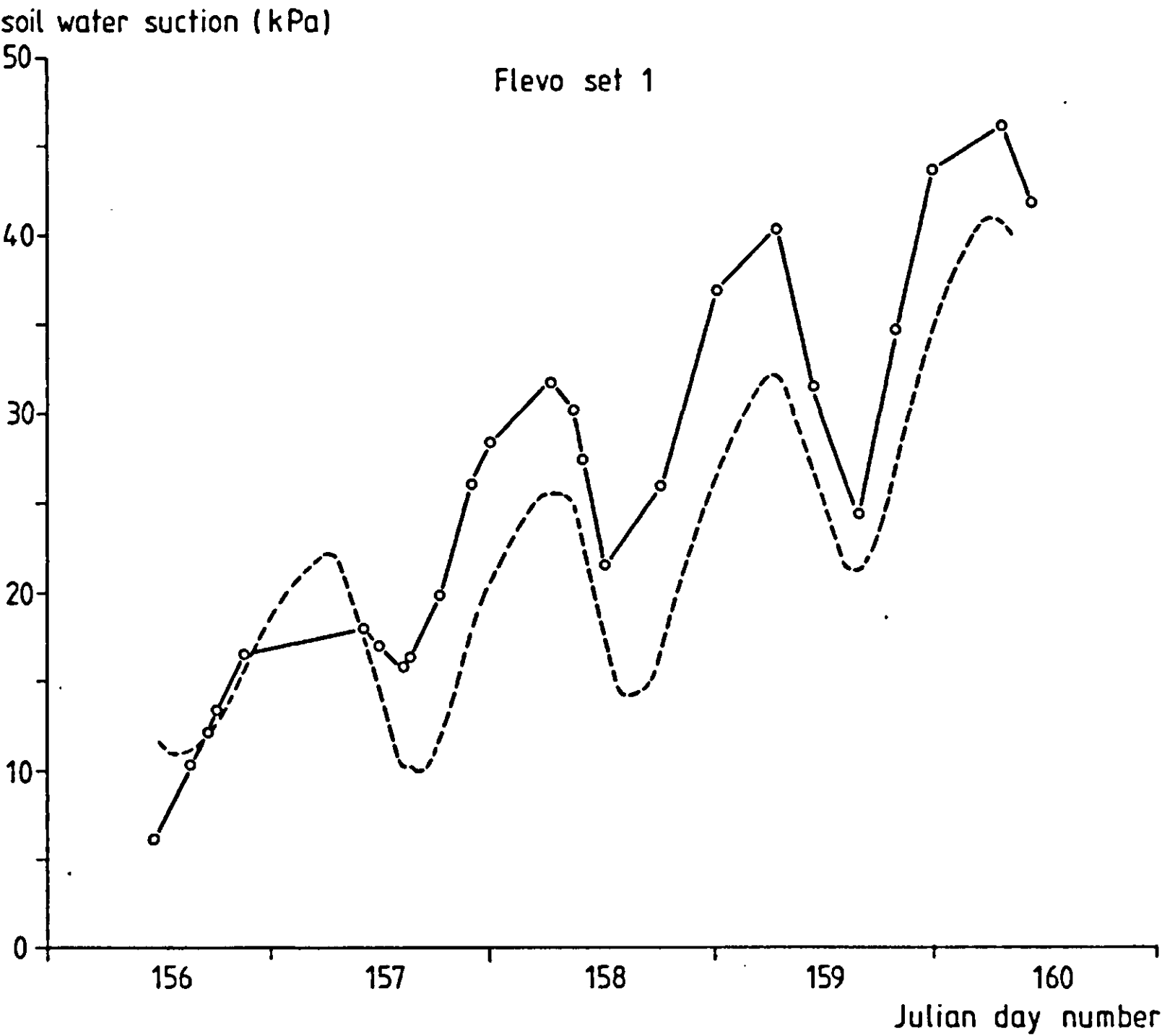
Figure 44. Soil water suction as measured by tensiometry in the field (——) at 4 cm depth on silt loam. The broken line shows the course, calculated on the basis of field-measured temperature and moisture content values, combined with the laboratory-measured $p(T)$ relationship (Equation 89) (undisturbed core samples).

100
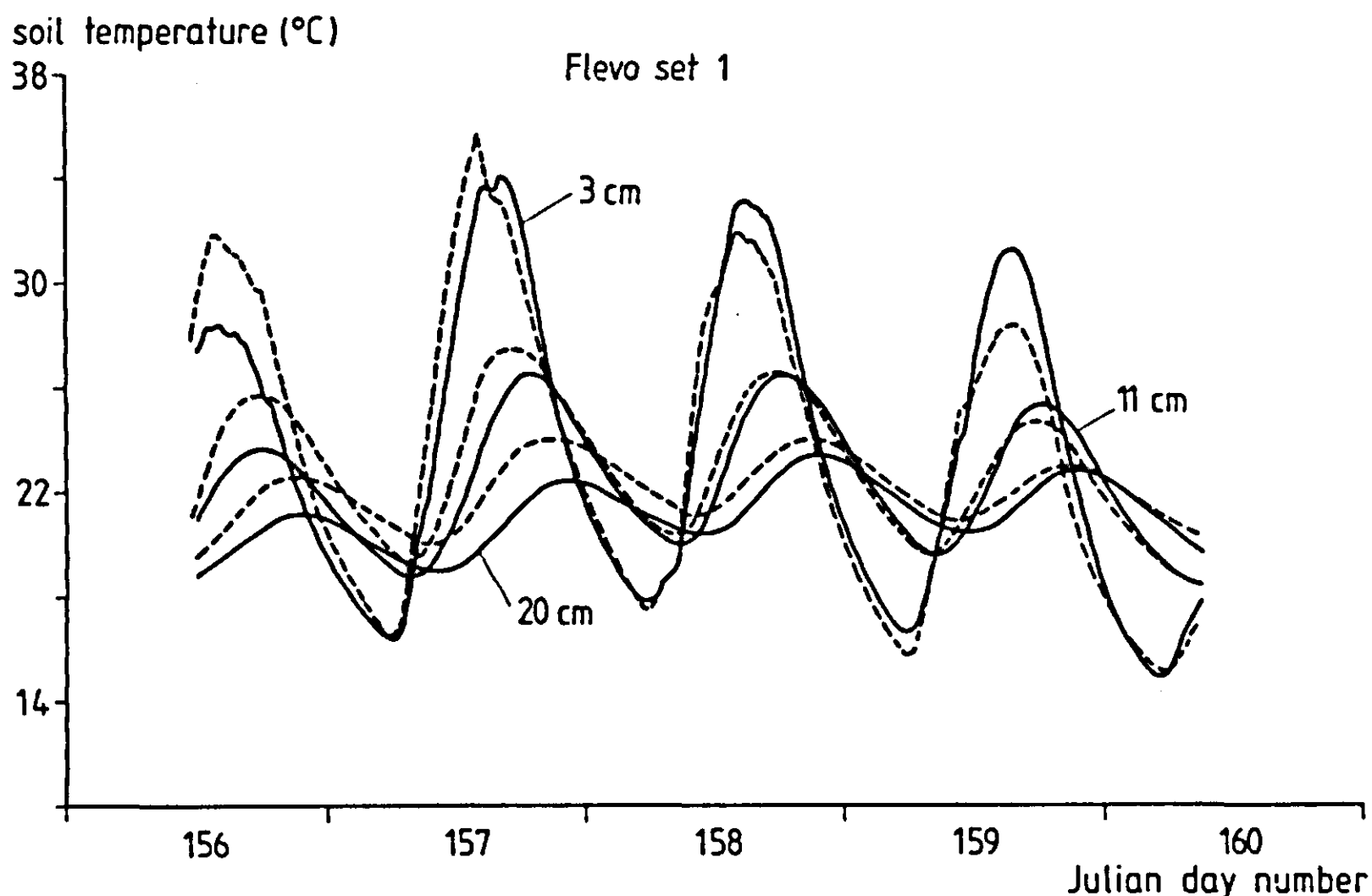
Figure 45. Measured (——) and simulated (---) soil temperatures at three depths, Flevo-1.

ured parameters *a*, *b* and *c* (undisturbed core samples of the same soil were used). It is concluded from Figure 44 that the observed diurnal pattern in tensiometer pressure may be ascribed fully to temperature fluctuations, without taking moisture migration into account.

Soil temperatures (Figure 45) appear to be predicted well at night, but not satisfactorily during daytime. Overestimation occurs at depths of 0.11 and 0.20 m. At 0.03 m depth, daytime temperatures are either over- or underestimated. On day 156, this discrepancy is associated with an overestimation of the soil heat flux, at the expense of the latent heat loss. For this particular day, *q* values for the soil temperature are unacceptably high (Figure 46). The reason for this behaviour can only be speculated, at this stage.

5.1.3 Flevo-2

The weather was very changeable during the Flevo-2 experiment (see Section 4.4). Over a five-day period, cloudy and rainy days alternated with days exhibiting intermittent sunshine. As a result, surface energy fluxes and soil conditions show strongly fluctuating patterns; a specific feature for this data set is the course of the surface soil heat flux, which shifted frequently during daytime from negative to positive and vice versa.

Tables 11 and 12 again list the input and output variables, along with the associated error intervals. The following options were used in running the model for the Flevo-2 case:

101
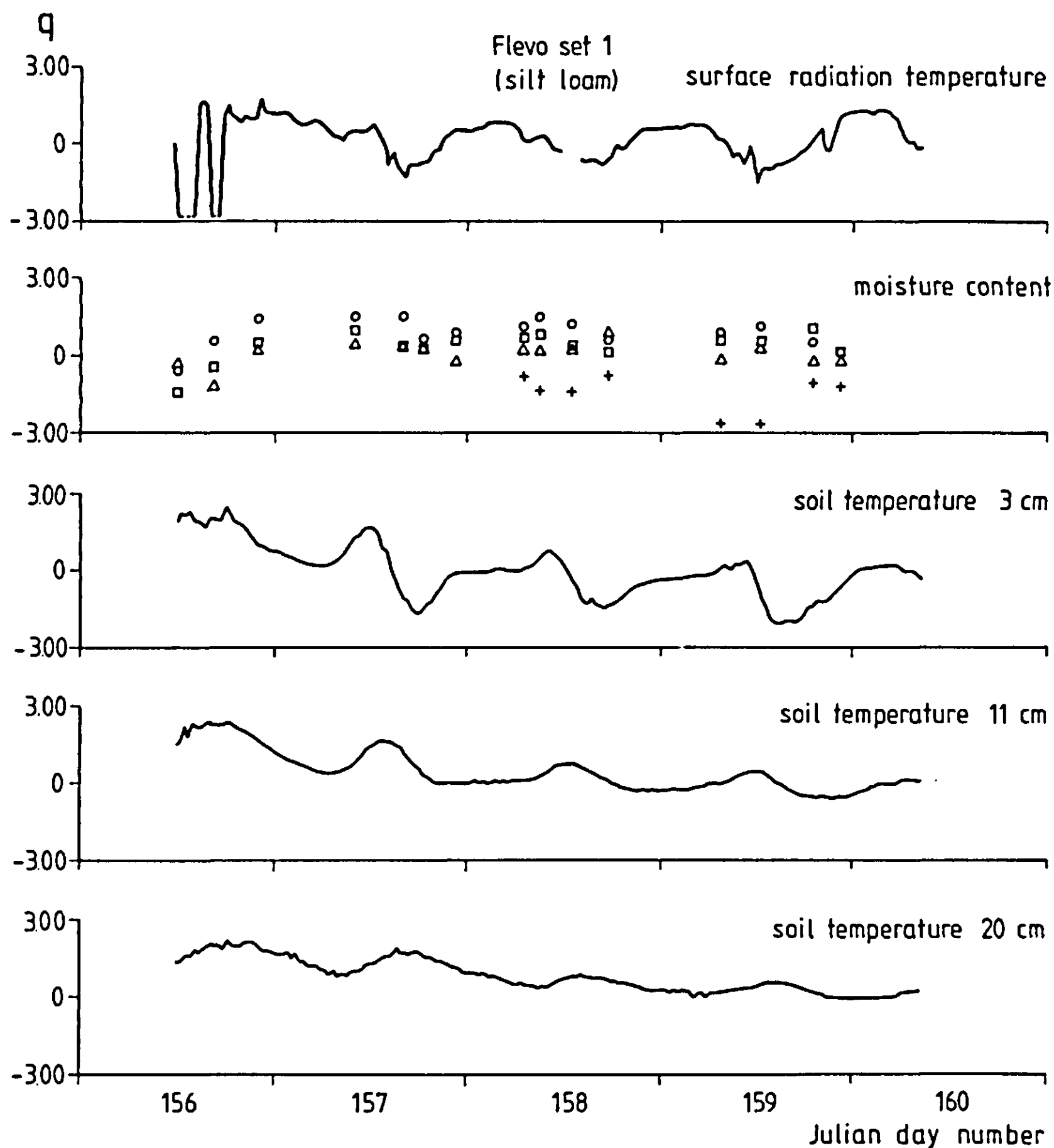
Figure 46. Values of q for the soil state variables, Flevo-1.

SWBLD   = 0 (no boundary layer simulation)
SWMFLP = 0 (hydrology formulated in terms of $K - p$)
SWKTB   = 0 (hydraulic conductivity function specified in van Genuchten parameters)
SWGRAV = 1 (gravity term included in water flow equation)
SWCHTB = 1 (thermal conductivity specified in table)
SWRNET = 0 (net radiation is not used as boundary condition)

The occurrence of rain during several days prescribes that the gravity term be taken into account. In the simulation run, the measured total of 33 mm precipitation was distributed uniformly over the 41-hour time span during which it was registered, resulting in an average flux of 0.81 mm h^{-1}. Apart from the above, the treatment of this data set was identical to the procedure described

in the previous case. Because of the predominantly moist conditions, very little difference was found between the behaviour of loam and silt loam soils; therefore only the results for the silt loam are presented.

Figures 47-50 show the surface fluxes as measured and simulated, and Figure 51 depicts the corresponding courses of the evaluation variable q. The developments in the soil state variables can be seen from Figures 52-55, whereas Figure 56 gives the $q(t)$ series as calculated for the various output variables. It is emphasized that all results shown and discussed are the output of one particular simulation run, with all inputs specified according to Table 11, i.e. within the limits given in that table.

Evaluation of flux predictions

The net radiation for this data set is predicted very well, with the exception of day numbers 176-177 (Figure 47); this discordance is associated with an increase in soil albedo which occurred because of surface drying, but which was not effectuated in the simulation because surface drying was not predicted correctly. The latter will be discussed below. Note that the night-time values are also described accurately.

For the soil heat flux, the same applies as was stated for the Flevo-1 data set. Fluctuations in surface temperature and soil heat flux on the scale of one hour are more pronounced in the Flevo-2 case. Therefore, $q(t)$ reaches extreme peak values. Some overestimation seems to occur during the first half of the day, whereas during the second half, the soil heat flux is underestimated.

Finally, a comparison with the Flevo-1 data clearly shows the expected relation between soil heat flux and net radiation during night-time as an interesting fea-
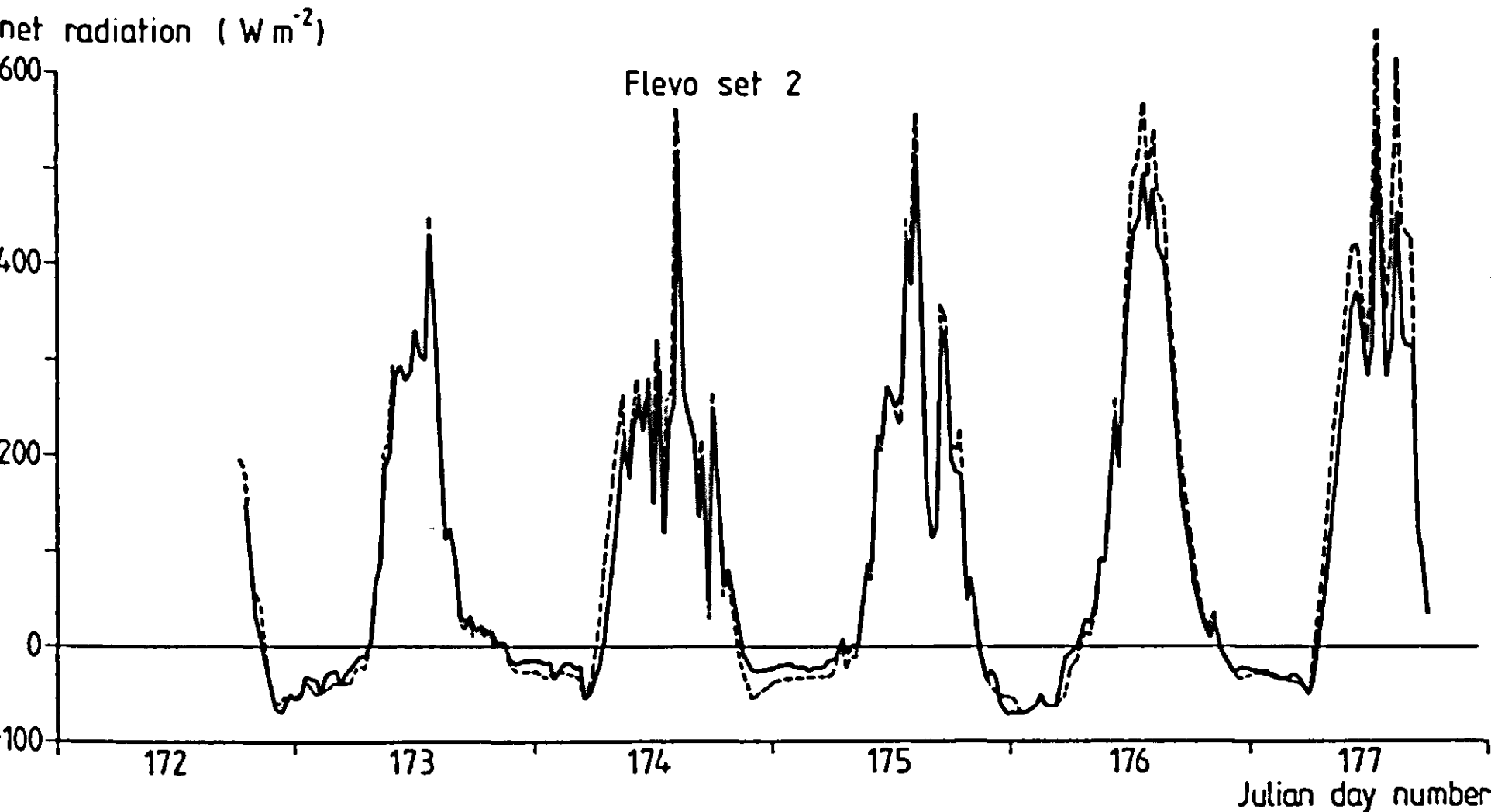
Figure 47. Measured (——) and simulated (---) net radiation, Flevo-2.
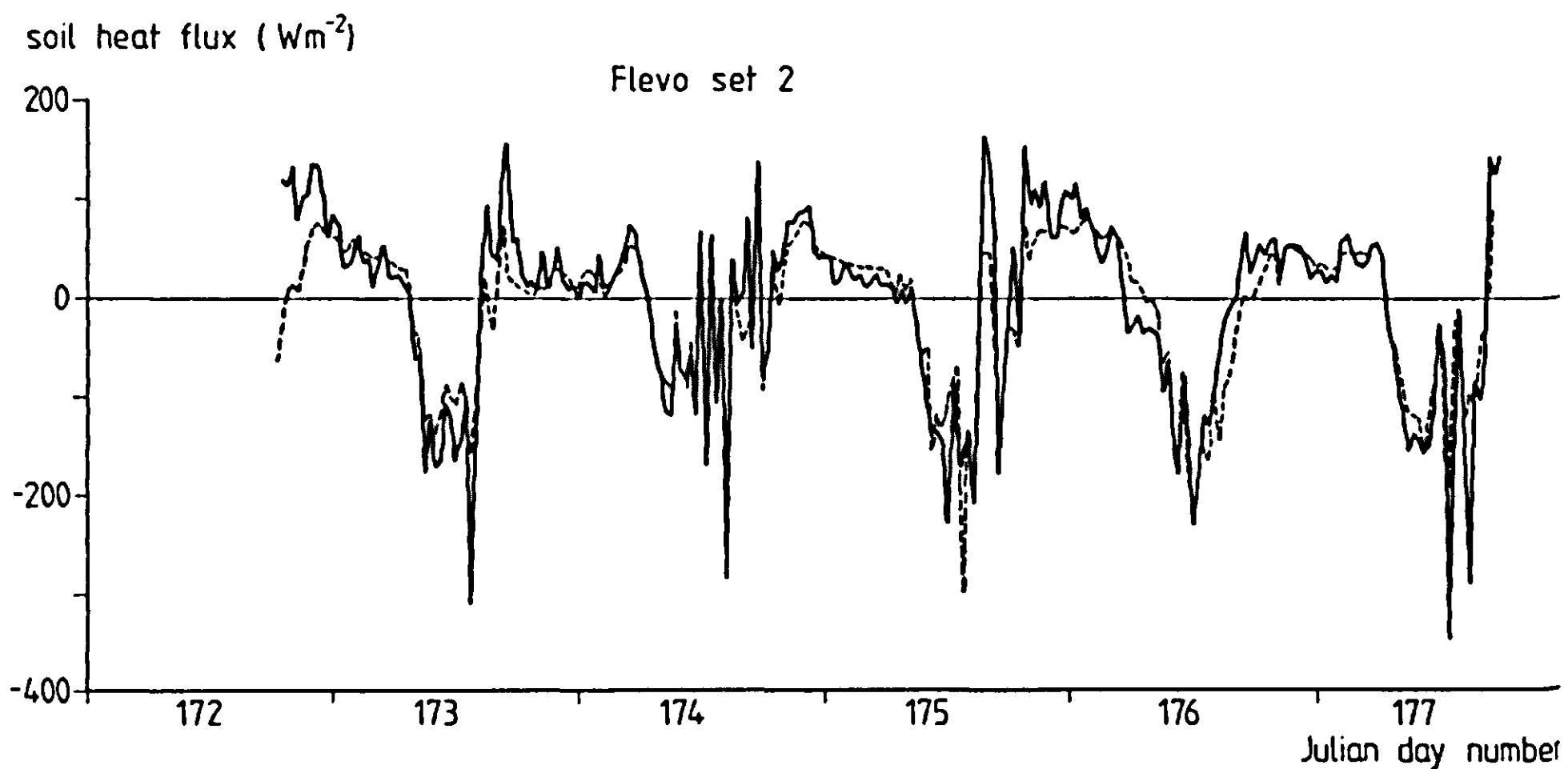
Figure 48. Measured (——) and simulated (---) soil heat flux, Flevo-2.
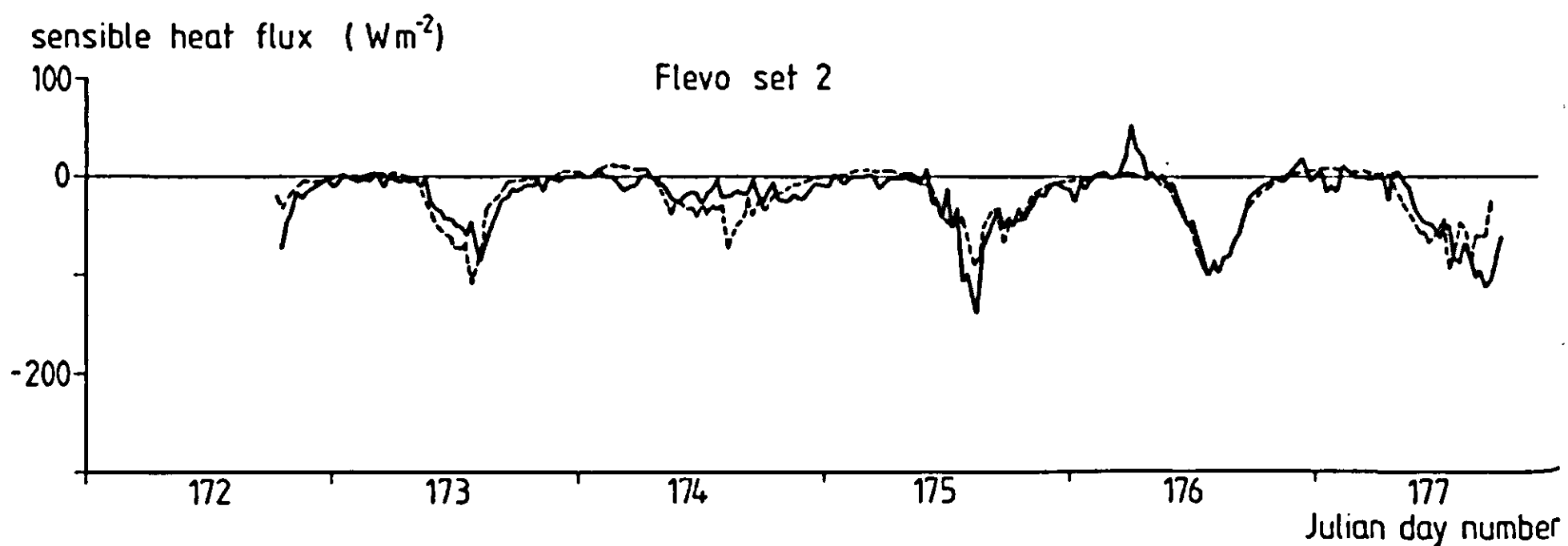
Figure 49. Measured (——) and simulated (---) sensible heat flux, Flevo-2.
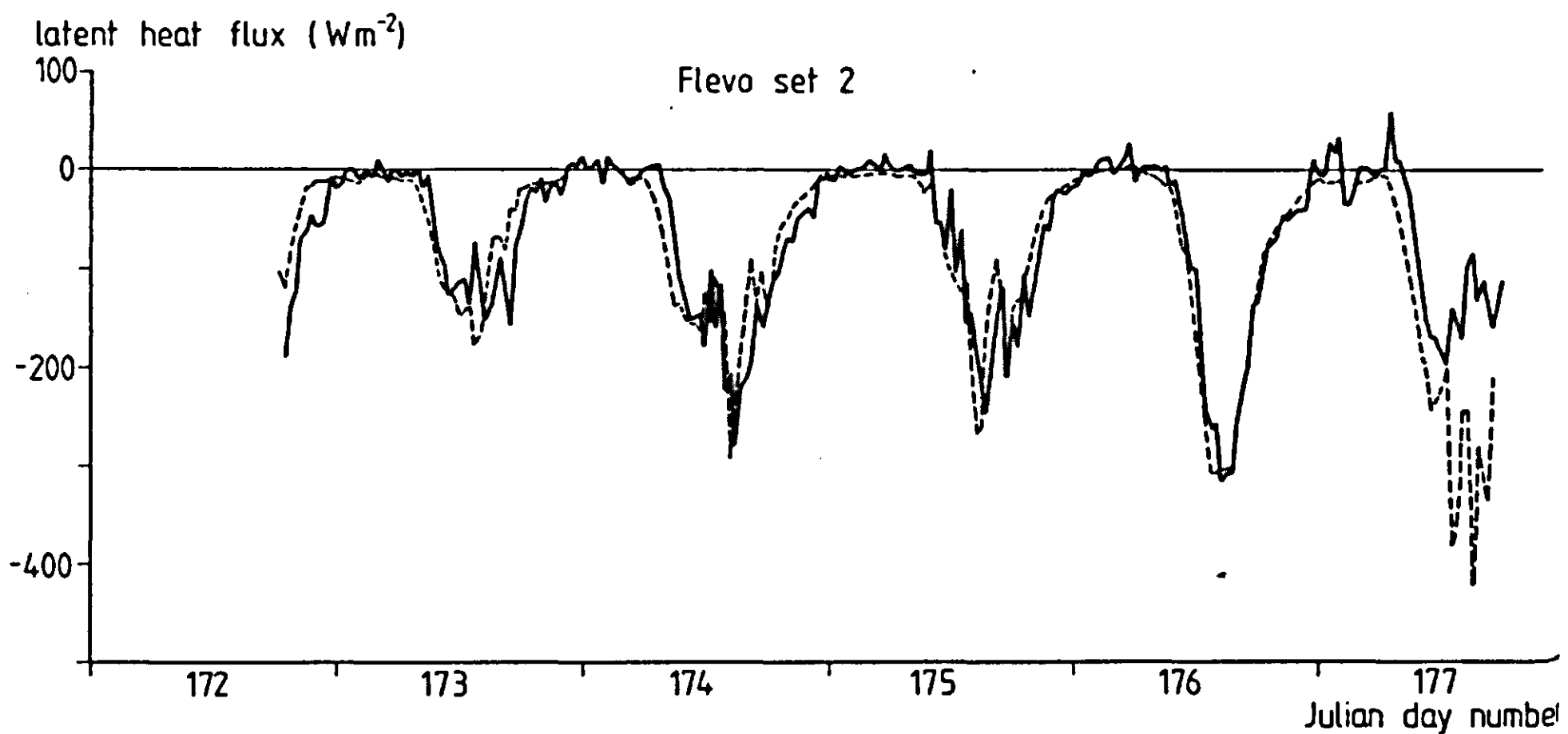
Figure 50. Measured (——) and simulated (---) latent heat flux, Flevo-2.
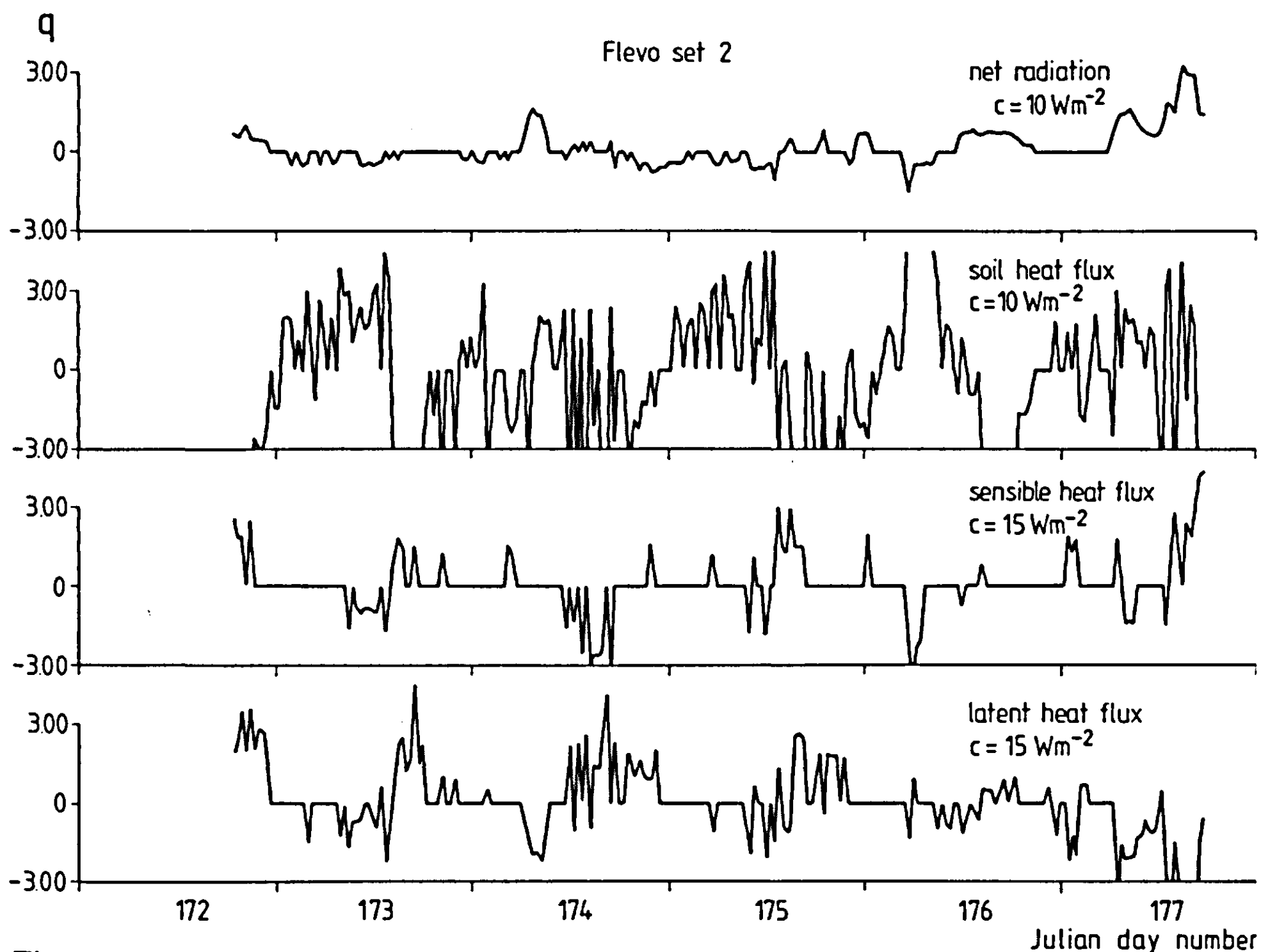
Figure 51. Values of q for the surface fluxes, Flevo-2.

ture, radiation being maintained by soil cooling.

The latent and sensible heat fluxes (Figures 49 and 50) are predicted accurately, again with the exception of day 177. As stated earlier, the wet conditions prevented differences in topsoil behaviour, associated with texture, from becoming evident. The courses of $q(t)$ for the sensible and latent heat fluxes are considered acceptable, although a small phase shift seems to occur.

Evaluation of state variable predictions

Predicted radiation temperature closely follows the measured curve (Figure 52), although the fluctuations at the half-hour scale are slightly smaller. The deviation observed for the night 175-176 might have the same causes as discussed for the Flevo-1 data set. It is not clear why radiation temperature was overestimated on day 176. An underestimation caused by too slow surface drying would be expected, as observed for day 177.

The moisture contents in the top 15 mm (Figure 53) were generally overestimated. Rain occurred on days 173-175, during which no measurements of moisture content were made. The hydraulic soil properties as measured and used for this simulation run were taken from the top 5 cm layer. Within this layer, however, changes of soil properties with depth may cause the predictions

105
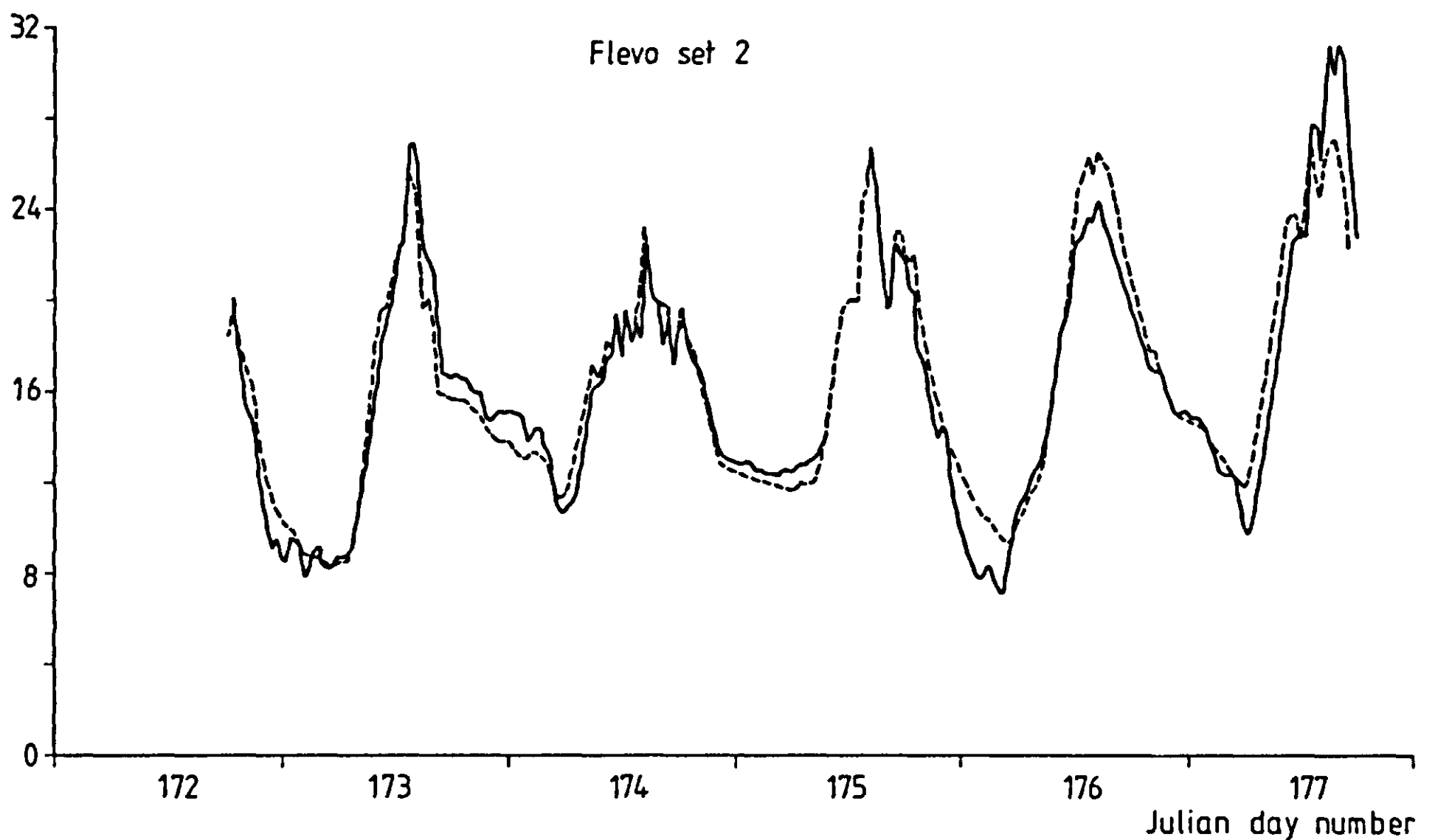
Figure 52. Measured (——) and simulated (---) surface radiation temperature, silt loam, Flevo-2. For the loam, almost identical courses were measured and simulated.
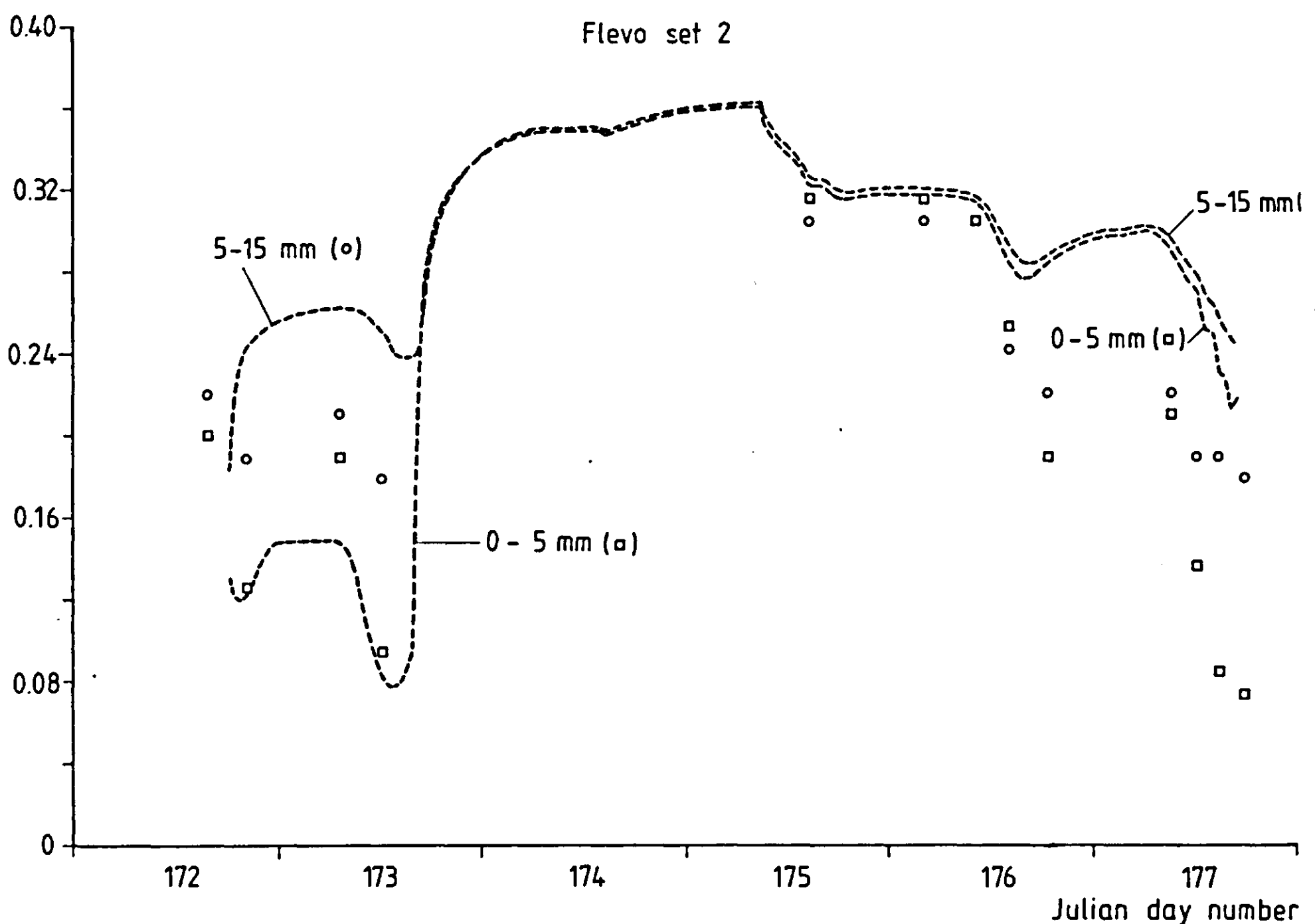
Figure 53. Soil moisture content at two depths, silt loam, Flevo-2. Symbols represent observations, broken lines simulation results. The loam soil showed similar developments for this data set.

106
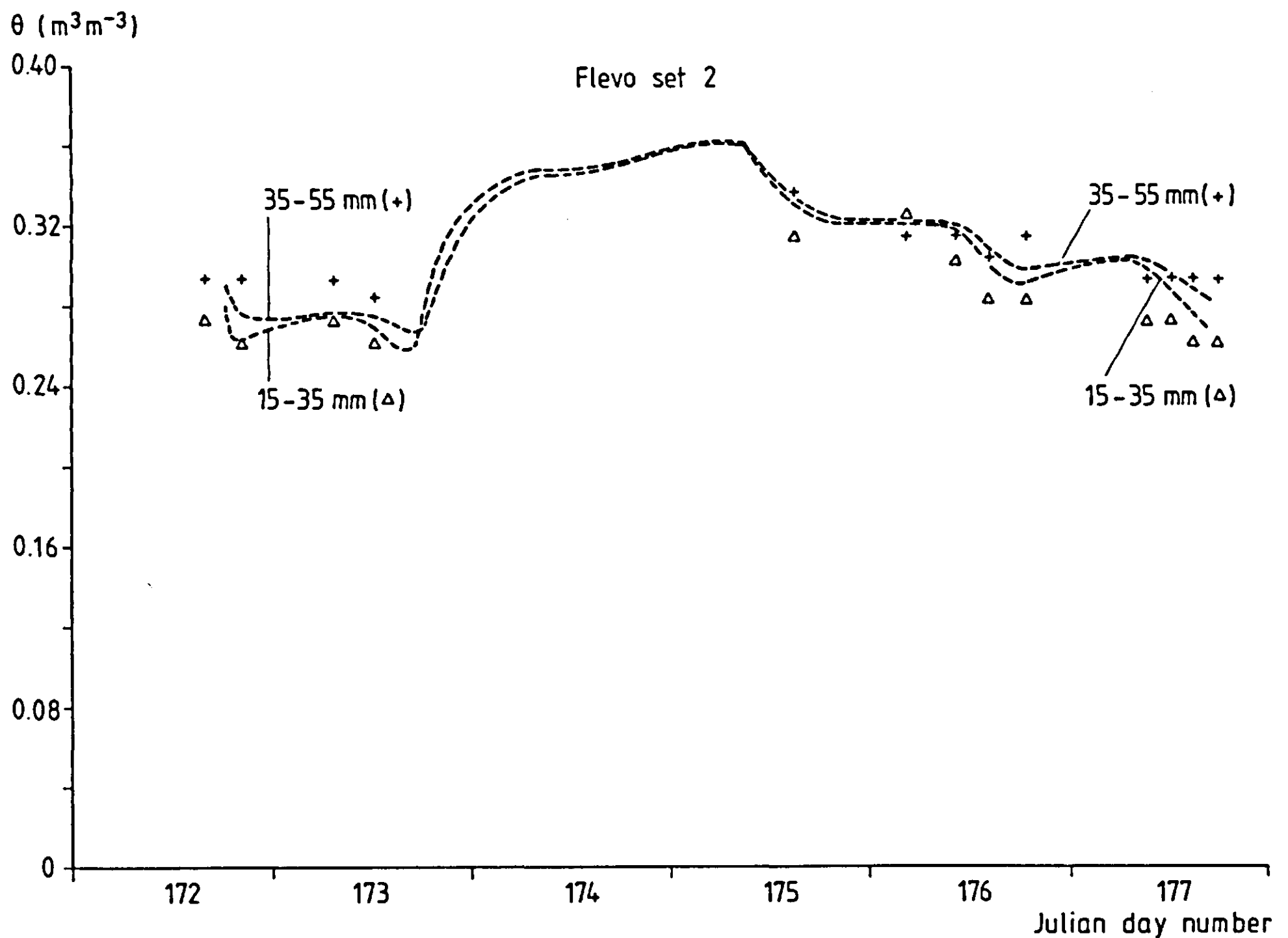
Figure 54. Soil moisture content at two depths, silt loam, Flevo-2. The loam soil showed similar developments for this data set.
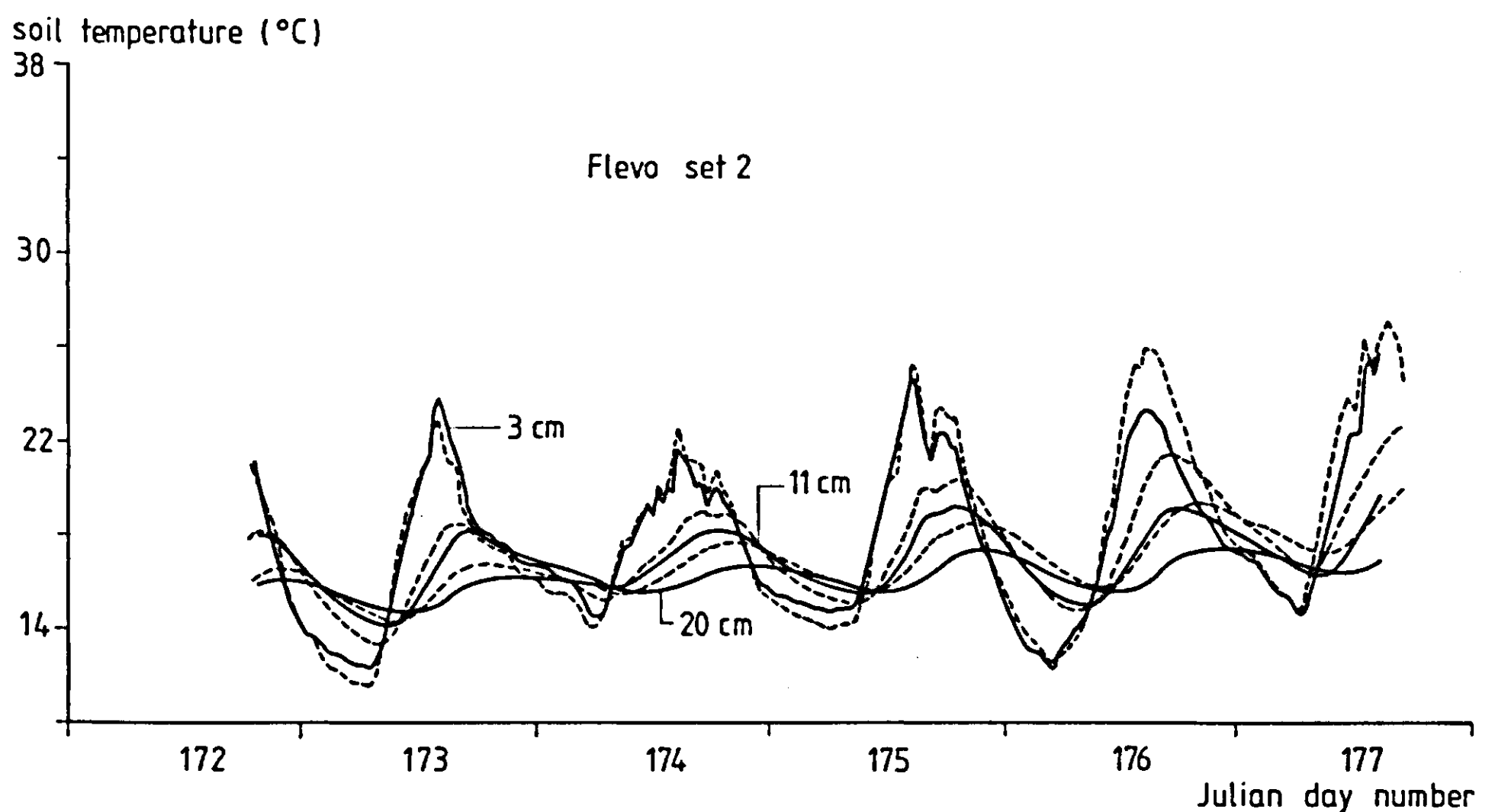
Figure 55. Measured (——) and simulated (---) soil temperatures at three depths, Flevo-2.
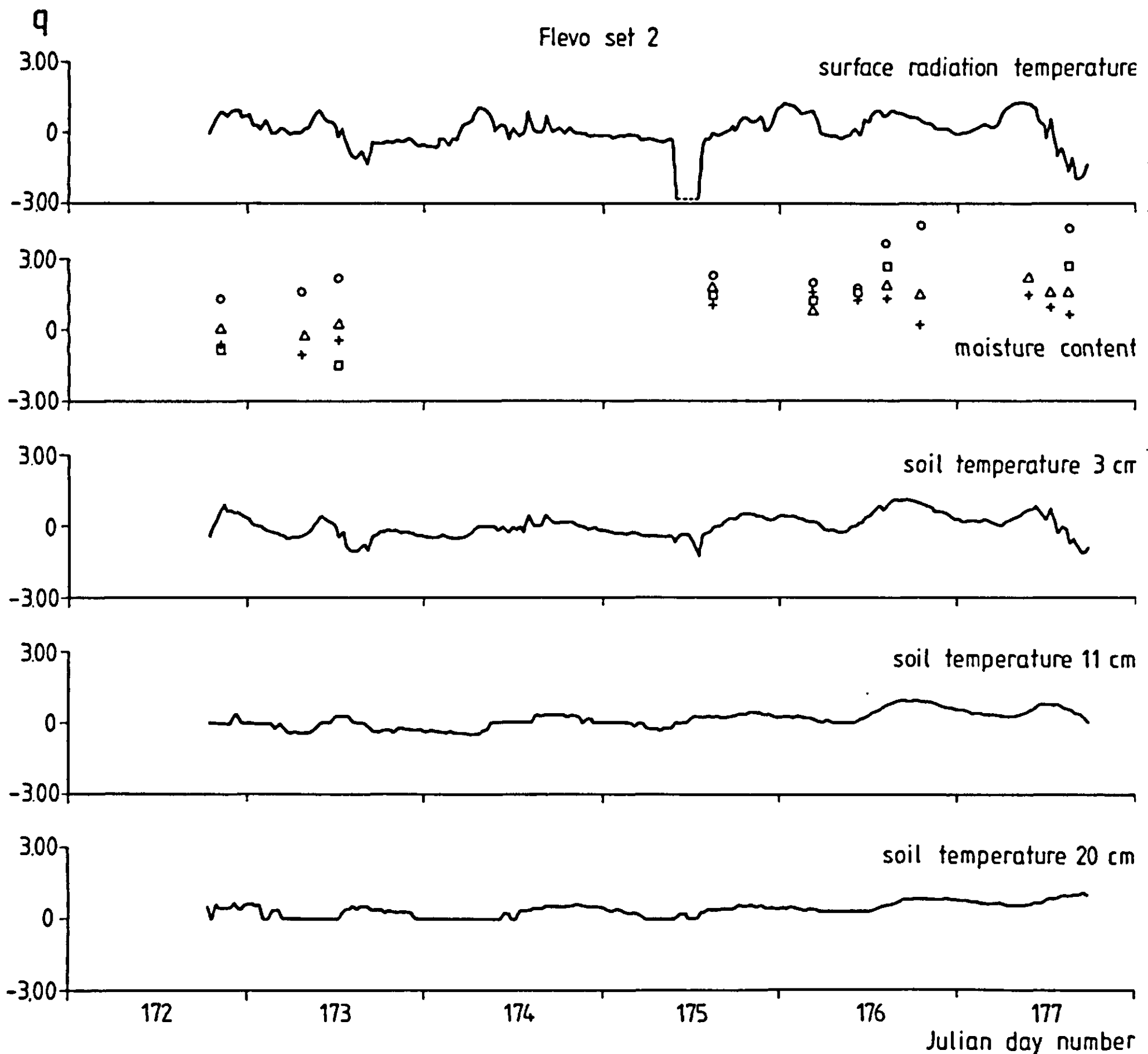
Figure 56. Values of q for the soil state variables, Flevo-2.

of moisture content at 15-55 mm to be a few per cent above or below the actual value. Such deviations have a strong effect on the surface-drying process, which apparently was not simulated correctly after the rain had ceased. Even when the uncertainties in all the measurements are taken into account, it must be noted that the simulated results differ from the observations, as can be seen from Figure 56. It must be concluded that for situations where rain and surface drying are intermittent, a good description of the movement of water in the top-soil requires extremely detailed soil information. For operational purposes, such information will rarely be available.

The soil temperatures were described satisfactorily, with q remaining close to zero for all depths taken into consideration (Figures 55 and 56).

108

5.2 Evaluation of simulated boundary layer development

Since no suitable data sets were available for a validation of the complete SALSA model (option A), the performance of the 'atmosphere component' of the model could only be tested to a limited extent. Some features of predicted developments will therefore merely be discussed qualitatively. It may be recalled that the equations expressing the atmospheric transport processes and the production rates of kinetic energy are identical to those used by Nieuwstadt & Driedonks (1979) in their boundary layer model (with the exception of the surface exchange coefficients). The latter model was validated with experimental data for the case of nocturnal boundary layer development, so the atmospheric component of SALSA has been validated to some extent at least, although for a different context (i.e. not including soil processes).
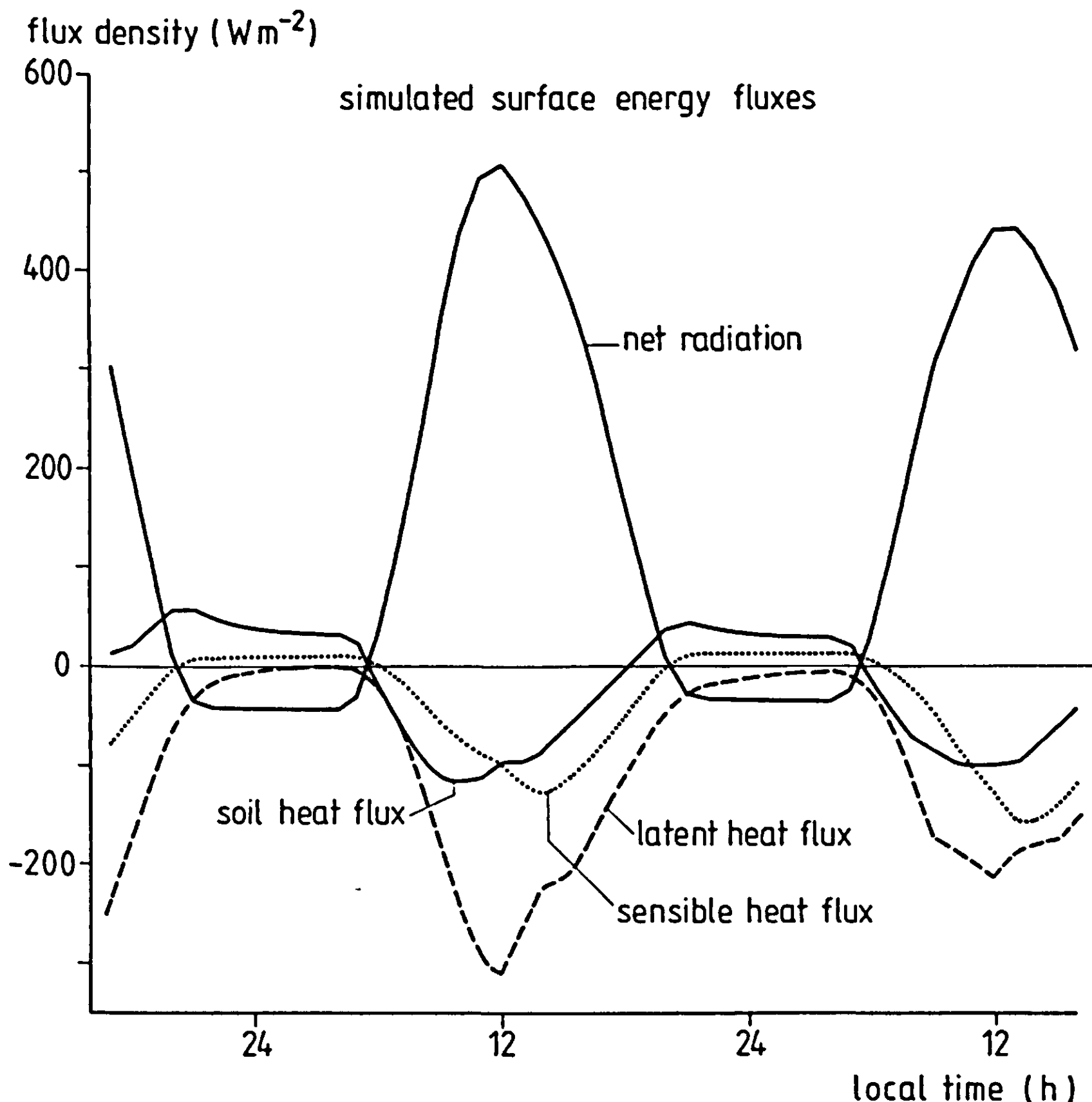
Figure 57. Surface fluxes as simulated by SALSA, Option A. For the combination of system parameter values chosen here, see text.

All the results presented in this section were generated by one single simulation run, unless mentioned otherwise. Conditions for this run were a geostrophic wind speed of 10 m s^{-1}, a very smooth surface ($z_0 = 0.1$ mm) and an initial potential temperature of 20 °C throughout the atmosphere. Initial conditions of wind speed and specific humidity were obtained by 'idling' for 48 h at constant surface temperature and surface humidity conditions. Initial conditions for the soil state variables were taken from day 156, Flevo-1 set. Soil properties were also taken from that data set (silt loam).

Simulation then started at the end of the afternoon (16.00 h) and proceeded to cover a period of 48 h. For global radiation, the measured data of day 159, Flevo-1 set, were used (Figure 11). The atmosphere was divided into 11 layers, doubling in thickness from the surface upward, with a thickness of 3 m for the first compartment.

Figure 57 depicts the terms of the surface energy balance, and Figure 58 shows the simulated conditions at screen height. The results are feasible if compared qualitatively with the observations presented in Section 4.5. Calculated
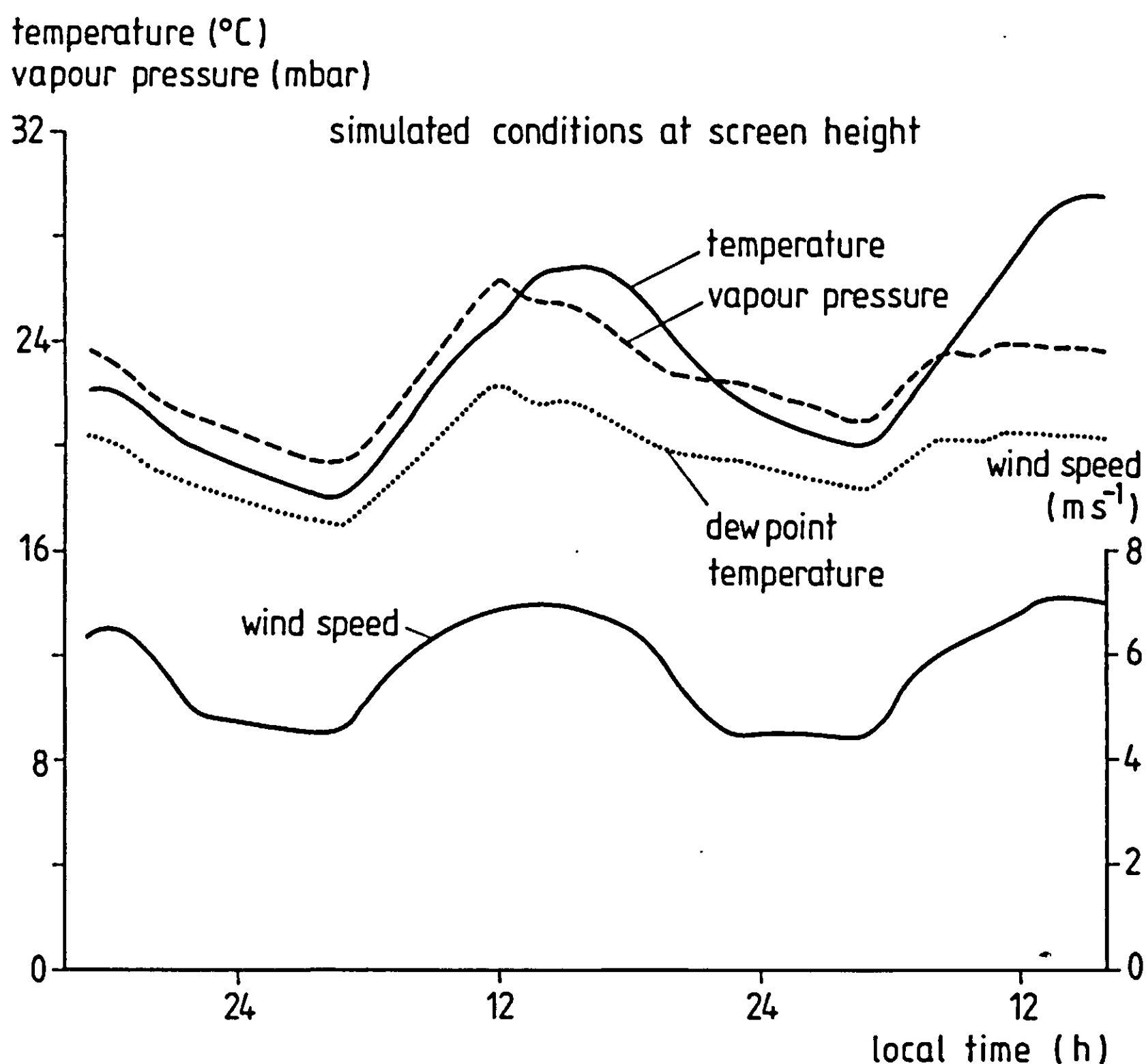
Figure 58. Atmospheric conditions at 1.5 m above the surface as simulated by SALSA, Option A.

110
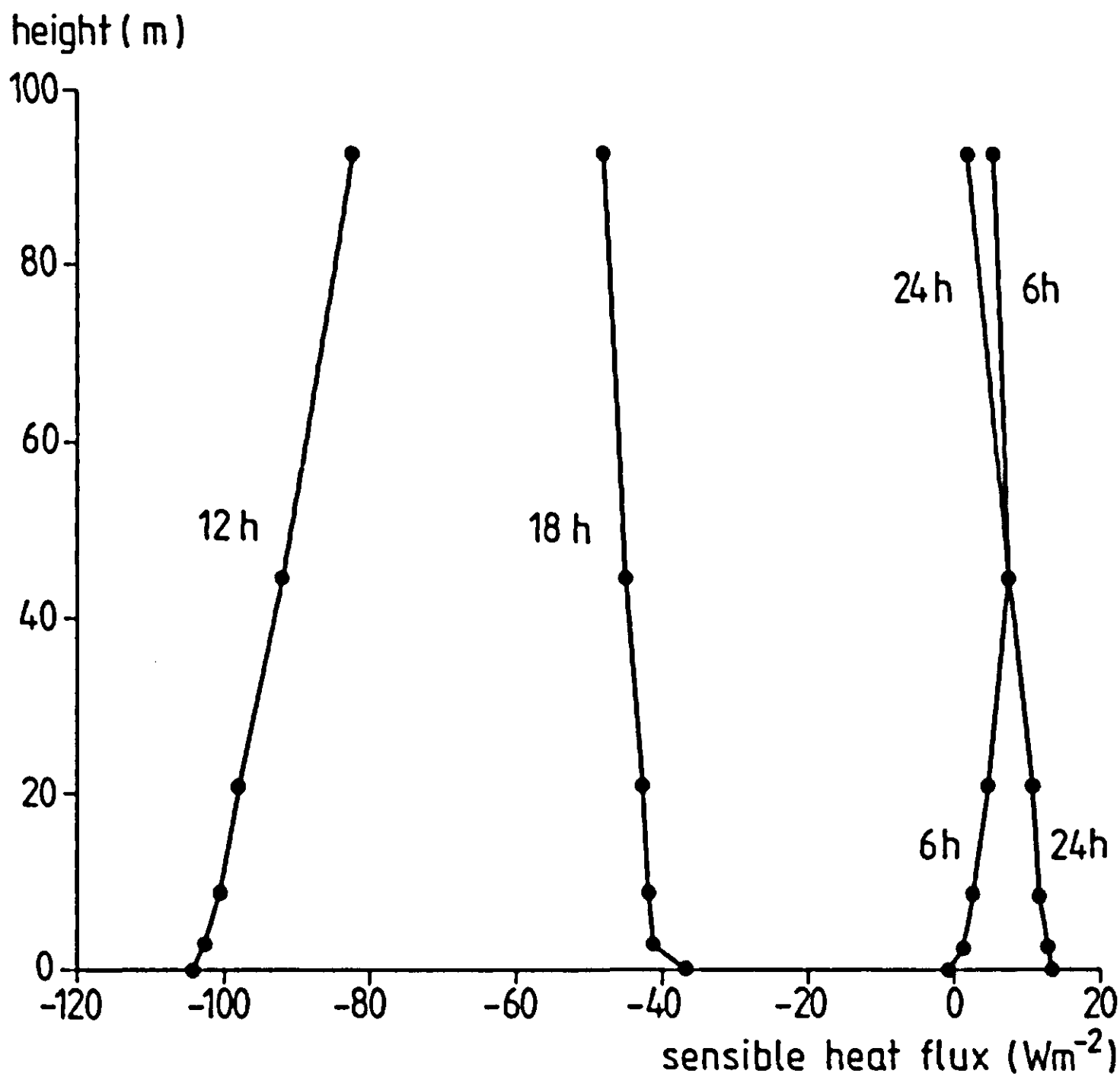
Figure 59. Profiles of the sensible heat flux in the lower atmosphere, as simulated by SALSA Option A for different times of the day.

dewpoint temperature was added here as an extra check on the behaviour of simulated conditions at 1.5 m. Predicted developments in this comparatively conservative quantity are interpreted as reasonable.

Figure 59 shows the sensible heat flux in the lower atmosphere at various times of the day. In the mixed layer, fluxes should be approximately linear with height; this appears to be the case, except for the lower 15 m. Below that height, the heat flux divergence predicted at noon, as seen from the graph, accounts for a maximum rise in air temperature of about 1 K h^{-1}, which is viewed as a realistic value for this time of the day. The normalized flux of momentum, τ_x/ρ (see Equation 34), is presented in a similar way in Figure 60, and a more or less linear relation, as is generally expected, is found for this case too.

The development of the potential temperature profile is demonstrated in Figure 61. This figure illustrates the appearance of the nocturnal temperature inversion, which subsequently disappears in the morning hours. The difference in boundary layer height between day and night can also be seen from this graph. The increase in maximum temperature at Stevenson screen height – observed on the third day as compared with the second day – is attributed to the drying of the soil surface. The corresponding developments in specific humidity

111
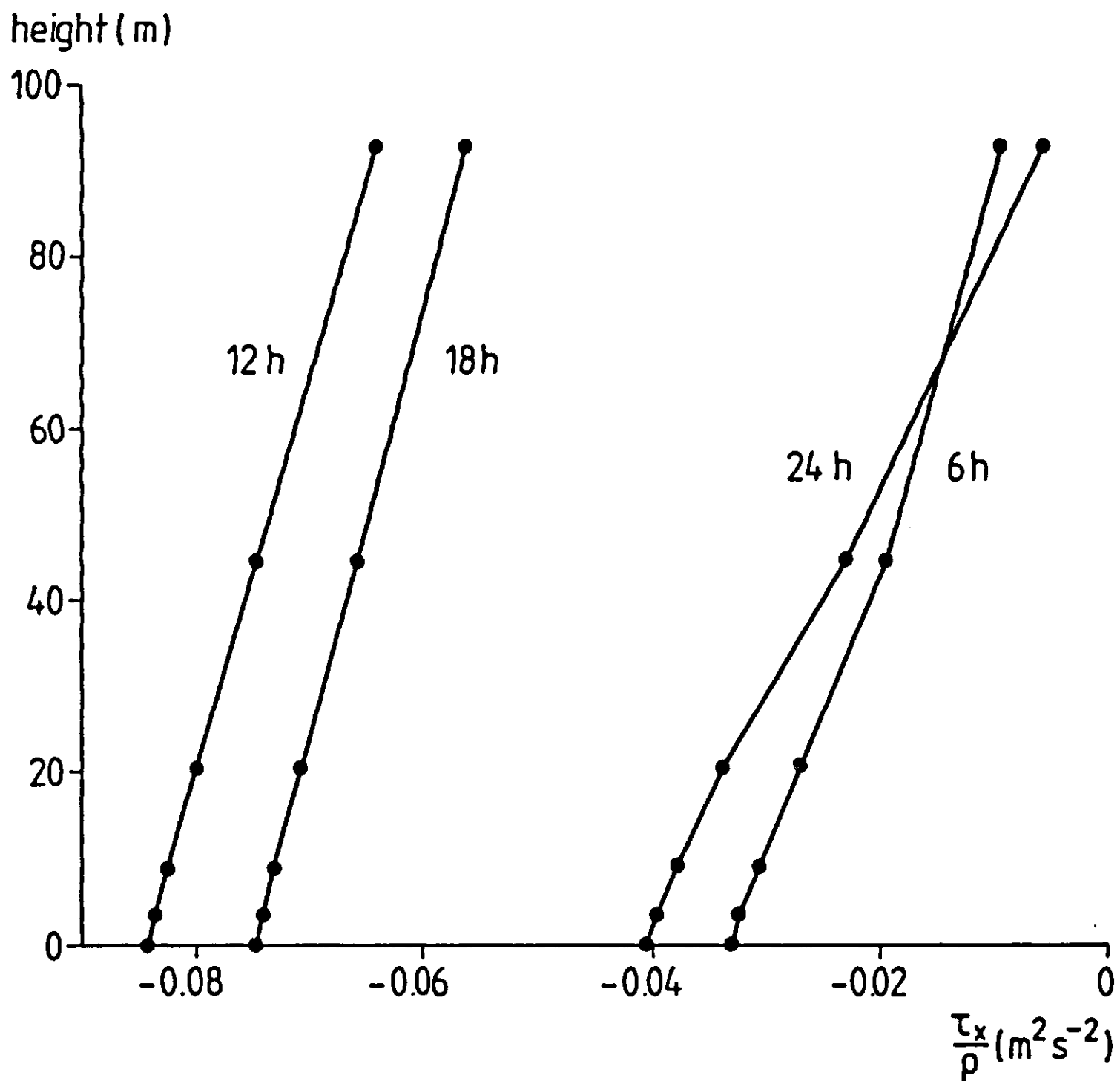
Figure 60. Profiles of the normalized flux of momentum in direction x, as simulated by SALSA Option A for different times of the day.
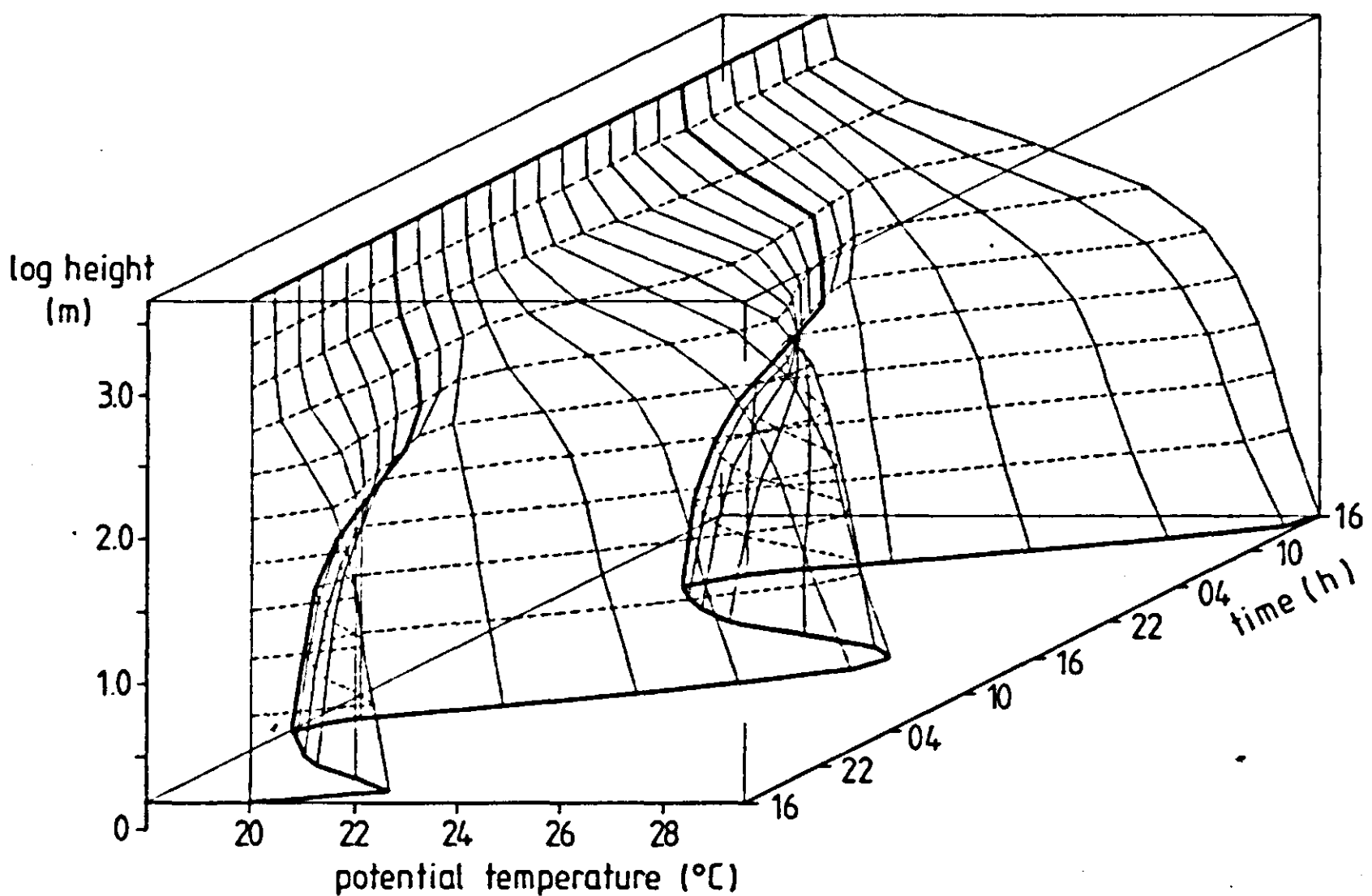
Figure 61. Development of potential temperature in the lower atmosphere, as simulated by SALSA Option A.
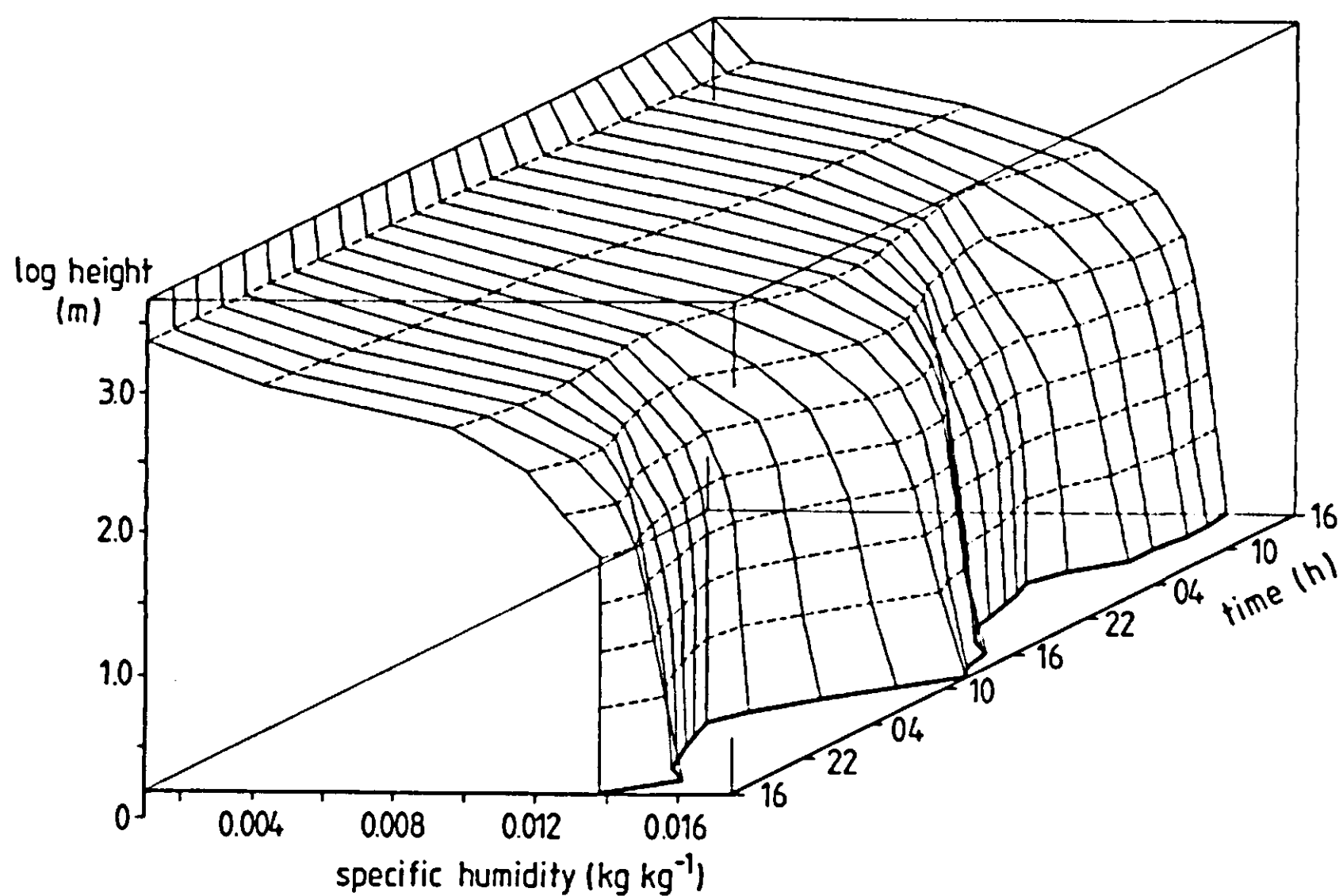
Figure 62. Development of specific humidity in the lower atmosphere, as simulated by SALSA Option A.
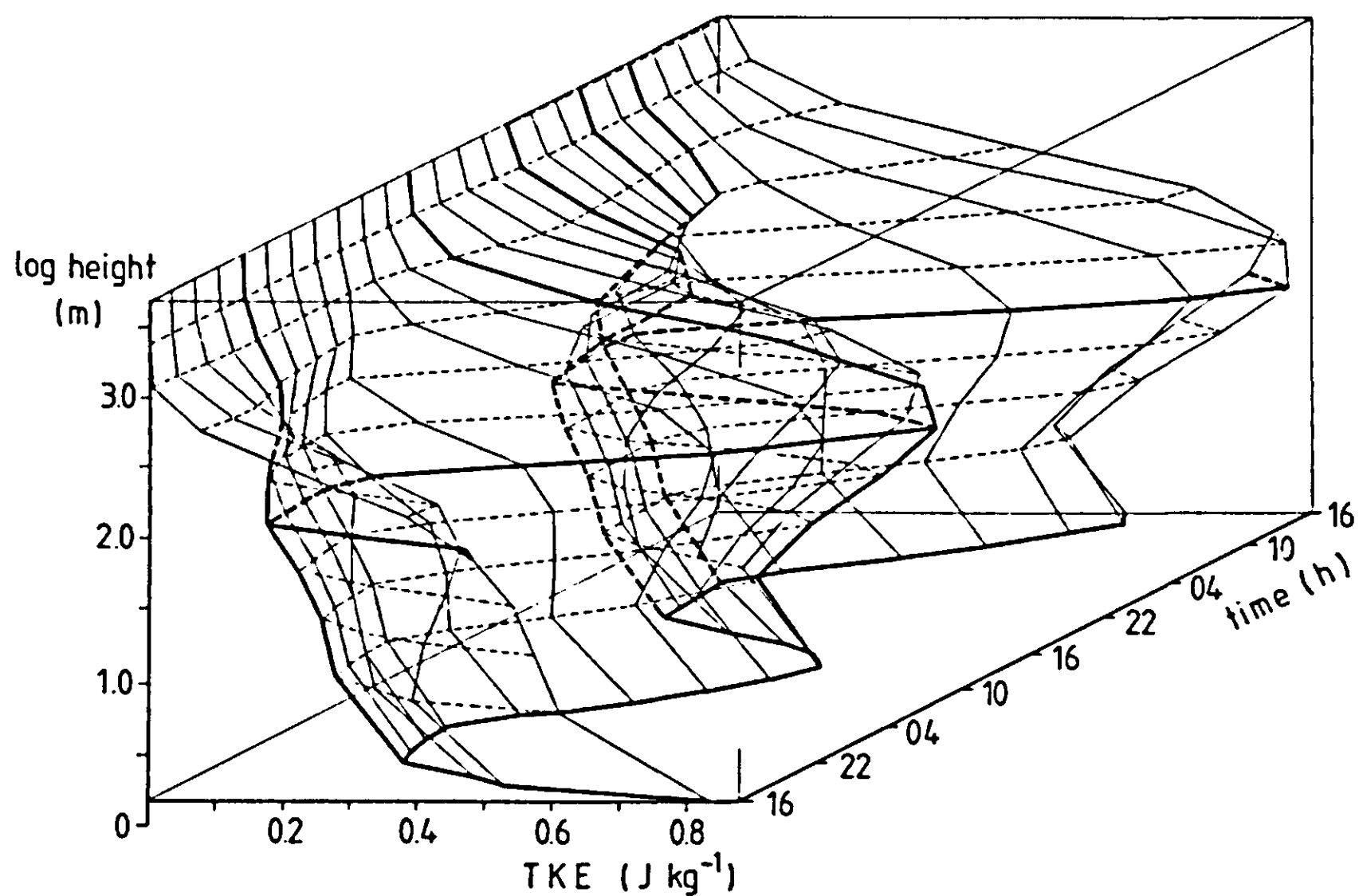
Figure 63. Development of turbulent kinetic energy, as simulated by SALSA Option A.
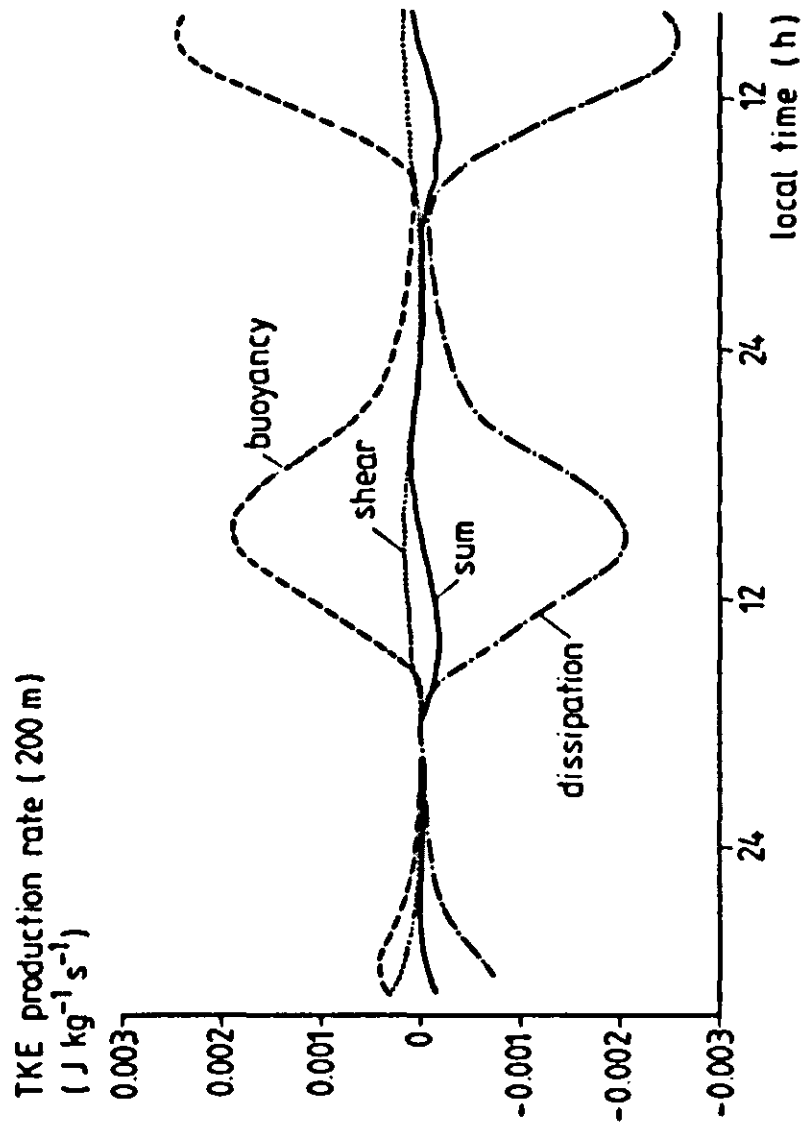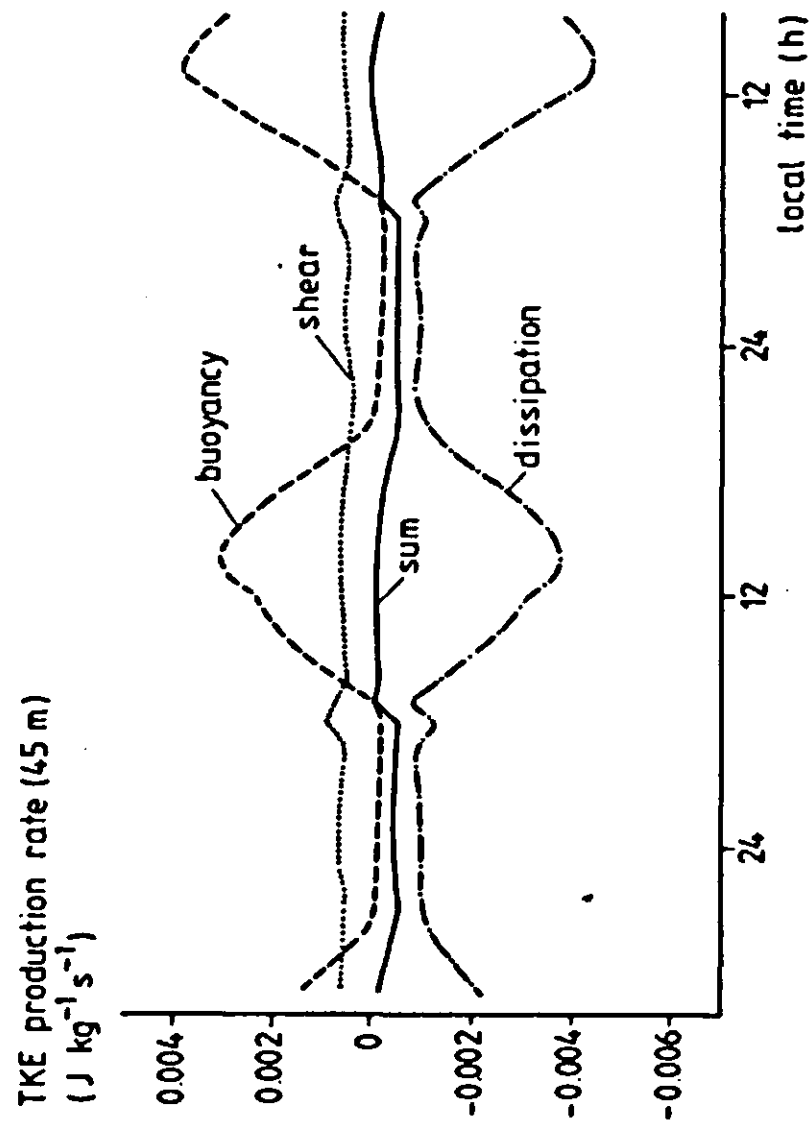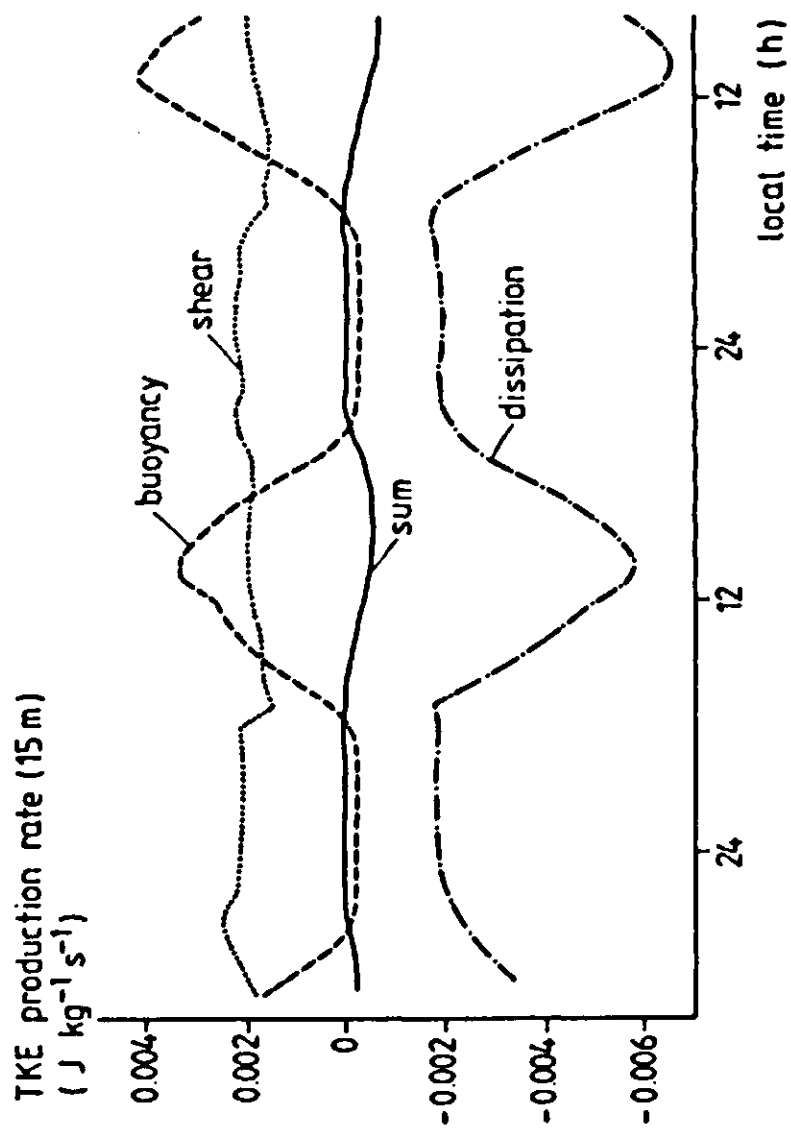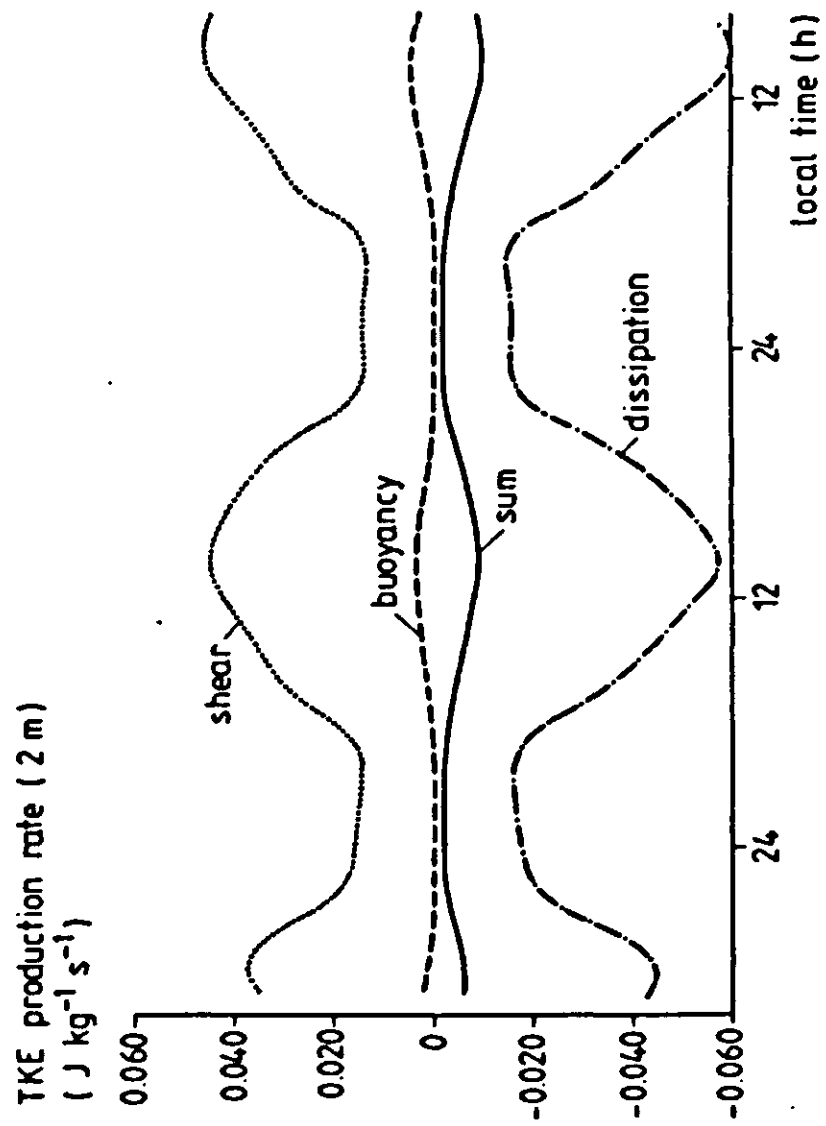
Figures 64-67. Simulated production rates of turbulent kinetic energy at different heights in the atmospheric boundary layer.

are shown in Figure 62. The profiles of turbulent kinetic energy for the same simulation run are shown in Figure 63.

The courses of turbulent kinetic energy production terms at different fixed heights are depicted in Figures 64-67. It can be observed that the sum of the various terms is relatively close to zero during most of the time at all four heights, which is in accordance with general experience.

In a more detailed study of model sensitivity, the effects of soil processes on conditions in the lower atmosphere, and vice versa, will be discussed in the next chapter.

6 Sensitivity analysis

The term 'sensitivity analysis' has been used in the literature on modelling to indicate a wide range of activities related to the study of model or system behaviour. This chapter will focus on aspects of system sensitivity that may be relevant to the interpretation of thermal infrared imagery. A number of processes and parameter effects will be treated in detail, but the analysis is by no means complete or exhaustive. It is merely an illustration of how simulation models can elucidate system dynamics, in this particular case reflected in the course of surface temperature that is of interest to remote sensing.

First, a brief introduction, in Section 6.1, will discuss some of the 'sensitivity indicators' that may be used in sensitivity analysis. The remainder of the chapter is devoted to various aspects related to sensitivity. Section 6.2 is included to demonstrate the relevance of mutual dependence of soil and atmosphere in studying surface behaviour. In terms of sensitivity analysis, the case treated in Section 6.2 is intended to reveal how sensitive the modelled surface processes are to including feedback from the atmosphere. In previous studies of surface behaviour this feedback has been ignored.

The effects of changes in system parameters on surface temperature and evaporation rate will be studied in Section 6.4. These effects have a direct bearing on thermal remote sensing. A systematic analysis along the lines described in Section 6.4, however, first requires some simplification of the model in order to eliminate a number of interactions that mask the main effects sought for. For this purpose, the process of topsoil drying must first be studied (Section 6.3). The development of drying stages in relation to soil properties, and the concept of 'drying front' are central to this section.

6.1 Indicators of sensitivity

Several functions can be used to express the sensitivity of systems. The most common expressions for the local sensitivity of some output variable $y(t)$ to changes in a system parameter p are the absolute sensitivity $\partial y(t)/\partial p$ and the relative sensitivity $\partial \ln y(t)/\partial \ln p$ (e.g. Horowitz, 1963; Himmelblau & Bischoff, 1968; France & Thornley, 1984; McCuen, 1973). Coleman & DeCoursey (1976) advocated the use of the form $\partial \ln y(t)/\partial \ln(p - p_0)$ to reduce the effect of the choice of the reference level p_0 for the relevant parameter.

Two basically different ways may be followed to derive these functions for a given system. In the study of biological systems, the 'parameter perturbation method' is widely applied to approximate the differential of interest as a finite difference quotient: changes in output variables are registered as a response to

perturbations in system parameters.

A more systematic approach was developed in the field of systems control engineering. The method, yielding the time courses of the differentials $\partial y(t)/\partial p$, was described by Tomovic & Vukobratovic (1972) in their extensive treatise on 'general sensitivity theory'. For a system with n state variables, the solution of the sensitivity functions of one state variable to one parameter requires the formulation and solution of n extra differential equations, including the formulation of $n^2 + n$ partial differentials. These sensitivity equations are added to the system model itself and solved along with the equations describing the system dynamics. Unfortunately, this method appears to be unpractical in the present case, but it is mentioned because of its general validity and elegance (see also ten Berge, 1986).

The parameter perturbation method

A less elaborate method of sensitivity analysis is to perturb parameters to ascertain sensitivity to them. Usually, the finite difference form of the absolute sensitivity, $\Delta y(t)/\Delta p$, is calculated as an indicator. In Section 6.4, the particular choice of the sensitivity indicator will be discussed further. The pertubation method may still call for extensive calculation when applied to systems that involve a large number of parameters. In a detailed example of sensitivity analysis, Steinhorst et al. (1978) demonstrated how an excessive number of simulation runs can be reduced by the use of 'macro-parameters'. In their terminology, a macro-parameter represents a group of system parameters that are perturbed simultaneously. A high value for a given macro-parameter then implies high values for all system parameters contained in that macro-parameter. If the system appears to be insensitive to a certain macro-parameter, then sensitivity to the individual parameters needs no further study. The above authors varied the macro-parameters in different combinations according to a fractional, factorial design, and subsequently evaluated the main and interaction effects by doing an analysis of variance of the output variables. For selected macro-parameters, the individual parameters were then studied in more detail. For this approach to be valid, negative interaction must be absent among parameters grouped into one macro-parameter.

In the SALSA model, most processes of interest – and hence the parameters involved – interact to some extent and moreover, the model is not very large, so that the use of macro-parameters is not warranted. A perturbation scheme that allows for analysis of possible interaction phenomena, however, is valuable and will be employed in studying the sensitivity of surface fluxes and conditions as discussed in Section 6.4.

6.2 The relevance of boundary layer development to surface processes

The real-world mutual dependence of soil and atmosphere conditions calls for a model formulation in which atmosphere conditions develop on the basis

118

of the computed surface fluxes. Below, the validity (in sensitivity studies) of the generally accepted alternative where boundary conditions measured at Stevenson screen height are imposed on the soil subsystem, will be questioned. The courses of state variables close to the surface can themselves be expected to depend on soil parameter values.

The contrast between simulation results from options A and B, respectively, of the SALSA model can be demonstrated to show the importance of the feedback mentioned. The problem then arises that for the latter case a series of boundary conditions must be generated, to allow for a fair comparison. To overcome this difficulty, the complete version of SALSA (option A) was run for two contrasting sets of soil parameters, which resulted in two different time series of simulated conditions at screen height. These conditions are air temperature, humidity, and wind speed, 'registered' at one-hour intervals for a period of four days. Subsequently, the courses of these variables, obtained as simulation output for the one soil type, were imposed as boundary conditions for the other soil – and vice versa – in a simulation run with SALSA option B. So, four runs were made in total. The soils used in this 'cross-combination' differed only in their hydraulic properties (moisture characteristic, hydraulic conductivity curve, and matric flux potential curve). The corresponding parameters are given in Table 13. Other parameter values, initial conditions, parameter values, geostrophic wind and global radiation were identical in all four runs. Then, if the effect of soil conditions on surface fluxes via screenheight conditions (i.e. feedback via the atmosphere) is negligible, the two runs (differing only in screen-height conditions) for a given soil will result in identical courses of the surface fluxes and state variables.

Two contrasting soils were selected from the variety of soils listed in Table 8 : Mont Cenis silt loam (Vachaud, 1966), and Sable S2 (Stroosnijder, 1982). The initial soil water pressure for both cases was taken to be -5 kPa, to represent field conditions shortly after thorough wetting. Free drainage was allowed at the lower boundary of the sytem. For the boundary conditions geostrophic

Table 13. Hydraulic properties of Mont Cenis silt loam and Sable S2.

	Mont Cenis silt loam	Sable S2	Units
α	$1.810 \ 10^{-4}$	$10.020 \ 10^{-4}$	Pa^{-1}
n	1.281	1.374	–
θ_r	0.000	0.000	–
θ_s	0.442	0.410	–
θ_i	0.380	0.230	–
K_s	$1.400 \ 10^{-8}$	$409.6 \ 10^{-8}$	$kg \ m^{-1}s^{-1}Pa^{-1}$
A	$150.4 \ 10^{-6}$	$470.9 \ 10^{-6}$	$kg \ m^{-1}s^{-1}$
B	0.167	$0.046 \ 10^{-1}$	–

wind speed and global radiation, the same data as mentioned in Section 5.4 were used.

Simulated drying of the topsoil appears to proceed very differently for the two soils. Whereas the Mont Cenis silt loam is able to replenish the drying surface layers with subsoil water for several days, the Sable S2 soil rapidly develops a dry surface layer under the imposed conditions. If the surface fluxes and atmosphere conditons at Stevenson screen height are examined, it becomes clear how these are related to soil properties. Figure 68 shows the predicted behaviour of air temperature, humidity, and wind speed as developed over the two soils. The increase in daily maximum vapour pressure over the course of several days is less pronounced for Sable S2 than for Mont Cenis silt loam, because the latter maintains a higher evaporation rate. The reverse is true, as expected, for air temperature, which rises more rapidly in the case of Sable S2.

The surface fluxes of sensible and latent heat as simulated for the Mont Cenis soil by SALSA option A are depicted in Figure 69. The same figure also shows the fluxes that result when at Stevenson screen height the conditions, 'generated' over Sable S2 soil, are imposed on the Mont Cenis silt loam system. The low vapour pressure and high air temperature acquired over the Sable S2 surface, induce an increased evaporation rate and a suppressed sensible heat flux when combined with the moist Mont Cenis soil surface. This happens to the extent that, during the last day of the simulated period, the direction of the sensible heat flux is reversed to supply heat from the 'warm' atmosphere to the surface, cooled by excessive evaporation. Discrepancies become more pronounced as time proceeds. A slight phase shift can be observed between the time series as obtained by the two model versions. This is because conditions at screen height, generated at given instants (e.g. 16.00 h) by the 'option A' simulations, were maintained at their fixed values during one hour (16.00-17.00 h) in the simulations with the abridged (Option B) model.

Results analogous to those shown in Figure 69 were obtained for the Sable S2 soil, where the reverse effect could be observed when this sandy soil was confronted with the most air 'generated' over the silt loam. The contrast in that case was less pronounced, however, since soil conditions rather than atmospheric conditions were limiting evaporation.

The graphs presented clearly expose the relevance of soil behaviour to changes in air properties, and vice versa. This example serves to illustrate that for an accurate simulation, especially of surface drying of bare soils, atmospheric boundary conditions that are in accordance with the development stage of the drying process must be used.

120
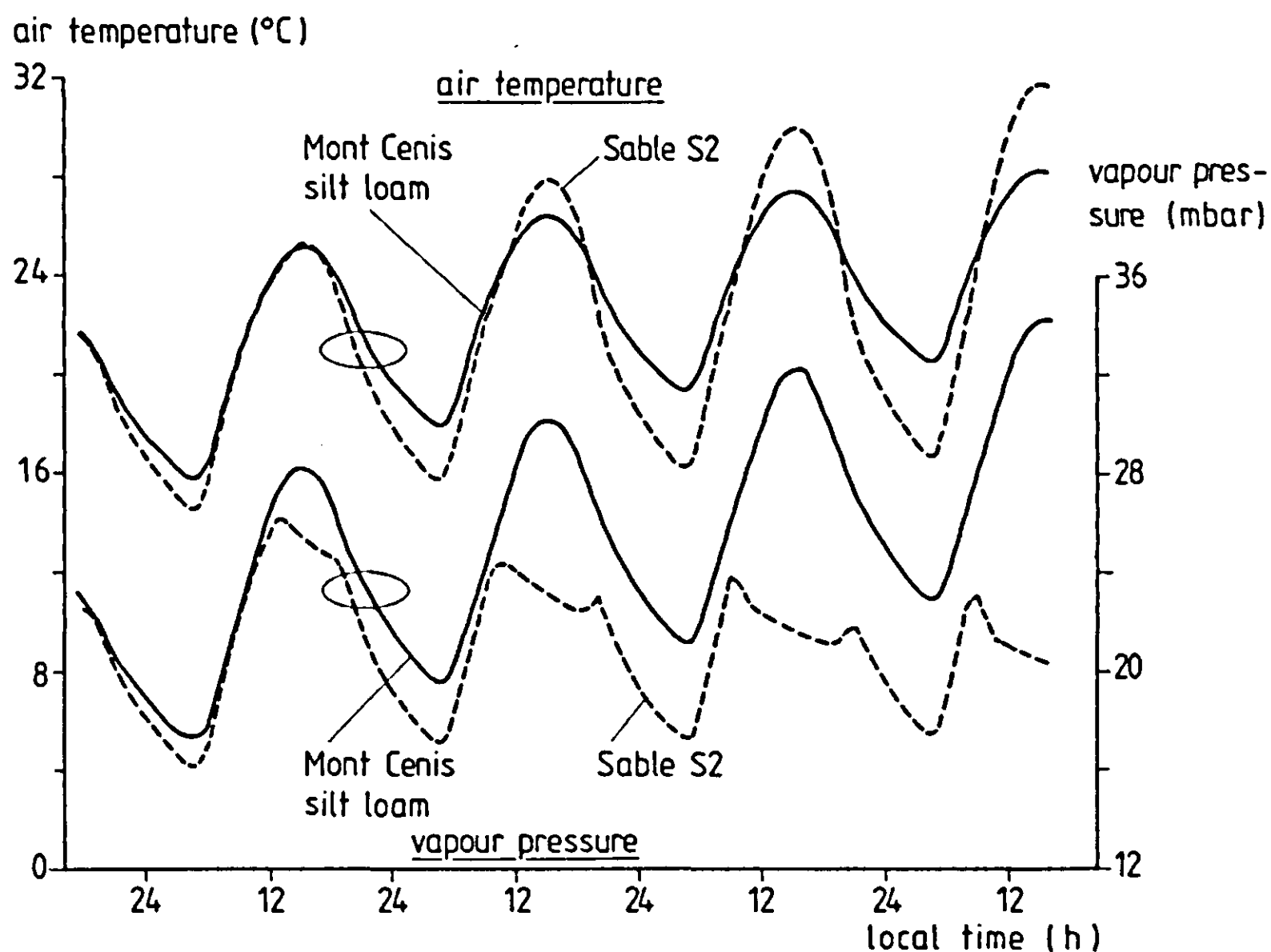
Figure 68. Simulated atmospheric conditions at 1.5 m above the surface for a silt loam and a sand soil; initial soil water pressure was — 5 kPa in both cases.
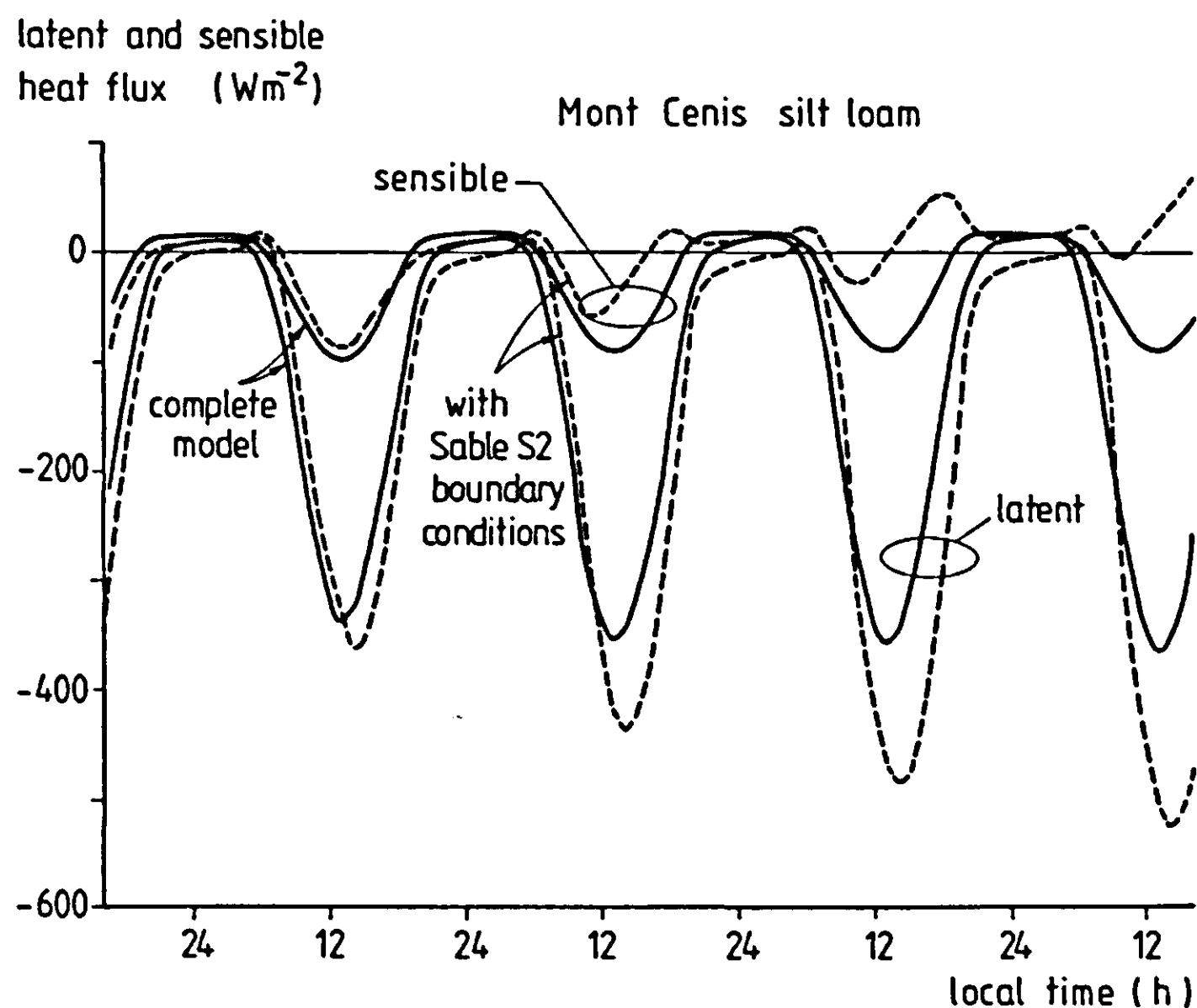
Figure 69. Surface fluxes of sensible and latent heat, simulated for a silt loam under different boundary conditions. The difference between solid and broken lines indicates the relevance of mutual soil-atmosphere feedback on flux prediction. See text.

121

6.3 Soil drying

The soil moisture content profile, as developing from a given initial state as a function of hydraulic properties and meteorological conditions, dominates the surface energy balance in a complicated manner. All transport coefficients, capacities and radiative properties are related to soil moisture content. The results of simulations with a model that describes the entire process of surface drying itself, therefore, can hardly be generalized in terms of sensitivity to basic soil parameters, other than those which directly affect moisture flow. Moreover, it often takes several days for moisture profiles to develop, whereas the characteristic pattern in surface fluxes and state variables is based on 24-hour cycles. For these reasons, the drying process has been separated into distinct stages, two of which may be approximated as stationary.

The three stages of drying
Three classic schematized stages of drying (Fisher, 1923) are used here. Stage I is defined by evaporation at the soil surface, where water supply is not limiting. Saturation deficit of the atmosphere, radiation, and some 'exchange resistance' largely determine the evaporation rate, which could be referred to as 'potential evaporation' (although soil properties affect this flux too, as will be shown). The second stage, known as the 'falling rate' stage, represents a transient case, characterized by the development of the dry surface layer and an evaporation rate decreasing in time. By definition, Stage II cannot be treated as a steady state situation. In Stage III of the drying process, water evaporates from below a dry surface layer and is transported to the surface by diffusion in the vapour phase.

This schematic separation of stages was originally based on laboratory observations, and has not been studied extensively under field circumstances. Nevertheless, the concept has been supported by observations of Idso et al. (1974) for a field situation. The Flevo data for Swifterbant loam (cf. Chapter 5) are also in accordance with this separation of stages.

The limitations of the above simplification will first be viewed on the basis of SALSA simulations of Stage II, taking into account full soil-water-heat interactions. The present section therefore deals with the development of the dry surface layer (the evolution of Stages I, II and III), in relation to the physical properties of the soil under given meteorological conditions. An understanding of surface drying provides a useful background for interpreting the results of a simplified sensitivity analysis (Section 6.4). To study the Stage II development, no *a priori* assumptions were made on the movement of liquid, vapour and heat in the soil, other than those outlined in Chapter 2. Interactions between the different soil phases were included, and developments in the atmospheric boundary layer were also simulated.

The aspects that merit discussion are the definition and behaviour of the drying front, and the role of the latent soil heat flux. Such aspects are not only

122

of relevance to the validity of the Stage III concept, they also have a wider significance – for example, for dry-farming practices. Stage II can be viewed as the non-ideal Stage III situation, where interactions between soil water and dry surface layer are still relevant. Therefore, an analysis of Stage II allows for a refinement of the conclusions arrived at in Section 6.4.

The major physical soil characteristics that affect surface drying are the hydraulic conductivity curve and the moisture characteristic. As discussed in Subsection 2.6.2, these two curves can be combined into the matric flux potential curve $\Phi(\theta)$, which can conveniently be approximated for most soils by a simple expression (Equation 64). The parameters A and B in this expression (see also Table 8) play a key role in the development of drying fronts. To investigate their influence, the process of evaporation under free drainage conditions will be studied below. (Some examples of measured $\Phi(\theta)$ curves can be found in ten Berge et al., 1987).

The drying of topsoil under a given evaporative demand largely depends on the soil's ability to supply water to the evaporating surface, a property that can be expressed in the parameters A and B, mentioned above. Under the condition of free-drainage, however, the choice of a reference level for determination of these parameters is problematic. In the preceeding chapters, A and B were taken to relate to saturation as a starting point of the $\Phi(\theta)$ curve. To render such parameters useful to the description of the drying phenomenon in the absence of a water table, it seems more appropriate to use the 'field capacity' concept in a definition of the reference level. This becomes clear if one realizes that the extremely high A values found for some sandy soils (Table 8) are caused by high K values pertaining only to the θ range close to saturation. If these high water contents occur only during a brief period upon wetting – that is when moisture content at field capacity lies far below this range – then the section of the $\Phi(\theta)$ curve that corresponds to this high degree of saturation plays no role in the surface drying process. In other words, in studying the effects of A and B by sensitivity analysis, it is inconvenient to take into account a gravity term that should be amended simultaneously with changes in A or B. So the problem comes down to defining a suitable moisture content θ_{ref} where gravity can be ignored. This moisture content then serves as a reference to the values A' and B', thus replacing θ_s in the definition of the independent variable x. The superscripted 'prime' notation in A' and B' serves to indicate this change in reference level.

The reference moisture content θ_{ref} could be designated as 'field capacity', following one of the accepted definitions. Here, field capacity will be defined as the volumetric water content that corresponds to a hydraulic conductivity of 1 mm d^{-1}. Then, the values found for A' range between 0.5 10^{-5} and 3.0 10^{-5} kg m^{-1} s^{-1} for the soils listed in Table 8. As compared with the A values, this implies a strong decrease of the absolute value, obviously, and also of the variation in this parameter among soils. The constant B' varies between

0.05 and 0.5 for the different soils, which is somewhat higher than the range for B indicated in Table 8.

Using these four extremes for A' and B' in four different combinations, four one-week simulation runs were made, in all cases starting from an initial moisture content of 0.30 over the whole profile. The remaining conditions and system parameters were chosen as described in Section 5.2. Small steps were used when discretizing the soil, to allow for a relatively accurate moisture profile description. From the top downward, compartments of 3×2, 3×3, 3×4 and 3×5 mm were used for the upper 12 layers. The effects of changes in A' and B' on the development of the dry surface layer are discussed below. Figures 70 and 71 show the simulated courses of latent heat flux and surface temperature, respectively. These characterize the specific situations elaborated upon below.

The main questions to be discussed are: (1) how pronounced is the developing drying front as a function of A' and B' and (2) to what extent do these parameters affect the rate at which the dry surface layer arises and grows. The drying front phenomenon was studied earlier, for example by van Keulen & Hillel (1974), who based their analysis on the shape of the water diffusivity function. Menenti (1984) also discussed the phenomenon and included a theoretical analysis of preferential evaporation sites within a pore system. The present analysis will focus only on the role of the two macroscopic parameters A' and B'. It may be recalled that vapour diffusivity within the soil is considered to be independent of moisture content here. While no general consensus has
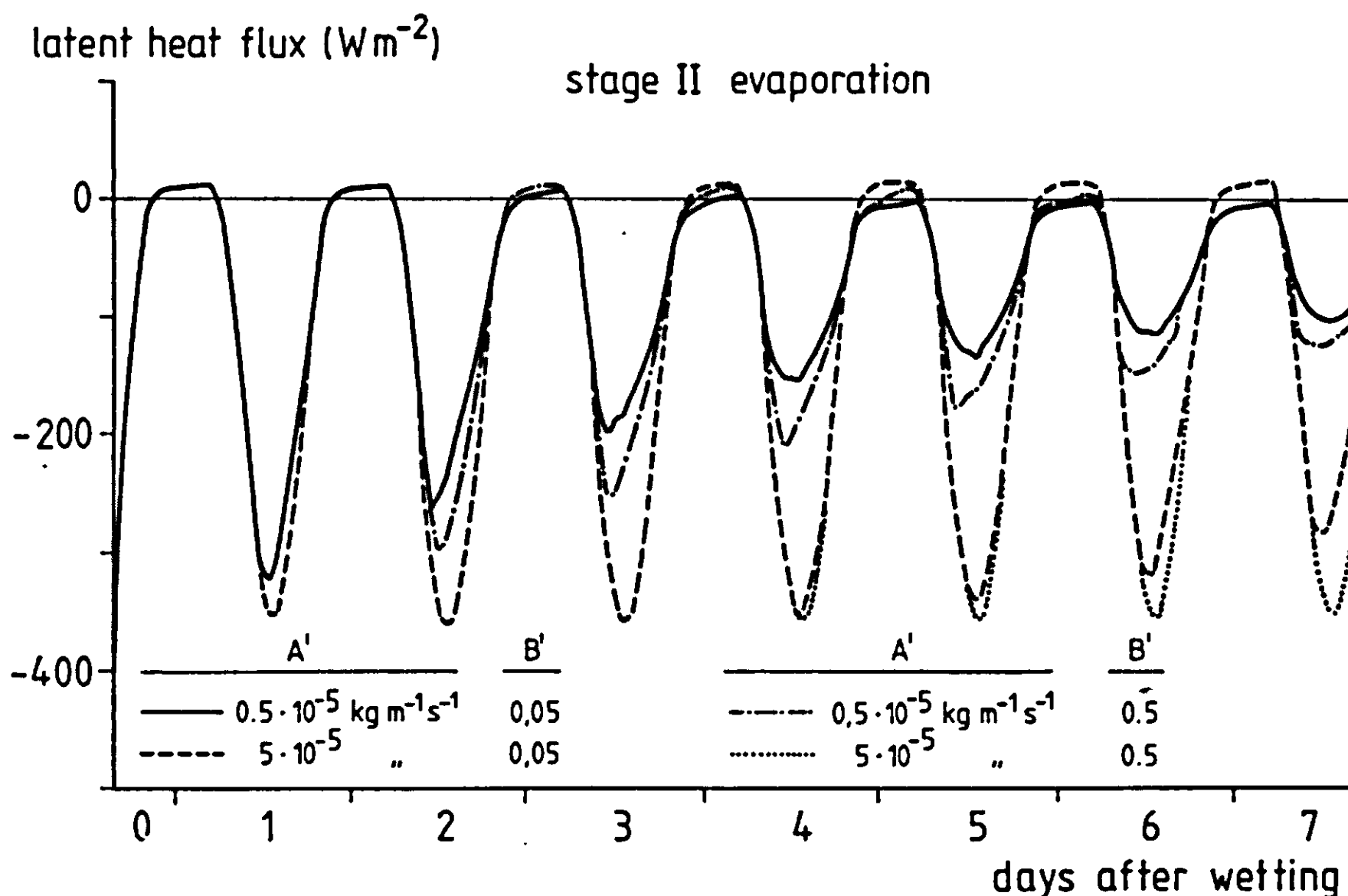
Figure 70. Latent heat flux, simulated for a one-week drying sequence, for different combinations of soil hydraulic parameters A' and B'.

124

surface radiation temperature (°C)
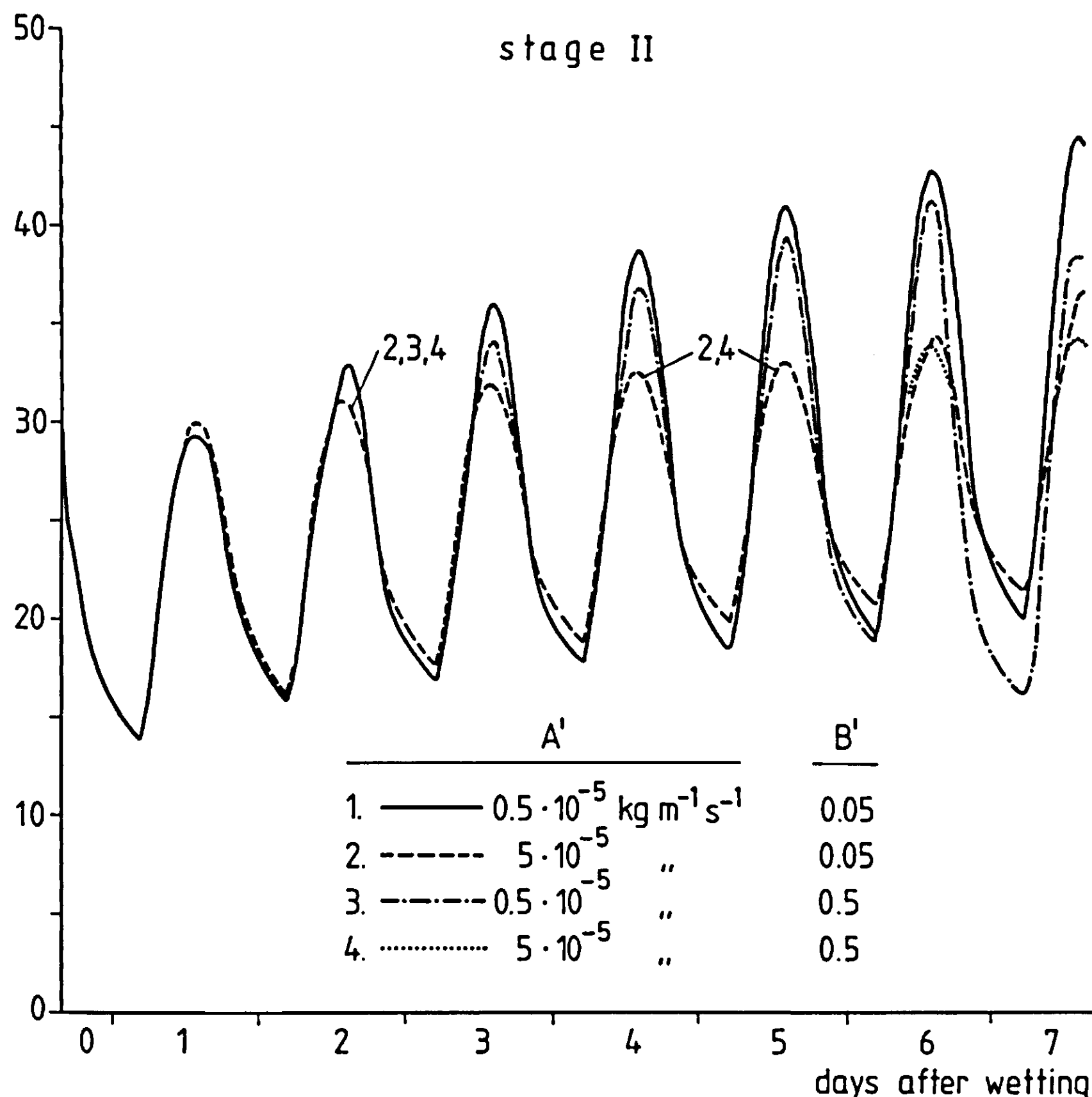
Figure 71. Surface temperature, simulated for a one-week drying sequence, for different combinations of soil hydraulic parameters A' and B'.

yet been reached on this topic (Chapter 2), the issue of surface drying would be obscured by adopting any more refined relation to describe vapour diffusivity in soil.

Daytime: definition and shape of the drying front

Various thresholds can be used to define the drying front. In view of the scheme to be followed in the next section, which employs three distinct stages of drying, a suitable definition seems to be the depth at which the vapour flux equals a certain fraction of the surface vapour flux. By locating the depths corresponding to different values for this fraction, a qualitative measure of the existence of such a drying front becomes available. An example is given in Figure 72, which describes surface drying for two soils. There are three conclusions: (1)
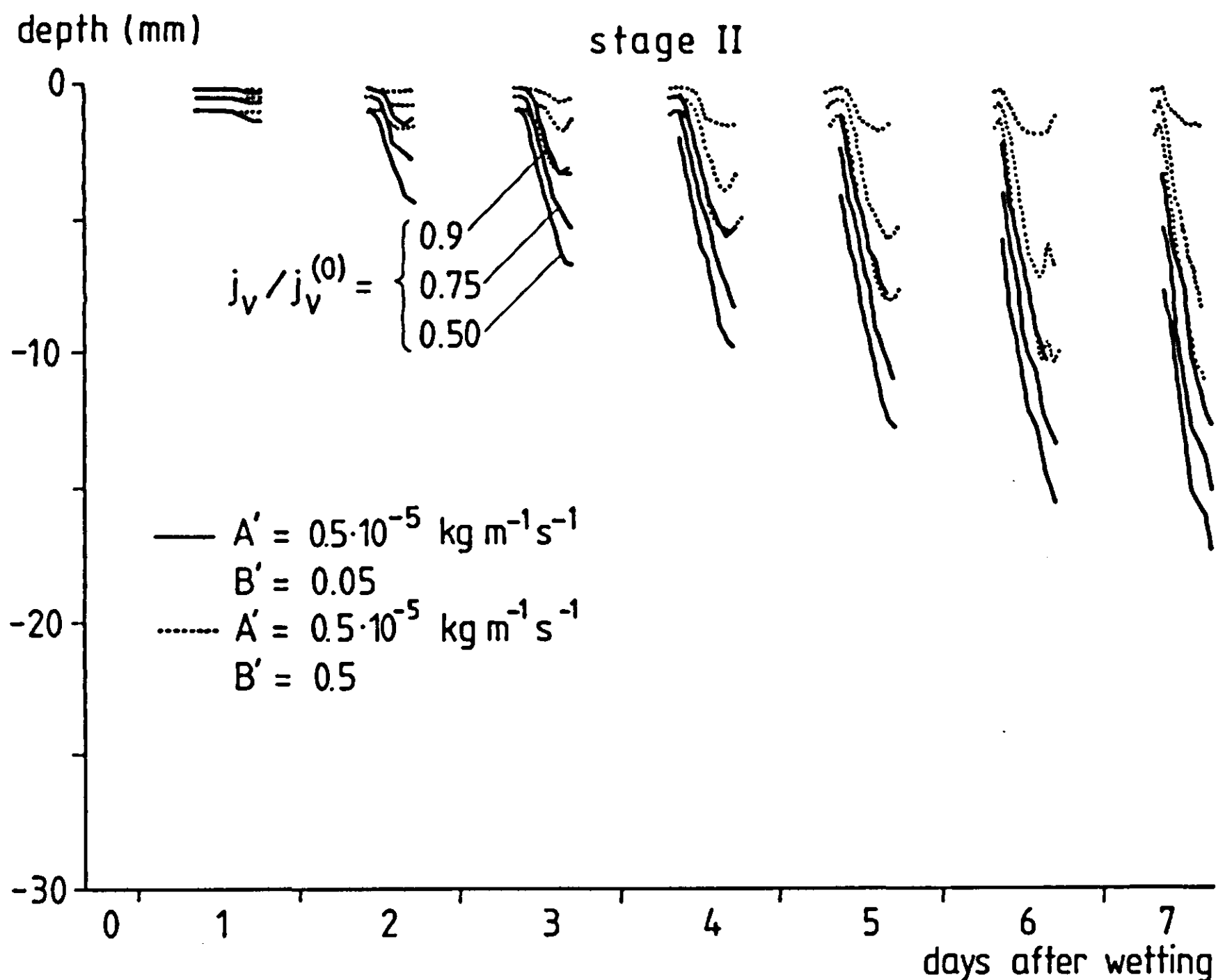
Figure 72. Depth at which the vapour flux equals selected fractions of the surface vapour flux; the courses for only two of the soils mentioned in Figures 70 and 71 are depicted: $A' = 5.10^{-6}$ kg m^{-1}s^{-1}, $B' = 0.05$ (solid) and 0.5 (dotted). (The remaining two soils – with $A' = 5.10^{-5}$ kg m^{-1}s^{-1} – developed no dry surface layer). Only daytime data (09.00-17.00 h) are plotted.

during each day, the 'evaporation zone' moves downward over a considerable distance, (2) the 'evaporation zone' is diffuse, and (3) as B' increases, the front becomes less pronounced. With reference to the sensitivity analysis of the simplified model (next section), it must now be noted that these three effects tend to decrease the impact that the thickness of the dry layer has on the output variables for Stage III simulation. So, in reality, the sensitivity to that thickness will be less than simulated for the idealized Stage III case (Section 6.4).

The moisture content profiles, as developed after one week of drying, are shown in Figure 73. This diagram also shows that a lower B' value creates a more pronounced drying front, not only in terms of $J_v/J_v(0)$ as appears from Figure 72, but also in terms of the θ-z profile.

An interesting feature is the relation with surface temperature. Comparison with Figure 71 reveals that the soil with the lowest A' and B' values reaches the highest surface temperatures during daytime, is the most effective in pre-
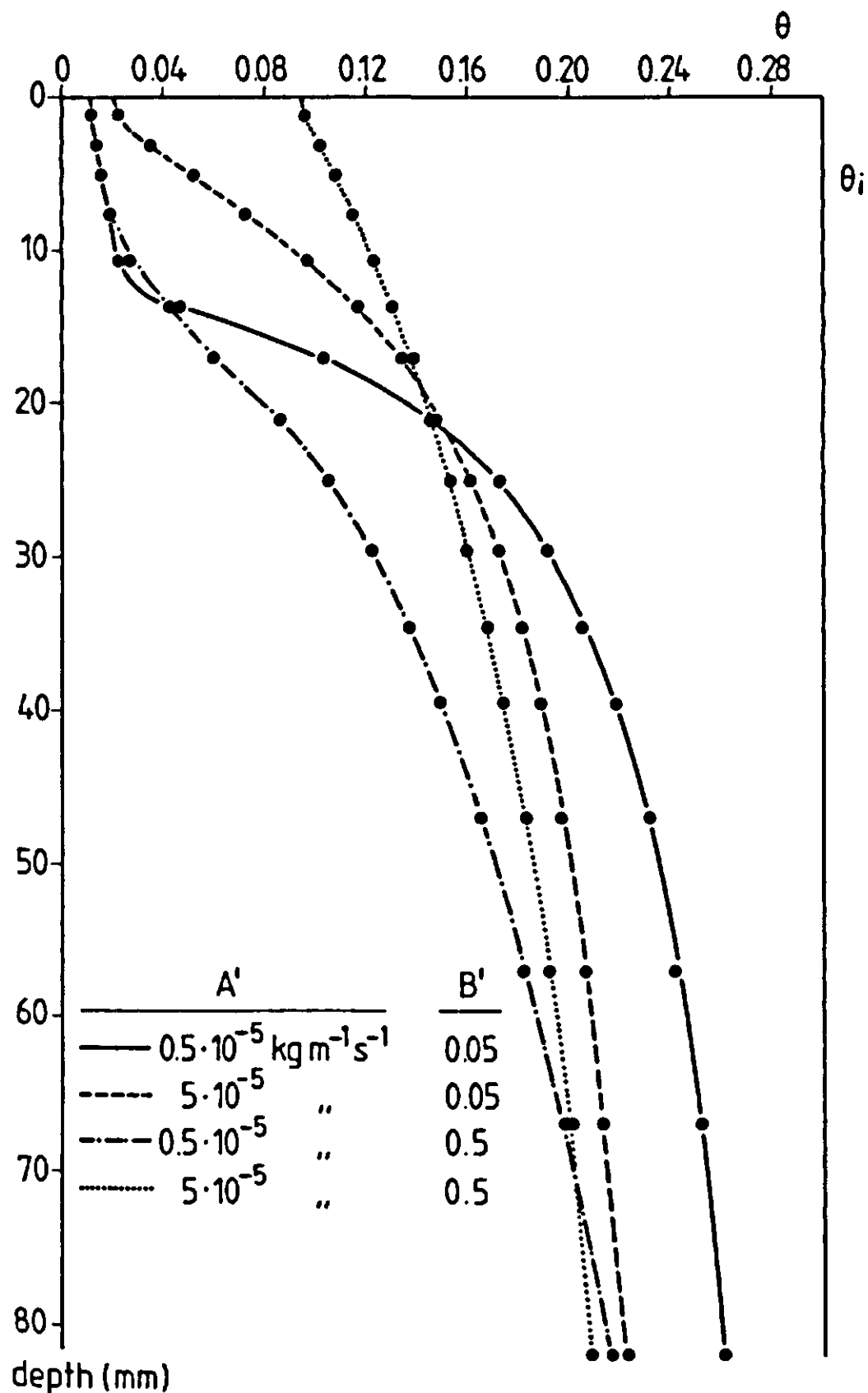
Figure 73. Simulated moisture content profiles after one week of drying for different combinations of soil hydraulic parameters A' and B'.

serving soil moisture (Figure 70), and accordingly shows the highest moisture content below the dry top layer. This highlights a general misconception encountered frequently in remote sensing literature: it is often assumed that the warmer spots on daytime thermal imagery indicate lower soil moisture contents. In fact they represent lower evaporation rates. The results shown here indicate that the reverse is true where soils differing by A' and B' values are present within the same region, i.e. subject to the same boundary conditions.

Other criteria that can be used to define a drying front are maximum vapour flux divergence, or maximum liquid flux convergence. Also, the zero flux plane for soil water vapour may serve as a valid criterion: below this plane, vapour moves downward during daytime, whereas from this depth upward it moves towards the surface. It is then assumed that molecular diffusion is the governing transport process for soil water vapour. A comparison between these criteria is given by ten Berge (1986) on the basis of SALSA simulations. It appears

that as soon as surface drying has commenced, the three criteria do not yield very different courses for the depth of drying front, which behaves largely as depicted in Figure 72. The same source demonstrates that the parameter A' is by far the most important in determining the rate of dry layer development, and consequently of the rate at which evaporation decreases in time.

Night-time: vapour condensation

In the sensitivity analysis for drying Stage III (Section 6.4), interaction between water vapour and dry soil will be omitted. It has already been shown that during Stage II, the dry top layer is rewetted at night. This process tends to decrease the sensitivity of output variables – e.g. surface temperature – to the thickness of the dry top layer during daytime. Part of this redistribution of moisture results from vapour movement. In view of the Stage III assumptions, it may be questioned how realistic an inert toplayer is with respect to thermal behaviour at night. A brief analysis based on SALSA simulations is given below.

The fast-drying soil, for which Figures 70 and 71 have shown some characteristic developments, is used here as an example to illustrate the night-time process of interest. Figure 74 gives a simulated impression of the energy fluxes involved as drying proceeds. Sixty to seventy per cent of net radiation (R_n about -70 W m^{-2}) appears to be countered by the soil heat flux at the surface. (As explained in Subsection 5.1.2, this surface conduction flux includes the effect of condensation: it is enhanced when vapour from subsoil condensates in the top soil compartment and releases the heat of condensation, thereby raising temperature.) In this example, the remainder of net radiation is countered by downward atmospheric transport of sensible and/or latent heat towards the surface. The surface conduction term supplies heat from the uppermost soil compartment (2 mm) to the radiating surface. It is interesting to follow the heat fluxes at some depth below the surface. For this, a depth of 9 mm was chosen; this depth lies well within the range over which the drying front passes during daytime. The simulated conduction flux and net latent heat flux, both at 9 mm, are also depicted in Figure 74. Net latent heat flux is defined here as the total amount of heat evolved from condensation in the 0–9 mm layer per unit of time and surface, i.e. the latent heat flux (vapour flux times heat of vaporization) at $z = 9$ mm minus its value at the surface.

It can be observed that the cooling of the 0–9 mm layer plays no significant role during the major part of the night: the sum of the two terms at 9 mm almost equals the surface conduction flux: the subsoil provides all the heat required to maintain R_n, apart from the atmospheric fluxes. The distribution over the two terms at 9 mm, however, changes drastically in time as the top layer dries out. During the first four nights, conduction is the governing mechanism of heat supply. In the nights following, conduction becomes less dominant (λ decreases because of surface drying) and the contribution of distillation increases.

128
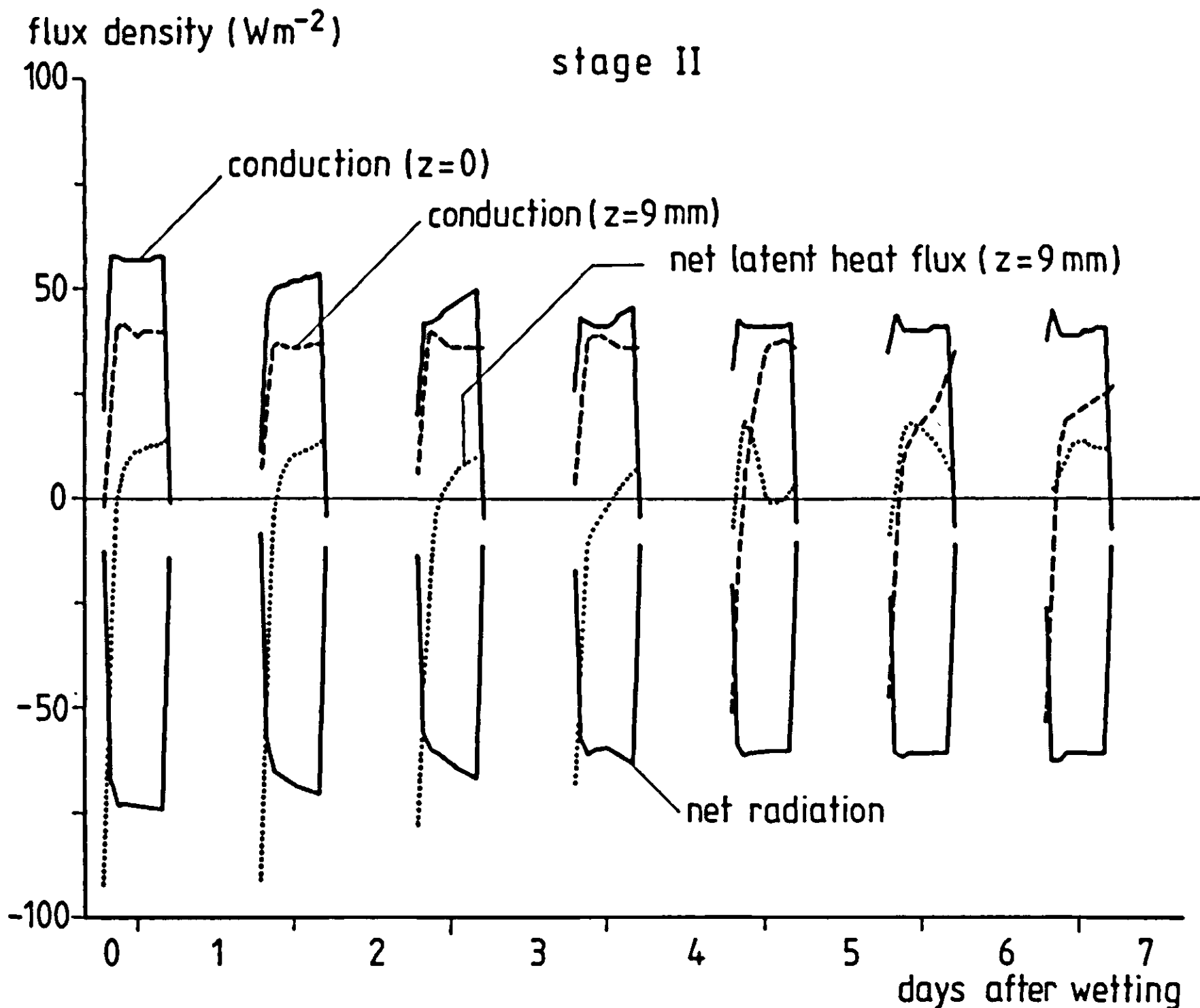
Figure 74. Energy fluxes in the top 9 mm of soil during drying; $A' = 0.5 \ 10^{-5}$ kg $m^{-1}s^{-1}$ and $B' = 0.05$. Only the time intervals where $R_n < 0$ are shown.

The course of early evening net latent heat flux shows an increase during the drying sequence: in the first half of the week, net water loss resulting from evaporation from the 0–9 mm layer remains positive for a few hours after R_n has become negative; this is compensated for by positive (upward) conduction at $z = 9$ mm. In the second half of the week, net condensation starts as soon as one hour after R_n has turned negative. This sudden change is explained on the basis of soil relative humidity, which drops below 100% during the afternoon. The role of relative humidity becomes apparent in the fifth and following nights, where distillation into the dry toplayer delivers enough heat for the conduction term at 9 mm to be negative (downward!) during the early evening hours; this were impossible had vapour diffusion been governed by the temperature gradient only. The decrease of the net latent heat flux after some hours is associated with relative humidity approaching the value of 100%; this occurs rapidly (steep decrease in fifth night) as long as only a thin soil layer has dried out down to low values of relative humidity.

For the example shown here, it can be concluded that condensation in the top layer compensates for up to 25% of net radiation, and for up to 40% of the

129

conduction term at $z = 0$, that is, 40% of the total heat supplied by the soil to the surface. Such a contribution is not negligible. In view of the sensitivity study discussed in Section 6.4 it can therefore be stated that in reality, the sensitivity of output variables – at night – to the thermal soil properties will be less than indicated in that section.

6.4 Sensitivity of certain variables to major soil parameters; Drying Stages I and III

The question arises which indicator of sensitivity is most suitable to provide a basis for thermal infrared imagery interpretation. Limiting the discussion to absolute sensitivity as defined in Section 6.1, a choice could be made between an approximation of the differential sensitivity $\partial y/\partial p$, and the integral sensitivity $\Delta y/\Delta p$. Although both indicators have their advantages in specific cases, they share the disadvantage that division by dp and Δp, respectively, introduces a dependence on the scale chosen to express p, and thus precludes a direct comparison between the effects of different parameters. Moreover, the sensitivity itself becomes interesting mainly if combined with a certain interval Δp. It is assumed that one is primarily interested in the range of values that some output variable might attain, because of possible field variations in specified parameters. Attention is therefore focused here on the quantity Δy, which corresponds to a maximum range Δp, rather than on true sensitivity. The choice of Δp inevitably introduces some bias, but the gain is a direct picture of the relative importance of parameters.

The key parameters governing the surface energy balance under given meteorological conditions are albedo, emissivity, thermal conductivity and heat capacity of the soil, and roughness length. The effects of these parameters will be studied for Stages I and III. The procedure involved uses a simplified version of the SALSA model, which excludes soil-water interaction.

In the sensitivity trials to be discussed, the following working definition of the stages will be applied. Stage I is treated as a steady state, evaporation taking place at the surface, the driving force being only the linearized gradient of vapour density between the evaporation site and screen height. In Stage III, the evaporating 'surface' is situated at a fixed depth below the soil surface, and the water transport is considered to be entirely in the vapour phase above this depth, the driving force again being the linearized vapour density gradient. Compared with Stage I, the 'resistance' to vapour transport is now increased by a diffusion term to account for transport in the soil. For both Stages I and III, all interactions between water vapour and soil material in the dry layer (including liquid water) are omitted. Aside from the above, the model employed is the complete SALSA model, i.e. including atmospheric developments. Again, the radiation data for day 156, Flevo-1 data set, are used to define the energy flux boundary condition at the surface, and a geostrophic wind of 10 m s^{-1} is assumed in the following examples.

130

The two cases I and III are treated separately. Two values are assigned to all system parameters considered, based on the extremes to be expected under field conditions. A complete two-level factorial design is used to define the different combinations of high/low parameter values. For n parameters, this results in 2^n combinations.

The simplified model was run for all combinations, and the output was treated by analysis of variance (ANOVA) for each point in time (one-hour intervals). ANOVA yields the main effects of parameters, and the interactions of various orders between parameters.

Analysis of Stage I

For the 'wet soil' situation, the parameters to be varied are albedo, emissivity, roughness length (z_o), thermal conductivity λ, and heat capacity (C). As the latter (thermal) soil properties usually vary simultaneously, they were lumped into a single parameter, thermal inertia, defined as $P \equiv \sqrt{\lambda C}$. The frequent use of the thermal inertia concept in remote sensing literature is another reason for using this particular parameter here. With the resulting four independent parameters, 16 simulation runs were made, each for a period of 48 hours, of which only the last 24 hours were analysed, to reduce the effects of initial conditions. Table 14 lists the values chosen for the parameters involved, based upon moist soil conditions.

The output variables for which sensitivity was investigated are surface temperature, latent heat flux, and temperature and saturation deficit of the air at a height of 1.5 m height above the surface. Surface temperature was selected, because it is the variable of main interest in thermal remote sensing, and latent heat flux was chosen because of its relevance to agronomy. The other two variables were inspected in order to reveal the effect of soil conditions on the state

Table 14. Parameter values used in sensitivity analysis.

	Stage I		Stage III		Units
albedo	0.08	0.14	0.14	0.38	–
emissivity	0.94	0.98	0.92	0.92	–
thermal cond. topsoil	0.60	2.30	0.20	0.40	$W\,m^{-1}K^{-1}$
thermal cond. subsoil	0.60	2.30	0.60	2.30	$W\,m^{-1}K^{-1}$
heat capacity topsoil	$1.70\ 10^6$	$3.00\ 10^6$	$3.00\ 10^5$	$6.00\ 10^5$	$J\,m^{-3}K^{-1}$
heat capacity subsoil	$1.70\ 10^6$	$3.00\ 10^6$	$1.70\ 10^6$	$3.00\ 10^6$	$J\,m^{-3}K^{-1}$
thermal inertia topsoil	1000	2630	250	500	$J\,m^{-2}K^{-1}s^{-0.5}$
thermal inertia subsoil	1000	2630	1000	2630	$J\,m^{-2}K^{-1}s^{-0.5}$
thickness top layer	–	–	0.009	0.04	m
vapour diffusivity	–	–	$0.22\ 10^{-4}$	$1.10\ 10^{-4}$	$m^2\,s^{-1}$
roughness length	0.50	50	0.50	50	mm
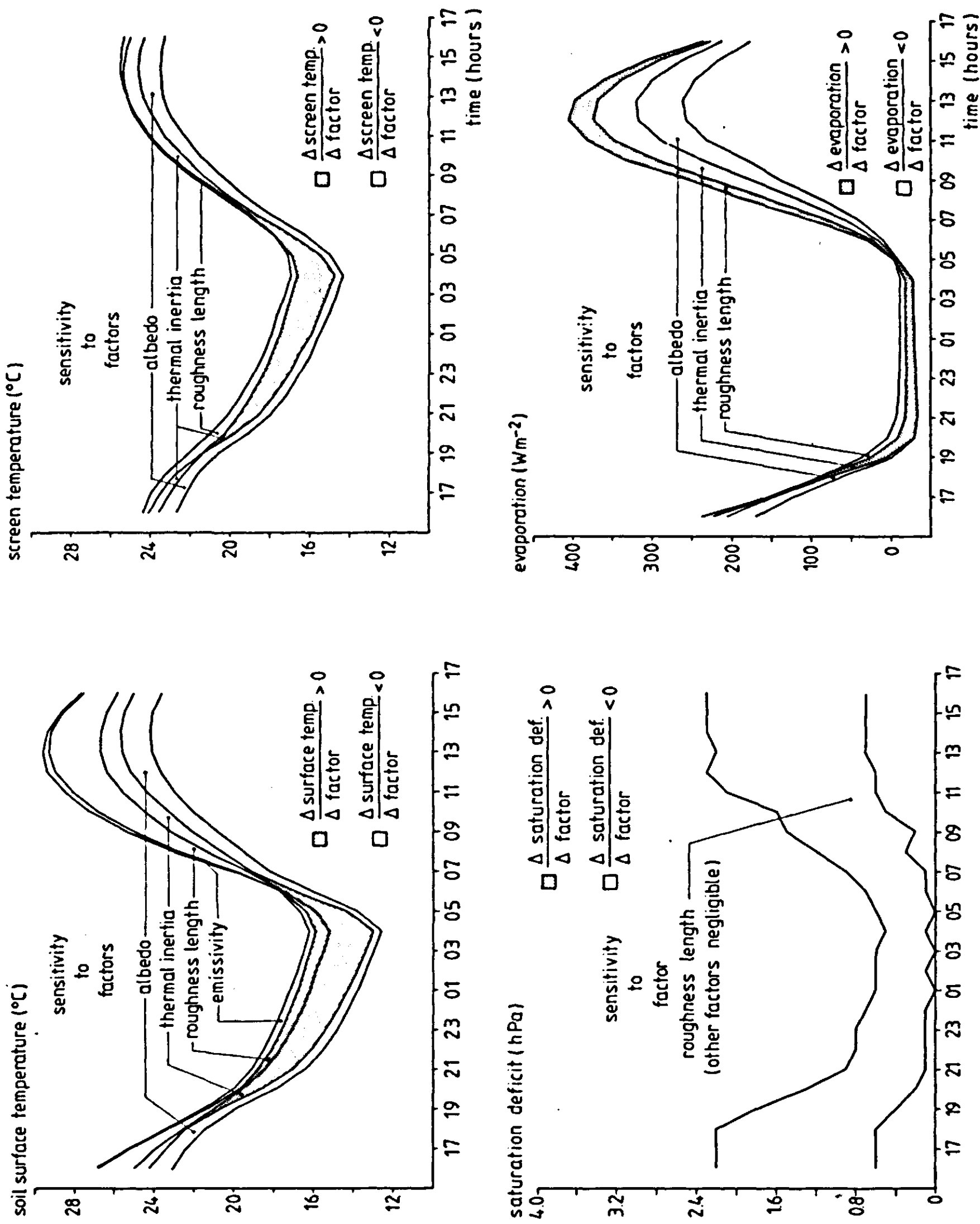
Figure 75-78. Results of a sensitivity analysis for stage I evaporation. For explanation see text.

of the lower atmosphere. For 25 hourly values and 4 output variables, a total of 100 ANOVAs were carried out.

Figures 75-78 show the main effects of parameter changes as they vary in time. These graphs merit some explanation. The information of interest is exclusively in the width and shading of the individual bands. The curves delineating these bands have no intrinsic meaning, because they result from addition of the individual effects of parameter variations. Also, the position of a particular band with respect to the vertical axis has no meaning: the total width of the entire band, obtained for each point in time by summation of individual bands, is centred around the mean course of the corresponding output variable. The order in which the bands have been placed on the graphs is arbitrary; only the width of the bands is relevant. The mean curve itself is not depicted here, in order to focus attention on sensitivity rather than on absolute values. Individual band widths, measured in the units of the ordinate, directly show the absolute change in the output variable induced by changing the indicated factor over the range mentioned in Table 14. The shading of each band determines whether the factor effect is positive or negative, as indicated in the figures. Bands narrower than 0.15 K, 0.15 K, 0.5 hPa, and 10 W m^{-2} were omitted from the figures for surface temperature, screen temperature, saturation deficit and latent heat flux, respectively.

If one is interested in the actual values of the output variables for a selected combination of parameter values, these can be derived from the figures. In such factorial designs, the realization of a dependent variable – in the absence of interaction among parameters – is expressed as the mean M plus half the sum of effects of all parameters 'present' (i.e. at high value), minus half the summed effects of parameters 'absent'(i.e. at low value). Thus, for a case with factors (parameters) a, b, and c 'present' and d, e, and f 'absent', the value of the dependent variable, noted as (abc), would be calculated as

$$(abc) = M + \tfrac{1}{2}(A + B + C - D - E - F) \qquad \text{Equation 96}$$

The capital letters in this expression refer to the effects of parameters (factorial effect totals), to be read from the figures as band width and shading. In the case where interaction occurs, the relevant interaction effects should be added to the RHS. In that situation, a plus sign must be assigned to combinations of letters appearing on the LHS (e.g. AC), and also to combinations of letters that are both absent on the LHS (e.g. DE); interaction effects between parameters that do not all pertain to either the 'absent' or 'present' class (e.g. AD, BEF, etc.) should be given a minus sign. In this case of potential evaporation, the combinations AB, AC etc which could be added to the RHS to represent interaction effects, are all negligible: the effects are smaller than the chosen critical minimum values mentioned earlier. In other cases (e.g. drying Stage III) interaction may be considerable. A detailed treatment of the statistics of factorial experiments can be found in Snedecor & Cochran (1967).

From Figure 75 it can be seen that the variations in surface temperature, as expected to arise in the field from variations in albedo, thermal inertia and roughness length, are all of the same order of magnitude during daytime. Emissivity appears to play a minor role (note that it is surface temperature and not the radiation temperature that is plotted).

During the night-time hours, thermal inertia dominates the variability of surface temperature. Factors of relevant influence on air temperature at Stevenson screen height are albedo and thermal inertia, but it can be observed that field variations in these parameters do not bring about changes of more than 1 or 2 K in air temperature in the case of Stage I evaporation. Saturation deficit, with very low overall values as expected at this stage, appears to be insensitive to all parameters; minor changes are caused by variations in roughness length, z_0. For the latent heat flux, the parameters albedo, thermal inertia and roughness length again have effects of comparable magnitude, each giving rise to variations of about 50 W m^{-2}.

Analysis of Stage III

In the simulation runs for Stage III, albedo, thermal inertia, and roughness length were again varied. In this case, however, the thickness of the dry top layer must be taken into account as a new parameter, while two values of the thermal inertia must now be chosen for the two layers considered. Moreover, vapour diffusivity is introduced as a system parameter. Variations in soil emissivity have been omitted from the perturbation scheme, because these appeared to have only a minor effect on the surface energy balance. So, with the resulting total of six parameters to be varied, a full factorial two-level design asks for $2^6 = 64$ simulation runs in the case of Stage III evaporation. The selected parameter values (Table 14) for the top layer are based on reported ranges for dry soils, and for the subsoil they are based on 'moist soil' values. This does not apply, of course, to the thickness of the dry toplayer (i.e. depth of the evaporation front); the values for this parameter are based upon soil conditions to be expected during dry spells in NW Europe. These values may therefore be considered as fairly arbitrary.

·The output variables examined are again the surface temperature, latent heat flux, and air temperature and saturation deficit at screen height. The main effects are shown, along with some first-order interaction effects, in the Figures 79-82. As in the previous case, these figures are the result of 100 analyses of variance (25 hourly values × 4 variables). For the interpretation of the graphs, see the explanation given for the Stage I case. In Figures 79-82, minimum values of 0.5 K, 0.3 K, 1 hPa and 10 W m^{-2} were used for bands to be plotted.

Whereas in the previous case the interactions were negligible, they are relevant at Stage III, at least for some parameters. It is recalled that an interaction effect AB between factors A and B is defined as the average response to A in the 'presence' (high value) of B, minus the average response to A in the 'absence' (low value) of B. The averages needed are taken over all possible combi-
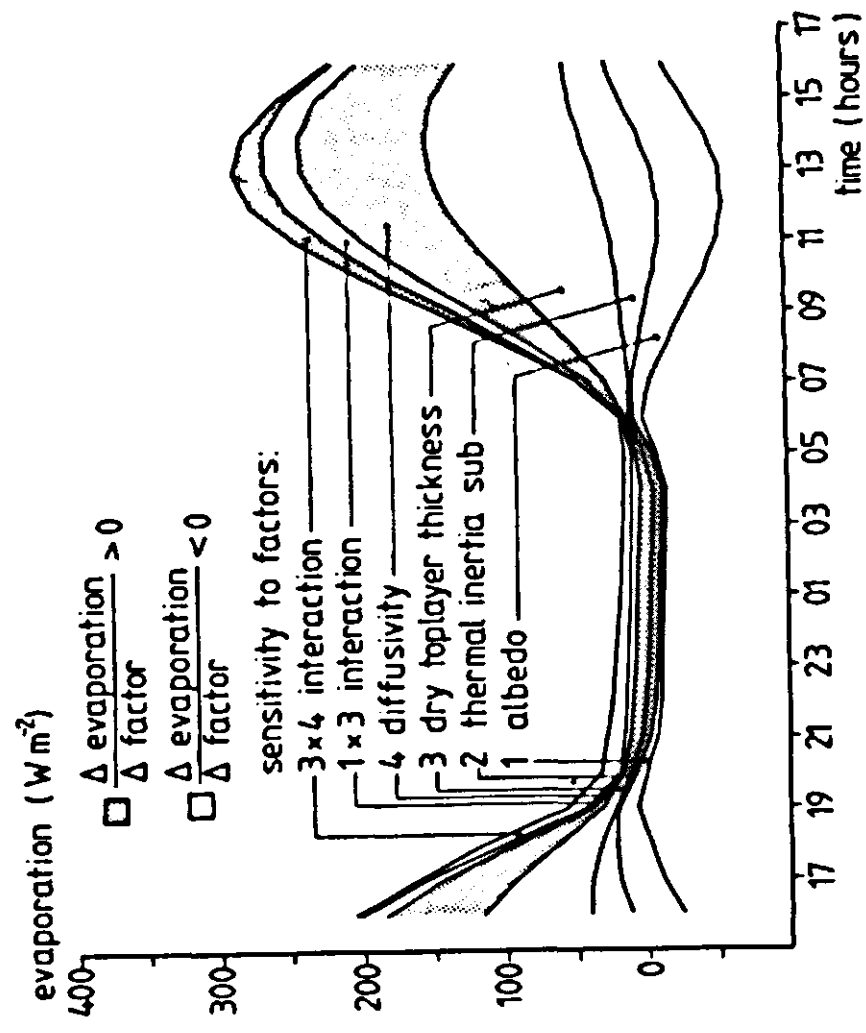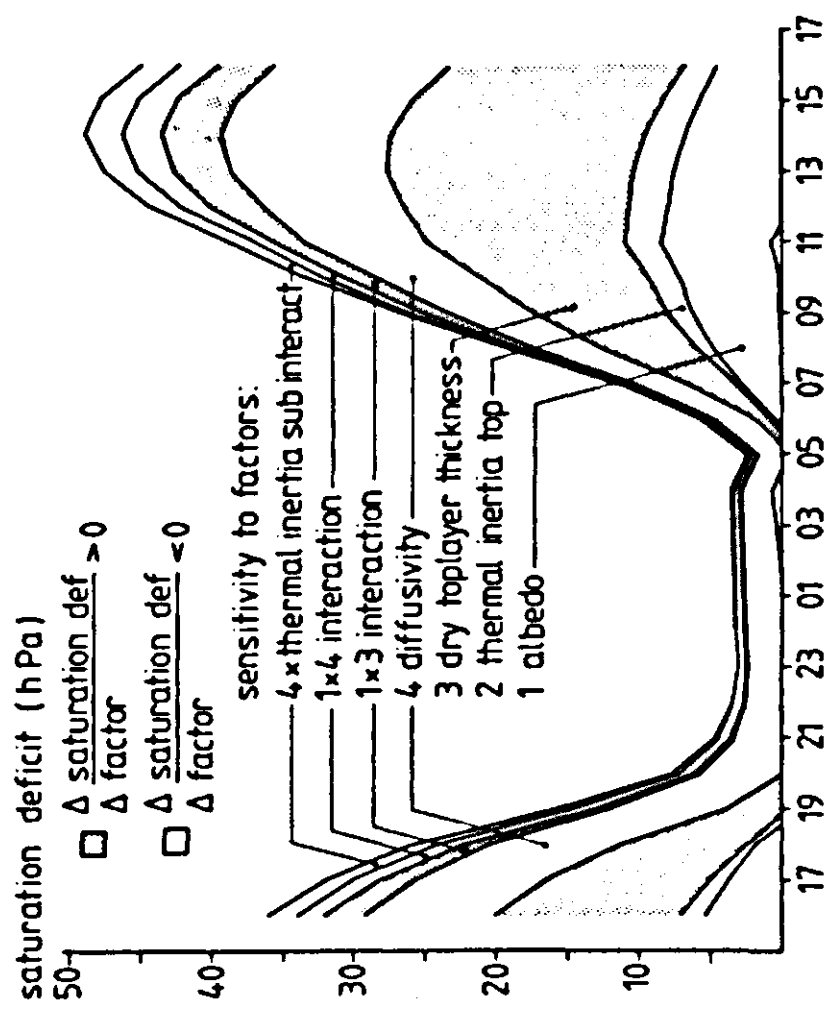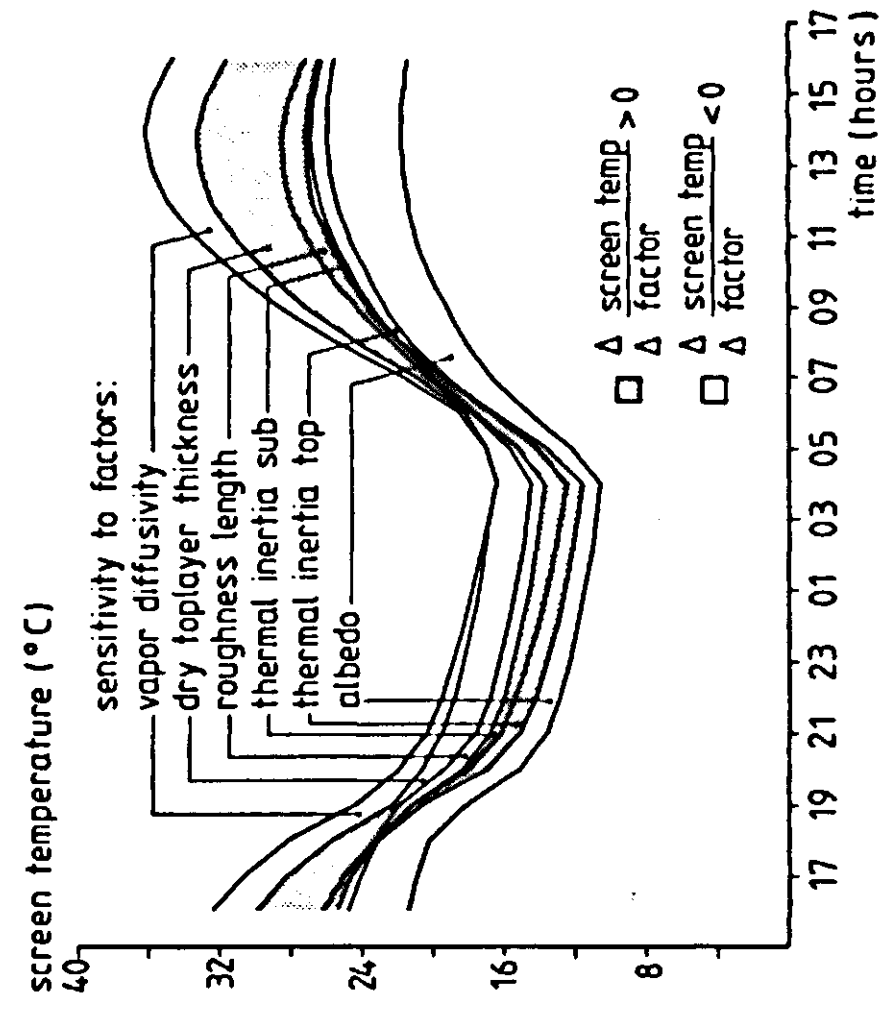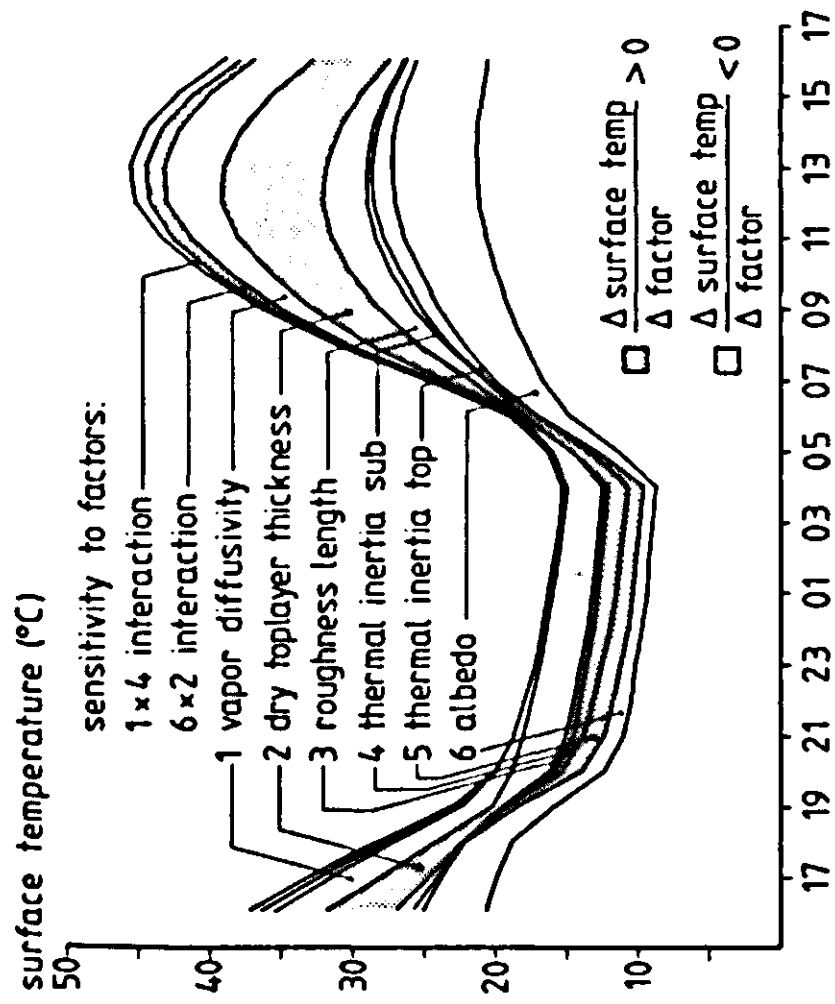
Figures 79-82. Results of a sensitivity analysis for stage III evaporation. For explanation see text.

135

nations of the remaining factors.

Of the six parameters studied, albedo and dry layer thickness have the most pronounced effect on surface temperature (Figure 79; note the scale differences with the Stage I figures). During the daytime the roughness length and vapour diffusivity also appear to be important parameters. Thermal inertia, especially of the subsoil (> 1 cm depth), plays only a minor role during the day. In this respect, some caution must be excercised when reading the figures, since the ranges chosen for topsoil inertia and subsoil ineitia are different (Table 14). Thus, a certain fraction of the effect attributed to the thickness of the dry top layer results, in fact, from the difference between topsoil and subsoil thermal inertia. During the night-time hours, thermal inertia dominates. For screen temperature, similar effects can be observed from Figure 80. As expected, the soil parameters that are most important to the latent heat flux (Figure 82) also determine the saturation deficit of the air. The latter appears to be extremely sensitive to various soil properties, as seen from Figure 81. This is not surprising, because soil conditions that promote high surface and air temperatures are associated with low evaporation rates. Figure 81 serves as another illustration (see Section 6.2) of the necessity to simulate (and not impose as boundary conditions) the developments in the lower atmosphere when simulating surface processes.

6.5. Comments on the relation $T_s - LE$

The effect of changes in system parameters on the course of various output variables has been demonstrated for the idealized drying Stages I and III. As mentioned, a complete factioral design was used in combination with analysis of variance to identify the respective effects. The same data were also submitted to an analysis of covariance in order to ascertain the relation between two output variables, and to identify the amount of 'noise' in this relation ascribed to variations in the system parameters distinguished. The variables of interest to thermal remote sensing are the surface temperature T_s and the latent heat flux LE (negative away from surface). Analysis of covariance based on a linear regression between two variables results in a 'meta-model' expression of the dependent variable as a linear combination of independents:

$$T_s = \overline{T_s} + \beta(\overline{LE} - LE) + \tfrac{1}{2}(A + B + C - D - E - F) \qquad \text{Equation 97}$$

Of course, such 'meta-models' are only valid under the boundary conditions imposed when generating them. This expression applies to the example where factors a, b and c are present, and d, e, and f absent; β is here the regression coefficient, and the capitals are the main effects of the independent variables (system parameters) corrected for the covariate. In this case, T_s is the dependent and LE is used as the covariate. As the relation between these two variables is mainly of interest during daytime, only the data for the 08.00-20.00 h. period

136

are given. Figure 83 shows the results for the Stage III case. Clearly, albedo is the strongest source of noise in the T_s — LE relationship, the main effect ranging between -2 and -8 K. Roughness length and dry layer thickness show effects that are comparable in absolute magnitude (but of opposite sign), as expected. Vapour diffusivity and thermal inertia, the latter of both topsoil and subsoil, appear to have a minor influence on surface temperature, when LE is included as the covariate.

The same analysis of the simulated Stage I data yielded small effects for albedo, thermal inertia and emissivity (± 1.2, -1.0 to $+1.5$, and -0.15 to $+0.10$ K, respectively). Roughness length, on the other hand, showed an effect of approximately the same magnitude as found for the Stage III data, ranging from -4 to $+1.5$ K for an increase of this parameter over the range indicated in Section 6.4.

In conclusion, it must be stated that interpretation of deviations (from the mean) in surface temperature – as derived from thermal imagery – in terms of deviations in evaporation rate is dangerous, as deduced from Figure 83. With the reported regression coefficients and knowledge of the main parameter effects, it can be shown that a 1 K deviation from the mean surface temperature, interpreted as being caused by a difference in evaporation rate, results in a value of 30-40 W m^{-2} for this estimated deviation in evaporation rate from its
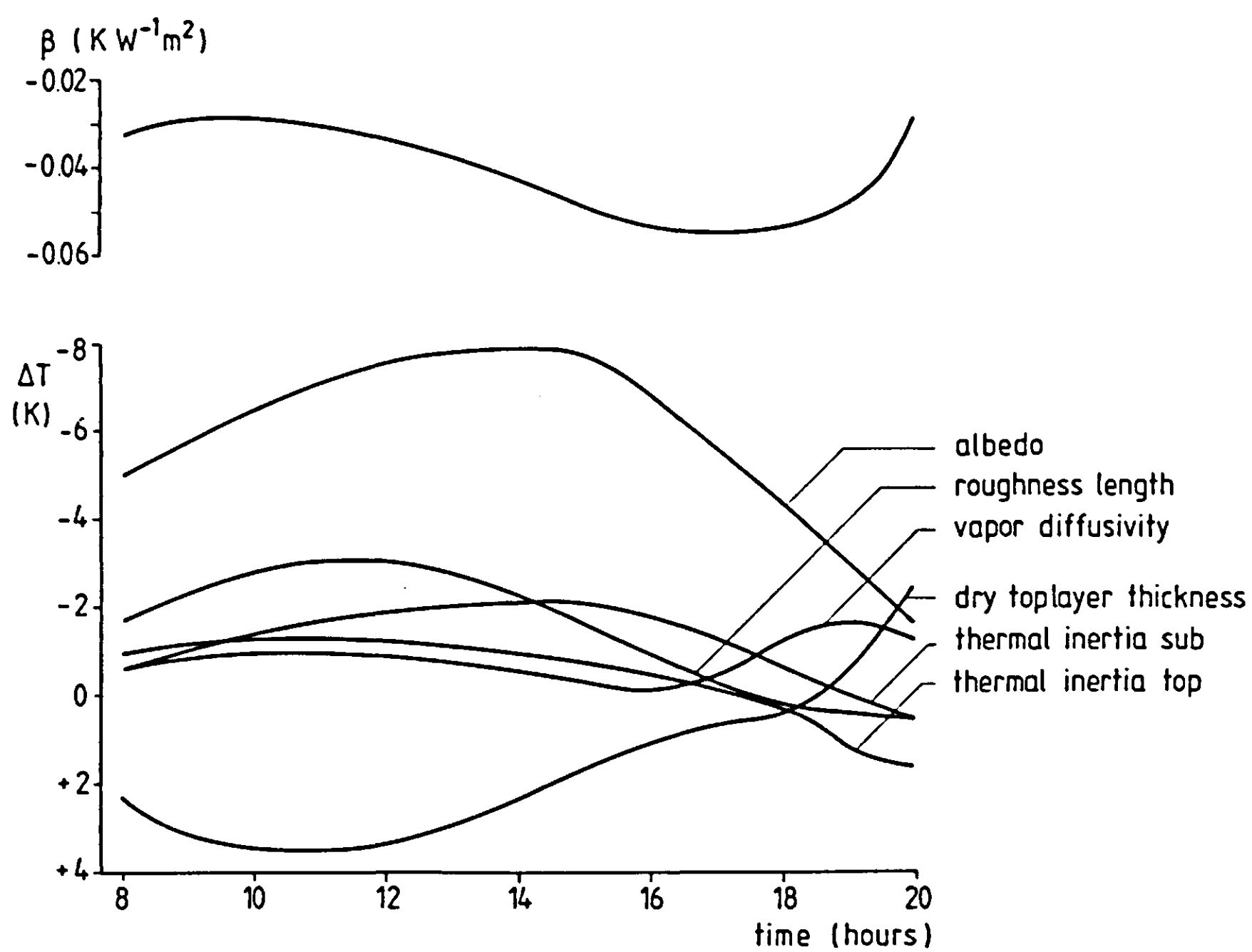
Figure 83. Main effects of various system parameters on surface temperature in stage III, corrected for covariate LE; the course of the regression coefficient β between surface temperature and latent heat flux is also indicated.

mean. As variations of several K can apparently be ascribed to variations in system parameters over the ranges indicated in Table 14 without being associated with differences in evaporation rate, considerable errors can be expected in the estimates of LE derived from observed surface temperature.

7 Thermal remote sensing and bare soil

This chapter summarizes the approaches to thermal data interpretation as applied in literature to the various types of land surfaces, and attempts to assess the feasibility of these procedures in the interpretation of bare soil imagery.

Many studies have been done on thermal sensing of land surface types such as rock surfaces and deserts where, in contrast to most soils, evaporation is negligible (Abrams et al., 1984; Tosi, 1983). Vegetated surfaces also behave very differently from bare soils, because virtually no conduction and related temperature gradients are involved in supplying the required energy for transpiration. Also, the evaporated water can be extracted from a larger soil volume by the dispersed root system, thus largely 'bypassing' soil physical constraints to water movement. Examples of the application of thermal techniques to surveying vegetated surfaces can be found in Jackson et al. (1977), Hatfield et al. (1983), Nieuwenhuis (1985) and many others.

The demand for regional hydrological information on bare soil surfaces may be illustrated by the work of Ward et al. (1982), Moore et al. (1983), England et al. (1983), and Menenti (1984). It is now generally recognized that remotely sensed data are indispensable for estimating surface variables on a regional scale. The inevitable generalizing and simplifying assumptions involved in imagery interpretation, however, must be checked carefully. Deterministic models, such as the one presented in this monograph, may be used to test the validity of such assumptions. This is seen as a typical and very useful application of dynamic simulation in remote sensing science.

In the light of the experiments, simulations and sensitivity analyses discussed in the previous chapters, the potential capabilities of thermal remote sensing for bare soil can now be suggested. To do this, the assumptions involved and the additional ground information required for several approaches to interpreting thermal imagery will be inspected briefly. It will be assumed that continuous diurnal records of the surface temperature can be obtained, in spite of the problems of timing and atmospheric distortion that are often encountered in practice (e.g. Kahle et al., 1984).

In discussing the prospects for thermal remote sensing of bare soil, a distinction must be made between two types of information pertinent to the soil surface: the information regarding the value of certain state variables, and the information on the surface fluxes. Of the latter group, attention will only be paid to the latent heat flux, because of its direct significance to hydrology and agronomy.

7.1 Estimation of soil state variables

7.1.1 Soil temperature

The variable obviously involved in thermal survey is the temperature of the soil, albeit that it is the surface radiation temperature that is observed directly. This variable itself is of no direct agronomic value. The radiation emitted by the surface is generated in the top 10-100 μm skin only. The dependence of radiation temperature on true surface temperature T_s implies that uncertainties in the emissivity ε introduce an error in the derived value for T_s. If the soil emissivity in the relevant spectral window is known with an accuracy of $\pm$ 0.04 (cf. Table 3), the surface temperature can be estimated with an accuracy of $\pm$ 3 K at best, disregarding uncertainty in sky radiation and atmospheric distortion.

Although surface temperature plays a central role in many of the surface processes, the course of soil temperature at various depths below the surface is of more general agronomic interest. Information on temperatures in the top few centimetres of soil may be relevant to the characterization of conditions for germination and root growth. Such information could also be valuable for predicting pest development. To obtain estimates of subsurface soil temperatures, a measured course of surface temperature should be combined with a model describing heat transport in the soil. The general analytical model that describes, for conduction, the development of soil temperature with depth and time in terms of Fourier series, was extensively discussed by van Duin (1956) and by van Wijk (1963). Application of such models in the above manner yields a first estimate of expected errors in predicted soil temperatures, because of uncertainties in the thermal soil properties. For the Flevo field experiments, inaccuracies in λ (θ) and C (θ) were estimated to be as high as $\pm$ 15% and 10%, respectively. This results in an error of $\pm$ 12-13% in the damping depth D of the diurnal temperature wave. Using these values in the Fourier model, one finds that the relative error in amplitude of soil temperature $^{A}T(z)$ increases from zero at the surface to 20% at the depth where $^{A}T(z) = 0.25\ ^{A}T(0)$. If the surface temperature has an amplitude of 20 K, this implies a maximum error of $\pm$ 1 K in $^{A}T(z)$ at any depth. Ignoring trends resulting from seasonal changes or from meteorological events on a synoptic scale, the average diurnal soil temperature might be taken as constant with depth. So, the average surface temperture should be a fair indicator of average soil temperature. With a possible offset in average temperature of 3 K caused by the error in observing the surface temperature (mentioned earlier), it may be stated that altogether the actual value of soil temperature can be predicted with no better accuracy than $\pm$ 3-4 K. The effect of errors in D on the phase shift is then ignored, and the thermal properties should be known with less than 15% inaccuracy, as stated. Compliance with the latter condition can be considered exceptional.

In the above, it was assumed that the soil moisture content was known, be-

140

cause thermal properties depend strongly on moisture content (cf. Chapter 2). This variable changes with depth, and bulk density also varies, therefore the errors to be expected in modelled subsurface temperature are much larger than the figures indicated here. Another aspect that has a bearing on uncertainty is the latent heat term, accounting for an accelerated decline of soil heat flux with depth where subsurface evaporation occurs. Clearly, this effect tends to reduce the diurnal amplitude of soil temperature at any depth. The error analysis presented in Chapter 5 takes into account all the sources of error mentioned here, as well as the effects of spatial variability on the initial temperature chosen. The standard deviations given in Table 12 for the errors in predicted soil temperatures, therefore, can be used as an indication of total error caused by subsurface effects. If that fraction of the variance in T_{rs} (surface radiation temperature) that results from error sources that affect both surface temperature T_s and soil temperature $T(z)$ is now subtracted from the calculated variance in soil temperature (Table 12), an estimate is obtained of the uncertainties involved in predicting soil temperature $T(z,t)$ from observed T_s. Finally, then, the offset of ± 3 K must be added to find the accuracy that can be attained in deriving bare soil temperatures from remotely sensed surface temperature. Following this procedure, one finds standard deviations of the error in soil temperature that range between 4 and 5 K. (Note that detailed information about thermal and hydraulic properties of the soil is assumed to be available, as in the experiments discussed.) It must be concluded that the combined use of remotely sensed surface temperature and detailed physical models does not improve the estimation of soil temperatures beyond the accuracy already attained by empirical models that use global radiation and air temperature as inputs.

7.1.2 Soil moisture content

Perhaps the item placed highest on the list of state variables to be derived from thermal surface information is the soil moisture content. This quantity is obviously somehow indirectly related to temperature. Numerous field studies have provided evidence of relations between surface moisture content and the behaviour of surface temperature (Vleck & King, 1983; Cihlar, 1980; Idso et al., 1975a,b,c; Heilman & Moore, 1980; Reginato et al., 1976; ten Berge et al., 1983). In the literature, the dynamics of surface temperature have been expressed in terms of diurnal amplitude of surface temperature, or in terms of difference between maximum surface and maximum air temperature, or momentary values have simply been used. The resulting empirical relations, however, could never be generalized to yield dependable formulas for image interpretation. Anyway, starting from the idea that moisture content affects thermal properties (conductivity and heat capacity), it was hoped that the concept of thermal inertia, that was originally developed for geological applications, could also be applied to bare soils. From inertia, then, information on the soil moisture content would have to be derived subsequently.

In situations where conduction is the predominant heat transfer mechanism in homogeneous soils, combination of Fourier's law

$$G_s = -\lambda \frac{\partial T}{\partial z}$$

Equation 98

with a sinusoidal behaviour of the surface temperature T_s yields the relation between surface heat flux G_s, the frequency ω and the amplitude of the surface temperature wave $^A T_s$ (van Wijk, 1963):

$$\int_{t_1}^{t_2} G_s(t)dt = A T_s \cdot \sqrt{(\omega \lambda C)} \cdot \int_{t_1}^{t_2} \sin(\omega t + \pi/4)dt$$

Equation 99

When referring to the diurnal cycle, the term $\sqrt{(\omega \lambda C)}$ is sometimes called the 'diurnal heat capacity' (Price, 1980). Thermal inertia is defined as $P \equiv \sqrt{(\lambda C)}$ (although some authors have interpreted 'thermal inertia mapping' simply as the regional registration of the diurnal amplitude of surface temperature). The 'thermal inertia approach' basically combines remote measurements of T_s with estimates of $G_s(t)$ to solve Equation 99 for $\sqrt{(\lambda C)}$. In the case of soil moisture mapping, this thermal property is subsequently translated into volumetric moisture content. Such a translation requires specific soil information, primarily on bulk density, but also on mineralogical composition. Pratt & Ellyett (1979) discussed these $P - \theta$ relations extensively. It may be stated that such specific soil information will generally not be available for remote sensing applications. In the case of close-range thermal sensing, e.g. of trial fields to evaluate soil management effects, the situation may be more favorable. Bulk density and moisture content near the soil surface can hardly ever be considered homogeneous with respect to depth, a necessary assumption made in the inertia analysis.

Aside from the above, the major difficulty of the inertia methods is in the estimation of the surface heat flux, G_s. All procedures explicitly or implicitly involve estimating – or complete ignoring – the remaining terms of the surface energy balance, i.e. net radiation R_n and the sensible and latent heat fluxes H and LE in the lower amosphere. Frequently, the sum of these two is large, and since G_s is found by subtracting this term from R_n, relative errors in G_s are large. Price (1977, 1980) formulated an analytical expression to relate daily mean evaporation rate and the diurnal heat capacity to the amplitude of surface temperature. His procedure involves using an explicit function for global radiation, and assuming that diurnal variations in H and LE depend linearly on T_s. Because G_s is depends on the surface energy budget, this method still requires estimation of the atmospheric exchange coefficients for heat and vapour; the courses of air temperature and humidity near the surface must also be known. Whereas the measurement or estimation of the latter on a regional scale presents some difficulties that might be overcome, estimating the coefficients for turbulent heat and vapour transport from simple measurements is not

feasible at present. Wind speed and the parameter z_0 govern the exchange of sensible heat and latent heat in Drying Stage I. For surfaces in Drying Stage III, the latent heat flux to the atmosphere is dominated by vapour diffusivity and 'soil vapour path length' (Chapter 6). Uncertainties in all these parameters are large for any operational field situation. Compared with the absolute value of G_s, large errors in the calculated values of H and LE must therefore be expected. In other words, the estimated G_s is relatively sensitive to these parameters. Little is known about vapour diffusivity near the soil surface under field circumstances (cf. Chapter 2). The behaviour of effective z_0 values over non-homogeneous terrain has been studied and dramatic and unexpected shifts in this parameter have been found (Kroon, 1985). Even for homogeneous trial fields, it appears difficult to determine z_0 with sufficient accuracy to render it useful for application in models of the surface energy balance (Chapter 5). The ranges chosen for parameter variation in the sensitivity analysis presented in Chapter 6 were based on possible field variations. It is probably not realistic to assume that these intervals can be narrowed down for the purpose of interpreting regional terrain imagery.

Other authors have proposed analytical approaches somewhat different from that of Price. Hechinger (1979) and England et al. (1983) based their analyses on Fourier series methods. The latter group determined the coefficient for atmospheric heat exchange, the total evaporation 'resistance' (including the soil diffusion term) and the thermal inertia of the soil simultaneously by an optimization procedure, minimizing the sum of squares between predicted and measured surface temperature. Since, at least during daytime, bare soil surface temperature is more sensitive to the transport parameters that govern H and LE than to the thermal inertia of the soil (cf. Chapter 6), it can be expected that this method does not give reliable estimates of the latter parameter either.

Alternatively, 'look-up tables' or graphs have been used (Rosema, 1979; van der Griend et al., 1985; Schieldge et al., 1980). These are created by running numerical simulation algorithms for a variety of boundary conditions and soil parameters. The simulated courses of surface variables that are obtained are then combined into nomograms that can be used to infer thermal inertia when a number of estimated or measured parameters and also the observed amplitude of surface temperature are entered. Clearly, this approach suffers basically from the same weaknesses mentioned above.

The concept of thermal admittance, being the reciprocal of complex thermal conductance, has been proposed as an alternative to thermal inertia; it theoretically allows using phase shifts of the temperature wave to account for variations of soil properties with depth (Byrne & Davis, 1980; Menenti, 1984). Aside from the fact that phase shifts can only be established under very regular boundary conditions, it can be expected that the same problems as described for inertia will present themselves, when the concept is applied to bare soils.

The figures shown in Chapter 6 demonstrate that surface temperature is most sensitive to thermal soil proporties in the early morning. During daytime, other

143

parameters dominate. Therefore, information on thermal properties is masked when minimum surface temperatures are combined with maximum surface temperatures to yield the temperature amplitude as an indicator of thermal inertia. One could consider using the night-time half of the surface heat flux curve instead, in combination with the difference between minimum surface temperature and some reference temperature, for which the air temperature at dusk can be an appropriate variable. The nocturnal part of the diurnal soil heat flux G_s should then be established on the basis of net radiation. At night the turbulent fluxes H and LE are usually negligible and G_s is closely tied to R_n (cf. Chapter 5). Recently, the remote assessment of R_n has become more feasible. In deriving inertia from an estimated heat flux, the proposed procedure would imply the reverse of the method described by Hares et al. (1985) to determine the half-daily heat flux: combining a measured ΔT_s with an estimated value of the thermal inertia, based on observed moisture content, to derive the heat intake by the soil during the day. Naturally, the problems associated with translating inertia to soil moisture content remain unresolved.

Whereas thermal inertia appears to be an unattractive variable for monitoring soil water status, the combined use of a transport model and remotely sensed flux boundary conditions could be thought of as an alternative. Such an approach was followed by Nieuwenhuis (1985) in water budgetting for crops. Stroosnijder et al. (1984) proposed an analogous procedure for bare soils, combined with microwave measurements. In this way, it might be possible to keep track of total soil moisture storage for bare soils too, provided that the course of the latent heat flux can be assessed sufficiently accurately.

For a correct simulation of the distribution of water in the soil, and notably of the impact that the diurnal cycle has on this distribution, accurate information on soil hydraulic parameters would be required. To characterize a soil in this respect, the parameters A', B' and θ_{ref} – as introduced in Section 6.4 – are considered suitable. However, these properties themselves have a dynamic character wherever tillage, soil slaking, crust formation and other changes of soil structure are common. Consequently, they cannot be determined on a sufficiently large scale by ground measurements. Yet, the accurate knowlegde of hydraulic parameters is crucial for a sensible simulation of soil water movement. The possibility of deriving such parameters from observed courses of regional evaporation over longer periods after initial wetting – under boundary conditions known by ground observation – would be an interesting topic for further research. Admittedly, the accuracy attained in the simulation of surface soil moisture dynamics is limited, even in cases where extensive data on physical soil properties are available. This is especially so where wetting and drying alternate. The experimental studies treated in this report serve to illustrate this (Chapters 4 and 5).

7.2 Estimation of the latent heat flux

Measured surface temperature has been used in various ways to estimate evaporation rates, either from crop canopies or bare soil surfaces. Among the earliest detailed field studied was the one described by Idso et al. (1975a,b,c) and Reginato et al. (1976). These authors reported mostly linear relations between relative evaporation rate E/E_0 and diurnal amplitude of surface temperature, and also between E/E_0 and maximum surface temperature minus air temperature T_a. (E_0 represents the evaporation flux under non-limiting water supply.) They used daily totals to express evaporation, and concluded that the linear relations they obtained could be used successfully to estimate daily evaporation totals from thermal data for a specific site. They commented that the relations were valid throughout the year. At first this may seem surprising, with net radiation changing. It can be understood, however, that the distortion resulting from changes in radiation is not so pronounced: an increase in net radiation will generally reduce the quotient E/E_0 but also enhance the maximum difference between surface and air temperature. Thus, data points are translated along the curve one is seeking. In contrast, changes in the governing wind speed, are expected to bring about deviations, because increasing wind speed decreases both relative evaporation E/E_0 and $(T_s - T_a)_{max}$ simultaneously. For a wheat crop, Jackson et al. (1977) employed the difference between crop canopy and air temperature $(T_c - T_a)$ in the early afternoon as an indicator of evapotranspiration ET. Their analysis explicitly involved the net radiation term, but the ground heat flux was assumed to be negligible on a daily basis; evapotranspiration was then expressed as

$$ET = R_n - B(T_c - T_a) \qquad \text{Equation 100}$$

where B is an empirical constant. The value of B was found to be independent of wind speed for the specific experimental site in Arizona.

There is no evident reason why this approach would not be valid for the calculation of evaporation from bare soil. More experimental work is required to validate the above class of relationships for a wider range of environmental conditions, but much can be done already on the basis of simulation with soil-atmosphere models. Unfortunately, the results reported by Reiniger et al. (1982) are not encouraging.

Nieuwenhuis et al. (1985) modified the above formulation and replaced net radiation by the daily potential evapotranspiration, thus basing the 'reference value' of ET not only on available energy but also implicitly on the turbulent exchange coefficient. In addition, they proposed using the difference between actual canopy temperature and the canopy temperature under potential transpiration, instead of canopy temperature minus air temperature. The daily potential evapotranspiration was then calculated by one of the accepted standard formulations. The calibration constant B, appearing in Equation 100, was

found to change with the modifications introduced, as can be expected. The Nieuwenhuis formulation certainly asks for due attention in the case of evaporation from bare soil. In view of the results given in Chapter 6, however, it may be anticipated that variations in roughness length and albedo introduce a considerable scatter in the values of the calibration constant B.

A procedure proposed by Hatfield et al. (1983) uses net radiation, surface and air temperature, and aerodynamic resistance, as inputs to estimate momentary values for ET. They obtained good results for various crops. For bare soils, however, their assumption of the soil heat flux being negligible will certainly be violated; it also seems that estimating z_0 is more difficult for bare soil surfaces than for crops, especially when the surface is fairly smooth.

Other studies of regional evapotranspiration are those by England et al. (1983) and Reiniger et al. (1982). The latter authors used numerical algorithms combined with ground-measured surface temperatures as inputs, in order to calculate cumulative daily evapotranspiration. The figures obtained were not consistent with the ground-measured evapotranspiration and it was concluded that the use of thermal imagery did not improve ground-measured ET rates. The authors ascribed the discrepancy to temporal variations in surface temperature and to the difficulties encountered in the determination of the surface roughness parameter.

As mentioned earlier (Subsection 7.1.2), England et al. (1983) attempted to estimate evaporation by an optimization procedure, matching observed and calculated surface temperatures by adjusting three parameters: the atmospheric heat transfer coefficient, an 'overall' evaporation resistance, and the thermal inertia of the soil. Such an approach does indeed seem more feasible for the determination of fluxes than for the determination of thermal inertia and the derived moisture content, as discussed in Subsection 7.1.2. Compared with the other approaches mentioned earlier, it has the advantage that no empirical constants are used. Two of the three parameters mentioned as outputs from their model are indeed closely related to surface temperature as illustrated by the figures in Section 6.4. The third, thermal inertia, should probably be omitted from the optimisation procedure, as the authors suggested.

Yet another approach for estimating evaporation from bare soil by making use of thermal imagery was applied by Menenti (1984). He expressed the actual latent heat flux at the surface as a linear combination of the two partial differentials $\partial LE/\partial T_s$ and $\partial LE/\partial a$, where T_s is the surface temperature and a the soil albedo. Both T_s and a were obtained from remotely sensed data. The method involves using a reference point where LE, T_s and a are known.

Alternatively, Menenti (1984) demonstrated the use of three reference points to form a plane, representing LE as a linearized function of T_s and a. Both these methods seem to be promising: they do not require estimates of atmospheric boundary conditions or difficult-to-obtain parameters such as roughness length, except for the reference points. The use of ground-based experimental sites – in this case to collect the required reference data – is generally a prerequi-

site for a sensible estimation of the latent heat flux. It must be remembered, however, that even small errors in the measurement of T_s result in large errors in calculated LE values. Large errors in LE are also caused when variations in soil or environmental factors result in deviations of T_s that are not related to variations in LE. This problem is shared with all the other methods discussed; for an example to illustrate it, the reader is referred to Chapter 6 (Figure 83).

Appendix 1   Derivation of Equation 50

The assumption of local equilibrium implies that for any state i the difference $H_{w_i} - TS_{w_i}$ is the same. This term, therefore, should also be equal to $H_w - TS$, where H_w and S are the specific enthalpy and specific entropy corresponding to the extramatric state of soil water (i.e. the reference state; see also Section 2.6). Combining Equations 48 and 49 then gives the total heat flux as

$$J_q = TJ_s + H_w \Sigma J_{w_i} - TS \, \Sigma J_{w_i} \qquad \text{Equation A.1}$$

where the summation ΣJ_{w_i} represents the total water flux J_w.

The continuity equation applied to the total heat flux gives the rate of change in 'volumetric heat content' $\partial(CT)/\partial t$ as the convergence of the total heat flux

$$\frac{\partial(CT)}{\partial t} = -\frac{\partial J_q}{\partial z} \qquad \text{Equation A.2}$$

The RHS of this equation may now be further identified by introducing the total entropy flux density:

$$J_s = -\frac{\lambda \nabla T}{T} + \Sigma S_{w_i} J_{w_i} \qquad \text{Equation A.3}$$

where the second term on the RHS represents the flux of entropy 'carried' by mass, and the first represents conduction.
Combining Equations A.1 and A.3 gives

$$J_q = -\lambda \nabla T + H_w J_w + T \Sigma J_{w_i}(S_{w_i} - S) \qquad \text{Equation A.4}$$

Upon introduction of the latent heat of phase transition (from state i to the reference state) as $\Delta H_i = T(S - S_{w_i})$, Equation A.4 is written as

$$J_q = -\lambda \nabla T + H_w J_w - \Sigma J_{w_i} \Delta H_i \qquad \text{Equation A.5}$$

Combining Equations A.2 and A.5 finally yields Equation 50. It is then assumed that most of the transported water, in whatever state, returns to the extramatric state after transportation.

Appendix 2   Program structure diagrams of SALSA

The figures in this appendix show the structure of the SALSA algorithm and of the principal underlying subroutines. The program structure diagrams are given in Nassi-Shneiderman notation (Nederlands Normalisatie Instituut, 1979; Martin & MacClure, 1988).
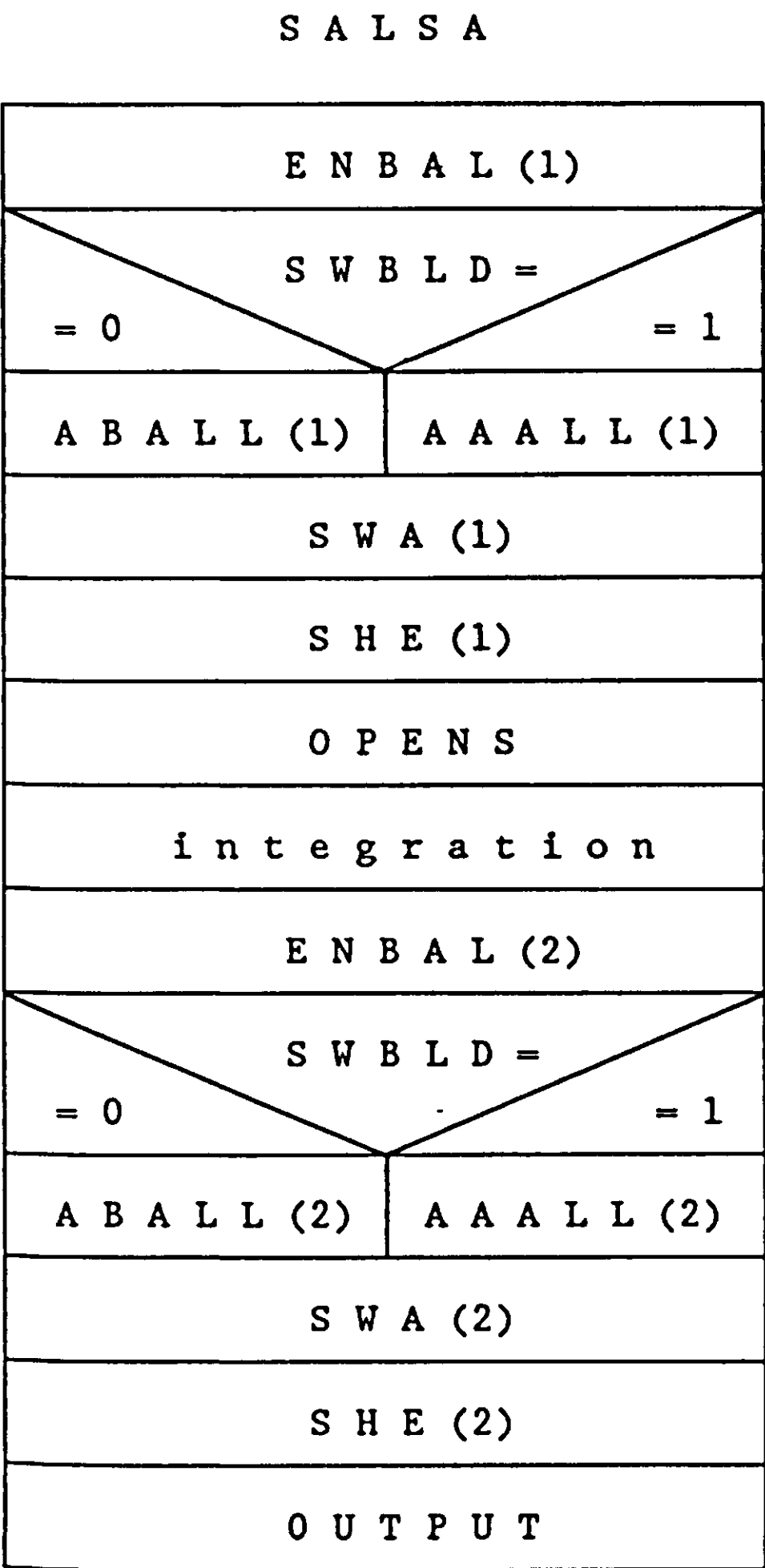
S A L S A

Figure A.1. Main program of SALSA, which comprises the principal underlying subroutines ENBAL, AAALL, ABALL, SWA, and SHE; see Figures A.2 - A.6, respectively.

E N B A L (I T A S K)

```
┌─────────────────────────────────────┐
│             I T A S K =              │
│   = 1                       = 2      │
├──────────────────┬───────────────────┤
│   E N B I N I    │    E N B R A      │
└──────────────────┴───────────────────┘
```
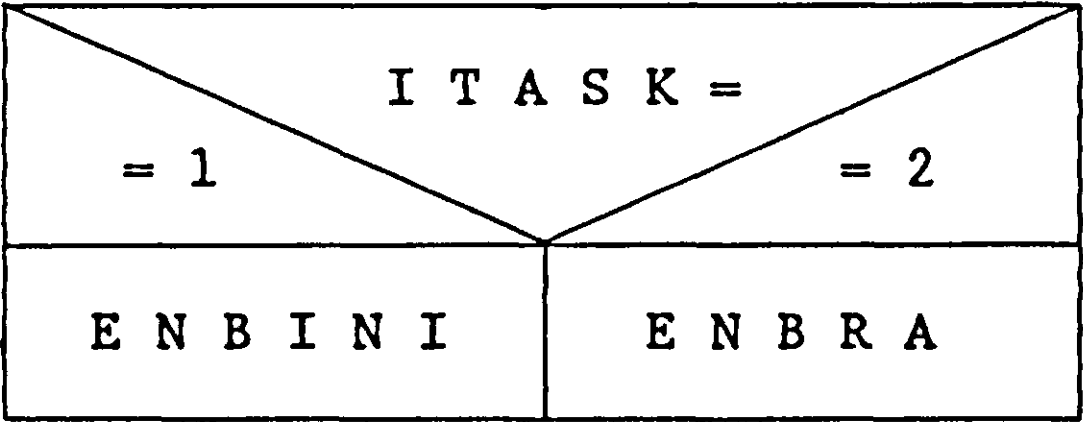
Figure A.2. Program structure diagram of ENBAL.

A A A L L (I T A S K)

```
┌─────────────────────────────────────┐
│             I T A S K =              │
│   = 1                       = 2      │
├──────────────────┬───────────────────┤
│                  │   A A A L L K     │
│    A A I N I     ├───────────────────┤
│                  │   A A A L L F     │
├──────────────────┼───────────────────┤
│                  │   A A T K E P     │
│    A D I S C R   ├───────────────────┤
│                  │   A A D D T       │
└──────────────────┴───────────────────┘
```
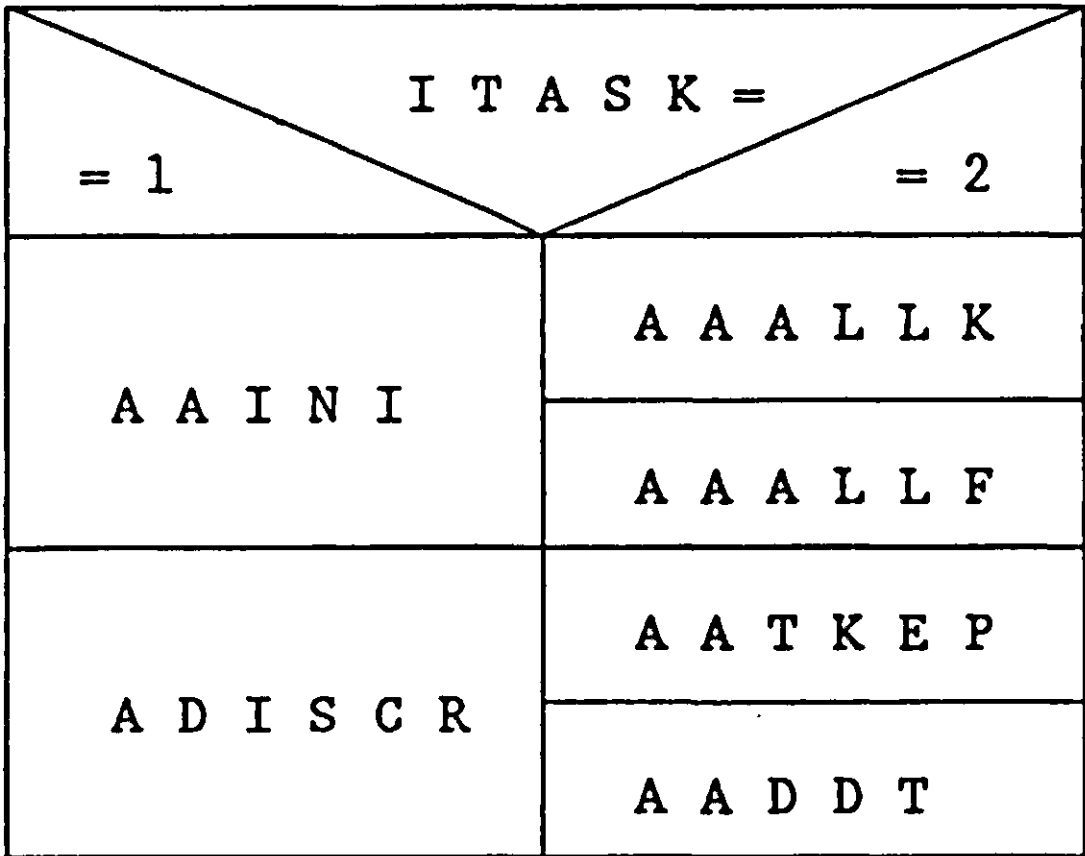
Figure A.3. Program structure diagram of AAALL.

A B A L L (I T A S K)

```
┌─────────────────────────────────────┐
│             I T A S K =              │
│   = 1                       = 2      │
├──────────────────┬───────────────────┤
│   A B I N I      │    A B R A        │
└──────────────────┴───────────────────┘
```
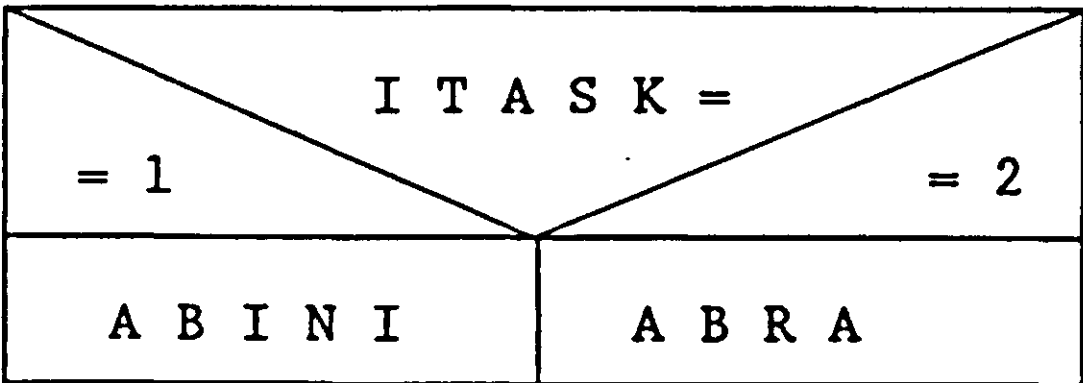
Figure A.4. Program structure diagram of ABALL.

152

S W A (I T A S K)

	I T A S K =			
	= 1		= 2	

S W A I N I	S W A V S			
	S W A V D			
	S W A V F			
	S W M F L P =			
	= 1		= 0	
	S W M T B =		S W A L P R	
	= 1	= 0		
	S W A L M T	S W A L M C	S W K T B =	
			= 0	= 1
	S W G R A V =		S W A L K C	S W A L K T
	= 0	= 1		

S D I S C R	S W K T B =		S W A L K A	
	= 0	= 1		
	SWALKC	SWALKT	S W G R A V =	
			= 0	= 1
	S W A L K A		-	S W A L G R
	S W A L G R			
	S W A L F M		S W A L F K	
	S W A D D T			
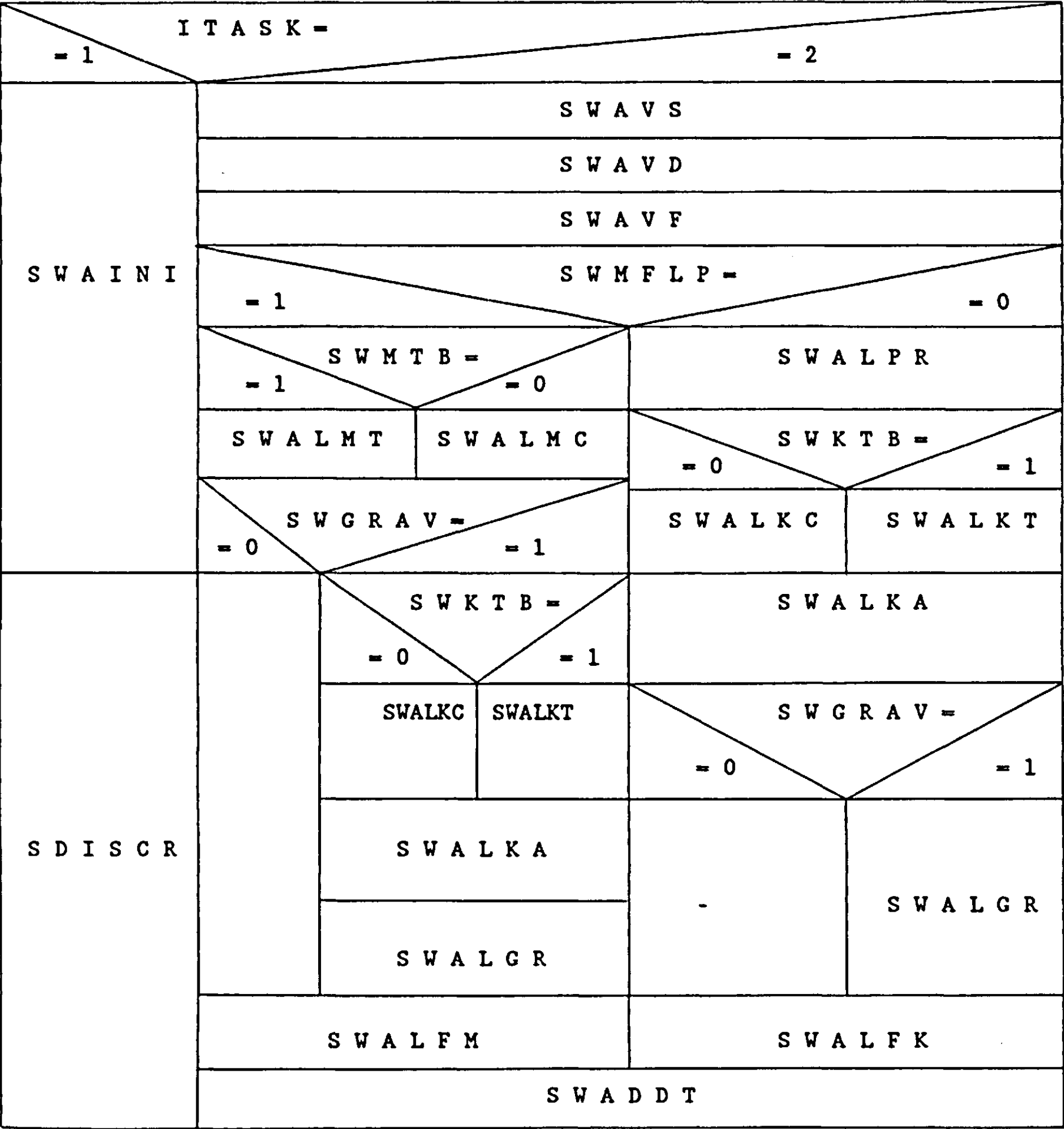
Figure A.5. Program structure diagram of SWA.

153

SHE (ITASK)

ITASK =		
= 1		= 2
SHEINI	SHECHC	
	SWCHTB =	
	= 0	= 2
	SHECCC	SHECCT
SDISCR	SHECCA	
	SHECF	
	SHEVF	
	SHEDDT	
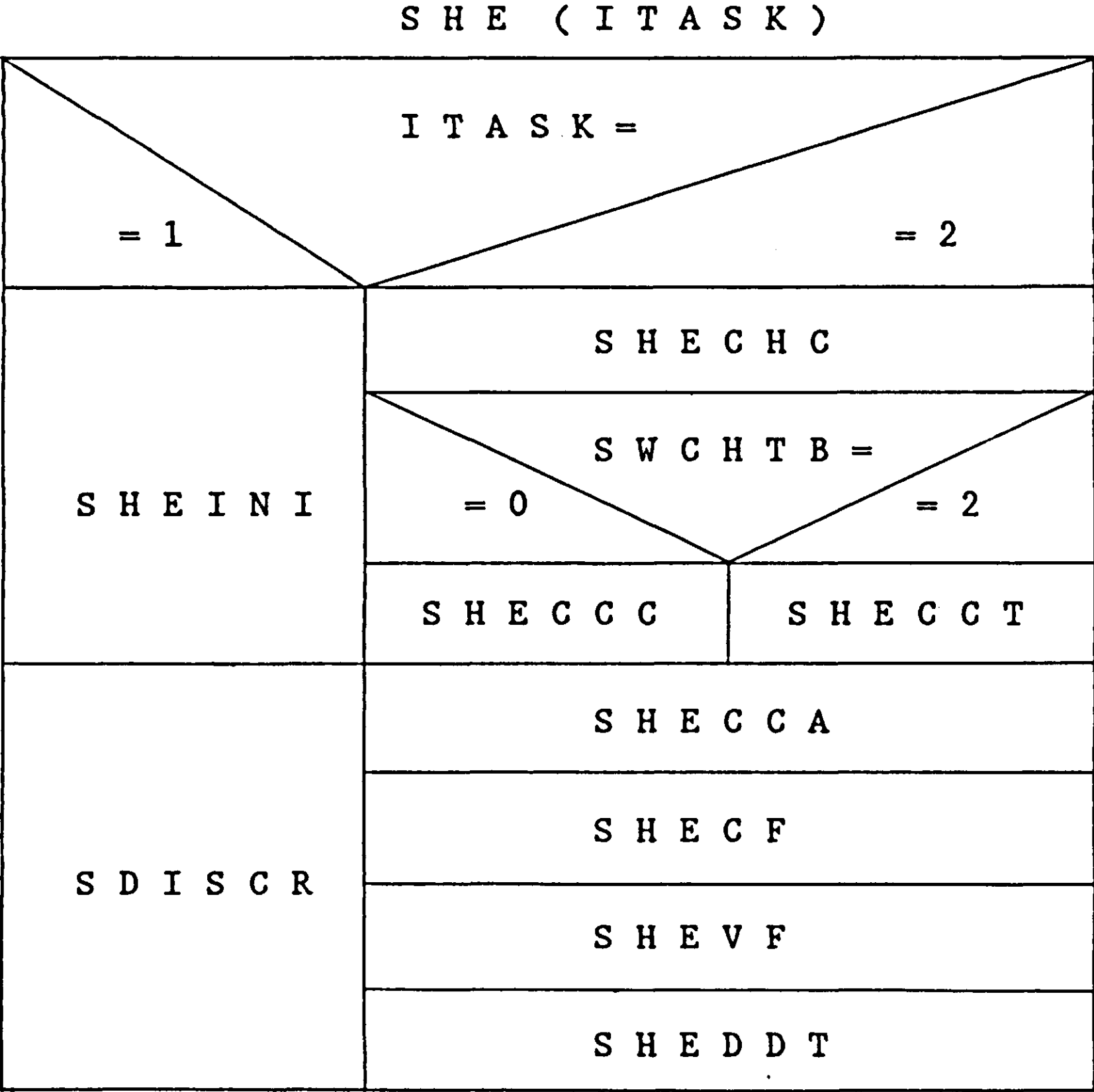
Figure A.6. Program structure diagram of SHE.

Appendix 3 Listings of SALSA modules

```
******************************************************************
*                                                                *
*             SOIL-ATMOSPHERE LINKING SIMULATION ALGORITHM       *
*                 S     A     L     S     A                       *
*                                                                *
*                   AUTHOR:  H.F.M. TEN BERGE                     *
*                   DATE: MARCH 1990                             *
*           ADRESS:  CENTER FOR AGROBIOLOGICAL RESEARCH (CABO)    *
*             P.O. BOX 14, 6700 AA WAGENINGEN, THE NETHERLANDS    *
*                                                                *
******************************************************************
      FIXED I,ISW,N,NN,SWBLD
/     DIMENSION CHSOIL(26),DZ(26),HFLCON(26),HFLVAP(26),HFLX(26)
/     DIMENSION QFLX(12),QII(11),TCM(25),TCMM(11),TII(25),TKEFLX(12)
/     DIMENSION TKEII(11),TPFLX(12),TPII(11),UII(11),UVOFLX(12)
/     DIMENSION VII(11),VVOFLX(12),WFLLIQ(26),WFLVAP(26),WFLX(26)
/     DIMENSION WII(25),Z(26),ZZ(12)
******************************************************************
      INITIAL
      NOSORT
******************************************************************
*-----run control
      PARAM STDAY-0., STHOUR-0.,READEL-1800.
      TIMER TIME-57600.,FINTIM-403200.,PRDEL-3600.
      METHOD MILNE
*-----initialization surface energy balance
      CALL ENBAL(1,CH1,CLOC,Q1,T1,TP1,RAD,RAH,RAV,QS,W1,E,GLORAD,H,...
             ATPRES,LE,NETRAD,RADEMI,SWBLD,TS,TSAPP)
*-----initialization atmosphere
      IF (SWBLD.EQ.1) THEN
        CALL AAALL(1,E,H,QII,TKEII,TPII,TS,UII,VII,DQDT,DTKEDT,DTPDT,...
             DUDT,DVDT,NN,QFLX,RAH,RAM,RAV,TCMM,TKEFLX,TPFLX,...
             UVOFLX,VVOFLX,ZZ)
        DO 10 I-1,NN
           QI(I)-QII(I)
           TKEI(I)-TKEII(I)
           TPI(I)-TPII(I)
           UI(I)-UII(I)
           VI(I)-VII(I)
10      CONTINUE
      ELSE
        CALL ABALL(1,H,TP1,TS,U1,RAH,RAM,RAV)
      ENDIF
*-----initialization soil (water)
      CALL SWA(1,T,RAIN,WII,DWDT,DZ,N,QS,TCM,WFLLIQ,WFLVAP,WFLX,Z)
      DO 20 I-1,N
         WI(I)-WII(I)
20    CONTINUE
*-----initialization soil (heat)
      CALL SHE(1,TII,TS,W,CHSOIL,DTDT,GFLX,HFLCON,HFLVAP,HFLX)
      DO 30 I-1,N
         TI(I)-TII(I)
30    CONTINUE
*-----opening weather file
      CALL OPENS
```

```
*****************************************************************
        DYNAMIC
        NOSORT
*****************************************************************
*-----integration
        Q   -INTGRL(QI,DQDT,11)
        T   -INTGRL(TI,DTDT,25)
        TKE-INTGRL(TKEI,DTKEDT,11)
        TP -INTGRL(TPI,DTPDT,11)
        U   -INTGRL(UI,DUDT,11)
        V   -INTGRL(VI,DVDT,11)
        W   -INTGRL(WI,DWDT,25)
*-----updating of surface conditions
        IF(SWBLD.EQ.1) THEN
            Q1-Q(1)
            TP1-TP(1)
        ENDIF
        W1-W(1)
        T1-T(1)
        CH1-CHSOIL(1)
*-----reading of measured boundary conditions
        IF(KEEP.EQ.0.OR.IMPULS(0.,READEL).EQ.0) THEN
            CONTINUE
        ELSEIF(SWBLD.EQ.1) THEN
            READ(50,40) RAD,RAIN,CLOC
40          FORMAT(21X,F6.2,19X,F4.2,1X,F4.2)
        ELSE
            READ(50,50) RAD,TP1,VPA,U1,RAIN,CLOC
50          FORMAT(21x,F6.2,1x,F5.2,1x,F6.1,1X,F4.2,1X,F4.2,1X,F4.2)
            Q1-(VPA/ATPRES)*(5./8.)
        ENDIF
*-----solution of surface energy balance
        CALL ENBAL(2,CH1,CLOC,Q1,T1,TP1,RAD,RAH,RAV,QS,W1,E,GLORAD,H,...
                   ATPRES,LE,NETRAD,RADEMI,SWBLD,TS,TSAPP)

*-----calculation of rates in atmosphere
        IF(SWBLD.EQ.1) THEN
         CALL AAALL(2,E,H,Q,TKE,TP,TS,U,V,DQDT,DTKEDT,DTPDT,DUDT,DVDT,...
                    NN,QFLX,RAH,RAM,RAV,TCMM,TKEFLX,TPFLX,UVOFLX,...
                    VVOFLX, ZZ)
        ELSE
         CALL ABALL(2,H,TP1,TS,U1,RAH,RAM,RAV)
        ENDIF
*-----calculation of rates in soil (water)
        CALL SWA(2,T,RAIN,W,DWDT,DZ,N,QS,TCM,WFLLIQ,WFLVAP,WFLX,Z)
*-----calculation of rates in soil (heat)
        CALL SHE(2,T,TS,W,CHSOIL,DTDT,GFLX,HFLCON,HFLVAP,HFLX)
*-----output preparation
        IF(KEEP.EQ.1) THEN
            ISW-IMPULS(0.,PRDEL)
            CALL OUTPUT(DELT,GFLX,H,ISW,LE,NETRAD,STDAY,STHOUR,TIME,TSAPP)
        ENDIF
*****************************************************************
        TERMINAL
*****************************************************************
        CALL CLOSES
*       for reruns:
*       END RERUN ...
*       CALL OPENS
END
STOP
* insert subroutines here
ENDJOB
```

```
      SUBROUTINE AAALL(ITASK,E,H,Q,TKE,TP,TS,U,V,
     $                 DQDT,DTKEDT,DTPDT,DUDT,DVDT,NN,QFLX,RAH,RAM,
     $                 RAV,TCMM,TKEFLX,TPFLX,UVOFLX,VVOFLX,ZZ)
      IMPLICIT  REAL (A-Z)
      INTEGER   ITASK,NN
      DIMENSION DQDT(11),DTKEDT(11),DTPDT(11),DUDT(11),DVDT(11)
      DIMENSION DZZ(12),EPRBUO(12),EPRDIS(12),EPRSRX(12),EPRSRY(12)
      DIMENSION INVLM(12),KH(12),KM(12),KV(12),Q(11),QFLX(12),TCMM(11)
      DIMENSION TKE(11),TKEFLX(12),TP(11),TPFLX(12),U(11),UVOFLX(12)
      DIMENSION V(11),VVOFLX(12),ZZ(12)
      DATA VG/0./
      IF(ITASK.EQ.1) THEN
         CALL AAINI(ALPHA,CORIOL,NN,UG,TCMM,INVCOR,Q,TKE,TP,U,
     $              V,YUC)
         CALL ADISCR(NN,TCMM,DZZ,ZZ)
      ELSE
         CALL AAALLK(INVCOR,NN,TCMM,TKE,TP,TPFLX,TS,U,UVOFLX,V,VVOFLX,
     $               YUC,ZNOT,ZZ,KH,KM,KV,RAH,RAM,RAV)
         CALL AAALLF(DZZ,E,H,KH,KM,KV,NN,Q,RAM,TKE,TP,U,V,QFLX,TKEFLX,
     $               TPFLX,UVOFLX,VVOFLX)
         CALL AATKEP(DZZ,INVLM,NN,TKE,TP,TPFLX,U,UVOFLX,
     $               V,VVOFLX,YUC,EPRBUO,EPRDIS,EPRSRX,EPRSRY)
         CALL AADDT(CORIOL,EPRBUO,EPRDIS,EPRSRX,EPRSRY,NN,QFLX,TCMM,
     $              TKEFLX,TPFLX,U,UG,UVOFLX,V,VG,VVOFLX,DQDT,DTKEDT,
     $              DTPDT,DUDT,DVDT)
      ENDIF
      RETURN
      END


      SUBROUTINE AAALLF(DZZ,E,H,KH,KM,KV,NN,Q,RAM,TKE,TP,U,V,
     $                  QFLX,TKEFLX,TPFLX,UVOFLX,VVOFLX)
      IMPLICIT REAL (A-Z)
      INTEGER I,NN
      DIMENSION DZZ(12),KH(12),KM(12),KV(12),Q(11),QFLX(12)
      DIMENSION TKE(11),TKEFLX(12),TP(11),TPFLX(12),U(11)
      DIMENSION UVOFLX(12),V(11),VVOFLX(12)
      DATA CP,RHOAIR/1.E3,1.2/
      DATA TINY/1.E-5/
      UVOFLX(1)=U(1)/(RAM+TINY)
      VVOFLX(1)=V(1)/(RAM+TINY)
      TPFLX(1) =H/(RHOAIR*CP)
      QFLX(1)  =E/RHOAIR
      TKEFLX(1)=0.0
      DO 10 I=2,NN
         UVOFLX(I)=KM(I)*(U(I)-U(I-1))/DZZ(I)
         VVOFLX(I)=KM(I)*(V(I)-V(I-1))/DZZ(I)
         TPFLX(I) =KH(I)*(TP(I)-TP(I-1))/DZZ(I)
         QFLX(I)  =KV(I)*(Q(I)-Q(I-1))/DZZ(I)
         TKEFLX(I)=KM(I)*(TKE(I)-TKE(I-1))/DZZ(I)
10    CONTINUE
      RETURN
      END


      SUBROUTINE AAALLK(INVCOR,NN,TCMM,TKE,TP,TPFLX,TS,U,
     $                  UVOFLX,V,VVOFLX,YUC,ZNOT,ZZ,
     $                  KH,KM,KV,RAH,RAM,RAV)
      IMPLICIT  REAL (A-Z)
      INTEGER   I,NN
      DIMENSION INVLH(12),INVLM(12),KH(12),KM(12),KV(12),OBU(12)
      DIMENSION PHIH(12),PHIM(12),PSIHTB(18),PSIMTB(18),RMOFLX(12)
      DIMENSION STAPAR(12),TCMM(11),TKE(11),TKEAV(12),TP(11),TPAV(12)
      DIMENSION TPFLX(12),U(11),UVOFLX(12),V(11),VVOFLX(12),ZZ(12)
      DATA PSIHTB/ -3.0,2.77, -2.0,2.43, -1.5,2.2, -1.0,1.88,
     $             -0.5,1.39, -0.25,0.96, -0.1,0.53, 0.0,0.0,
     $             1.0,-4.7/
```

```fortran
      DATA PSIMTB/ -3.0,1.74, -2.0,1.5, -1.5,1.34, -1.0,1.12,
     $             -0.5,0.79, -0.25,0.54, -0.1,0.28, 0.0,0.0,
     $             1.0,-4.7/
      DATA KAR,G,TZERO/0.41,9.8,273.2/
      DATA TINY/1.E-5/
      TPAV(1)=0.5*(TS+TP(1))
      DO 10 I=2,NN
          TPAV(I)=(TP(I)*TCMM(I)+TP(I-1)*TCMM(I-1))/(TCMM(I)+TCMM(I-1))
10    CONTINUE
      DO 20 I=1,NN
          RMOFLX(I)=SQRT(UVOFLX(I)**2+VVOFLX(I)**2)
          OBU(I)=(TPAV(I)+TZERO)*((ABS(RMOFLX(I)))**1.5)/
     $           (KAR*G*TPFLX(I)+TINY)
          STAPAR(I)=ZZ(I)/(OBU(I)+TINY)
          IF(STAPAR(I).LT.-3.) THEN
              STAPAR(I)=-3.
          ELSEIF(STAPAR(I).GT.1.0) THEN
              STAPAR(I)=1.0
          ELSE
              CONTINUE
          ENDIF
          IF(I.EQ.1) STAPAR(I)=0.5*STAPAR(I)
          IF(STAPAR(I).LT.0.) THEN
              PHIM(I)=(1.-16.*STAPAR(I))**(-0.25)
              PHIH(I)=PHIM(I)*PHIM(I)
          ELSE
              PHIM(I)=1.+4.7*STAPAR(I)
              PHIH(I)=PHIM(I)
          ENDIF
          INVLM(I)=PHIM(I)/(KAR*ZZ(I))+INVCOR
          INVLH(I)=PHIH(I)/(KAR*ZZ(I))+INVCOR
20    CONTINUE
      DO 30 I=2,NN
          TKEAV(I)=(TCMM(I)*TKE(I)+TCMM(I-1)*TKE(I-1))/(TCMM(I)+
     $             TCMM(I-1))
          KM(I)=(1./INVLM(I))*((YUC*TKEAV(I))**0.5)
          IF(TKEAV(I).LE.0.) KM(I)=0.0
          KH(I)=KM(I)*INVLM(I)/INVLH(I)
          KV(I)=KH(I)
30    CONTINUE
      PSIM=LINT(PSIMTB,18,STAPAR(1))
      PSIH=LINT(PSIHTB,18,STAPAR(1))
      SURWIN=SQRT(U(1)**2.+V(1)**2.)
      RAM=((ALOG(ZZ(1)/ZNOT)-PSIM)**2)/(SURWIN*KAR**2+TINY)
      RAH=(ALOG(ZZ(1)/ZNOT)-PSIH)*(ALOG(ZZ(1)/ZNOT)-PSIM)/
     $    (SURWIN*KAR**2+TINY)
      RAV=RAH
      RETURN
      END


      SUBROUTINE AADDT(CORIOL,EPRBUO,EPRDIS,EPRSRX,EPRSRY,NN,QFLX,
     $                 TCMM,TKEFLX,TPFLX,U,UG,UVOFLX,V,VG,VVOFLX,
     $                 DQDT,DTKEDT,DTPDT,DUDT,DVDT)
      IMPLICIT REAL(A-Z)
      INTEGER I,NN
      DIMENSION ACCPRX(12),ACCPRY(12),DIVQ(12),DIVTKE(12),DIVTP(12)
      DIMENSION DIVUVO(12),DIVVVO(12),DQDT(11),DTKEDT(11),DTPDT(11)
      DIMENSION DUDT(11),DVDT(11),EPRBUO(12),EPRDIS(12),EPRSRY(12)
      DIMENSION EPRSRX(12),QFLX(12),TCMM(11),TKEFLX(12),TPFLX(12)
      DIMENSION U(11),UVOFLX(12),V(11),VVOFLX(12)
      DO 10 I=1,NN
          DIVUVO(I)=(UVOFLX(I+1)-UVOFLX(I))/TCMM(I)
          DIVVVO(I)=(VVOFLX(I+1)-VVOFLX(I))/TCMM(I)
```

158

```
      DIVTP(I)  =(TPFLX(I+1)-TPFLX(I))/TCMM(I)
      DIVTKE(I)-(TKEFLX(I+1)-TKEFLX(I))/TCMM(I)
      DIVQ(I)   =(QFLX(I+1)-QFLX(I))/TCMM(I)
10    CONTINUE
      DO 20 I=1,NN
          ACCPRY(I)=-CORIOL*(U(I)-UG)
          ACCPRX(I)=+CORIOL*(V(I)-VG)
20    CONTINUE
      DO 30 I=1,NN
          DTKEDT(I)=EPRSRX(I)+EPRSRY(I)+EPRBUO(I)+EPRDIS(I)+DIVTKE(I)
          DUDT(I)=ACCPRX(I)+DIVUVO(I)
          DVDT(I)=ACCPRY(I)+DIVVVO(I)
          DTPDT(I)=DIVTP(I)
          DQDT(I)=DIVQ(I)
30    CONTINUE
      RETURN
      END


      SUBROUTINE AAINI(
     $                 ALPHA,CORIOL,NN,UG,TCMM,
     $                 INVCOR,QI,TKEI,TPI,UI,VI,YUC)
      IMPLICIT REAL (A-Z)
      INTEGER NN,NN2,NN3,NN4,NN5,NN6,NN7
      DIMENSION QI(11),TCMM(11),TKEI(11),TPI(11),UI(11),VI(11)
      CALL RDSINT('NN',NN)
      CALL RDSREA('YUC',YUC)
      CALL RDSREA('CORIOL',CORIOL)
      CALL RDSREA('ZNOT',ZNOT)
      CALL RDSREA('UG',UG)
      CALL RDSREA('ALPHA',ALPHA)
      CALL RDSREA('ATPRES',ATPRES)
      CALL RDAREA('QI',QI,11,NN2)
      CALL RDAREA('TKEI',TKEI,11,NN3)
      CALL RDAREA('TPI',TPI,11,NN4)
      CALL RDAREA('UI',UI,11,NN5)
      CALL RDAREA('VI',VI,11,NN6)
      CALL RDAREA('TCMM',TCMM,11,NN7)
      IF(NN2.NE.NN) CALL ERROR('AAINI','INCONSISTENT COMPARTMNT NR')
      IF(NN3.NE.NN) CALL ERROR('AAINI','INCONSISTENT COMPARTMNT NR')
      IF(NN4.NE.NN) CALL ERROR('AAINI','INCONSISTENT COMPARTMNT NR')
      IF(NN5.NE.NN) CALL ERROR('AAINI','INCONSISTENT COMPARTMNT NR')
      IF(NN6.NE.NN) CALL ERROR('AAINI','INCONSISTENT COMPARTMNT NR')
      IF(NN7.NE.NN) CALL ERROR('AAINI','INCONSISTENT COMPARTMNT NR')
      INVCOR=CORIOL/(ALPHA*ABS(UG))
      RETURN
      END


      SUBROUTINE AATKEP(DZZ,INVLM,NN,TKE,TP,TPFLX,U,UVOFLX,V,VVOFLX,
     $                 YUC,
     $                 EPRBUO,EPRDIS,EPRSRX,EPRSRY)
      IMPLICIT REAL (A-Z)
      INTEGER I,NN
      DIMENSION DUDZZ(12),DVDZZ(12),DZZ(12),EPRBUO(12),EPRDIS(12)
      DIMENSION EPRSRX(12),EPRSRY(12),INVLM(12),TKE(11),TP(11)
      DIMENSION TPFLX(12),U(11),UVOFLX(12),V(11),VVOFLX(12)
      DATA G,TZERO/9.8,273.2/
      DUDZZ(1)=U(1)/DZZ(1)
      DVDZZ(1)=V(1)/DZZ(1)
      DO 10 I=2,NN
          DUDZZ(I)=(U(I)-U(I-1))/DZZ(I)
          DVDZZ(I)=(V(I)-V(I-1))/DZZ(I)
10    CONTINUE
      DO 20 I=1,NN
```

```fortran
      EPRSRX(I)-(UVOFLX(I)*DUDZZ(I)*DZZ(I)+UVOFLX(I+1)*DUDZZ(I+1)*
     $           DZZ(I+1)) /(DZZ(I)+DZZ(I+1))
      EPRSRY(I)-(VVOFLX(I)*DVDZZ(I)*DZZ(I)+VVOFLX(I+1)*DVDZZ(I+1)*
     $           DZZ(I+1))/(DZZ(I)+DZZ(I+1))
      EPRBUO(I)--(TPFLX(I)*DZZ(I)+TPFLX(I+1)*DZZ(I+1))*G/((TP(I)+
     $           TZERO)*(DZZ(I)+DZZ(I+1)))
      EPRDIS(I)--((YUC*TKE(I))**1.5)*(INVLM(I)+INVLM(I+1))/2.
 20   CONTINUE
      EPRDIS(1)--((YUC*TKE(1))**1.5)*INVLM(1)
      RETURN
      END


      SUBROUTINE ABALL(ITASK,H,TP1,TS,U1,
     $                 RAH,RAM,RAV)
      IMPLICIT REAL (A-Z)
      INTEGER ITASK
      IF (ITASK.EQ.1) THEN
         CALL ABINI(ZNOT,ZZ1)
      ELSE
         CALL ABRA(H,TP1,TS,U1,ZNOT,ZZ1,
     $             RAH,RAM,RAV)
      ENDIF
      RETURN
      END


      SUBROUTINE ABINI(
     $                 ZNOT,ZZ1)
      IMPLICIT REAL (A-Z)
      CALL RDSREA('ZNOT',ZNOT)
      CALL RDSREA('ZMEA',ZMEA)
      ZZ1-0.5*ZMEA
      RETURN
      END


      SUBROUTINE ABRA(H,TP1,TS,U1,ZNOT,ZZ1,
     $                RAH,RAM,RAV)
      IMPLICIT REAL (A-Z)
      DIMENSION PSIHTB(18),PSIMTB(18)
      DATA PSIHTB/ -3.0,2.77, -2.0,2.43, -1.5,2.2, -1.0,1.88,
     $             -0.5,1.39, -0.25,0.96, -0.1,0.53, 0.0,0.0,
     $             1.0,-4.7/
      DATA PSIMTB/ -3.0,1.74, -2.0,1.5, -1.5,1.34, -1.0,1.12,
     $             -0.5,0.79, -0.25,0.54, -0.1,0.28, 0.0,0.0,
     $             1.0,-4.7/
      DATA RHOAIR,CP,G,KAR,TZERO/1.2,1.0E3,9.8,0.41,273.2/
      DATA TINY/1.E-5/
      TPAV1-0.5*(TS+TP1)
      TPFLX1-H/(RHOAIR*CP)
      RMOFL1-U1/(RAM+TINY)
      OBU1-(TPAV1+TZERO)*(ABS(RMOFL1)**1.5)/(KAR*G*TPFLX1+TINY)
      STAPR1-0.5*ZZ1/(OBU1+TINY)
      IF(STAPR1.LT.-3.) THEN
         STAPR1--3.
      ELSEIF(STAPR1.GT.1.0) THEN
         STAPR1-1.0
      ELSE
         CONTINUE
      ENDIF
      PSIM-LINT(PSIMTB,18,STAPR1)
      PSIH-LINT(PSIHTB,18,STAPR1)
      SURWIN-U1
      RAM-((ALOG(ZZ1/ZNOT)-PSIM)**2)/(SURWIN*KAR**2+TINY)
      RAH-(ALOG(ZZ1/ZNOT)-PSIH)*(ALOG(ZZ1/ZNOT)-PSIM)/
```

```
     $     (SURWIN*KAR**2+TINY)
      RAV=RAH
      RETURN
      END

      SUBROUTINE ADISCR(NN,TCMM,
     $                        DZZ,ZZ)
      IMPLICIT REAL (A-Z)
      INTEGER I,NN
      DIMENSION DZZ(12),TCMM(11),ZZ(12)
      ZZ(1)=0.5*TCMM(1)
      SUM=0.
      DO 10 I=2,NN
          ZZ(I)=SUM+TCMM(I-1)
          SUM=ZZ(I)
10    CONTINUE
      DZZ(1)=0.5*TCMM(1)
      DO 20 I=2,NN
          DZZ(I)=0.5*(TCMM(I-1)+TCMM(I))
20    CONTINUE
      RETURN
      END

      SUBROUTINE CLOSES
      CLOSE(50)
      CLOSE(51)
      RETURN
      END

      SUBROUTINE ENBAL(ITASK,CH1,CLOC,Q1,T1,TP1,RAD,RAH,RAV,QS,W1,
     $                 E,GLORAD,H,ATPRES,LE,NETRAD,RADEMI,
     $                 SWBLD,TS,TSAPP)
      IMPLICIT REAL (A-Z)
      INTEGER ITASK,SWNET,SWBLD
      IF(ITASK.EQ.1) THEN
          CALL ENBINI(ADRY,ATPRES,AWET,CH1,CLON,DZ1,EDRY,EMIASS,EWET,
     $                LONREF,RAH,RAV,SKYA,SKYB,SKYTEM,SWBLD,
     $                SWNET,WCRITA,WSAT1)
      ELSE
          CALL ENBRA(ADRY,ATPRES,AWET,CH1,CLOC,CLON,DZ1,EDRY,EMIASS,
     $               EWET,LONREF,NETRAD,Q1,QS,RAD,RAH,RAV,SKYA,SKYB,
     $               SKYTEM,SWNET,T1,TP1,W1,WCRITA,WSAT1,
     $               E,GLORAD,H,LE,RADEMI,TS,TSAPP)
      ENDIF
      RETURN
      END

      SUBROUTINE ENBINI(
     $                ADRY,ATPRES,AWET,CH1,CLON,DZ1,EDRY,EMIASS,EWET,
     $                LONREF,RAH,RAV,SKYA,SKYB,SKYTEM,SWBLD,
     $                SWNET,WCRITA,WSAT1)
      IMPLICIT REAL (A-Z)
      INTEGER N1,SWNET,SWBLD
      DIMENSION TCM(25)
      CALL RDINIT(52,53,'RUNCON.DAT')
      CALL RDSREA('ADRY',ADRY)
      CALL RDSREA('ATPRES',ATPRES)
      CALL RDSREA('AWET',AWET)
      CALL RDSREA('CLON',CLON)
      CALL RDSREA('EDRY',EDRY)
      CALL RDSREA('EMIASS',EMIASS)
      CALL RDSREA('EWET',EWET)
      CALL RDSREA('LONREF',LONREF)
      CALL RDSREA('SKYA',SKYA)
```

161

```
                CALL RDSREA('SKYB',SKYB)
                CALL RDSREA('SKYTEM',SKYTEM)
                CALL RDSINT('SWNET',SWNET)
                CALL RDSINT('SWBLD',SWBLD)
                CALL RDSREA('WCRITA',WCRITA)
                CALL RDSREA('WSAT1',WSAT1)
                CALL RDAREA('TCM',TCM,25,N1)
                DZ1=0.5*TCM(1)
                CH1=1.
                RAH=100.
                RAV=100.
                RETURN
                END


                SUBROUTINE ENBRA(ADRY,ATPRES,AWET,CH1,CLOC,CLON,DZ1,EDRY,EMIASS,
             $                  EWET,LONREF,NETRAD,Q1,QS,RAD,RAH,RAV,SKYA,SKYB,
             $                  SKYTEM,SWNET,T1,TP1,W1,WCRITA,WSAT1,
             $                  E,GLORAD,H,LE,RADEMI,TS,TSAPP)
                IMPLICIT REAL (A-Z)
                INTEGER SWNET
                DATA RHOCP,RHOAIR,BOLZ,TZERO,LVAP/1.2E3,1.2,5.67E-8,273.2,
             $                                    2.45E6/
                VPA=(8./5.)*Q1*ATPRES
                EMISKY=(SKYA+SKYB*(SQRT(VPA/100.)))*(1.+CLON*CLOC*CLOC)
                LONGIN=EMISKY*BOLZ*((TP1+TZERO)**4.)
                ALB=AWET+(ADRY-AWET)*(WCRITA-W1)/WCRITA
                IF(W1.GT.WCRITA) ALB=AWET
                EMISOI=EDRY+(EWET-EDRY)*W1/WSAT1
                TSOLD=0.
                TSNEW=T1
10              IF(ABS(TSNEW-TSOLD).GT.0.1) THEN
                    TSOLD=TSNEW
                    H=RHOCP*(TP1-TSOLD)/RAH
                    RADEMI=-EMISOI*BOLZ*(TSOLD+TZERO)**4.
                    HFLCON=CH1*(T1-TSOLD)/DZ1
                    IF(SWNET.EQ.1) THEN
                        NETRAD=RAD
                        GLORAD=99999.
                    ELSE
                        GLORAD=RAD
                        NETRAD=(1-ALB)*GLORAD+(1.-LONREF)*LONGIN+RADEMI
                    ENDIF
                    SUM=H+NETRAD+HFLCON
                    DFDX=(-RHOCP/RAH)+(-4.*EMISOI*BOLZ*(TSOLD+TZERO)**3.)+
             $          (-CH1/DZ1)
                    TSNEW=TSOLD-SUM/DFDX
                    GOTO 10
                ENDIF
                TS=TSNEW
                E=RHOAIR*(Q1-QS)/RAV
                LE=LVAP*E
                TSAPP=((-RADEMI+(1.-EMISOI)*BOLZ*(SKYTEM+TZERO)**4.)/
             $        (EMIASS*BOLZ))**0.25-TZERO
                RETURN
                END


                SUBROUTINE OPENS
                OPEN(50,STATUS='OLD',FILE='WEATHER.DAT')
                OPEN(51,STATUS='NEW',FILE='OUT.DAT')
                RETURN
                END
```

```fortran
      SUBROUTINE OUTPUT(DELT,GFLX,H,ISW,LE,NETRAD,STDAY,STHOUR,TIME,
     $                  TSAPP)
      IMPLICIT REAL (A-Z)
      INTEGER ISW
      TSINT=TSINT+TSAPP*DELT
      RNINT=RNINT+NETRAD*DELT
      GINT=GINT+GFLX*DELT
      HINT=HINT+H*DELT
      LEINT=LEINT+LE*DELT
      SUMTIM=SUMTIM+DELT
      IF (ISW.EQ.1) THEN
          HOURS=STHOUR+TIME/3600.
          HOUR=AMOD(HOURS,24.)
          DAY=STDAY+HOURS/24.
          TSPRI=TSINT/SUMTIM
          RNPRI=RNINT/SUMTIM
          GPRI=GINT/SUMTIM
          HPRI=HINT/SUMTIM
          LEPRI=LEINT/SUMTIM
          BOW=0.
          IF(HOUR.GT.8..AND.HOUR.LT.20.) BOW=HPRI/LEPRI
          WRITE(51,*) DAY,HOUR,TSPRI,RNPRI,GPRI,HPRI,LEPRI,BOW
*--------other output variables user choice;
*         adapt OUTPUT argument list
          TSINT=0.
          RNINT=0.
          GINT=0.
          HINT=0.
          LEINT=0.
          SUMTIM=0.
      ELSE
          CONTINUE
      ENDIF
      RETURN
      END


      SUBROUTINE SDISCR(N,TCM,
     $                  DZ,Z)
      IMPLICIT REAL (A-Z)
      INTEGER I,N
      DIMENSION DZ(26),TCM(25),Z(26)
      DZ(1)=0.5*TCM(1)
      DO 10 I=2,N
          DZ(I)=0.5*(TCM(I)+TCM(I-1))
10    CONTINUE
      DZ(N+1)=0.5*TCM(N)
      Z(1)=0.5*TCM(1)
      DO 20 I=2,N
          Z(I)=Z(I-1)+0.5*(TCM(I-1)+TCM(I))
20    CONTINUE
      RETURN
      END


      SUBROUTINE SHE(ITASK,T,TS,W,
     $               CHSOIL,DTDT,GFLX,HFLCON,HFLVAP,HFLX)
      IMPLICIT REAL (A-Z)
      INTEGER ITASK,N,NCHTB,SWCHTB
      DIMENSION BDRAT(26)
      DIMENSION CHAV(26),CHSLO2(26),CHSLO5(26),CHSOIL(26),CHTB(100)
      DIMENSION DTDT(25),DZ(26),FC(26),FO(26),FQ(26)
      DIMENSION HCSOIL(26),HFLCON(26),HFLVAP(26),HFLX(26)
      DIMENSION KFCSA(26),KFCSW(26),KFSA(26),KFSW(26),POR(26)
      DIMENSION T(25),TCM(25),W(25),WFLVAP(26),Z(26)
```

163

```
*       physical constants
        DATA CHA,CHW/25.E-3,0.57/
        DATA HCC,HCO,HCQ,HCW,LVAP/2.4E6,2.5E6,2.1E6,4.2E6,
     $                          2.45E6/
        IF (ITASK.EQ.1) THEN
            CALL SHEINI(
     $                  BDRAT,CHSL02,CHSL05,CHTB,FC,FO,FQ,KAW,KFCSA,
     $                  KFCSW,KFSA,KFSW,KWA,N,NCHTB,POR,SWCHTB,TCM,T)
            CALL SDISCR(N,TCM,
     $                  DZ,Z)
        ELSE
            CALL SHECHC(FC,FO,FQ,HCC,HCO,HCQ,HCW,N,W,
     $                  HCSOIL)
            IF(SWCHTB.EQ.0) THEN
                CALL SHECCC(CHA,CHSL02,CHSL05,CHW,KAW,KFCSA,KFCSW,
     $                  KFSA,KFSW,KWA,N,POR,W,
     $                  CHSOIL)
            ELSE
                CALL SHECCT(BDRAT,CHTB,N,NCHTB,W,
     $                  CHSOIL)
            ENDIF
            CALL SHECCA(CHSOIL,N,TCM,
     $                  CHAV)
            CALL SHECF(CHAV,DZ,N,T,TS,
     $                  HFLCON)
            CALL SHEVF(LVAP,N,WFLVAP,
     $                  HFLVAP)
            CALL SHEDDT(HCSOIL,HFLCON,HFLVAP,N,TCM,
     $                  GFLX,HFLX,DTDT)
        ENDIF
        RETURN
        END


        SUBROUTINE SHECCA(CHSOIL,N,TCM,
     $                      CHAV)
        IMPLICIT REAL (A-Z)
        INTEGER I,N
        DIMENSION CHAV(26),CHSOIL(26),TCM(25)
        CHAV(1)=CHSOIL(1)
        DO 10 I=2,N
            CHAV(I)=(CHSOIL(I-1)*TCM(I-1)+CHSOIL(I)*TCM(I))/
     $                  (TCM(I-1)+TCM(I))
10      CONTINUE
        RETURN
        END


        SUBROUTINE SHECCC(CHA,CHSL02,CHSL05,CHW,KAW,KFCSA,KFCSW,
     $                      KFSA,KFSW,KWA,N,POR,W,
     $                      CHSOIL)
        IMPLICIT REAL (A-Z)
        INTEGER I,N
        DIMENSION CHSL02(26),CHSL05(26),CHSOIL(26),FA(26),KFCSA(26)
        DIMENSION KFCSW(26),KFSA(26),KFSW(26),POR(26),W(25)
        DO 10 I=1,N
            FA(I)=POR(I)-W(I)
            IF(W(I).LE.0.02) THEN
                CHSOIL(I)=1.25*(CHW*W(I)*KWA+FA(I)*CHA+KFCSA(I))/
     $                  (KFSA(I)+KWA*W(I)+FA(I))
            ELSEIF(W(I).LT.0.05) THEN
                CHSOIL(I)=CHSL02(I)+(W(I)-0.02)*(CHSL05(I)-CHSL02(I))/0.03
            ELSE
                CHSOIL(I)=W(I)*CHW+FA(I)*KAW*CHA+KFCSW(I)/(W(I)+KAW*
     $                  FA(I)+KFSW(I))
```

164

```
            ENDIF
10      CONTINUE
        RETURN
        END


        SUBROUTINE SHECCT(BDRAT,CHTB,N,NCHTB,W,
      $                   CHSOIL)
        IMPLICIT REAL (A-Z)
        INTEGER I,N,NCHTB
        DIMENSION BDRAT(26),CHTB(100),CHSOIL(26),W(25)
        DO 10 I=1,N
           CHSOIL(I)=BDRAT(I)*LINT(CHTB,NCHTB,W(I))
10      CONTINUE
        RETURN
        END


        SUBROUTINE SHECF(CHAV,DZ,N,T,TS,
      $                   HFLCON)
        IMPLICIT REAL (A-Z)
        INTEGER I,N
        DIMENSION CHAV(26),DZ(26),HFLCON(26),T(25)
        HFLCON(1)=-(TS-T(1))*CHAV(1)/DZ(1)
        DO 10 I=2,N
           HFLCON(I)=CHAV(I)*(T(I)-T(I-1))/DZ(I)
10      CONTINUE
        HFLCON(N+1)=0.
        RETURN
        END


        SUBROUTINE SHECHC(FC,FO,FQ,HCC,HCO,HCQ,HCW,N,W,
      $                   HCSOIL)
        IMPLICIT REAL (A-Z)
        INTEGER I,N
        DIMENSION FC(26),FO(26),FQ(26),HCSOIL(26),W(25)
        DO 10 I=1,N
           HCSOIL(I)=FC(I)*HCC+FQ(I)*HCQ+FO(I)*HCO+W(I)*HCW
10      CONTINUE
        RETURN
        END


        SUBROUTINE SHEDDT(HCSOIL,HFLCON,HFLVAP,N,TCM,
      $                   GFLX,HFLX,DTDT)
        IMPLICIT REAL (A-Z)
        INTEGER I,N
        DIMENSION DIVHFL(26),DTDT(25),HCSOIL(26),HFLCON(26),HFLVAP(26)
        DIMENSION HFLX(26),TCM(25)
        DO 10 I=1,N
           HFLX(I)=HFLCON(I)+HFLVAP(I)
10      CONTINUE
        HFLX(N+1)=0.
        GFLX=HFLX(1)
        DO 20 I=1,N
           DIVHFL(I)=(HFLX(I+1)-HFLX(I))/TCM(I)
           DTDT(I)=-DIVHFL(I)/HCSOIL(I)
20      CONTINUE
        RETURN
        END


        SUBROUTINE SHEINI(
      $                   BDRAT,CHSL02,CHSL05,CHTB,FC,FO,FQ,
      $                   KAW,KFCSA,KFCSW,KFSA,KFSW,KWA,N,NCHTB,POR,
      $                   SWCHTB,TCM,TI)
        IMPLICIT REAL (A-Z)
        INTEGER I,N,N2,N3,N4,NCHTB,SWCHTB
```

```fortran
      DIMENSION BD(26),BDRAT(26),CHSLO2(26),CHSLO5(26),CHTB(100)
      DIMENSION FC(26),FO(26),FQ(26),KFCSA(26),KFCSW(26),KFSA(26)
      DIMENSION KFSW(26),POR(26),TCM(25),TI(25)
      DATA CHA,CHC,CHO,CHQ,CHW/25.E-3,2.9,0.25,8.8,0.57/
      CALL RDSREA('BDSTAN',BDSTAN)
      CALL RDSREA('FC1',FC1)
      CALL RDSREA('FO1',FO1)
      CALL RDSREA('FQ1',FQ1)
      CALL RDSREA('GA',GA)
      CALL RDSREA('GC',GC)
      CALL RDSREA('GO',GO)
      CALL RDSREA('GQ',GQ)
      CALL RDSREA('GW',GW)
      CALL RDSREA('POR1',POR1)
      CALL RDSINT('N',N)
      CALL RDSINT('SWCHTB',SWCHTB)
      CALL RDAREA('TCM',TCM,25,N2)
      CALL RDAREA('TI',TI,25,N3)
      CALL RDAREA('BD',BD,25,N4)
      CALL RDAREA('CHTB',CHTB,100,NCHTB)
      IF(N2.NE.N) CALL ERROR('SHEINI','INCONSISTENT COMPARTMNT NR')
      IF(N3.NE.N) CALL ERROR('SHEINI','INCONSISTENT COMPARTMNT NR')
      IF(N4.NE.N) CALL ERROR('SHEINI','INCONSISTENT COMPARTMNT NR')
      DO 10 I=1,N
         BDRAT(I)=BD(I)/BDSTAN
         FC(I)=FC1*BDRAT(I)
         FO(I)=FO1*BDRAT(I)
         FQ(I)=FQ1*BDRAT(I)
         POR(I)=1.-FC(I)-FO(I)-FQ(I)
10    CONTINUE
      IF(SWCHTB.NE.1) THEN
      KAW=.66/(1.+((CHA/CHW)-1.)*GA)+.33/(1.+((CHA/CHW)-1.)*(1.-2.*GA))
      KQW=.66/(1.+((CHQ/CHW)-1.)*GQ)+.33/(1.+((CHQ/CHW)-1.)*(1.-2.*GQ))
      KOW=.66/(1.+((CHO/CHW)-1.)*GO)+.33/(1.+((CHO/CHW)-1.)*(1.-2.*GO))
      KCW=.66/(1.+((CHC/CHW)-1.)*GC)+.33/(1.+((CHC/CHW)-1.)*(1.-2.*GC))
      KWA=.66/(1.+((CHW/CHA)-1.)*GW)+.33/(1.+((CHW/CHA)-1.)*(1.-2.*GW))
      KQA=.66/(1.+((CHQ/CHA)-1.)*GQ)+.33/(1.+((CHQ/CHA)-1.)*(1.-2.*GQ))
      KOA=.66/(1.+((CHO/CHA)-1.)*GO)+.33/(1.+((CHO/CHA)-1.)*(1.-2.*GO))
      KCA=.66/(1.+((CHC/CHA)-1.)*GC)+.33/(1.+((CHC/CHA)-1.)*(1.-2.*GC))
      DO 20 I=1,N
         CHSLO2(I)=1.25*(KWA*.02*CHW+KOA*FO(I)*CHO+KQA*FQ(I)*CHQ+KCA*
     $             FC(I)*CHC+(POR(I)-.02)*CHA)/(KWA*.02+KOA*FO(I)+KQA*
     $             FQ(I)+KCA*FC(I)+(POR(I)-0.02))
         CHSLO5(I)=(.05*CHW+KOW*FO(I)*CHO+KQW*FQ(I)*CHQ+KCW*FC(I)*CHC+
     $             KAW*(POR(I)-.05)*CHA)/(.05+KOW*FO(I)+ KQW*FQ(I)+KCW*
     $             FC(I)+KAW*(POR(I)-.05))
         KFCSA(I)=KOA*FO(I)*CHO+KQA*FQ(I)*CHQ+KCA*FC(I)*CHC
         KFSA(I)=KOA*FO(I)+KQA*FQ(I)+KCA*FC(I)
         KFCSW(I)=KOW*FO(I)*CHO+KQW*FQ(I)*CHQ+KCW*FC(I)*CHC
         KFSW(I)=KOW*FO(I)+KQW*FQ(I)+KCW*FC(I)
20    CONTINUE
      ELSE
         CONTINUE
      ENDIF
      RETURN
      END

      SUBROUTINE SHEVF(LVAP,N,WFLVAP,
     $                 HFLVAP)
      IMPLICIT REAL (A-Z)
      INTEGER I,N
      DIMENSION HFLVAP(26),WFLVAP(26)
      DO 10 I=1,N
```

```
            HFLVAP(I)-LVAP*WFLVAP(I)
10      CONTINUE
        HFLVAP(N+1)-0.
        RETURN
        END


        SUBROUTINE SWA(ITASK,T,RAIN,W,
     $                    DWDT,DZ,N,QS,TCM,WFLLIQ,WFLVAP,WFLX,Z)
        IMPLICIT REAL (A-Z)
        INTEGER I,ITASK,N,NMTB,NKTB,SWGRAV,SWKTB,SWMFLP,SWMTB
        DIMENSION DAV(26),DWDT(25),DZ(26),HRH(26),K(26),KAV(26)
        DIMENSION KSAT(26),KTB(100),MFLP(26),MTB(100),P(26),RH(26),T(25)
        DIMENSION TCM(25),VGA(26),VGM(26),VGN(26),VPD(26),W(25),W15(26)
        DIMENSION W30(26),WFLLGR(26),WFLLIQ(26),WFLVAP(26),WFLX(26)
        DIMENSION WREL(26),WREL15(26),WRES(26),WSAT(26),Z(26)
        DATA DNOT,RHOL,MH2O,G,RGAS,TZERO/2.29E-5,1.E3,18.E-3,9.8,8.31,
     $                                  273.2/
        IF (ITASK.EQ.1) THEN
            CALL SWAINI(BCARY,HRH,KSAT,KTB,MFA,MFB,MTB,N,NKTB,NMTB,
     $                  SCALE,SWGRAV,SWKTB,SWMFLP,SWMTB,TCM,VGA,VGM,
     $                  VGN,W15,W30,W,WREL15,WRES,WSAT)
            CALL SDISCR(N,TCM,DZ,Z)
        ELSE
            CALL SWAVS(HRH,N,T,W,W15,W30,QS,RH,VPD)
            CALL SWAVD(BCARY,DNOT,N,T,TZERO,W,WSAT,DAV)
            CALL SWAVF(E,DAV,DZ,N,VPD,WFLVAP)
            DO 10 I-1,N+1
                WFLLGR(I)-0.
10          CONTINUE
            IF(SWMFLP.EQ.0) THEN
                CALL SWALPR(MH2O,N,RGAS,RH,RHOL,SCALE,T,TZERO,VGA,VGM,VGN,
     $                      W,W15,WRES,WSAT,P,WREL)
                IF(SWKTB.EQ.0) THEN
                    CALL SWALKC(KSAT,N,VGM,W,WREL,WRES,K)
                ELSE
                    CALL SWALKT(KTB,NKTB,N,W,K)
                ENDIF
                CALL SWALKA(K,N,SCALE,KAV)
                IF(SWGRAV.EQ.1) THEN
                    CALL SWALGR(N,RHOL,G,KAV,WFLLGR)
                ENDIF
                CALL SWALFK(DZ,KAV,N,P,RAIN,WFLLGR,WFLLIQ)
            ELSE
                IF(SWMTB.EQ.1) THEN
                    CALL SWALMT(MTB,NMTB,N,SCALE,W,MFLP)
                ELSE
                    CALL SWALMC(MFA,MFB,N,SCALE,W,WMFO,MFLP)
                ENDIF
                IF(SWGRAV.EQ.1) THEN
                    IF(SWKTB.EQ.1) THEN
                        CALL SWALKT(KTB,NKTB,N,W,K)
                    ELSE
                        CALL SWALKC(KSAT,N,VGM,W,WREL,WRES,K)
                    ENDIF
                    CALL SWALKA(K,N,SCALE,KAV)
                    CALL SWALGR(N,RHOL,G,KAV,WFLLGR)
                ENDIF
                CALL SWALFM(DZ,MFLP,N,RAIN,WFLLGR,WFLLIQ)
            ENDIF
            CALL SWADDT(N,RHOL,TCM,WFLLIQ,WFLVAP,WFLX,DWDT)
        ENDIF
        RETURN
        END
```

```fortran
      SUBROUTINE SWADDT(N,RHOL,TCM,WFLLIQ,WFLVAP,
     $                  WFLX,DWDT)
      IMPLICIT REAL (A-Z)
      INTEGER I,N
      DIMENSION DIVWFL(26),DWDT(25),TCM(25)
      DIMENSION WFLLIQ(26),WFLVAP(26),WFLX(26)
      DO 10 I-1,N+1
          WFLX(I)-WFLLIQ(I)+WFLVAP(I)
10    CONTINUE
      DO 20 I-1,N
          DIVWFL(I)-(WFLX(I+1)-WFLX(I))/TCM(I)
          DWDT(I)-DIVWFL(I)/RHOL
20    CONTINUE
      RETURN
      END


      SUBROUTINE SWAINI(
     $                  BCARY,HRH,KSAT,KTB,MFA,MFB,MTB,N,NKTB,NMTB,
     $                  SCALE, SWGRAV,SWKTB,SWMFLP,SWMTB,TCM,VGA,VGM,
     $                  VGN,W15,W30,WI,WREL15,WRES,WSAT)
      IMPLICIT REAL (A-Z)
      INTEGER I,N,N2,N3,NKTB,NMTB,SWMFLP,SWKTB,SWMTB,SWGRAV
      DIMENSION FC(26),HRH(26),KSAT(26),KTB(100),MTB(100)
      DIMENSION TCM(25),VGA(26),VGM(26),VGN(26),W15(26),W30(26)
      DIMENSION WI(25),WREL15(26),WRES(26),WSAT(26)
      DATA RHOL,RHOCLY/1.E3,2650./
      CALL RDSINT('N',N)
      CALL RDSINT('SWMFLP',SWMFLP)
      CALL RDSINT('SWKTB',SWKTB)
      CALL RDSINT('SWMTB',SWMTB)
      CALL RDSINT('SWGRAV',SWGRAV)
      CALL RDSREA('WSAT1',WSAT1)
      CALL RDSREA('WRES1',WRES1)
      CALL RDSREA('VGA1',VGA1)
      CALL RDSREA('VGN1',VGN1)
      CALL RDSREA('KSAT1',KSAT1)
      CALL RDSREA('SCALE',SCALE)
      CALL RDSREA('MFA',MFA)
      CALL RDSREA('MFB',MFB)
      CALL RDSREA('WMFO',WMFO)
      CALL RDSREA('A',A)
      CALL RDSREA('FC1',FC1)
      CALL RDSREA('BCARY',BCARY)
      CALL RDAREA('TCM',TCM,25,N2)
      CALL RDAREA('WI',WI,25,N3)
      IF(N2.NE.N) CALL ERROR('SWAINI','INCONSISTENT COMPARTMNT NR')
      IF(N3.NE.N) CALL ERROR('SWAINI','INCONSISTENT COMPARTMNT NR')
      CALL RDAREA('MTB',MTB,100,NMTB)
      CALL RDAREA('KTB',KTB,100,NKTB)
      DO 10 I-1,N
          WSAT(I)-WSAT1
          WRES(I)-WRES1
          VGA(I)-VGA1
          VGN(I)-VGN1
          FC(I)-FC1
          VGM(I)-1.-1./VGN(I)
          KSAT(I)-KSAT1
          HRH(I)-RHOL/(A*FC(I)*RHOCLY)
          W30(I)-1./HRH(I)
          WREL15(I)-(((VGA(I)*15.0E05)**VGN(I))+1.)**(-VGM(I))
          W15(I)-(WSAT(I)-WRES(I))*WREL15(I)+WRES(I)
10    CONTINUE
      RETURN
      END
```

168

```fortran
      SUBROUTINE SWALFK(DZ,KAV,N,P,RAIN,WFLLGR,
     $                  WFLLIQ)
      IMPLICIT REAL (A-Z)
      INTEGER I,N
      DIMENSION DZ(26),KAV(26),P(26),WFLLIQ(26),WFLLGR(26)
      WFLLIQ(1)=AMAX1(-RAIN/86400.,KAV(1)*P(1)/DZ(1)+WFLLGR(1))
      WFLLIQ(1)=AMIN1(0.,WFLLIQ(1))
      DO 10 I=2,N
          WFLLIQ(I)=-KAV(I)*(P(I-1)-P(I))/DZ(I)+WFLLGR(I)
10    CONTINUE
      RETURN
      END


      SUBROUTINE SWALFM(DZ,MFLP,N,RAIN,WFLLGR,
     $                  WFLLIQ)
      IMPLICIT REAL (A-Z)
      INTEGER I,N
      DIMENSION DZ(26),MFLP(26),WFLLIQ(26),WFLLGR(26)
      WFLLIQ(1)=AMAX1(-RAIN/86400.,MFLP(1)/DZ(1)+WFLLGR(1))
      WFLLIQ(1)=AMIN1(0.,WFLLIQ(1))
      DO 10 I=2,N
          WFLLIQ(I)=(MFLP(I)-MFLP(I-1))/DZ(I)+WFLLGR(I)
10    CONTINUE
      RETURN
      END


      SUBROUTINE SWALGR(N,RHOL,G,KAV,
     $                  WFLLGR)
      IMPLICIT REAL (A-Z)
      INTEGER I,N
      DIMENSION KAV(26),WFLLGR(26)
      DO 10 I=1,N
          WFLLGR(I)=-KAV(I)*RHOL*G
10    CONTINUE
      RETURN
      END


      SUBROUTINE SWALKA(K,N,SCALE,
     $                  KAV)
      IMPLICIT REAL (A-Z)
      INTEGER I,N
      DIMENSION K(26),KAV(26)
      KAV(1)=K(1)
      DO 10 I=2,N
          KAV(I)=(SCALE**2)*SQRT(K(I-1)*K(I))
10    CONTINUE
      RETURN
      END


      SUBROUTINE SWALKC(KSAT,N,VGM,W,WREL,WRES,
     $                  K)
      IMPLICIT REAL (A-Z)
      INTEGER I,N
      DIMENSION K(26),KSAT(26),VGM(26),W(25),WREL(26),WRES(26)
      DO 10 I=1,N
          IF(W(I).LE.WRES(I)) THEN
              K(I)=0.0
          ELSE
              K(I)=KSAT(I)*SQRT(WREL(I))*(1.-(1.-WREL(I)**
     $            (1./VGM(I)))**VGM(I))**2.
          ENDIF
10    CONTINUE
      RETURN
      END
```

```fortran
      SUBROUTINE SWALKT(KTB,NKTB,N,W,
     $                  K)
      IMPLICIT REAL (A-Z)
      INTEGER I,N,NKTB
      DIMENSION K(26),KTB(100),W(25)
      DO 10 I=1,N
         K(I)=LINT(KTB,NKTB,W(I))
10    CONTINUE
      RETURN
      END


      SUBROUTINE SWALMC(MFA,MFB,N,SCALE,W,WMFO,
     $                  MFLP)
      IMPLICIT REAL (A-Z)
      INTEGER I,N
      DIMENSION MFLP(26),W(25)
      DO 10 I=1,N
         MFLP(I)=-SCALE*MFA*(1.-W(I)/WMFO)/(MFB+1.-W(I)/WMFO)
         IF(W(I).GE.WMFO) MFLP(I)=0.
10    CONTINUE
      RETURN
      END


      SUBROUTINE SWALMT(MTB,NMTB,N,SCALE,W,
     $                  MFLP)
      IMPLICIT REAL (A-Z)
      INTEGER I,N,NMTB
      DIMENSION MFLP(26),W(25),MTB(100)
      DO 10 I=1,N
         MFLP(I)=SCALE*LINT(MTB,NMTB,W(I))
10    CONTINUE
      RETURN
      END


      SUBROUTINE SWALPR(MH2O,N,RGAS,RH,RHOL,SCALE,T,TZERO,VGA,VGM,VGN,
     $                  W,W15,WRES,WSAT,
     $                  P,WREL)
      IMPLICIT REAL(A-Z)
      INTEGER I,N
      DIMENSION RH(26),T(25),VGA(26),VGM(26),VGN(26),W(25),W15(26)
      DIMENSION WREL(26),WRES(26),WSAT(26),P(26)
      DO 10 I=1,N
         WREL(I)=(W(I)-WRES(I))/(WSAT(I)-WRES(I))
         IF(W(I).GE.W15(I)) THEN
            P(I)=-(1./VGA(I))*(WREL(I)**(-1./VGM(I))-1.)**(1./VGN(I))
            P(I)=P(I)/SCALE
         ELSE
            P(I)=RHOL*RGAS*(T(I)+TZERO)*(ALOG(RH(I)))/MH2O
            P(I)=P(I)/SCALE
         ENDIF
10    CONTINUE
      RETURN
      END


      SUBROUTINE SWAVD(BCARY,DNOT,N,T,TZERO,W,WSAT,
     $                  DAV)
      IMPLICIT REAL (A-Z)
      INTEGER I,N
      DIMENSION DATM(26),DAV(26),T(25),W(25),WSAT(26)
      DO 10 I=1,N
         DATM(I)=DNOT*((T(I)+TZERO)/TZERO)**1.75
         IF(W(I).GE.WSAT(I)) DATM(I)=0.
         DAV(I)=BCARY*SQRT(DATM(I)*DATM(I-1))
```

170

```
10      CONTINUE
        RETURN
        END

        SUBROUTINE SWAVF(E,DAV,DZ,N,VPD,
     $                   WFLVAP)
        IMPLICIT REAL(A-Z)
        INTEGER I,N
        DIMENSION DAV(26),DZ(26),VPD(26),WFLVAP(26)
        WFLVAP(1)=-E
        DO 10 I=2,N
            WFLVAP(I)=DAV(I)*(VPD(I)-VPD(I-1))/DZ(I)
10      CONTINUE
        RETURN
        END

        SUBROUTINE SWAVS(HRH,N,T,W,W15,W30,
     $                   QS,RH,VPD)
        IMPLICIT REAL (A-Z)
        INTEGER I,N
        DIMENSION HRH(26),RH(26),T(25),VPD(26),VPDS(26),VPDSTB(34)
        DIMENSION W(25),W15(26),W30(26)
        DATA VPDSTB/0.0,4.84E-3, 4.0,6.35E-3, 8.0,8.26E-3, 12.,1.06E-2,
     $              16.,1.36E-2, 20.,1.73E-2, 24.,2.17E-2, 28.,2.72E-2,
     $              32.,3.37E-2, 36.,4.16E-2, 40.,5.10E-2, 44.,6.22E-2,
     $              48.,7.55E-2, 52.,9.06E-2, 56.,1.09E-1, 60.,1.29E-1,
     $              64.,1.54E-1/
        DO 10 I=1,N
            VPDS(I)=LINT(VPDSTB,34,T(I))
            IF(W(I).GE.W15(I)) THEN
                RH(I)=1.0
            ELSEIF(W(I).GT.W30(I)) THEN
                RH(I)=0.8+0.2*(W(I)-W30(I))/(W15(I)-W30(I))
            ELSE
                RH(I)=HRH(I)*W(I)*0.8
            ENDIF
            VPD(I)=RH(I)*VPDS(I)
10      CONTINUE
        RHS=RH(1)
        QS=RHS*LINT(VPDSTB,34,T(1))
        RETURN
        END
```

Appendix 4   List of variables in SALSA modules

Array variables are indicated by brackets.

A	gravimetric moisture content on clay at relative humidity of 0.8	$kg\ kg^{-1}$
ACCPRX()	acceleration by pressure gradient in x-direction	$m\ s^{-2}$
ACCPRY()	acceleration by pressure gradient in y-direction	$m\ s^{-2}$
ADRY	albedo of dry soil	-
ALB	soil albedo	-
ALPHA	empirical constant in turbulent length scale	-
ANGLE()	wind direction with respect to geostrophic wind	-
ATPRES	atmospheric pressure	Pa
AWET	albedo of wet soil	-
BCARY	vapour diffusion enhancement factor	-
BD()	dry soil bulk density	$kg\ m^{-3}$
BDSTAN	standard dry soil bulk density	$kg\ m^{-3}$
BOLZ	Stefan-Boltzmann constant	$W\ m^{-2}K^{-4}$
BOW	Bowen ratio	-
CHA	thermal conductivity of air	$W\ m^{-1}K^{-1}$
CHAV()	soil thermal conductivity averaged	$W\ m^{-1}K^{-1}$
CHC	thermal conductivity of clay	$W\ m^{-1}K^{-1}$
CHO	thermal conductivity of organic matter	$W\ m^{-1}K^{-1}$
CHQ	thermal conductivity of quartz	$W\ m^{-1}K^{-1}$
CHSLO2()	soil thermal conductivity at 2% vol. moisture	$W\ m^{-1}K^{-1}$
CHSLO5()	soil thermal conductivity at 5% vol. moisture	$W\ m^{-1}K^{-1}$
CHSOIL	bulk soil thermal conductivity	$W\ m^{-1}K^{-1}$
CHW	thermal conductivity of water	$W\ m^{-1}K^{-1}$
CLOC	cloud cover	-
CLON	parameter in sky emissivity	-
CORIOL	Coriolis parameter	s^{-1}
CP	heat capacity of air	$J\ kg^{-1}K^{-1}$
DATM	water vapour diffusivity in free air	m^2s^{-1}
DAV()	average vapour diffusivity	m^2s^{-1}
DAY	day number	d
DIVHFL()	divergence of soil heat flux	$J\ m^{-3}s^{-1}$
DIVQ()	divergence of specific humidity flux atmosphere	s^{-1}
DIVTKE()	divergence of kinetic energy flux atmosphere	m^2s^{-3}
DIVTP()	divergence of potential temperature flux	$K\ s^{-1}$
DIVUVO()	divergence of 'x-wind velocity flux'	$m\ s^{-2}$
DIVVVO()	divergence of 'y-wind velocity flux'	$m\ s^{-2}$
DIVWFL()	divergence of soil water flux	$kg\ m^{-3}s^{-1}$
DNOT	water vapour diffusivity at standard temperature	m^2s^{-1}
DQDT()	rate of change of specific humidity atmosphere	s^{-1}
DTDT()	rate of change of soil temperature	$K\ s^{-1}$
DTKEDT()	rate of change of turbulent kinetic energy	$J\ kg^{-1}s^{-1}$
DTPDT()	rate of change of potential air temperature	$K\ s^{-1}$
DUDT()	rate of change of wind speed x-direction	$m\ s^{-2}$
DUDZZ()	vertical gradient of wind speed x-direction	s^{-1}
DVDT()	rate of change of wind speed y-direction	$m\ s^{-2}$
DVDZZ()	vertical gradient of wind speed y-direction	s^{-1}
DWDT()	rate of change of soil water content	s^{-1}
DZ()	distance between centres of soil compartments	m
DZZ()	distance between centres of atmosphere compartments	m
E	water vapour flux atmosphere	$kg\ m^{-2}s^{-1}$
EDRY	dry soil emissivity	-
EMIASS	soil emissivity 'assumed' by thermal sensor	-
EMISKY	sky emissivity	-
EMISOI	soil emissivity	-

EPRBUO()	production rate kinetic energy by buoyancy	$J\ kg^{-1}s^{-1}$
EPRDIS()	production rate kinetic energy by dissipation	$J\ kg^{-1}s^{-1}$
EPRSRX()	production rate kinetic energy by friction in x-direction	$J\ kg^{-1}s^{-1}$
EPRSRY()	production rate kinetic energy by friction in y-direction	$J\ kg^{-1}s^{-1}$
EWET	wet soil emissivity	-
FA()	volume fraction of air in soil	-
FC()	volume fraction of clay in soil	-
FC1	volume fraction of clay in soil	-
FINTIM	finish time for simulation run	s
FO()	volume fraction of organic matter in soil	-
FO1()	volume fraction of organic matter in soil	-
FQ()	volume fraction of quartz in soil	-
FQ1	volume fraction of quartz in soil	-
G	acceleration due to gravity	$m\ s^{-2}$
GA	air shape factor, de Vries	-
GC	shape factor of clay particles, de Vries	-
GFLX	soil heat flux at the surface (=sum of conductive and latent term;=calorimetric heat flux)	$W\ m^{-2}$
GINT	time-integrated surface soil heat flux	$J\ m^{-2}$
GLORAD	global radiation	$W\ m^{-2}$
GO	shape factor organic particles, de Vries	-
GPRI	time-averaged surface soil conduction heat flux	$W\ m^{-2}$
GQ	shape factor quartz particles, de Vries	-
GW	shape factor water isles, de Vries	-
H	sensible heat flux	$W\ m^{-2}$
HCA	volumetric heat capacity of air	$J\ m^{-3}K^{-1}$
HCC	volumetric heat capacity of clay	$J\ m^{-3}K^{-1}$
HCO	volumetric heat capacity of organic matter	$J\ m^{-3}K^{-1}$
HCQ	volumetric heat capacity of quartz	$J\ m^{-3}K^{-1}$
HCSOIL()	volumetric heat capacity of bulk soil	$J\ m^{-3}K^{-1}$
HCW	volumetric heat capacity of water	$J\ m^{-3}K^{-1}$
HFLCON()	soil conduction heat flux	$W\ m^{-2}$
HFLVAP()	soil latent heat flux	$W\ m^{-2}$
HFLX()	total soil heat flux	$W\ m^{-2}$
HINT	time-integrated sensible heat flux	$J\ m^{-2}$
HOUR	hour in diurnal cycle	h
HOURS	number of hours simulated	h
HPRI	time-averaged sensible heat flux	$W\ m^{-2}$
HRH()	inverse of bulk volumetric moisture content at relative humidity 0.8	-
INVCOR	component of inverse length scale atmosphere due to earth rotation	m^{-1}
INVLH()	component of inverse length scale atmosphere associated with dimensionless gradients at compartment interfaces	m^{-1}
INVLM()	component of inverse length scale atmosphere associated with dimensionless gradients at compartment interfaces	m^{-1}
K()	soil hydraulic conductivity	$kg\ m^{-1}s^{-1}Pa^{-1}$
KAR	Von Karman constant	-
KAV()	average soil hydraulic conductivity	$kg\ m^{-1}s^{-1}Pa^{-1}$
KAW	auxiliary variable thermal conductivity	-
KCA	auxiliary variable thermal conductivity	-
KCW	auxiliary variable thermal conductivity	-
KFCSA()	auxiliary variable thermal conductivity	-
KFCSW()	auxiliary variable thermal conductivity	-
KFSA()	auxiliary variable thermal conductivity	-
KFSW()	auxiliary variable thermal conductivity	-
KH()	transport coefficient for heat in atmosphere	m^2s^{-1}
KM()	transport coefficient for momentum in atmosphere	m^2s^{-1}
KOA	auxiliary variable thermal conductivity	-
KOW	auxiliary variable thermal conductivity	-
KQA	auxiliary variable thermal conductivity	-

KQW	auxiliary variable thermal conductivity	-
KSAT()	saturated soil hydraulic conductivity	s
KSAT1	saturated soil hydraulic conductivity	s
KV()	transport coefficient for vapour in atmosphere	$m^2 s^{-1}$
KWA	auxiliary variable thermal conductivity	-
LE	latent surface heat flux atmosphere	$W\ m^{-2}$
LEINT	time-integrated latent heat flux	$J\ m^{-2}$
LEPRI	time-averaged latent heat flux	$W\ m^{-2}$
LONGIN	downward longwave radiation	$W\ m^{-2}$
LONREF	soil reflectivity for longwave radiation	-
LVAP	latent heat of vaporisation	$J\ kg^{-1}$
MAIR	molar mass of air	$kg\ mol^{-1}$
MFA	parameter in matric flux potential function	$kg\ m^{-1} s^{-1}$
MFB	parameter in matric flux potential function	-
MFLP()	matric flux potential	$kg\ m^{-1} s^{-1}$
MH2O	molar mass of water	$kg\ mol^{-1}$
N	number of soil compartments (max 25)	-
NETRAD	net radiation	$W\ m^{-2}$
NN	number of atmosphere compartments (max 11)	-
OBU()	Monin-Obukhov lenghth at compartment interfaces	m
P()	soil water pressure	Pa
PHIH()	dimensionless gradient of temperature at compartment interfaces	-
PHIM()	dimensionless wind shear at compartment interfaces	-
PI	mathematical constant	rad
POR()	soil porosity	-
POR1	soil porosity	-
PSIH	Paulson stability correction factor for heat	-
PSIM	Paulson stability correction factor for momentum	-
Q()	specific humidity atmosphere	-
Q1	specific humidity at screen height	-
QFLX()	'specific humidity flux' atmosphere	$m\ s^{-1}$
QI()	initial specific humidity atmosphere	-
QS	specific humidity at the surface	-
RADEMI	emittance by the soil surface	$W\ m^{-2}$
RAH	atmospheric resistance to heat transfer	$s\ m^{-1}$
RAIN	rainfall	mm
RAM	atmospheric resistance to momentum transfer	$s\ m^{-1}$
RAV	atmospheric resistance to vapour transfer	$s\ m^{-1}$
READEL	input time interval	s
RGAS	Gas constant	$J\ mol^{-1} K^{-1}$
RH()	relative humidity soil air	-
RHOAIR	density of air	$kg\ m^{-3}$
RHOCLY	particle density of clay	$kg\ m^{-3}$
RHOCP	volumetric heat capacity of air	$J\ kg^{-1} K^{-1}$
RHOL	density of soil water	$kg\ m^{-3}$
RHS	relative humidity of surface soil air	-
RMOFLX()	vertical 'flux of horizontal windvelocity'	$m^2 s^{-2}$
RNINT	time-integrated net radiation	$J\ m^{-2}$
RNPRI	time-averaged net radiation	$W\ m^{-2}$
SCALE	hydraulic scale length parameter	-
SKYA	parameter in sky emissivity	-
SKYB	parameter in sky emissivity	-
SKYTEM	sky radiation temperature	K
STAPAR()	stability parameter atmosphere at compartment interfaces	-
STDAY	starting day of simulation	d
STHOUR	starting hour of simulations	h
SURWIN	wind velocity at screen height	$m\ s^{-1}$
SWBLD	switch for boundary layer development	-
SWCHTB	switch for soil thermal conductivity from table	-
SWGRAV	switch for gravitational component of water flow	-
SWKTB	switch for hydraulic conductivity from table	-
SWMFLP	switch for matric flux potential formulation	-
SWMTB	switch for matric flux potential from table	-
SWNET	switch for net radiation input	-

T()	soil temperature	C
T1	air temperature at screen height	C
TCM()	thickness of soil compartments	m
TCMM()	thickness of atmosphere compartments	m
TI()	initial soil temperature	C
TKE()	turbulent kinetic energy	$J\ kg^{-1}$
TKEAV()	average turbulent kinetic energy at compartment interfaces	$J\ kg^{-1}$
TKEFLX()	flux of turbulent kinetic energy	$m^3 s^{-3}$
TKEI()	initial turbulent kinetic energy	$J\ kg^{-1}$
TP()	potential temperature atmosphere	C
TPAV()	average potential temperature at interfaces	C
TPFLX()	'temperature flux' atmosphere	$K\ m\ s^{-1}$
TPI()	initial potential temperature	C
TS	soil surface temperature	C
TSAPP	apparent surface temperature	C
TSINT	time-integrated apparent surface temperature	C s
TSPRI	time-averaged apparent surface temperature	C
TZERO	Kelvin temperature at 0 Centigrades	K
U()	wind speed x-direction	$m\ s^{-1}$
U1	wind speed x-direction at screen height	$m\ s^{-1}$
UG	geostrophic wind speed x-direction	$m\ s^{-1}$
UI()	initial wind speed x-direction	$m\ s^{-1}$
UVOFLX()	vertical 'flux of wind speed in x-direction'	$m^2 s^{-2}$
V()	wind speed y-direction	$m\ s^{-1}$
V1	wind speed y-direction at screen height	$m\ s^{-1}$
VG	geostrophic wind speed y-direction	$m\ s^{-1}$
VGA()	Van Genuchten parameter in soil moisture characteristic	Pa^{-1}
VGA1	Van Genuchten parameter in soil moisture characteristic	Pa^{-1}
VGM()	Van Genuchten parameter in soil moisture characteristic	-
VGM1	Van Genuchten parameter in soil moisture characteristic	-
VGN()	Van Genuchten parameter in soil moisture characteristic	-
VGN1	Van Genuchten parameter in soil moisture characteristic	-
VI()	initial wind speed y-direction	$m\ s^{-1}$
VPA	vapour pressure of air at screen height	Pa
VPD()	vapour density in soil air	$kg\ m^{-3}$
VPDS()	saturated vapour density in soil air	$kg\ m^{-3}$
VVOFLX()	vertical 'flux of wind speed in y-direction'	$m^2 s^{-2}$
W()	soil water content	-
W15()	soil water content at 1.5 MPa (pF 4.2)	-
W30()	soil water content at 30 MPa (pF 5.5)	-
WCRITA	moisture content beyond which albedo remains constant during wetting	-
WFLIN	surface water intake	$kg\ m^{-2} s^{-1}$
WFLLIQ()	liquid soil water flux	$kg\ m^{-2} s^{-1}$
WFLLGR()	liquid soil water flux due to gravity	$kg\ m^{-2} s^{-1}$
WFLVAP()	vapour soil water flux	$kg\ m^{-2} s^{-1}$
WFLX()	soil water flux	$kg\ m^{-2} s^{-1}$
WI()	initial soil water content	-
WMFO	reference moisture content in matrix flux potential	-
WREL()	relative soil moisture content	-
WREL15()	relative soil moisture content at 1.5 MPa	-
WRES()	residual soil moisture content	-
WRES1	residual soil moisture content	-
WSAT()	saturated soil moisture content	-
WSAT1	saturated soil moisture content	-
YUC	empirical parameter in atmospheric transfer	

176

	coefficient	-
Z()	depth in soil	m
ZNOT	roughness length	m
ZZ()	height in atmosphere	m

Appendix 5   Example of input files

```
***********************************************************************
* WEATHER.DAT input file to SALSA model. Columns from left to *
* right: day, month, date, hour, minutes, RAD: global or net *
* radiation (W/m2; indicate by option switch SWNET in        *
* RUNCON.DAT), TP1: dry bulb temperature (Centigrades), VPA: *
* vapour pressure (Pa), U1: wind speed (m/s), RAIN: rain (mm),*
* CLOC: cloud cover (-).                                      *
* First five columns are skipped when reading.               *
* Remove this heading prior to reading.                      *
***********************************************************************
172.  6. 21. 19.  0. 316.40 18.15 1464.6 2.88  .00  .00
172.  6. 21. 19. 30. 209.66 17.25 1413.3 2.31  .00  .00
172.  6. 21. 20.  0. 146.19 17.10 1441.4 1.91  .00  .00
172.  6. 21. 20. 30. 126.00 17.40 1517.4 1.72  .00  .00
172.  6. 21. 21.  0.  72.63 16.65 1615.1  .87  .00  .00
172.  6. 21. 21. 30.  38.01 14.60 1444.5  .93  .00  .00
172.  6. 21. 22.  0.   7.72 12.95 1368.4  .51  .00  .00
172.  6. 21. 22. 30.   0.00 12.10 1291.0  .66  .00  .00
172.  6. 21. 23.  0.   0.00 12.50 1327.0 1.28  .00  .00
172.  6. 21. 23. 30.   0.00 12.50 1327.0 1.02  .00  .00
173.  6. 22.  0.  0.   0.00 11.40 1229.9  .47  .00  .00
173.  6. 22.  0. 30.   0.00 11.85 1308.5 1.21  .00  .00
173.  6. 22.  1.  0.   0.00 12.30 1349.0 2.21  .00  .00
173.  6. 22.  1. 30.   0.00 12.10 1331.0 2.65  .00  .00
173.  6. 22.  2.  0.   0.00 11.80 1264.0 2.96  .00  .00
173.  6. 22.  2. 30.   0.00 11.15 1247.3 2.34  .00  .00
173.  6. 22.  3.  0.   0.00 11.30 1260.0 1.82  .00  .00
173.  6. 22.  3. 30.   0.00 11.50 1277.0 2.03  .00  .00
173.  6. 22.  4.  0.   0.00 11.50 1277.0 1.97  .00  .00
173.  6. 22.  4. 30.   0.00 10.95 1230.3 2.40  .00  .00
173.  6. 22.  5.  0.   0.00 10.85 1221.8 2.72  .00  .00
173.  6. 22.  5. 30.   0.00 10.90 1226.0 2.78  .00  .00
173.  6. 22.  6.  0.   7.72 10.95 1230.3 2.89  .00  .00
173.  6. 22.  6. 30.  17.82 10.80 1217.5 3.40  .00  .00
```

173.	6.	22.	7.	0.	12.05	10.80	1217.5	2.56	.00	.00
173.	6.	22.	7.	30.	35.13	11.20	1251.5	2.59	.00	.00
173.	6.	22.	8.	0.	124.56	12.15	1295.5	2.93	.00	.00
173.	6.	22.	8.	30.	151.96	12.75	1349.5	3.60	.00	.00
173.	6.	22.	9.	0.	312.07	14.10	1424.4	3.13	.00	.00
173.	6.	22.	9.	30.	338.03	15.55	1497.8	3.41	.00	.00
173.	6.	22.	10.	0.	451.98	16.80	1542.0	3.91	.00	.00
173.	6.	22.	10.	30.	460.64	17.35	1556.4	3.98	.00	.00
173.	6.	22.	11.	0.	431.79	17.50	1528.0	4.26	.00	.00
173.	6.	22.	11.	30.	450.54	18.40	1583.2	4.42	.00	.00
173.	6.	22.	12.	0.	524.10	18.60	1560.0	4.37	.00	.00
173.	6.	22.	12.	30.	493.81	18.70	1525.5	4.38	.00	.00

```
****************************************************************
* This file RUNCON.DAT provides non-dynamic input data to the SALSA    *
* model. The only other input file is WEATHER.DAT, which provides dyn-  *
* amic boundary conditions.                                            *
* The file RUNCON.DAT is designed to be read by the routines RDSREA    *
* (single REAL), RDSINT (single INTEGER), and RDAREA (array of REALs).  *
* These routines are included in the utilities library TTUTIL (Rappoldt *
* and Van Kraalingen, 1989). They allow including any amount of comment *
* lines and blanks in this input file. Also the order of variables lis- *
* ted is arbitrary.                                                    *
* The TTUTIL library is automatically linked on the CABO-VAX and on the *
* VAX of the Wageningen Agricultural University.                       *
****************************************************************


* OPTION SWITCHES
SWMFLP - 1     ! -0 for k-p option
*                -1 for matric flux potential
SWKTB - 1      ! -0 for k-theta Van Genuchten
*                -1 for k-theta from table
SWMTB - 0      ! -0 for matric flux potential calculation from MFA and MFB
*                -1 for matric flux potential from table
SWGRAV - 1     ! -0 to exclude gravity term in water flux density eq.
*                -1 to include gravity in water flux density eq.
SWCHTB - 0     ! -0 for soil thermal conductivity De Vries
*                -1 for conductivity from table
SWNET - 0      ! -0 for measured global radiation as boundary condition
*                -1 for measured net radiation as boundary condition
SWBLD - 1      ! -0 to exclude simulation of atmospheric boundary layer
*                -1 to include atmospheric boundary layer. For SWBLD-1,
*                   only 'screen height boundary condition' is radiation
*                   (net or global)


* DISCRETIZATION SOIL. Number of compartments
N - 25         ! max 25
* thickness soil compartments from top downward. Number of elements
* should be equal to N
TCM - 3*0.002,3*0.003,3*0.004,3*0.005,3*0.010,3*0.020,0.030,
      0.040,5*0.060     ! units: m


* INITIAL SOIL CONDITIONS. Volumetric moisture content and temperature.
* Number of elements should be equal to N.
WI - 25*0.30   ! units: m3/m3
TI - 25*20.    ! units: Centigrades
```

* HYDRAULIC SOIL PROPERTIES
* characteristic volumetric water contents
* if SWMFLP-1, water contents higher than WMFO should be avoided
WSAT1 - 0.36 ; WRES1 - 0.12 ; WMFO - 0.36   ! units: m3/m3
* gravimetric moisture content at soil rel hum - 0.8
A - 0.1   ! units: kg water/ kg clay
* vapour diffusion enhancement factor (Cary)
BCARY - 2.   ! dimensionless
* van genuchten alpha, n
VGA1 - 1.8E-4   ! units: 1/Pa
VGN1 - 1.3   ! dimensionless
* hydraulic scale length
SCALE - 2.   ! dimensionless
* matric flux potential parameters
MFA - 1.5E-4   ! units: kg/(m.s)
MFB - 0.15   ! dimensionless
* table of matric flux potential against water content.
* if SWMTB-1, water contents should not be outside range indicated here.
* odd positions are moisture contents, even are matric flux potential.
* matric flux potential defined negative for unsaturated soil.
* total number of pairs max 50.
MTB- 0.,-200., 0.2, -200, 0.3,-150., 0.32,-100., 0.36,0. ! units as MFA
* hydraulic conductivity at saturation
KSAT1 - 1.4E-8   ! units: kg/(m.Pa.s)
* table of hydraulic conductivity against water content.
* if SWKTB=1, water contents should not be outside range indicated here.
* odd positions are moisture contents, even are hydraulic conductivity.
* total number of pairs max 50.
KTB-0.,0., 0.10,0., 0.20,1.E-11, 0.25,1.E-10, 0.30,1.E-9,
    0.35,1.E-8, 0.36,1.4E-8   ! units: as KSAT1

* SOIL COMPOSITION. FC1+FO1+FQ1 should equal (1.-porosity)
* volume fraction clay
FC1 - 0.09   ! units: m3/m3
* volume fraction quartz
FQ1 - 0.35   ! units: m3/m3
* volume fraction organic matter
FO1 - 0.01   ! units: m3/m3
* porosity
POR1 - 0.55
* reference value bulk density (at which FC1, FO1 and FQ1 are defined)
BDSTAN - 1300.   ! units: kg/m3
* table of bulk density for all soil compartments from top downwards
* number of elements should be equal to N
BD - 25*1.05

* THERMAL SOIL PROPERTIES
* shape factors for De Vries formulation of soil thermal conductivity
* all dimensionless
GA - 0.2
GC - 0.01
GO - 0.5
GQ - 0.14
GW - 0.14
* table of soil thermal conductivity against water content
* odd positions are moisture contents, even are thermal conductivities
* max number of pairs 50.
CHTB - 0.0, 0.2, 0.5,2.0   ! units: W/(m.K)

* RADIATIVE PROPERTIES SOIL AND ATMOSPHERE
* soil albedo when dry
ADRY - 0.3   ! dimensionless
* soil albedo when wet
AWET - 0.15   ! dimensionless
* moisture content at which albedo reaches minimum
WCRITA - 0.25   ! m3/m3
* soil emissivity when dry
EDRY - 0.9   ! dimensionless
* soil emissivity when wet
EWET - 0.93   ! dimensionless
* soil emissivity 'assumed' by sensor
EMIASS - 1.0   ! dimensionless
* longwave reflectivity
LONREF - 0.1   ! dimensionless
* cloud coefficient
CLON - 0.1   ! dimensionless
* sky parameter
SKYA - 0.65   ! dimensionless
* sky parameter
SKYB - 0.04   ! hPa**(-0.5)
* sky temperature
SKYTEM - 0.0   ! Centigrades

* DISCRETIZATION ATMOSPHERE. Number of compartments
NN - 11   ! max 11
* thickness of atmosphere compartments from surface upward. Number of
* elements should be equal to NN
TCMM - 3.,6.,12.,24.,48.,96.,192.,384.,768.,1536.,3072.   ! units: m

```
* INITIAL ATMOSPHERE CONDITIONS. Number of elements should be equal
* to NN. Specific humidity, turbulent kinetic energy, potential temp-
* erature, and wind speed (x, y), respectively.
QI   - 5*0.013,0.012,0.011,0.009,0.004,0.001,0.001  ! units: kg/kg
TKEI- 0.83,0.61,0.57,0.54,0.48,0.38,0.22,0.075,
      0.006,0.001,0.0005                            ! units: J/kg
TPI  - 11*20.                                       ! units: Centigrades
UI   - 2.76,3.99,4.93,5.86,6.94,8.3,9.9,10.5,3*10.0 ! units: m/s
VI   - 1.11,1.57,1.89,2.15,2.33,2.30,1.59,-.39,-.99,
      -.06,-.06                                     ! units: m/s


* ATMOSPHERE PARAMETERS
* constant relating transport coeff to TKE
YUC - 0.2                                           ! dimensionless
* Coriolis parameter
CORIOL - 1.37E-4                                    ! units: 1/s
* roughnesss length
ZNOT - 0.001                                        ! units: m
* geostrophic wind speed x-direction
UG - 10.                                            ! units: m/s
* length scale parameter
ALPHA - 4.E-4                                       ! dimensionless
* atmospheric surface pressure
ATPRES - 1.E5                                       ! units: Pa
* measurement height of atmospheric boundary conditions.
* only for SWBLD=0 option
ZMEA - 0.5                                          ! units: m


* that is it
```

Appendix 6   List of symbols

Symbol	Description	Unit
a	parameter in soil water pressure – temperature relation	$Pa\,K^{-1}$
a	parameter in dimensionless gradient atmosphere	-
a	sky emissivity parameter	-
a	albedo	-
a_{dry}	dry soil albedo	-
a_{wet}	wet soil albedo	-
A	gravimetric soil moisture content at $h = 0.8$	$kg\,kg^{-1}$
A	parameter in $\Phi(\theta)$ relation with saturation as reference	$kg\,m^{-1}s^{-1}$
A'	parameter in $\Phi(\theta)$ with field capacity as reference	$kg\,m^{-1}\,s^{-1}$
b	sky emissivity parameter	$mbar^{-1/2}$
b	parameter in soil water pressure-temperature relationship	$m^3\,m^{-3}$
B	parameter in $\Phi(\theta)$ function with saturation as reference	-
B'	parameter in $\Phi(\theta)$ function with field capacity as reference	-
c	cloud cover	-
c	parameter in soil water pressure-temperature relationship	$Pa\,K^{-1}$
c	constant relating transport coefficient to turbulent kinetic energy	-
C_a	volumetric heat capacity air	$J\,m^{-3}\,K^{-1}$
C_c	volumetric heat capacity clay	$J\,m^{-3}\,K^{-1}$
C_o	volumetric heat capacity organic matter	$J\,m^{-3}\,K^{-1}$
C_p	heat capacity of air at constant pressure	$J\,kg^{-1}\,K^{-1}$
C_q	volumetric heat capacity quartz	$J\,m^{-3}\,K^{-1}$
C_s	volumetric heat capacity bulk soil	$J\,m^{-3}\,K^{-1}$
C_w	volumetric heat capacity water	$J\,m^{-3}\,K^{-1}$
D_a	water vapour diffusivity in free air	$m^2\,s^{-1}$
D_e	effective water vapour diffusivity	$m^2\,s^{-1}$
e	turbulent kinetic energy	$J\,kg^{-1}$
e	vapour pressure	Pa
E	surface water vapour flux	$kg\,m^{-2}\,s^{-1}$

f	Coriolis parameter	s^{-1}
f_a	volume fraction air	$m^3\,m^{-3}$
f_c	volume fraction clay	$m^3\,m^{-3}$
f_o	volume fraction organic matter	$m^3\,m^{-3}$
f_q	volume fraction quartz	$m^3\,m^{-3}$
g	gravitional acceleration	$m\,s^{-2}$
g_a	air shape factor	-
G	soil heat flux density at the surface	$W\,m^{-2}$
h	relative humidity soil air	-
H	sensible heat flux (atmosphere)	$W\,m^{-2}$
$\underline{H}$	partial specific enthalpy	$J\,kg^{-1}$
$\Delta\overline{H}_a$	heat of adsorption (heat of wetting)	$J\,kg^{-1}$
ΔH_v	heat of vaporisation	$J\,kg^{-1}$
H_w	partial specific enthalpy of soil water in a reference state	$J\,kg^{-1}$
ΔH_*	heat of vaporisation	$J\,mol^{-1}$
J_l	flux density of liquid water	$kg\,m^{-2}\,s^{-1}$
J_s	total entropy flux density	$W\,m^{-2}\,K^{-1}$
J_v	water vapour flux density	$kg\,m^{-2}\,s^{-1}$
J_w	total water flux density	$kg\,m^{-2}\,s^{-1}$
J_{w_i}	flux density of water in state i	$kg\,m^{-2}\,s^{-1}$
J_q	total heat flux density	$W\,m^{-2}$
k	lag (in semivariance)	-
k	Von Kármán constant	-
K	hydraulic conductivity	$kg\,m^{-1}Pa^{-1}s^{-1}$
K_H	transport coefficient (atmosphere) for heat	$m^2\,s^{-1}$
K_M	transport coefficient (atmosphere) for momentum	$m^2\,s^{-1}$
K_r	conductivity at location r	$kg\,m^{-1}Pa^{-1}s^{-1}$
K_s	hydraulic conductivity at saturation	$kg\,m^{-1}Pa^{-1}s^{-1}$
K_{sc}	field scaled conductivity	$kg\,m^{-1}Pa^{-1}s^{-1}$
K_V	transport coefficient (atmosphere) for vapour	$m^2\,s^{-1}$
l	length scale (atmosphere)	m
L	latent heat of vaporisation ($= \Delta H_v$)	$J\,kg^{-1}$
L	Monin-Obukhov length	m
LE	latent heat flux density (atmosphere)	$W\,m^{-2}$
LE_{pot}	potential latent heat flux density (atmosphere)	$W\,m^{-2}$
m	Van Genuchten parameter	-
M	molecular mass	$kg\,mol^{-1}$

186

n	cloud parameter	-
n	Van Genuchten parameter	-
p	soil water pressure (extramatic phase)	Pa
p'	soil water pressure (matric phase)	Pa
p	pressure (atmosphere)	Pa
$\tilde{p}$	soil vapour pressure	Pa
p_r	soil water pressure at location r	Pa
p_{sc}	field scaled soil water pressure	Pa
q	specific humidity	kg kg^{-1}
q	scaled deviation	-
r_a	atmospheric resistance	s m^{-1}
r_{aH}	atmospheric resistance to heat transfer	s m^{-1}
r_{aM}	atmospheric resistance to momentum transfer	s m^{-1}
r_{aV}	atmospheric resistance to vapour transfer	s m^{-1}
R	gas constant	$\text{J mol}^{-1}\text{ K}^{-1}$
R	radiance	$\text{W sr}^{-1}\text{ m}^{-2}$
R'	reflectance	W m^{-2}
R_{le}	emittance	W m^{-2}
R_{glob}	global radiation (radiant flux density)	W m^{-2}
R_{ld}	longwave downward radiation	W m^{-2}
R_n	net radiation	W m^{-2}
Ri	Richardson number	-
S	partial specific entropy of soil water in 'extramatric' state	$\text{J kg}^{-1}\text{ K}^{-1}$
S'	partial specific entropy of soil water in 'matric' state	$\text{J kg}^{-1}\text{ K}^{-1}$
S	partial specific entropy of soil water in a reference state	$\text{J kg}^{-1}\text{ K}^{-1}$
$\tilde{S}$	partial specific entropy of soil water in vapour state	$\text{J kg}^{-1}\text{ K}^{-1}$
S_{w_i}	partial specific entropy of soil water in state i	$\text{J kg}^{-1}\text{ K}^{-1}$
t	time	s
T	temperature	°C or K
T_a	air temperature	°C
T_s	surface temperature	°C
T_{sr}	surface radiation temperature (8–14 μm)	°C or K
u	wind speed (in x direction)	m s^{-1}
u'	temporal deviation from $\bar{u}$	m s^{-1}
u^*	friction velocity	m s^{-1}
$\bar{u}$	time-averaged wind speed	m s^{-1}
u_g	geostrophic wind speed (in x direction)	m s^{-1}

v	wind speed (in y direction)	$\mathrm{m\,s^{-1}}$
v'	temporal deviation from $\bar{v}$	$\mathrm{m\,s^{-1}}$
$\bar{v}$	time averaged wind speed	$\mathrm{m\,s^{-1}}$
V	specific volume of 'extramatic' water	$\mathrm{m^3\,kg^{-1}}$
V'	specific volume of 'matric' water	$\mathrm{m^3\,kg^{-1}}$
$\tilde{V}$	specific volume of water vapour	$\mathrm{m^3\,kg^{-1}}$
v_g	geostrophic wind speed (in y direction)	$\mathrm{m\,s^{-1}}$
x	horizontal space coordinate	m
y	horizontal space coordinate	m
z	vertical space coordinate	m
z_m	measurement height	m
z_o	roughness length	m
α	constant in formulation length scale atmosphere	-
α	absorptivity	-
α	Van Genuchten parameter in moisture characteristic expression	$\mathrm{Pa^{-1}}$
α_r	scale factor of location r	-
β	parameter in dimensionless gradient atmosphere	-
β	regression coefficient	$\mathrm{K\,W^{-1}\,m^2}$
β	Bowen ratio	-
β	phenomenological diffusion enhancement coefficient	-
γ	semivariance	-
ε_{dry}	dry soil emissivity	-
ε_{sky}	apparent sky emissivity	-
ε_{wet}	wet soil emissivity	-
ζ	stability parameter	-
η	dynamic viscosity	$\mathrm{Pa\,s}$
η_3	component in the z-direction of unit vector along rotation axis	-
θ	volumetric moisture content	$\mathrm{m^3\,m^{-3}}$
θ	potential temperature	K
θ_{crit}	volumetric moisture content at which albedo reaches minimum value	$\mathrm{m^3\,m^{-3}}$
θ_r	residual moisture content	$\mathrm{m^3\,m^{-3}}$
θ_s	volumetric moisture content at saturation	$\mathrm{m^3\,m^{-3}}$
$\theta_{1.5}$	soil moisture content at $p = -1.5\,\mathrm{MPa}$	$\mathrm{m^3\,m^{-3}}$
θ_{30}	soil moisture content at $p = -30\,\mathrm{MPa}$	$\mathrm{m^3\,m^{-3}}$
θ^*	scaled temperature	K
λ	thermal conductivity soil	$\mathrm{W\,m^{-1}\,K^{-1}}$
λ	wavelength	$\mu\mathrm{m}$

λ_a	thermal conductivity air	$W\,m^{-1}\,K^{-1}$
λ_c	thermal conductivity clay	$W\,m^{-1}\,K^{-1}$
λ_o	thermal conductivity organic matter	$W\,m^{-1}\,K^{-1}$
λ_q	thermal conductivity quartz	$W\,m^{-1}\,K^{-1}$
λ_w	thermal conductivity water	$W\,m^{-1}\,K^{-1}$
μ	chemical potential	$J\,kg^{-1}$
μ_{w_i}	chemical potential of water in phase i	$J\,kg^{-1}$
ν	kinematic viscosity air	$m^2\,s^{-1}$
ξ	correction factor for local temperature gradient	-
Ξ	relative moisture content	-
ρ	density of surface air	$kg\,m^{-3}$
ρ	reflectivity	-
ρ_c	density of clay	$kg\,m^{-3}$
ρ_l	longwave reflectivity	-
ρ_l	density of soil liquid	$kg\,m^{-3}$
ρ_v	water vapour density	$kg\,m^{-3}$
σ	Stefan-Bolzman constant	$W\,m^{-2}\,K^{-4}$
τ	transmissivity	-
τ_x	flux of x-momentum	$kg\,m^{-1}\,s^{-2}$
τ_y	flux of y-momentum	$kg\,m^{-1}\,s^{-2}$
φ	azimuth angle	rad
φ_M	dimensionless gradient of momentum	-
φ_H	dimensionless gradient of temperature	-
Φ	matric flux potential	$kg\,m^{-1}\,s^{-1}$
Φ_r	matrix flux potential at location r	$kg\,m^{-1}\,s^{-1}$
Φ_{sc}	field scaled matrix flux potential	$kg\,m^{-1}\,s^{-1}$
ψ	soil water potential	$J\,kg^{-1}$
ψ	elevation angle	rad
Ψ_H	stability correction factor (heat)	-
Ψ_M	stability correction factor (momentum)	-
Ω	angular frequency of earth's rotation	$rad\,s^{-1}$

References

Aase, J.K. & S.B. Idso, 1975. Solar radiation interactions with mixed prairie rangeland in natural and denuded conditions. Archiv für Meteorologie, Geophysik und Bioklimatologie, Serie B, 23: 255–264.

Abrams, M.J., A.B. Kahle, F.D. Palluconi & J.P. Schieldge, 1984. Geologic mapping using thermal images. Remote Sensing of Environment 16: 13–33.

Angstrom, A., 1925. The albedo of various surfaces of ground. Geografiska Annaler 7: 321–342.

Arya, L.M. & J.F. Paris, 1981. A physico-empirical model to predict the soil moisture characteristic from particle size distribution and bulk density data. Soil Science Society of America Journal 45: 1023–1030.

Asrar, G. & E.T. Kanemasu, 1983. Estimating thermal diffusivity near the soil surface using Laplace Transform: uniform initial conditions. Soil Science Society of America Journal 47: 397–401

Bavel, C.H.M. van & R. Lascano, 1979. CONSERVB, a numerical method to compute soil water content and temperature profiles under a bare surface. Rept. 3058-1 Texas A&M University, College Station.

Berge, H.F.M. ten, L. Stroosnijder, P.A. Burrough, A.K. Bregt & M.J. de Heus, 1983. Spatial variability of physical soil properties influencing the temperature of the soil surface. Agricultural Water Management 6: 213–226.

Berge, H.F.M. ten, 1986. Heat and water transfer at the bare soil surface: aspects affecting thermal imagery. Dissertation, Dept. of Soil Science and Plant Nutrition, Wageningen Agricultural University.

Berge, H.F.M. ten, K. Metselaar & L. Stroosnijder, 1987. Measurement of matric flux potential: a simple procedure for the hydraulic characterisation of soils. Netherlands Journal of Agricultural Science 35: 371–384.

Berge, H.F.M. ten & G.H. Bolt, 1988. Coupling between liquid flow and heat flow in porous media: a connection between two classical approaches. Transport in Porous Media 3: 35–49.

Boast, C.W. & T.M. Robertson, 1982. A micro-lysimeter method for determining evaporation from bare soil; description and laboratory evaluation. Soil Science Society of America Journal 46: 689–695.

Bolt, G.H. & P.H. Groenevelt, 1972. Coupling between transport processes in porous media. Proceedings 2nd IAHR-ISSS symposium on the fundamentals of transport phenomena in porous media. Guelph, Ontario.

Bouten, W. & A.R.P. Janse, 1979. Radar reflection in relation to slaking. Proceedings Workshop Bare Soils, EARSEL, Paris.

Bowers, S.A. & R.J. Hanks, 1965. Reflection of radiant energy from soils. Soil Science 100: 130–138.

Bresler, E., J. Heller, N. Diner, I. Ben Asher, A. Brandt & D. Goldberg, 1971. Infiltration from a trickle source: II. Experimental data and theoretical predictions. Soil Science Society of America Proceedings 35: 683–689.

Brooks, R.H. & A.T. Corey, 1964. Hydraulic properties of porous media. Hydrology Paper No. 3, Civ. Eng. Dept. Colorado State University, Fort Collins.

Brunt, D. 1939. Physical and dynamical meteorology. Cambridge university Press.

Budyko, M.I., 1958. Heat balance of the earth's surface. Translation by N.A. Stepanova, U.S. Department of Commerce, Washington D.C.

Buettner, K.J.K. & C.D. Kern, 1963. Infrared emissivity of the Sahara from Tyros data. Science, 142: 671.

Buettner, K.J.K. & C.D. Kern, 1965. The determination of infrared emissivities of terrestrial surfaces. Journal of Geophysical Research 70: 1329–1337.

Busch, N.E., 1973. On the mechanics of atmospheric turbulence. Workshop on micrometeorology. Ed. D.A. Haugen, American Meteorological Society 1–66.

Businger, J.A., J.C. Wyngaard, Y. Izumi & E.F. Bradley, 1971. Journal of the Atmospheric Sciences 28: 181–189.

Businger, J.A., 1975. Aerodynamics of vegetated surfaces. In: Heat and mass transfer in the biosphere. Eds. D.A. de Vries & N.H. Afgan. Scripta Wash. D.C.: 139–167.

Businger, J.A., 1981. Equations and concepts; in: Atmospheric turbulence and air pollution modelling. Ed. F.T.M. Nieuwstadt & H. van Dop, D. Reidel Publ.

Buttner, K. & E. Sutter, 1935. Abkülungs Grösse in den Dünen, Rückstrahlung Verschiedener Bodenbedeckungen. Strahlentherapie 54, 156–173.

Byrne, G.F. & J.R. Davis, 1980. Thermal inertia, thermal admittance and the effect of layers. Remote sensing of environment 9: 295–300.

Cary, J.W. and S.A. Taylor, 1962a. The interaction of the simultaneous diffusions of heat and water vapor. Soil Science Society of America Proceedings 26: 413–416.

Cary, J.W. & S.A. Taylor, 1962b. Thermally driven liquid and vapor phase transfer of water and energy in soil. Soil Science Society of America Proceedings 26: 417–420.

Cary, J.W., 1963. Onsager's relation and the non-isothermal diffusion of water vapor. Journal of Physical Chemistry 67: 126–129.

Cary, J.W., 1964. An evaporation experiment and its irreversible thermodynamics. International Journal of Heat and Mass Transfer 7: 531–538.

Cary, J.W., 1965. Water flux in moist soil: Thermal versus suction gradients. Soil Science 100: 168–175.

Cary, J.W., 1975. Soil water hysteresis: temperature and pressure effects. Soil Science 120: 308–311.

Cary, J.W., R.A. Kohl & S.A. Taylor, 1964. Water adsorption by dry soil and its thermodynamic functions. Soil Science Society of America Proceedings 28: 309–313.

Cary, J.W., 1979. Soil heat transducers and water vapor flow. Soil Science Society of America Journal 43: 835–839.

Cass, A., G.S. Campbell & T.L. Jones, 1984. Enhancement of thermal water vapor diffusion in soil. Soil Science Society of Ameria Journal 48: 25–32.

Chahal, R.S., 1965. Effect of temperature and trapped air on matric suction. Soil Science 100: 262–265.

Choudhury, B.J., T.J. Schmugge & T. Mo, 1982. A parametrisation of effective soil temperature for microwave emission. Journal of Geophysical Research 87: 1301–1304.

Chu, S.Y., G. Sposito & W.A. Jury, 1983. The cross-couping transport coefficient for the steady flow of heat in soil under a gradient of water content. Soil Science Society of America Journal 47: 21–25.

Cihlar, J., 1980. Soil water and plant canopy effects on remotely measured surface temperatures. International Journal of Remote Sensing 1: 167–173.

Cochran, P.H., L. Boersma & C.T. Youngberg, 1967. Thermal conductivity of a pumice soil. Soil Science Society of America Proceedings 31: 454–459.

Coleman, G. & G. DeCoursey, 1976. Sensitivity and model variance analysis applied to some evaporation and evapotranspiration models. Water Resources Research 12: 873–879.

Conaway, J. & C.H.M. van Bavel, 1967. Evaporation from a wet soil surface calculated from radiometrically determined surface temperatures. Journal of Applied Meteorology 6: 650–655.

Constantz, J., 1982. Temperature dependence of unsaturated hydraulic conductivity of two soils. Soil Science Society of America Journal 46: 466–470.

Coulson, K.L. & D.W. Reynolds, 1971. The spectral reflectance of natural surfaces. Journal of Applied Meteorology 10: 1285–1294.

Dane, J.H. & P.J. Wieringa, 1975. Effect of hysteresis on the prediction of infiltration, redistribution and drainage of water in a layered soil. Journal of Hydrology 25: 229–242.

Davidson, J.M., D.R. Nielsen & J.W. Biggar, 1963. The measurement and description of water flow through Columbia silt loam and Hesperia sand loam. Hilgardia 34: 601–617.

Dobson, M.C., F.T. Ulaby, M.T. Hallikainen & M.A. El Rayes, 1985. Microwave dielectric behaviour of wet soil; Part II: dielectric mixing models. Geoscience and Remote Sensing, GE-23: 35–46.

Driedonks, A.G.M., 1981. Dynamics of the well mixed atmospheric boundary layer. PhD thesis, Vrije Universiteit, Amsterdam.

Duin, R.H.A. van, 1956. Over de invloed van grondbewerking op het transport van warmte, lucht en water in de grond. Verslagen van Landbouwkundige onderzoekingen No 62.7, Wageningen Agricultural University.

Dyer, A.J., 1974. A review of flux-profile relationships. Boundary Layer Meteorology 7: 363–372.

East, W.H., 1950. Fundamental study of clay: X, waterfilms in monodisperse kaolinite fraction. Journal of the American Ceramics Society 33: 211–218.

Elrick, D.H., 1964. Note on an improved apparatus for soil moisture flow measurements. Soil Science Society of America Proceedings 28: 450–453.

Elseftawy, Atef & R.S. Mansell, 1975. Hydraulic conductivity calculations for unsaturated steady state and transient state flow in sand. Soil Science Society of America Proceedings 39: 599–603.

England, C.E., R. Gombeer, E. Hechinger, R.W. Herschy, A. Rosema (Ed.) & L. Stroosnijder, 1983. The Group Agromet Monitoring Project (GAMP): Application of Meteosat data for rainfall, evaporation, soil moisture and plant growth monitoring in Africa. ESA Journal 7: 169–188.

Farrell, D.A., E.L. Greacen and C.G. Gurr, 1966. Vapor transfer in soil due to air turbulence. Soil Science 102: 305–313.

Feddes, R.A., 1971. Water, heat and crop growth. PhD thesis, Wageningen, Agricultural University.

Fisher, E.A., 1923. Some factors affecting the evaporation of water from soil. Journal of Agricultural Science 13, 121–143.

Forrester, J.W., 1961. Industrial Dynamics, Massachusets Institute of Technology Press, Cambridge, Mass., USA.

France, J. & J.H.M. Thornley 1984. Mathematical models in agriculture. Butterworths, London.

Fuchs, M. & C.B. Tanner, 1966. Infrared thermometry of vegetation. Agronomy Journal 58: 596–601.

Fuchs, M. & C.B. Tanner, 1968. Surface temperature measurements of bare soils. Journal of Applied Meteorology 7: 303–305.

Fukuda, H., 1955. Air and vapor movement in soil due to wind gustiness. Soil Science 79: 249–258.

Gardner, R., 1955. Relation of temperature to moisture tension of soil. Soil Science 79: 257–265.

Geiger, R., 1961. Das Klima der bodennahen Luftschicht. 4th edition. Braunschweig, F. Vieweg & Sohn: 19–27.

Genuchten, M.Th. van, 1980. A closed-form equation for predicting the hydraulic conductivity of unsaturated soils. Soil Science Society of America Journal 44: 892–898.

Gerbermann, A.H., 1979. Reflectance of various mixtures of a clay soil and sand. Photogrammetric Engineering and Remote Sensing 45: 1145–1151.

Gold, A. & J. Ben Asher, 1976. Soil reflectance measurement using a photographic method. Soil Science Society of America Journal 40: 337–341.

Goudriaan, J., 1977. Crop micrometeorology, a simulation study. Simulation Monographs Pudoc, Wageningen.

Graser, E.A. & C.H.M. van Bavel, 1982. The effect of soil moisture upon soil albedo. Agricultural Meteorology 27: 17–26.

Green, R.E., R.J. Hanks & W.E. Larson, 1964. Estimates of field infiltration by numerical solution of the moisture flow equation. Soil Science Society of America Proceedings 28: 15–19.

Griend, A.A. van de, P.J. Camillo & R.J. Curney, 1985. Discrimination of soil physical parameters, thermal inertia and soil moisture from diurnal surface temperature fluctuations. Water Resources Research 21: 997–1009.

Groenevelt, P.H. & B.D. Kay, 1974. On the interaction of water and heat transport in frozen and unfrozen soils: II. The liquid phase. Soil Science Society of America Proceedings 38: 400–404.

Groot, S.R. de & P. Mazur, 1962. Non-equilibrium thermodynamics. North Holland Publishers, Amsterdam.

Gupta, S.C. & W.E. Larson, 1979. Estimating soil water retention characteristics from particle size distribution, organic matter content and bulk density data. Water Resources Research 15: 1633–1635.

Gupta, S.C., J.K. Radke & W.E. Larson, 1981. Predicting temperatures of bare and residue covered soils with and without a corn crop. Soil Science Society of America Journal 45: 405–412.

Gupta, S.K., 1983. A radiative transfer model for surface radiation budget studies. Journal Quantitative Spectroscopy and Radiation Transfer 5: 419–427.

Hadas, A., 1968. Simultaneous flow of water and heat under periodic heat fluctuations. Soil Science Society of America Proceedings 32: 297–301.

Hadas, A., 1969. A comparison between predicted and measured values of thermal conductivity of a moist soil under a steady and fluctuating thermal regime. Israel Journal of Agricultural Research 19: 151–160.

Hadas, A., 1977a. Evaluation of theoretically predicted thermal conductivities of soils under field and laboratory conditions. Soil Science Society of America Journal 41: 460–466.

Hadas, A., 1977b. Heat transfer in dry aggregated soil: I. Heat conduction. Soil Science Society of America Journal 41: 1055–1059.

Hahn, G.J. & S.S. Shapiro, 1967. Statistical Methods in Engineering. John Wiley, N.Y.

Hammel, J.E., R.I. Papendick & G.S. Campbell, 1981. Fallow tillage effects on evaporation and seedzone water content in a dry summer climate. Soil Science Society of America Journal 45: 1016–1022.

Haneghem, I.A. van, 1981. Een niet-stationaire naaldmethode (warmtegeleiding, warmtecapaciteit, contactweerstand). Dissertation Dept. of Physics, Wageningen Agricultural University.

Hanks, R.J., H.R. Gardner & M.L. Fairbourne, 1967. Evaporation of water from soils as influenced by drying with wind or radiation. Soil Science Society of America Proceedings 31: 593–598.

Hares, M.A., J. Ben Asher, A.D. Matthias & A.W. Warrick, 1985. A simple method to evaluate daily positive soil heat flux. Soil Science Society of America Journal 49: 45–47.

Haridasan, M. & R.D. Jensen, 1972. Effect of temperature on pressure head-water content relationship and conductivity of two soils. Soil Science Society of America 36: 703–708.

Hartmann, R., H. Verplancke & M. de Boodt, 1972. Het verband tussen de warmtegeleidbaarheid en het vochtgehalte van de bodem. Mededelingen van de Faculteit der Landbouwwetenschappen, Rijksuniversiteit Gent, 37:1249–1260.

Hatfield, J.L., A. Perrier & R.D. Jackson, 1983. Estimation of evapotranspiration at one time-of-day using remotely sensed surface temperatures. Agricultural Water Management 7: 341–350.

Hechinger, E., 1979. Contribution a l'interpretation de données de teledetection: étude d'un modèle thermique de sols et de son emploi pour la réalisation d'imges de telede-

tection dans le visible et l'infrarouge thermique. Thèse Université Louis Pasteur Strasbourg

Heide, G. van der & A.J. Koolen, 1980. Soil surface albedo and multispectral reflectance of shortwave radiation as a function of degree of soil slaking. Netherlands Journal of Agricultural Science 28: 252–258.

Heilman, J.L. & D.G. Moore, 1980. Thermography for estimating near-surface soil moisture under developing crop canopies. Journal of Applied Meteorology 19: 324–328.

Hillel, D., 1976. On the role of soil moisture hysteresis in the suppression of evaporation from bare soil under diurnally cyclic evaporativity. Soil Science 122: 309–314.

Hillel, D., 1980. Fundaments of soil physics. Academic Press, New York.

Himmelblau, D.M. & K.B. Bisschoff, 1968. Process analysis and simulation: deterministic systems. Wiley & Sons, NY.

Hopmans, J.W. & J.H. Dane, 1985. Effect of temperature-dependent hydraulic properties on soil water movement. Soil Science Society of America Journal 49: 51–58.

Hopmans, J.W. & J.H. Dane, 1986. Temperature dependence of soil water retention curves. Soil Science Society of America Journal 50: 562–567.

Horowitz, I.M., 1963. Synthesis of feedback systems. Academic Press, N.Y.

Horton, R. Jr., 1982. Determination and use of soil thermal properties near the soil surface. PhD thesis, Las Cruces, New Mexico.

IBM, 1975. Continuous System Modeling Program III (CSMP III), Program Reference Manual SH19–7001–2, Program Number 5734-X59, IBM Corp., White Plains, N.Y.

Idso, S.B. & R.D. Jackson, 1969. Comparison of two methods for determining infrared emittances of bare soils. Journal of Applied Meteorology 8: 168–169.

Idso, S.B. & R.J. Reginato, 1974. Assessing soil water status via albedo measurements. Proceedings Arizona Section of the American Water Resources Association and Hydrology section of the Arizona Academy of Science.

Idso, S.B., R.J. Reginato, R.D. Jackson, B.A. Kimball & F.S. Nakayama, 1974. The three stages of drying of a field soil. Soil Science Society of America Proceedings 38: 831–837.

Idso, S.B., T.J. Schmugge, R.D. Jackson & R.J. Reginato, 1975a. The utility of surface temperature measurements for the remote sensing of surface soil water status. Journal of Geophysical Research 80: 3044–3049.

Idso, S.B., R.J. Reginato, R.D. Jackson, 1975b. Assessing bare soil evaporation via surface temperature measurements. In: Hydrology and Water Resources in Arizona and the South West; Proceedings of the American Water Resources Association, Tempe, Arizona, 199–205.

Idso, S.B., R.D. Jackson, R.J. Reginato, B.A. Kimball & F.S. Nakayama, 1975c. The dependence of bare soil albedo on soil water content. Journal of Applied Meteorology 14: 109–113.

Jackson, R.D., 1973. Diurnal changes in soil water content. In: Field soil water regime, Soil Science Society of America Special Publication 5.

Jackson, R.D., R.J. Reginato, B.A. Kimball & F.S. Nakayama, 1974. Diurnal soil water evaporation: comparison of measured and calculated soil water fluxes. Soil Science Society of America Proceedings 38: 861–866.

Jackson, R.D., R.J. Reginato & S.B. Idso, 1977. Wheat canopy temperature: a practical tool for evaluating water requirements. Water Resources Research 13: 651–656.

Jacobs, P., 1982. The thermal behaviour of a three dimensional object placed in the open field. PhD thesis Wageningen Agricultural University.

Jensen, M.E., M. Asce & R.J. Hanks, 1967. Non-steady state drainage from porous media. Journal of the Irrigation and Drainage division. Proceedings of the American Society of Civil Engineers.Ir 3.

Journel, A.G. & C.J. Huijbregts, 1978. Mining Geostatistics. Academic Press, London.

Jurinak, J.J. 1963. Multilayer adsorption of water by kaolinite. Soil Science Society of America Proceedings 27: 269–272.

Jury, W.A. & J. Letey, 1979. Water vapor movement in soil: reconciliation of theory and experiment. Soil Science Society of America Journal 43: 823–827.

Kahle, A.B., J.P. Schieldge & R. Alley, 1984. Sensitivity of thermal inertia calculations to variations in environmental factors. Remote Sensing of Environment 16: 211–232.

Kalma, J.D. & R. Badham, 1972. The radiation balance of a tropical pasture. I. The reflection of shortwave radiation. Agricultural Meteorology 10: 251–259.

Katchalsky, A. & P.F. Curran, 1965. Non-equilibrium thermodynamics in biohysics. Harvard University Press, Cambridge, Mass.

Kay, B.D. & P.H. Groenevelt, 1974. On the interaction of water and heat transport in frozen and unfrozen soils: I. Basic theory. The Vapor phase. Soil Science Society of America Proceedings 38: 395–400.

Keulen, H. van, 1975. Simulation of water use and herbage growth in arid regions. Simulation Monographs, Pudoc, Wageningen.

Keulen, H. van & D. Hillel, 1974. A simulation study of the drying front phenomenon. Soil Science 118: 270–273.

Kijne, J.W. & S.A. Taylor, 1964. Temperature depence of soil water vapour pressure. Soil Science of America Proceedings 28: 595–599.

Kijne, J.W., 1969. Hydration of layer silicate surfaces and exchangable cations. Soil Science Society of America Proceedings 33: 979–980.

Kijne, J.W., 1969. On the interaction of water molecules and Montmorillonite surfaces. Soil Science Society of America Proceedings 33: 539–543.

Kimball, B.A. & E.R. Lemon, 1971. Air turbulence effects upon soil gas exchange. Soil Science Society of America Proceedings 35: 16–21.

Kimball, B.A. & R.D. Jackson, 1975. Soil heat flux determination: a null aligment method. Agricultural Meteorology 15: 1–9.

Kimball, B.A., R.D. Jackson, R.J. Reginato, F.S. Nakayama & S.B. Idso, 1976. Comparison of field measured and calculated soil heat fluxes. Soil Science Society of America Journal 40: 18–24.

Klute, A., 1952. A numerical method for solving the flow equation for water in unsaturated materials. Soil Science 73: 105–117.

Kondrat'ev, K.Y., 1954. The radiant energy of the sun, Leningrad, Chapter 9, Albedo of the underlying surface and clouds. English summary by A. Kurlent & P. Larson, McGill University.

Krischer, O. & H. Rohnalter, 1940. Wärmeleitung und Dampfdiffusion in feuchten Gutern. Verein Deutsch. Ing. Forchsungsheft 402: 1–18.

Kroon, L.J.M., 1985. Profile derived fluxes above inhomogeneous terrain: a numerical approach. Dissertation, Dept. of Physics, Wageningen Agricultural University.

Lamers, J.G., 1985. Soil slaking and the possibilities to record with infrared line scanning. International Journal of Remote Sensing 6: 153–165.

Lettau, H.H., 1957. Computation of heat budget constituents of the earth-air interface. In: Exploring the atmosphere's first mile, 1, 305. Eds. H.H. Lettau & D. Davidson, N.Y. Pergamon press.

Lynn, D.W., 1984. Surface material mapping in the English Fenlands using airborne multispectral scanner data. International Journal of Remote Sensing 4: 699–713.

Lynn, D.W., 1986. Monotemporal, multitemporal and multidate thermal infrared data acquisition from satellites for soil and surface material survey. International Journal of Remote Sensing 7: 213–231.

Mahrer, Y., 1982. A theoretical study of the effect of soil surface shape upon the soil temperature profile. Soil Science 134: 381–387.

Martin, J. & C.L. MacClure, 1988. Structure techniques: the basis for CASE. Prentice Hall, Englewood Cliffs, 776 pp.

McCuen, R.H., 1973. The role of sensitivity analysis in hydrologic modelling. Journal of Hydrology 18: 37–53.

Menenti, M., 1984. Physical aspects and determination of evaporation in deserts, applying remote sensing techniques. PhD thesis and Report 10 of Institute for Land and Water Management Research, Wageningen.

Miller, E.E., 1980. Similitude and scaling of soil water phenomena. In: Applications of Soil Physics. Ed. D. Hillel, Academic Press, N.Y.

Milly, P.C.D., 1982. Moisture and heat transport in hysteric, inhomogeneous porous media: a matric head based formulation and a numerical model. Water Resources Research 18: 489–498.

Milly, P.C.D., 1984a. A linear analysis of thermal effects on evaporation from soil. Water Resources Research 20: 1075–1085.

Milly, P.C.D., 1984b. A simulation analysis of thermal effects on evaporation from soil. Water Resources Research 20: 1087–1098.

Monteith, J.L., 1963. Gas exchange in plant communities. In: Environmental control of plant growth, Ed. E.T. Evans. Academic Press, New York: 95–112.

Monteith, J.L., 1973. Principles of environmental physics. Edward Arnold Publ.

Moore, R.E., 1939. Water conduction from shallow water tables. Hilgardia 12: 383–424.

Moore, R.E., 1940. The relation of soil temperature to soil moisture: pressure potential, retention and infiltration rate. Soil Science Society of America Proceedings 5: 61–64.

Moore, D.G., J.C. Harlan, J.L. Heilman, D.O. Ohlen & W.D. Rosenthal, 1983. Infrared remote sensing for monitoring rainfall. Agricultural Water Management 7: 363–378.

Mualem, Y., 1973. Modified approach to capillary hysteresis, based on a similarity hypothesis. Water Resources Research 9: 1324–1331.

Mualem, Y., 1976. A new model for predicting the hydraulic conductivity of unsaturated porous media. Water Resources Research 12: 513–522.

Mualem, Y. & G. Dagan, 1976. Development of methods, tools and solutions for unsaturated flow with application to watershed hydrology and other fields. US-Israel Binational Science Foundation, Report Research Project 442.

Mualem, Y. & H.J. Morel-Seytoux, 1978. Analysis of a capillary hysteresis model, based on a one-variable distribution function. Water Resources Research 14: 605–610.

Nagpal, N.K. & L. Boersma, 1973. Air entrapment as a possible error in the use of a cylindrical heat probe. Soil Science Society of America Proceedings 37: 828–832.

Nederlands Normalisatie Instituut, 1979. Programmastructuurdiagrammen (PSD), NEN 1422. Nederlands Normalisatie Instituut, Rijswijk, The Netherlands.

Nerpin, S.V. & A.F. Chudnovski, 1970. Physics of the soil. Israel Program of Scientific Translations, Kefer Press, Jerusalem.

Nielsen, D.R., R.D. Jackson, J.W. Cary & D.D. Evans, 1972. Soil water. American Society of Agronomy and Soil Science Society of America.

Nielsen, D.R., J.W. Biggar & K.T. Ehr, 1973. The spatial variability of field measured soil water properties. Hilgardia 42: 215–259.

Nielsen, D.R., 1982. Soil physics research: a leap into the future without the academia of the past. Whither soil research. Proceedings International Soil Science Society Congress India: 59–67.

Nielsen, D.R., P.M. & S.R. Vieira, 1983. Analyzing field measured soil water properties. Agricultural Water Management 6: 93–109.

Nielsen, D.R. & J. Bouma, 1985 (Eds). Soil Spatial Variability. Proceedings of a workshop of the ISSS and SSSA, November 1984, Las Vegas, USA.

Nieuwenhuis, G.J.A., 1985. Integration of remote sensing with a soil water balance simulation model (SWATRE). Paper presented at International Workshop on Hydrologic Applications of Space Technology, August 1985, Florida.

Nieuwenhuis, G.J.A., E.H. Smidt & H.A.M. Thunnissen, 1985. Estimation of regional evapotranspiration of arable crops from thermal infrared images. International Journal of Remote Sensing 6: 1319–1334.

Nieuwstadt, F.T.M. & A.G.M. Driedonks, 1979. The nocturnal boundary layer: a case study compared with model calculations. Journal of Applied Meteorology 18: 1397–1405.

Nieuwstadt, F.T.M. & H. van Dop, 1981. Atmospheric turbulence and air pollution modelling. Course 21–25 September 1981, The Hague, D. Reidel Publ. Comp.

Nimah, M.N. & R.J. Hanks, 1973. Model for estimating soil water, plant and atmospheric interrelations. I. Description and sensitivity. Soil Science Society of America Proceedings 37: 522–527.

Nimmo, J.R. & E.E. Miller, 1986. The temperature dependence of isothermal moisture potential characteristics of soils. Soil Science Society of America Journal 50: 1105–1113.

Obukhov, A.M., 1946. Turbulence in an atmosphere with a non-uniform temperature. Trudy Instituta Teoretisiskoj Geofiziki Academii Nauk SSSR (translation Boundary Layer Meteorology 2: 7–29).

Orchiston, H.D., 1953. Adsorption of water vapor. I. Soils at 25°C. Soil Science 76: 453–465.

Orchiston, H.D., 1954. Adsorption of water vapor. II. Clays at 25°C. Soil Science 78: 463–480.

Palluconi, F.D. 1983. Personal communication. Jet Propulsion Laboratory, California Institute of Technology, Pasadena.

Paulson, C.A., 1970. The mathematical representation of windspeed and temperature profiles in the unstable atmospheric surface layer. Journal of Applied Meteorology 9: 857–861.

Penning de Vries, F.W.T., D.M. Jansen, H.F.M. ten Berge & A. Bakema, 1989. Eco-physiological processes of growth of several annual crops. Simulation Monographs 29, Pudoc, Wageningen.

Philip, J.R., 1967. Sorption and infiltration in heterogeneous media. Australian Journal of Soil Research 5: 1–10.

Philip, J.R., 1971. General theorem on steady state infiltration from surface sources, with application to point and line sources. Soil Science Society of America Proceedings 35: 867–871.

Philip, J.R., 1980. Field heterogeneity: some basic issues. Water Resources Research 16: 443–448.

Philip, J.R. & D.A. de Vries, 1957. Moisture movement in porous materials under temperature gradients. Transactions of the American Geophysical Union 38: 222–231.

Piggin, I. & P. Schwertfeger, 1973. Variations in the albedo of wheat and barley crops. Archiv für Meteorologie, Geophysik und Bioklimatologie, Serie B, 21: 365–391.

Planet, W.G., 1970. Some comments on reflectance measurements of wet soils. Remote Sensing of Environment 1: 127–129.

Poulovassilis, A., 1962. Hysteresis of pore water, an application of the concept of independent domain. Soil Science 93: 405–412.

Pratt, D.A. & C.D. Ellyett, 1979. The thermal inertia approach to mapping of soil moisture and geology. Remote Sensing of Environment 8: 151–168.

Pratt, D.A., S.J. Foster & C.D. Ellyett, 1980. A calibration procedure for Fourier series thermal inertia models. Photogrammetric Engineering and Remote Sensing 46: 529–538.

Prevot, L., R. Bernard, O. Taconet, D. Vidal-Madjar & J.L. Thony, 1984. Evaporation from a bare soil, evaluated using a soil water transfer model and remotely sensed surface soil moisture data. Water Resources Research 20: 311–316.

Price, J.C., 1977. Thermal inertia mapping: A new view of the earth. Journal of Geophysical Research 82: 2582–2590.

Price, J.C., 1980. The potential of remotely sensed thermal infrared data to infer surface soil moisture and evaporation. Water Resources Research 16: 787–795.

Quirk, J.P., 1955. Significance of surface areas calculated from water vapor sorption isotherms by use of the B.E.T. equation. Soil Science 80: 423–430.

Raats, P.A.C., 1970. Steady infiltration from line sources and furrows. Soil Science Society of America Proceedings 34: 709–714.

Raats, P.A.C. & W.R. Gardner, 1971. Comparison of empirical relationships between pressure head and hydraulic conductivity and some observations on radially symmetric flow. Water Resources Research 7: 921–928.

Raats, P.A.C., 1975. Transformations of fluxes and forces describing the simultaneous transport of water and heat in unsaturated porous media. Water Resources Research 11: 938–942.

Raats, P.A.C., 1977. Laterally confined, steady flows of water from sources and sinks in unsaturated soils. Soil Science Society of America Proceedings 41: 294–304.

Rahi, G.S. & R.D. Jensen, 1975. Effect of temperature on soil water diffusivity. Geoderma 14: 115–124.

Rao, P.S.C., R.E. Jessup, A.C. Hornsby, D.K. Cassel & W.A. Pollans, 1983. Scaling soil microhydrologic properties of Lakeland and Konawa soils using similar media concepts. Agricultural Water Management 6: 277–290.

Rappoldt, C. & D.W.G. van Kraalingen, 1989. FORTRAN utility library TTUTIL. Internal Report nr 18, Dept. of Theoretical Production Ecology, Wageningen Agricultural University.

Rawitz, E., 1965. The influence of a number of environmental factors on the availability of soil moisture to plants. Ph.D. thesis Hebrew University, Rehovot, Israel.

Reginato, R.J., S.B. Idso, J.F. Vedder, R.D. Jackson, M.B. Blanchard & R. Goettelman, 1976. Soil water content and evaporation determined by thermal parameters obtained from ground-based and remote measurements. Journal of Geophysical Research 81: 1617–1620.

Reiniger, P., J. Huygen & J. Mégier & B. Seguin, 1982. Estimates of regional evapotranspiration in south-eastern France using thermal and albedo data from the heat capacity mapping mission satellite. Proceedings International Symposium of Remote Sensing of Environment 2: 1231–1238.

Reisenauer, A.E., 1963. Methods for solving problem of multidimensional partially saturated steady flow in soils. Journal of Geophysical Research 68: 5725–5733.

Richter, J., 1972. Zur Abhängigkeit des Bodenwasserpotentials von der Temperatur. Zeitschrift für Pflanzenernährung und Bodenkunde 131: 254–261.

Riha, S.J., K.J. McInnes, S.W. Childs & G.S. Campbell, 1980. A finite element calculation for determining thermal conductivity. Soil Science Society of America Journal 44: 1323–1325.

Ritsema, C.J., 1985. De invloed van de temperatuur op de bodemvochtspanning bij constant vochtgehalte. MSc thesis Wageningen Agricultural University, Dept. of Soil Science and Plant Nutrition.

Rose, D.A., 1963a. Water movement in porous materials. Part 1: Isothermal vapor transfer. British Journal of Applied Physics 14: 256–262.

Rose, D.A., 1963b. Water movement in porous materials. Part 2: The separation of the components of water movement. British Journal of Applied Physics 14: 491–496.

Rose, D.A., 1971. Water movement in dry soils. II. An analysis of hysteresis. Journal of Soil Science 22: 490–507.

Rosema, A., 1975. A mathematical model for simulation of the thermal behaviour of bare soils, based on heat and moisture transfer. NIWARS-publication No 11, Delft, The Netherlands.

Rosema, A., 1979. Thermal sensing of soil moisture, evaporation and crop yield. Communucation presented at the Ispra Course on the Application of Remote Sensing to Agricultural Production Forecasting, October 15–19, Ispra, Italy.

Rudraiah, N., B. Veerappa & S. Balachandra Rao, 1980. Effects of non-uniform thermal gradients and adiabatic boundaries on convection in porous media. Journal of Heat Transfer 102: 254–260.

Rudraiah, N., B. Veerappa. & S. Balachandra Rao, 1982. Convection in a fluid-saturated porous layer with non-uniform temperature gradient. International Journal of Heat and Mass Transfer 25: 1147–1156.

Russo, D. & E. Bresler, 1980. Field determinations of soil hydraulic properties. Soil Science Society of America Journal 44: 697–702.

Saha, R.S. & R.P. Tripathi, 1979. Effect of temperature on hydraulic conductivity of soil. Journal of the Indian Society of Soil Science 27: 220–224.

Shaykewich, C.F. & L. Stroosnijder, 1977. The concept of matrix flux potential applied to simulation of evaporation from soil. Netherlands Journal of Agricultural Science 25: 63–82.

Schieldge, J.P., A.B. Kahle, R.E. Alley & A.R. Gillespie, 1980. Use of thermal inertia properties for material identification. Society of Photo-Optical Instrumentation Engineers (SPIE) 238: 350–357.

Schurer, K., 1975. A method for measuring infrared emissivities of near-black surfaces at ambient temperatures. Infra Red Physics 16: 157–163.

Scotter, D.R., 1976. Liquid and vapor phase transport in soil. Australian Journal of Soil Research 14: 33–41.

Scotter, D.R. & P.A.C. Raats, 1969. Dispersion of water vapor in soil due to air turbulence. Soil Science 108: 170–176.

Sellers, W.D., 1965. Physical climatology. University of Chicago Press.

Sepaskhah, A.R. & L. Boersma, 1979. Thermal conductivity of soils as a function of temperature and water content. Soil Science Society of America Journal 43: 439–444.

Simmons, C.S., D.R. Nielsen & J.W. Biggar, 1979. Scaling of field-measured soil water properties. Hilgardia 47: 74–154.

Sisson, J.B., A.H. Ferguson & M.Th. van Genuchten, 1980. A simple method for predicting drainage from field plots. Soil Science Society of America Journal 44: 1147–1152.

Snedecor, G.W. & W.G. Cochran, 1967. Statistical methods. 6th edition. Iowa State University Press.

Sposito, 1986. The 'physics' of soil water physics. Water Resources Research 22: pp 83 S-88 S (supplement).

Staple, W.J., 1965. Moisture tension, diffusivity and drying. Canadian Journal of Soil Science 45: 78–85.

Staple, W.J., 1969. Moisture redistribution following infiltration. Soil Science Society of America Proceedings 33: 840–847.

Steinhorst, R.K., H.W. Hunt, G.S. Innis & K.P. Haydock, 1978. Sensitivity analysis of the ELM model. In: Grassland simulation model, Ecol. Studies 26. Ed. G.S. Innis, Springer New York.

Stigter, C.J., 1969. On measuring properties of soils by thermal methods with special reference to the contact method. Netherlands Journal of Agricultural Science 17: 41–49.

Stolp, J. & A.R.P. Janse, 1985. X-band radar backscatter for detecting spatial distribution of soil slaking. ITC-Journal, 1: 82–87.

Stroosnijder, L., 1982. Le milieu Sahelien et les terrains expérimentaux. In: La productivité des pâturages Sahelien, Eds. F.W.T. Penning de Vries et M.A. Djitèye, Pudoc, Wageningen.

Stroosnijder, L. & H.D.J. van Heemst, 1982. La meteorologie du Sahel et du terrain de l'etude. In: La productivité des paturages Saheliens, Ed. F.W.T. Penning de M.A. Vries & Djitèye, Pudoc, Wageningen.

Stroosnijder, L., R.J. Lascano, R.W. Newton & C.H.M. van Bavel, 1984. Estimating net rainfall, evaporation and water storage of a bare soil from sequential L-band emissivities. Proc. IGARSS '84. Symposium, Strasbourg 27–30 August 1984.

Taylor, S.A. & J.W. Cary, 1964. Linear equations for the simultaneous flow of matter and energy in a continuous soil system. Soil Science Society of America Proceedings 28: 167–172.

Taylor, S.A. & G.L. Stewart, 1960. Some thermodynamic properties of soil water. Soil Science Society of America Proceedings 24: 243–247.

Taylor, S.E., 1979. Measured emissivity of soils in the south-east United States. Remote Sensing of Environment 8: 359–364.

Tennekes, H. & J.L. Lumley, 1972. A first course in turbulence. MIT Press, Cambridge, Massachusetts.

Thom, A.S., 1975. Momentum, mass and heat exchange of plant communities. In: Vegetation and the atmosphere, Ed. J.L. Monteith, Academic Press, London.

Thomas, M.D., 1928. Aqueous vapor pressure of soils: 4. Influence of irreplaceable bases. Soil Science 25: 485–493.

Tomovic, R. & M. Vukobratovic, 1972. General sensitivity theory. American Elsevier Publishing Company, New York.

Tosi, N., 1983. A simulation model supporting HCMM investigation on geological objectives. International Journal of Remote Sensing 4: 353–369.

Tsang, L., E. Njoku & J.A. Kong, 1975. Microwave thermal emission from a stratified medium with non-uniform temperature distribution. Journal of Applied Physics 46: 5127–5133.

Unsworth, M.H. & J.L. Monteith, 1975. Longwave radiation at the ground. Quarterly Journal of the Royal Meteorological Society 101: 13–24.

Vachaud, G., 1966. Verification de la loi de Darcy generalisee et determination de la conductivité capilaire a partir d'un infiltration horizontale IHS Symp. Wageningen, 277–292.

Vauclin, M., R. Haverkamp & G. Vachaud, 1979. Resolution numerique d'une equation de diffusion non-lineaire. Presses Universitaire de Grenoble, France.

Vershinin, P.V., M.K. Melnikova & B.N. Michurin, 1966. Fundamentals of agrophysics; Translation US Dept. of Commerce.

Viswanadham, Y. 1982. Examination of the empirical flux-profile models in the atmospheric surface boundary layer. Boundary Layer Meteorology 22: 61–77.

Vleck, J. & D. King, 1983. Detection of subsurface soil moisture by thermal sensing: results of laboratory, close range and aerial studies. Photogrammetric Engineering and Remote Sensing 49: 1593–1597.

Vries, D.A. de, 1963. Thermal properties of soils. In: Physics of plant environment, Ed. W.R. van Wijk. North Holland Publishers, Amsterdam.

Vries, D.A. de, 1975. Heat transfer in soils. In: Heat and Mass Transfer in the Biosphere. Eds. N.H. Afgan & D.A. De Vries, Scripta Books.

Ward, N.R., G.G. Wilkinson, G. Dugdale & J.R. Milford, 1982. Soil moisture mapping in the Sahel by satellite. Proceedings of the Annual Technical Conference of the Remote Sensing Society, Liverpool.

Warrick, A.W., 1974. Time-dependent linearized infiltration. I. Point sources. Soil Science Society of America Proceedings 38: 383–386.

Warrick, A.W., G.J. Mullen & D.R. Nielsen, 1977. Scaling field measured soil hydraulic properties using a similar media concept. Water Resources Research 13: 355–362.

Warrick, A.W. & A. Amoozegar-Fard, 1979. Infiltration and drainage using spatially scaled soil hydraulic properties. Water Resources Research 15: 1116–1120.

Warrick, A.W. & D.R. Nielsen, 1980. Spatial variability of soil physical properties in the field. In: Applications of soil physics, Ed. D. Hillel, Academic Press, New York.

Wartena, L., 1973. Checking of some formulae for the calculation of longwave radiation from clear skies. Archief für Meteorologie, Geophysik und Bioklimatologie, Serie B, 21: 335–348.

Weeks, L.V., S.J. Richards & J. Letey, 1968. Water and salt transfer in soil resulting from thermal gradients. Soil Science Society of America Proceedings 32: 193–197.

Westcot, D. & P.J. Wierenga, 1974. Transfer of heat by conduction and vapor movement in a closed soil system. Soil Science Society of America Proceedings 38: 9–14.

Wierenga, P.J., D.R. Nielsen & R.M. Hagan, 1969. Thermal properties of a soil, based upon field and laboratory measurements. Soil Science Society of America Journal 44: 354–360.

Wijk, W.R. van, 1963. Physics of plant environment. North Holland Publishers, Amsterdam.

Wilkinson, G.E. & A. Klute, 1962. The temperature effect on the equilibrium energy status of water held by porous media. Soil Science Society of America Proceedings 26: 326–329.

Woodside, W. & J.H. Messmer, 1961. Thermal conductivity of porous media, (1) unconsolidated sands. Journal of Applied Physics 32: 1683–1699.

Index

Simulation Monographs 33

This book describes an analysis of processes and factors that affect the energy balance of bare soil, and the associated exchange of heat and moisture at the surface. After a brief treatment of basic transport theory, the processes of soil–atmosphere interaction are expressed in a simulation algorithm. This algorithm provides an instrument to study the 'conditioning' effect of soil on the lower atmosphere, and vice versa.
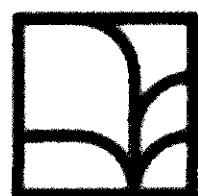
Examples of sensitivity analysis are presented, with emphasis on the behaviour of surface temperature. In remote sensing practice, surface temperature is estimated from thermal imagery; simulation algorithms can assist in its interpretation.

Field data of fluxes, state variables and soil properties are extensively discussed and are used to validate appropriate sections of the model.

The book provides a convenient introduction for meteorologists who wish to include soil processes in their studies, and for soil scientists interested in the basics of boundary-layer meteorology.